Biophysical studies on the structure and function of Archaerhodopsin-3

Javier Vinals Camallonga

St. Hugh's College

University of Oxford

Thesis submitted to the Board of the Medical Sciences Division in partial fulfillment of the requirements for the degree of

Doctor of Philosophy

Michaelmas 2019

To my family

Abstract

Light is indispensable for most life forms, and all organisms have evolved in order to harness or utilise its energy. Microbial rhodopsins are light-activated proteins that generate an electrochemical gradient across the membrane for vital functions of organisms. Recently, the use of light-activated proteins that generate an electrochemical gradient have gained attention in the field of optogenetics as tools to hyperpolarise or depolarise membranes, thus achieving neural silencing or as fluorescent voltage indicators, as well as in bioelectronics to develop biosensors or photovoltaic cells. Here we explore the biophysical characteristics of a microbial rhodopsin, AR3, resolving its structure for the first time, to give new insights into activity, and permit development of a mutant library of AR3, identifying target residues to achieve spectral tuning. This biophysical characterisation allows the identification of key molecules and networks that enhance the photocurrent of AR3 transferrable to other homolog microbial rhodopsins, thus providing new insights into better protein design for optogenetics and bioelectronics.

AR3 has been purified from its native organism (*Halorubrum sodomense*) and crystallised giving structures of the light-adapted (LA) state and the dark-adapted (DA) state with resolutions of 1.07 $\mathring{A}$ and 1.2 $\mathring{A}$, respectively. The resolution of these structures has allowed the identification of complex hydrogen bonding networks and residues important in ion transport, as well as water molecules. The differences between the DA and LA states have been also shown, as well as identifying key differences between AR3 and bR internal rearrangements. Furthermore, we use high-speed

AFM, serial crystallography and X-ray free electron lasers to identify conformational changes that take place in the protein during the photocycle in the early stages (using XFEL) and in the later stages (using HS-AFM).

AR3 has recently gained importance in the world of microbial rhodopsins due to its high photocurrent change upon illumination enabling neural silencing in optogenetics applications. Here we study the photocurrent properties of AR3 using a novel droplet interface bilayer system. We study the activity of AR3 over long periods of illumination and address the role that chromophores bound to the protein, such as retinal or bacterioruberin, might have in the photocurrent and bleaching of the protein.

Finally, we develop a mutant library of AR3 mutants with different spectral properties. We assess the proton pumping of the different mutants developed, as well as the photocurrent change and the action spectra, and study the effect in absorbance and photocurrent that different mutations have in key residues responsible for the proton pumping activity of the protein. Such mutants have potential applications for improved use in optogenetics, especially in red-shifted mutants.

Acknowledgements

Thank you, Tony, for giving me this wonderful opportunity to pursue a D.Phil in your laboratory at the University of Oxford. You gave me a chance to prove myself and achieve a dream of mine. These four years have been very challenging, but thanks to your help and support I have been able to get here, and I am forever grateful to you for believing in me.

I would like to thank Peter Judge for all his help during this degree. Peter you have been supportive and have helped me out whenever I needed it without question and I truly appreciate it. I truly appreciate your advice and counsel, and I believe I am a better scientist because of it. Also, I would like to thank Dr Juan Francisco Bada Juarez! Juan you have helped me and guided me every step of the way in the DPhil. You are such a great person, and a wonderful scientist, and I cannot wait to see what the future holds for you. I have truly enjoyed our talks about science, football or tennis, and having a friend like you is a treasure. I'd like to thank also Steven Lavington, and Henry Sawczyc. My DPhil companions throughout these tough years. Steve, I have learnt a lot from you, you are a great person and a very talented scientist that I have no doubt will do great things in the future. I have truly enjoyed our lunches with David, Juan and Florian, or our talks the last months of the DPhil to calm each other with the writing. Henry it has been great to get to know you. You are really great and fun to work with, you have helped me anytime if I needed help and you have been very supportive. You have been there whenever I have needed it and I am truly thankful for that.

Also thanks to many other members in the group that I have shared times during the years such as Mark Pfeil, Daniel Yin, Juan Carlos Munoz Garcia, Rosana Inacio dos Reis, Jason Yau, Felipe Santos Mendes, Peter

Fisher, Natalia Fontana, Costanze Cavalier, Juan Bolivar, and Claudia Cassidy. Thank you all for making my time at Oxford and the lab better than I could have asked for. Also, I would like to thank the students I have had throughout the years such as Owen Crowther, Sarah Frei, and Charlotte Hoskin. Owen it was incredible to work with you during your Master's thesis. You are incredibly hard-working, driven and curious which I believe will make you a top scientist. I learned a lot from you, and you made my experience in the lab and teaching very rewarding. I have no doubt that your DPhil will be fantastic, and I hope you enjoyed the time in the lab with me. Also thanks to Sarah, and Charlotte, although you were a few months in the lab, I really enjoyed working with you and I hope you learnt and enjoyed the experience.

I would also like to thank my collaborators. First, I would like to thank Dr Vanessa Restrepo-Schild, Charlotte-Hoskin, Prof Hagan Bayley for all the work done in the DIBs and electrophysiology. Vanessa and Charlotte working with you has been incredible. Our lunch meetings talking about experiments and brain storming ideas have been really fun. Thank you, Dr Isabel Moraes, for the X-ray crystallography work done here. For all the AFM work I'd like to thank Dr Pierre Emanuelle at Montpellier, and Dr Mikihiro Shibata at Kanazawa. Thank you for welcoming me into your city and laboratory and training me in the arts of AFM. For the XFEL work I'd like to thank also Dr Agata Butryn, Dr Danny Axford, and Dr Allen Orville as well as Dr Isabel Moraes. Moreover, this thesis could not be possible without the support and funding of the DSTL. Thank you very much for supporting these 4 years, and special thanks to Kenneth McEwan, Jonathan Piper, and Petra Oyston for their help and contact throughout these years.

Outside of work, I would like to thank all my friends in Oxford that have made my life much more fun outside the lab. David, Florian, Ulku, Joanna, St. Hugh's MCR people, Esther, Teresa, and many others, thank you very very much for making my experience at Oxford so wonderful and fun. I am very lucky to have you in my life.

Tambien me gustaria agradecer a todos mis amigos de Madrid su apoyo durante mi doctorado y todo mi tiempo en el extranjero. Vuestros mensajes y llamadas de Skype me han dado muchas fuerzas para seguir trabajando y llegar donde estoy. Cada vez que vuelvo a Madrid es como si nunca me hubiera ido, y solo vosotros podriais hacer eso. Muchisimas gracias!!

To Greta, I do not think I can put into words what you have done for me this DPhil. You have been my companion, my wisdom, and support through this. My DPhil would have been very bleak without you. This DPhil is partly yours.

A mis hermanos y hermanas Pepi, Claire-Elise, Alex, Rocio, Rafu y Micky. Muchisimas gracias por vuestra ayuda, consejo y apoyo durante todos mis años de estudio y vida en general. Soy muy afortunado de terner gente tan cojonuda a mi lado en mi vida. A mis sobrinos y sobrinas, os quiero mucho a todos y quiero que sepais que tambien me habeis ayudado mucho en este doctorado con vuestras sonrisas y amor.

Por ultimo me gustaria agredecer a mis padres, Rafaela y Jose. Cualquier cosa que ponga es poca. Vuestro sabio consejo y amor me han llevado en volandas toda mi vida. Cuando os he necesitado me habeis ayudado sin hacer preguntas ni reproches. Todo lo que hago en mi vida es para haceros orgullosos, y siempre intento ser la mejor persona que puedo ser como me habeis enseñado. Teneros como padres es el mayor regalo que me ha podido dar la vida.

List of Publications

Publications during Ph.D.

1. J. Segarra-Marti, R. Ramakrishnan, **J. Vinals**, A. J. Hughes. **Highlights from the Faraday discussion on photoinduced processes in nucleic acids and proteins**. *Chemical Communications*. 2018 54(34): 4207-4215.

Publications prior Ph.D.

1. Cassidy Hart, Nouf Abuladel, Madeleine Bee, Megan C. Kreider, Alexander C. CVitan, Moira M. Esson, Andrew Farag, Trisha Ibeh, Eleni N. Kalivas, Daniel-Mario Larco, Andrew Walker Long, Loukas Lymperopoulos, Zachary Mendel, Nancy Miles, Carly M. Zareba, James C. Schwabacher, Helen Slucher, **Javier Vinals**, John M. Heddleston, Wenyue Li, Douglas M. Fox and Matthew R. Hartings. **Protein-templated gold nanoparticle synthesis: protein organisation, controlled gold sequestration, and unexpected reaction products**. *Dalton Transactions*. 2017 46(47): 16465-16473.

List of publications in preparation

1. J. F. Bada Juarez, P. J. Judge, **J. Vinals**, D. Axford, A. Butryn, P. Aller, A. M. Orville, J. Birch, D. Sherrell, J. Beale, R. Owen, I. Moraes and A. Watts. **Working title: Detergent-free crystal structures of the dark- and light- adapted Archaerhodopsin 3, PDB 6GUX, 6GUY, and 6GUZ deposited August 2018**
2. **J. Vinals**, J. F. Bada Juarez, P. J. Judge, D. Axford, A. Butryn, P. Aller, A. M. Orville, J. Birch, D. Sherrell, J. Beale, R. Owen, E. Nango, T. Nakane, R. Tanake, S. Iwata, I. Moraes and A. Watts. **Working title: Study of the photocycle of Archaerhodopsin 3 using time-resolved serial femtosecond crystallography.**
3. **J. Vinals,** Charlotte Hoskin, Juan Francisco Bada Juarez, Vanessa Resterpo-Schild, Owen Crowther, Peter Judge, Mikihiro Shibata, Hagan Bayley, Anthony Watts. **Working title: Photocurrent and**

oligomeric state study of archaerhodopsin 3 from H.sodomense using droplet interface bilayer and high-speed atomic force microscopy

4. **J. Vinals,** Charlotte Hoskin, Juan Francisco Bada Juarez, Vanessa Resterpo-Schild, Owen Crowther, Peter Judge, Hagan Bayley, Anthony Watts. **Working title: Site-directed mutagenesis study of AR3 spectral properties and Proton Release Complex.**

Structures of Archaerhodopsin-3 deposited in Protein Data Bank

- PDB: 6GUX with a resolution of 1.3 Å
- PDB: 6GUY with a resolution of 2.2 Å
- PDB: 6GUZ with a resolution of 1.9 Å
- PDB: 6S6C with a resolution of 1.07 Å
- PDB: 6S63 with a resolution of 1.9 Å

Oral and Poster presentations

Oral presentations:

- 19^{th} IUPAB congress and 11^{th} EBSA congress in Edinburgh, UK (2017).
- Photoinduced Processes in Nucleic Acids and Proteins: Faraday Discussion congress in Kerala, India (2018).
- DSTL Synthetic Biology Showcase congress in Birmingham, UK (2018).
- 18^{th} International Conference on retinal proteins congress in Toronto, Canada (2019).
- Presentation at the Nano Life Science Institute at the University of Kanazawa in Kanazawa, Japan (2019).

Poster presentations:

- British Biophysical Society meeting in Liverpool, UK (2016)

- 19^{th} IUPAB congress and 11^{th} EBSA congress in Edinburgh, UK (2017).
- Photoinduced Processes in Nucleic Acids and Proteins: Faraday Discussion congress in Kerala, India (2018).
- DSTL Synthetic Biology Showcase congress in Birmingham, UK (2018).
- British Biophysical Society meeting in Southampton, UK (2018).
- 18^{th} International Conference on retinal proteins congress in Toronto, Canada (2019).
- 12^{th} and 10^{th} ICPB-IUPAB Congress in Madrid, Spain (2019).

Contents

List of Figures

List of Tables

List of abbreviations

∝HL Alpha hemolysin

ABC ATP-binding cassette

AFM Atomic force microscopy

ARs Archaerhodopsins

AR1 Archaerhodopsin-1

AR2 Archaerhodopsin-2

AR3 Archaerhodopsin-3

AR3 EC Archaerhodopsin-3 from *E. coli*

AR4 Archaerhodopsin-4

ATP Adenosine triphosphate

bR Bacteriorhodopsin

C-AFM Conductivity AFM

CD Circular Dichroism

CL Cardiolipin

ChR-2 Channelrhodopsin-2

DA Dark-adapted

DDM n-Dodecyl-β-D-Maltoside

DHB Droplet hydrogel bilayer

DIB Droplet interface bilayer

DLS Dynamic light scattering

DMPC 1,2-dimyristoyl-*sn*-glycero-3-phosphocholine

DPhPGLS O-phytanyl-*sn*-glycero-3-glycolipid sulphate

DPhPGP O-phytanyl-*sn*-glycero-3-phosphoryl-3'-sn-1'-phosphate

EBD Electron beam deposition

EM Electron microscopy

EPR Electron paramagnetic resonance

FTIR Fourier-transform infrared spectroscopy

GPI Glycosylphosphatidylinositol

GR *Gloeobacter violaceous*

GRAVY Grand average hydropathicity of the amino acids

H33342 2-(4-ethoxyphenyl)-5-(4-methyl-1-piperazinyl)-2,5-bi-1H-benzimidazole

HEK Human embryonic kidney

HR Halorhodopsin

H-AFM High-speed atomic force microscopy

IPTG Isopropyl β-D-1-thiogalactopyranosid

kDa Kilodalton

LA Light-adapted

LB *Luria bertani*

LCP Lipidic cubic phase

MFM Magnetic force microscopy

MSP Membrane scaffold protein

MWCO Molecular weight cut-off

NIR Near-infrared light

NMR Nuclear magnetic resonance

NpHR *Natromonas pharaonis*

OG N-Octyl β-D-glucopyranoside

ORF Open reading frame

PA Phosphatidic acid

PC Phosphatidylcholine

PDB Protein Data Bank

PE Phosphatidylethanolamine

PEG Polyethyleneglycol

PG Phosphatidylglycerol

PGP-ME Phosphatidyl glycerol methyl phosphate

PI Phosphatidyl inositol

PLB Planar lipid bilayer

PoXeR *Parvularcula oceani*

PR Proteorhodopsin

PRC Proton release complex

PS Phosphatidylserine

RBP Retinal binding pocket

SB Schiff Base

SEC Size-exclusion chromatography

SEM Scanning electron microscopy

SFX Serial femtosecond crystallography

SNR Signal-to-noise ratio

SPM Scanning probe microscopy

TIRF Total internal reflection fluorescence

UV-Vis Ultraviolet-Visible spectroscopy

w/v weight per volume ratio

XFEL X-ray free electron laser

XR Xanthorhodopsin

Chapter 1

Introduction

1.1 Biological membranes

1.1.1 Membrane features

All living organisms have biological membranes that separate the intracellular space from the extracellular space [1]. These membranes are composed of a diversified set of lipids, proteins and carbohydrates, and they act as barriers between different chemical environments [1, 2]. Each membrane has a different composition that varies depending on the organism, type of cell, or sub-cellular compartment [3, 4]. The uniqueness of each membrane makes them very challenging to study because defining their main purpose as mere structural barriers does not encompass their multiple functions [1, 5].

The fluid mosaic model (Figure 1.1) captures the high dynamicity of the constituent molecules of biological membranes [6, 7]. The principal constituents are amphiphilic lipids, which form bilayer structures in aqueous environments. Lipids establish these structures by arranging themselves on two layers, in which their hydrophobic components face each other on the inside and their polar parts face the aqueous phase outside [6, 7, 8]. Integral proteins insert themselves within this bilayer

structure and are thus stabilised by the hydrophobic contacts with the lipids ("Van der Waal forces"). Since hydrophobic interactions are non-covalent, the lipids and proteins are free to move and undergo conformational changes within the membrane [1, 2, 8].

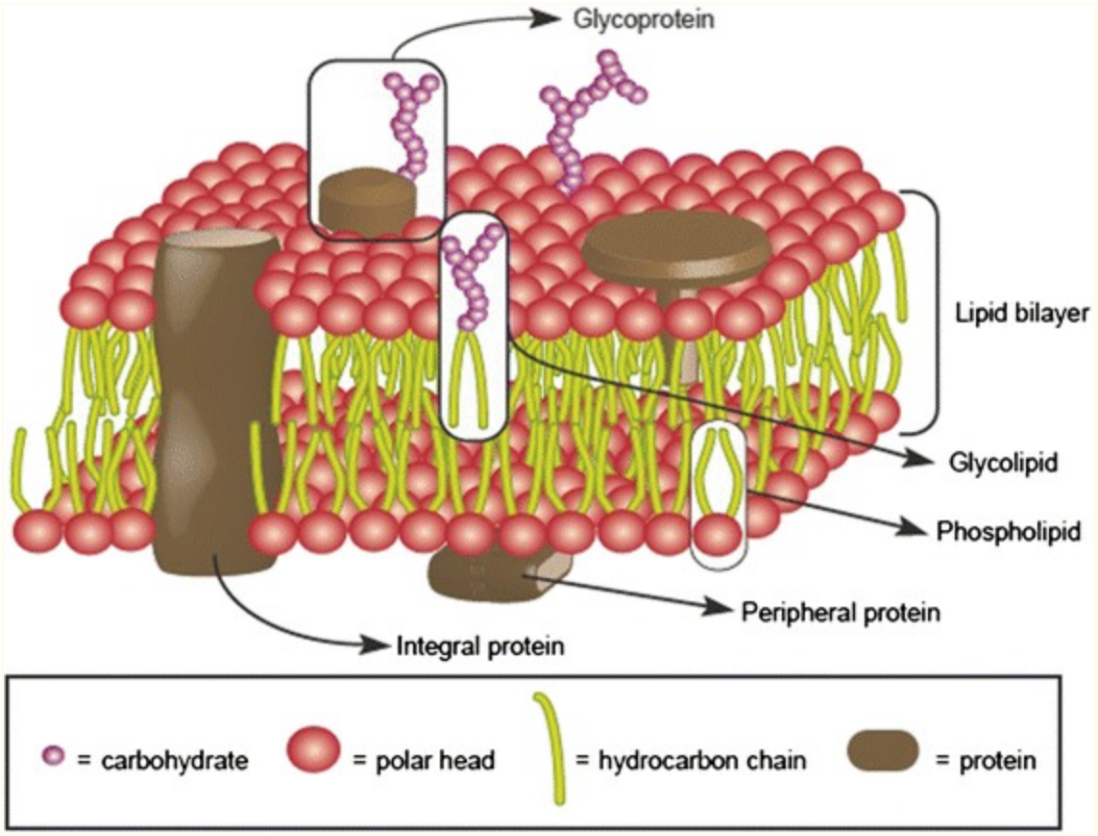

Figure 1.1: **Fluid mosaic model.** Illustration of a biological membrane where different molecules and integral proteins insert themselves into a lipid bilayer. Reproduced from [9].

.

1.1.2 Lipids

Lipids are the most abundant molecule type in membranes by number (around 40,000 different lipids are known) [10, 11]. They have a wide range of functions beyond structural, ranging from signalling activity to acting as energy sources, and they are

chemically diverse [12, 13, 14]. Within a single biological membrane, we can commonly find hundreds of chemically distinct lipids, that differ in many ways, from their headgroup, to the length of their acyl chain, or even in the number of double bonds present [12, 13, 14]. Despite this variety, the lipids found in biological membranes generally fall in one of three categories:

- Glycerophospholipids
- Sphingolipids
- Sterols

Glycerophospholipids generally present a structure built around a glycerol molecule that acts as a connector between the headgroup and the hydrophobic tail [1, 3]. The headgroup usually possesses a phosphate group esterified to the glycerol molecule, meanwhile two acyl or alkyl chains are esterified (Figure 1.2)[1, 2, 6]. Although all glycerophospholipids share the same structural template, the heterogeneity of the headgroups and, the lengths and composition of the acyl or alkyl chain creates a lot of diversity among them. The most common headgroups are phosphatidic acid (PA), phosphatidylserine (PS), phosphatidylinositol (PI), phosphatidylcholine (PC), phosphatidylethanolamine (PE), phosphatidylglycerol (PG), and diphosphatidylglycerol (CL or cardiolipin)[1, 2, 6]. These different headgroups provide important chemical and biological properties to glycerophospholipids [15]. They are further grouped into anionic (PS, PI, PG, and CL), which have a negative charge at neural pH, and zwitterionic (PE, PC) [6, 16, 17].

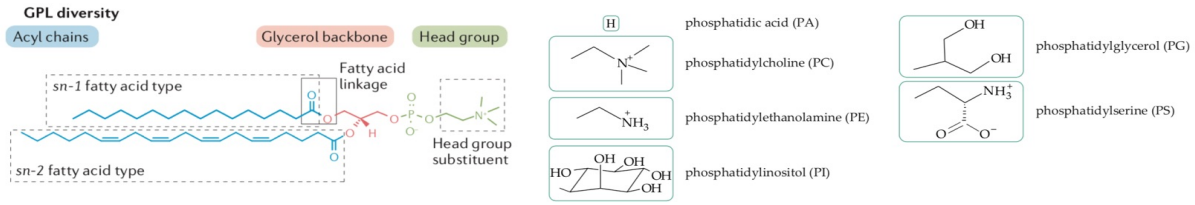

Figure 1.2: **Glycerophospholipid diversity.** Illustration of the glycerophospholpids backbone and the most common headgroups found in eukaryote. Adapted from [1, 18].

The second type of lipid are the sphingolipids. In sphingolipids, a sphingosine is linked to an acyl chain through an amide bond, while a phospho-ester linkage connects it to a headgroup (Figure 1.3) [19]. A special characteristic of sphingolipids is their capacity to form hydrogen bonds since they possess both an amide linkage and a hydroxyl group which contribute to the hydrogen bonding network in membranes, making them a more compact assembly [19, 20]. The most commonly occurring sphingolipid is sphingomyelin, mostly found in mammalian cells [21]. Finally, the third type of lipids are sterols, which are derived from isoprene [22]. A notable sterol found in eukaryotes is cholesterol (Figure 1.3), widely found in animal membranes [23].

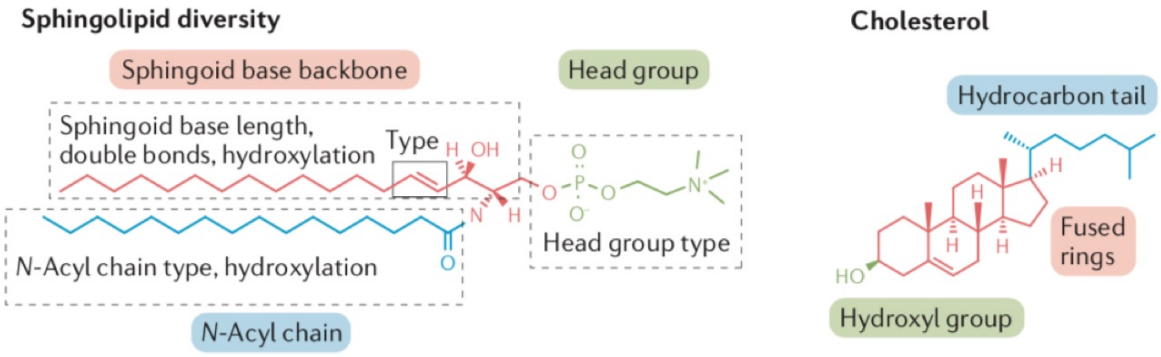

Figure 1.3: **Sphingolipids and Sterols.** Illustration of the backbone that makes up sphingolipids, and the right panel is showing cholesterol, the most common sterol in mammalian cells. Reproduced from [1].

The variety of lipid structures has an effect on the function of membranes, their curvature and their dynamics [24, 25]. The composition of membranes among different cells and organelles varies widely [16, 17]. Within the three domains of life, Eukarya and Bacteria share the features described above, meanwhile the Archaeal lipids differ significantly.

1.1.2.1 Archaeal Lipids

Many extremophiles can be found in the Archaeal phyla that can grow in extreme conditions where high concentrations of salt, or temperature as high as 110°C are found [26, 27]. Different studies have pointed to the lipids found in the membrane to be the key for these organisms to withstand such harsh conditions [27, 28]. The lipid composition of Archaea differs from those found in Eukarya or Bacteria in the ether linkage of isoprenoid chains to glycerol-1-phosphate with an *sn*-2 stereochemistry (Figure 1.4) [27, 29]. The headgroups do not change between the three domains of life (Figure 1.2), but further modification such as sulfonation or methylation is found [29, 30].

The variety of lipids in Archaea (Figure 1.4) is very rich, ranging from different length, presence of cyclopentane rings or constitution [27, 29]. Among the different lipids, the diether-structure lipids, also known as 'archaeols', are the most widespread [27, 29]. The saturated alkyl chains found in some organisms in Archaea play an important role in organisms living in high temperature environments, having a thermal stability as high as 100°C compared to those found in Bacteria that occur from -20°C to 60°C. Studies in liposomes constituted of POPC, or lipids found in *S. acidocaldatius* showed the endurance of the archaeal lipids compared to those of POPC at 100°C

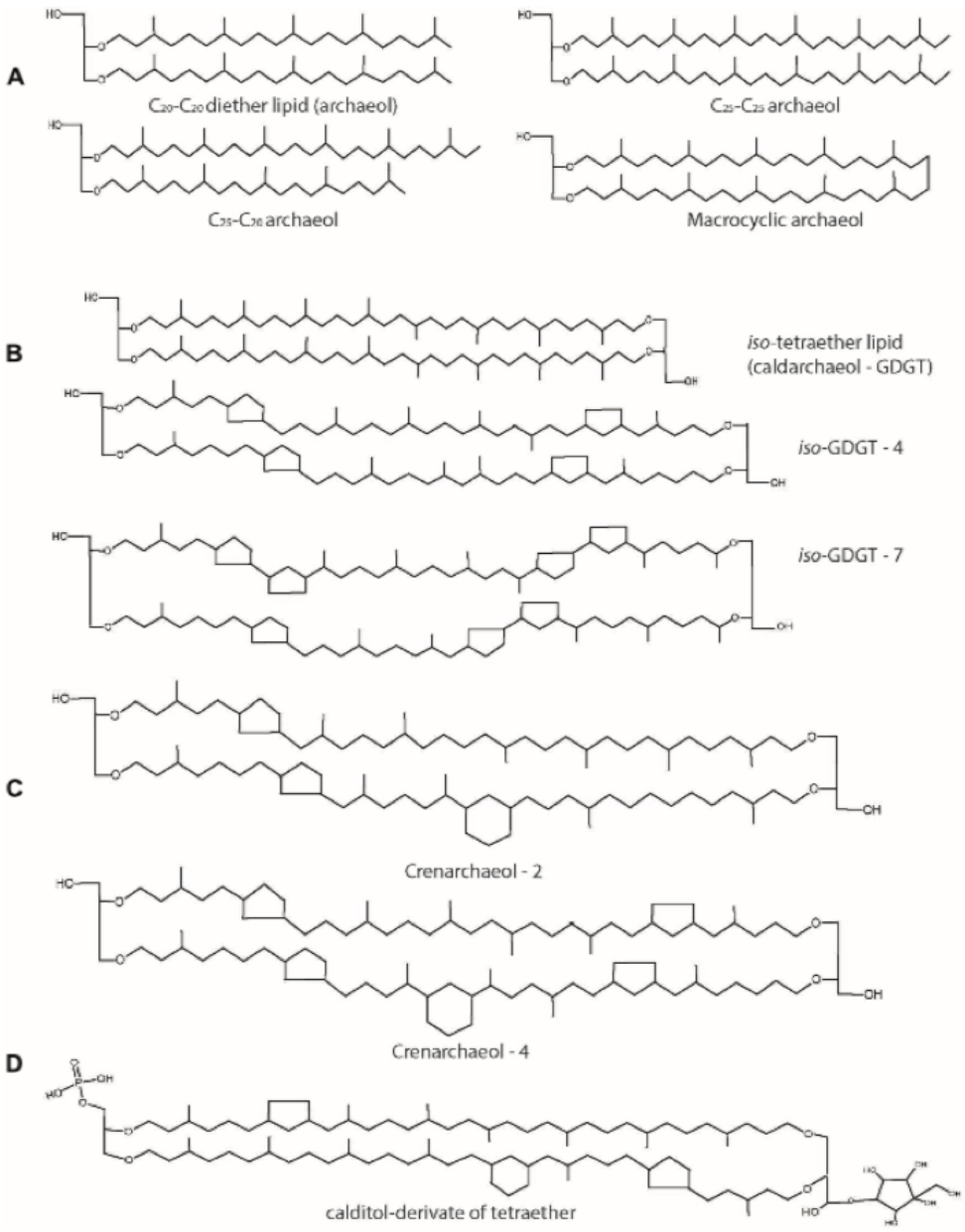

Figure 1.4: **Archaeal lipids.** a) Archeol lipids. b) Tetraether lipids. c) Crenarcheol lipids. d) Calditol lipids. Reproduced from [29].

where they degraded [31]. Additionally, headgroups have been shown to be important for the organisms survival in extreme conditions [29]. In high salt concentration environments, it has been shown that the lipid phosphatidylglycerol methyl phosphate (PGP-ME) contributes to the stability of the membrane and prevents aggregation

due to steric repulsion forces by the head group [32].

1.1.3 Membrane asymmetry

Asymmetry is mandatory in biology. Membranes are no exception and have been shown to have an asymmetric lipid composition in their two leaflets (inner and outer). One case of this asymmetry is observed in *Halobacterium salinarum* membranes, where the inner leaflet is more negatively charged than the outer leaflet at neutral pH establishing a dipole moment in the membrane believed to help in the oligomerisation of bacteriorhodopsin [33]. Asymmetry is believed to have a biological purpose for different cellular mechanisms such as apoptosis, controlling the membrane potential or strengthening the lipid bilayer [34, 35, 36].

Lipids can freely move within the membrane in three different ways; rotation, lateral diffusion (discussed in Section 1.1.2) and transverse diffusion (flipping). Flipping movement is the crossing of lipids from one leaflet to the other in the membrane [37]. Compared to the other movements, the rate of exchange in the flip movement is considerably slower due to it being dependent on the size, charge and polarity of the headgroup [38].

Membranes use the help of specific enzymes called 'flippases', that assist in the flipping of lipids from one leaflet to the other [39, 40]. In eukaryotic membranes, there are three different types of protein involved in flipping: ATP-binding cassette transporter (ABC transporters), aminophospholipid translocase, and Ca^{2+} dependent scramblase protein (Figure 1.5) [41]. ABC and aminophospholipid translocase use the ATP hydrolysis to transport lipids. ABC transports lipids from the inside to the outside of the membrane, meanwhile aminophospholipid translocase transports

lipids from the outside to the inner leaflet [42]. The third player, Ca^{2+} dependent scramblase protein, is independent of the direction to transport lipids, being able to transport lipids from one leaflet to another no matter what the direction is [43, 44].

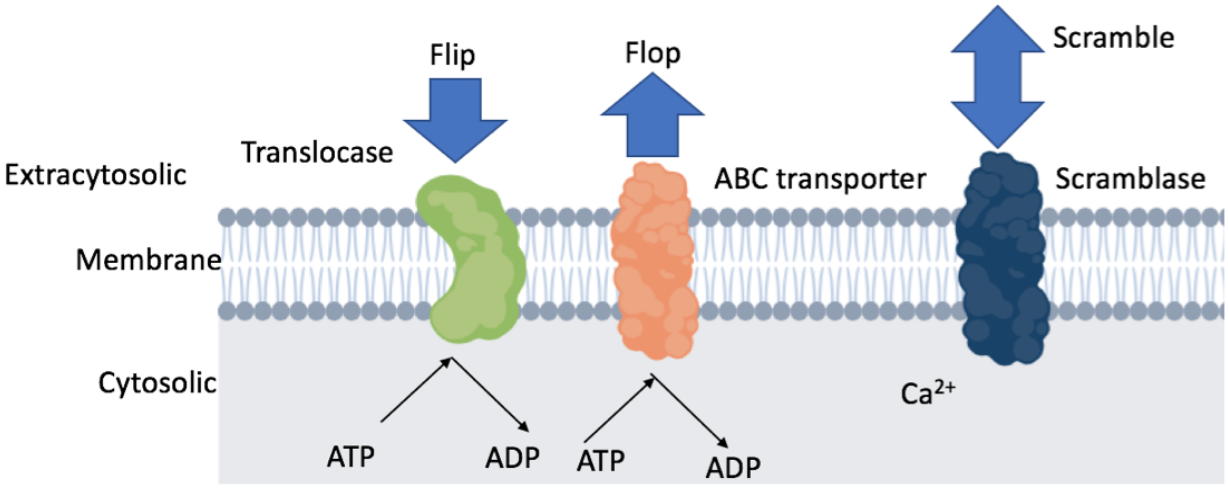

Figure 1.5: **Membrane asymmetry**. Illustration of lipid asymmetry and the different flippases present in the membrane that help the membrane to achieve this asymmetry.

Another consequence of membrane asymmetry is its modulation in membrane protein activity [45]. Electrostatic interactions are important for the binding of some proteins to biological membranes, and therefore the net charge and lipid composition of the leaflet plays a role in protein-protein interactions, as in the binding of cytochrome c and the lipid content, therefore modulates this coupling [45, 46]. Lipid asymmetry is important for many cellular mechanisms and protein modulation, and further studies that might shed some light and knowledge on this subject are a pressing need.

1.2 Membrane proteins

1.2.1 Introduction

Membrane proteins perform many different roles in cellular processes, from signal transduction to ion transport or cell to cell transmission, and represent ∼30% of the proteome [47]. In the pharmaceutical world, they are the target for ∼60% of known drugs [47, 48, 49]. Although promising, this area of work is challenged by a limited availability of known atomic structures [49]. Membrane proteins are usually classified into integral, and peripheral proteins, distinguished as intrinsic or extrinsic respectively according to the fluid mosaic model (Figure 1.1) based on their isolation accessibility [48].

Extrinsic proteins interact with the biomembrane via electrostatic interactions, hydrophobic interactions and hydrogen bonds [48, 6]. In contrast to intrinsic proteins, extrinsic proteins do not insert themselves into the bilayer [48]. Typically, their binding is to anionic lipids or charged residues [50, 51]. As an example, cytochrome c associates with the membrane through the interaction between its lysine cluster with anionic lipids [46, 52]. In many cases, proteins bind reversibly and regulate the activity of peripheral proteins [46, 52]. These proteins are known as amphiphilic, and regulation of the binding can be affected by substrates, effector molecules or ion presence [48].

An important type of extrinsic protein is the lipid-anchored protein. In this case, the protein is bound to the membrane through a glycosylated derivative of the lipid phosphatidylinositol (GPI) [53]. The lipid is bound to omega sites close to the C-terminus of the protein through an ethanolamine moiety, which anchors the protein

due to the interactions with the hydrophobic core of the bilayer [54, 55]. GPI proteins are frequently found in eukaryotes, constituting 0.5% of all eukaryotic proteins. The roles of these proteins vary from having a role in embryogenesis, to viability in fungi [53, 56].

Integral membrane proteins can only be removed from the membrane using detergent, organic solvents or polymers [57, 58]. They span the membrane so that their hydrophobic core is within the hydrophobic core of the lipid bilayer [6]. To date, most proteins with these characteristics found span the membrane with alpha helices or with numerous beta sheets [6, 57]. Their functionality ranges from transporters, receptors or photoreceptors. In this thesis, we will focus on this kind of proteins, specifically microbial rhodopsins.

1.2.2 Lipid-Protein interactions

Although lipids are essential in forming biological membranes, the functional specificity of most membranes is provided by proteins, and how their interactions with lipids might be crucial to get the whole picture [59]. In terms of membrane proteins, there are three different classes of lipids; annular lipids, non-annular lipids and bulk lipids [60, 61, 62]. Lipids present in the biological membrane, but not in proximity with membrane proteins are not affected by membrane proteins. On the other hand, the effect of membrane proteins on annular lipids (lipids around the membrane protein) are considerable [63].

Several studies have demonstrated that some proteins require specific lipids not only to facilitate insertion into the membranes and organisation, but also to regulate their function [64, 65]. For example, studies have shown the importance of lipid

interactions and bacteriorhodopsin (bR) for oligomeric organisation and the proton translocation activity of bR [66, 67, 68, 69]. The study of annular lipids have been mainly addressed through techniques such as electron paramagnetic resonance (EPR) and nuclear magnetic resonance (NMR) [63, 70].

Another type of lipid important in membrane proteins are the non-annular lipids. These lipids are deeply bound and embedded within membrane proteins in crevices or binding pockets, and they are also called lipid cofactors, as they are key in many proteins for their function [60, 61, 62, 71]. Many crystallographic studies with high resolution structures show the presence of these lipids within the membrane protein (Figure 1.6), suggesting a role in the structure of the protein as well as in their activity, although identification and characterisation is often incorrect [72, 73].

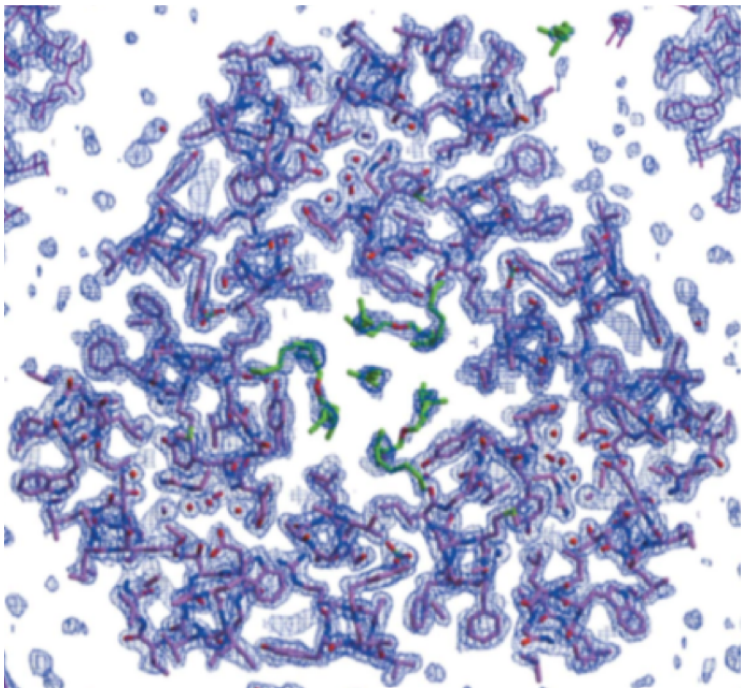

Figure 1.6: **Lipids within membrane proteins.** Lipid molecules (green) found in the trimer of archaerhodopsin-2 (AR2) represented in stick (blue). Electron density is represented by blue mesh. Lipids are represented by sticks (green) and are found in the middle of the trimer. Reproduced from [74].

1.2.3 Microbial Rhodopsins

Light is indispensable for most life forms, and all organisms have evolved in order to harness its energy. Microbial rhodopsins evolved to harness light energy through conformational changes within the protein scaffold [75]. Microbial rhodopsins are widespread, and there are more than 7000 different types in prokaryotic organisms [75]. Microbial rhodopsins have evolved to bind chromophores, most usually retinal molecule (vitamin A aldehyde), to absorb light at specific wavelengths in the visible range (Figure 1.7) [76].

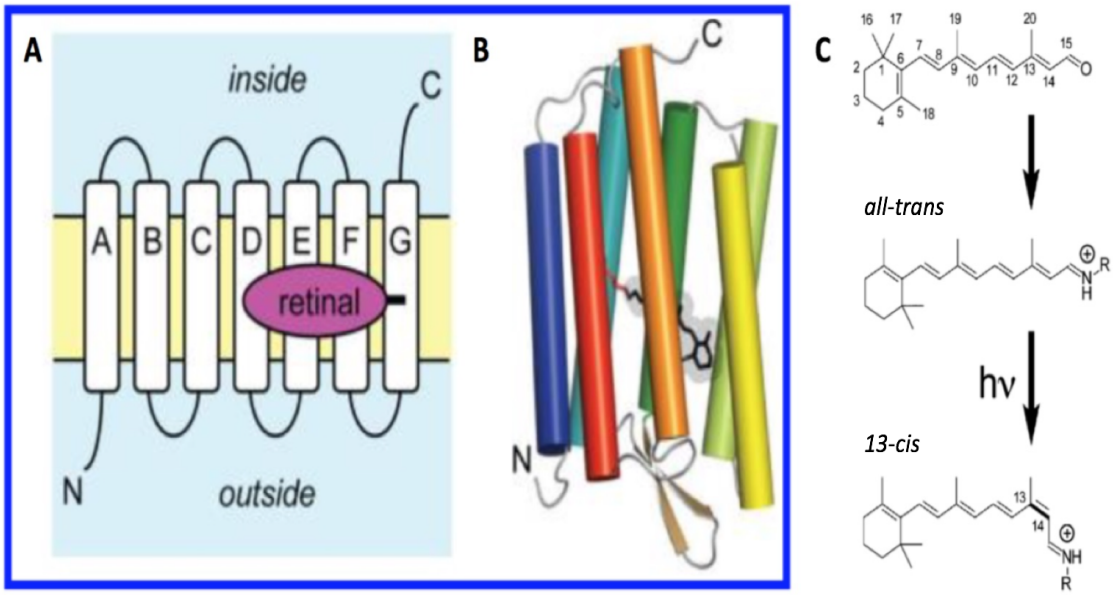

Figure 1.7: **Microbial rhodopsins.** A,B) Pictorial representation of a typical microbial rhodopsin with seven alpha helices spanning the transmembrane, with retinal covalently conjugated to the protein C) retinal isomerizes upon illumination going from an *all-trans* to a *13-cis* retinal. Reproduced from [77, 78].

The first microbial rhodopsin discovered was bacteriorhodopsin (bR) found in 1971 in the archaeal strain of *Halobacterium salinarum* [79]. Bacteriorhodopsin has been studied extensively due to its characteristics and its thermal and chemical stability, making it a good model for membrane protein structural studies. Microbial

rhodopsins have become a model in general for membrane proteins, and numerous biophysical methods have been developed using these proteins such, as electron microscopy (EM), atomic force microscopy (AFM), nuclear magnetic resonance (NMR), electron paramagnetic resonance (EPR) or X-ray crystallography [77].

Although microbial rhodopsins are very diverse in their structure and functionality, they share some features. These proteins are always integral membrane proteins spanning the membrane with seven alpha helices (Figure 1.7) [78]. Furthermore, they share a conserved lysine residue in the seventh helix to which the chromophore covalently binds through a Schiff base [76]. The chromophore bound to the protein is a derived aldehyde Vitamin-A also known as retinal. Retinal can be present in many isomeric forms (Figure 1.7) [76]. One form which is its most stable in organic solvents is the *all-trans* configuration, absorbing blue light [79]. When retinal is integrated in the protein, there is a spectral shift in the absorbance towards the red light, and this shift is known as an opsin shift [80]. Upon illumination, the retinal undergoes isomerisation from *all-trans* to *cis* configuration or from *cis* to *all-trans* configuration depending on the protein (Figure 1.7) [80]. This isomerisation triggers conformational changes throughout the entire protein, and distinct photo-intermediates have different absorption to specific wavelengths of light. This process is vital to the protein activity, such as ion transport, light-activated enzyme or photosensor [81].

Primarily, the activities of microbial rhodopsins are divided into:

- Photoenergy transducers; the protein harnesses energy from light via an electrochemical gradient to power the cell [75].

- Photosensors; the protein detects light levels to enable the organism to regulate its tactic behaviour and metabolism [75].

Microbial rhodopsins are very similar to visual pigments found in animals, and their structure and mechanisms are quite similar even though there is no common evolutionary origin [75]. Rhodopsins have been categorised into type I and type II rhodopsins [82]. Type I rhodopsins have *all-trans* retinal in its dark state. Within the type I rhodopsins, the most common proteins are those that act as light-driven pumps in prokaryotes with a function of photoenergy transducers (Figure 1.8) [83]. Although there are many different pumps such as sodium pumps, chloride pumps and proton pumps, this thesis will mainly focus on proton pumps.

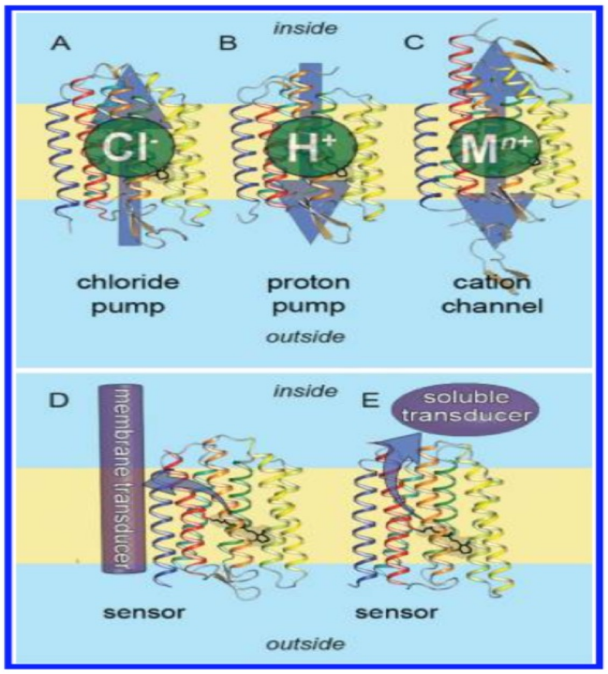

Figure 1.8: **Microbial rhodopsins diversity.** Illustration of the different functions found in microbial rhodopsins. A) inward chloride pump (halorhodopsin). B) outward proton pump (bacteriorhodopsin) C) cation channel (channelrhodopsin) D) photosensor stimulating transducer in bilayer (sensory rhodopsin II) E) photosensor stimulating transducer in cytoplasm (*Anabaena* sensory rhodopsin). Reproduced from [77].

The protein scaffold where the retinal is found in the protein is of great importance for the proteins activity. Across different microbial rhodopsins, the pocket where the retinal is found is highly conserved in a wide range of proteins [84]. The amino acids around the retinal binding pocket are key to the spectral characteristics, performing the photocycle, and their orientation and position are in many ways the basis of protein activity [75, 79, 85]. The retinal pocket determines the absorbance of the protein, and through different mutations a shift in the spectral absorbance of the protein towards the blue light (hypsochromic shift) or towards the red light (bathochromic shift) is achievable [86, 87]. Single mutations can be critical to the function of the protein, but also it can be critical to the absorbance of the protein since small changes in the side chains of the amino acids can alter the conformation of the retinal within the protein [88].

1.2.3.1 Bacteriorhodopsin

Halobacterium salinarum is a halophile that lives in lakes with high concentrations of salt and gives these lakes a purple characteristic colour due to the presence of bacteriorhodopsin in its membranes (Figure 1.9) [75]. Bacteriorhodopsin is found in domains within the archaeal plasma membrane called purple patches and is the only protein in these domains [89]. Together with some specific lipids in these domains, a 2-D matrix is formed where the protein is organised into functional trimers [89, 90]. The quantity of bacteriorhodopsin, together with the fact that is the only protein available in these patches facilitates its purification, even without detergent [89, 90].

bR is a photoreceptor that absorbs light via its retinal bound chromophore and triggers a proton translocation through the protein resulting in the transportation of

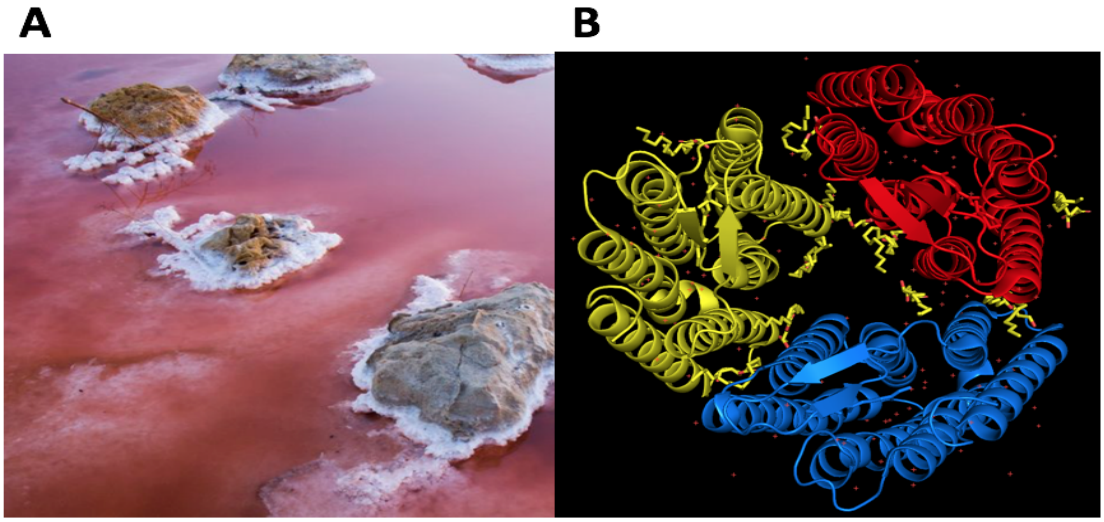

Figure 1.9: **Bacteriorhodopsin.** A) Depiction of a typical pink salt lake with bacteriorhodopsin B) Structural model of bacteriorhodopsin (PDB: 5ITC) in a trimer organisation (protein is represented in cartoon representation and lipids represented in sticks). Reproduced from [91].

protons out of the cells [92]. This generates a proton gradient across the membrane that is used by ATP synthase to synthesise adenosine triphosphate (ATP), and other transport reactions in the organism [93].

Electron microscopy (EM) revealed for the first time in 1975 that bR is an integral membrane protein that spans across the membrane with seven transmembrane helices (Figure 1.9) [94]. Its molecular weight is 27 kilodaltons (kDa) with 248 amino acids making up the protein [95, 96]. Since then, more than 126 structures of bR have been solved by (Figure 1.9) different techniques and submitted to the Protein Data bank (PDB) [89]. Several techniques including EM and X-ray crystallography showed how the retinal is sitting in the protein within the helices transversely bound through a Schiff base to a lysine residue (Lys 216) [89]. Furthermore, these techniques showed the organisation of the protein in the 2-D crystalline array in the *H. salinarum* membranes, and the specificity of the lipids within (Figure 1.9) [90, 97]. The organisation

in the membrane is about 1:9 protein/lipid ratio [94]. Crystallographic studies show there are around 30 lipids per trimer in the crystalline array, and 9 lipids per monomer where four would be in the cytoplasmic side, and other 5 would be in the extracellular side [98, 99]. These lipids are called archeol lipids (Figure 1.4) with the majority being polar lipids differing from other well-known lipids in the headgroups and not necessarily in the extent of the acyl chain, derived from a glycerol diether 1,2-di-O-phytanyl-*sn*-glycero-3-phosphoryl-3'-*sn*-1'-phosphate (DPhPGP) and a glycolipid sulphate (DPhGLS) [98, 100].

Upon illumination of bR (570nm), the retinal within the protein undergoes isomerisation which triggers a series of conformational changes in the protein that lead to proton translocation (Figure 1.10) [89]. Together the intermediates comprise the bR photocycle [101]. All these intermediates have different spectral properties [102]. The photocycle begins with the isomerisation of the retinal that changes from an *all-trans* configuration to a *13-cis* configuration [89] within picoseconds to produce the K (590 nm) intermediate [101]. Following this isomerisation, there is a disruption of a hydrogen bonding network due to the displacement of a water molecule (Wat-402) leading to the disconnection of the Schiff base and residue D85, accepting this proton from the Schiff base (L state with an absorbance maximum of 550 nm, Figure 1.10) [103].

The photocycle proceeds from the L to the M (410 nm) where the release of a proton from the proton release complex (PRC) composed by residues R82, E194, E204 to the extracellular side takes place [89, 105, 106]. At this point there is a proton switch where the Schiff base is disconnected from D85 and is reprotonated by the

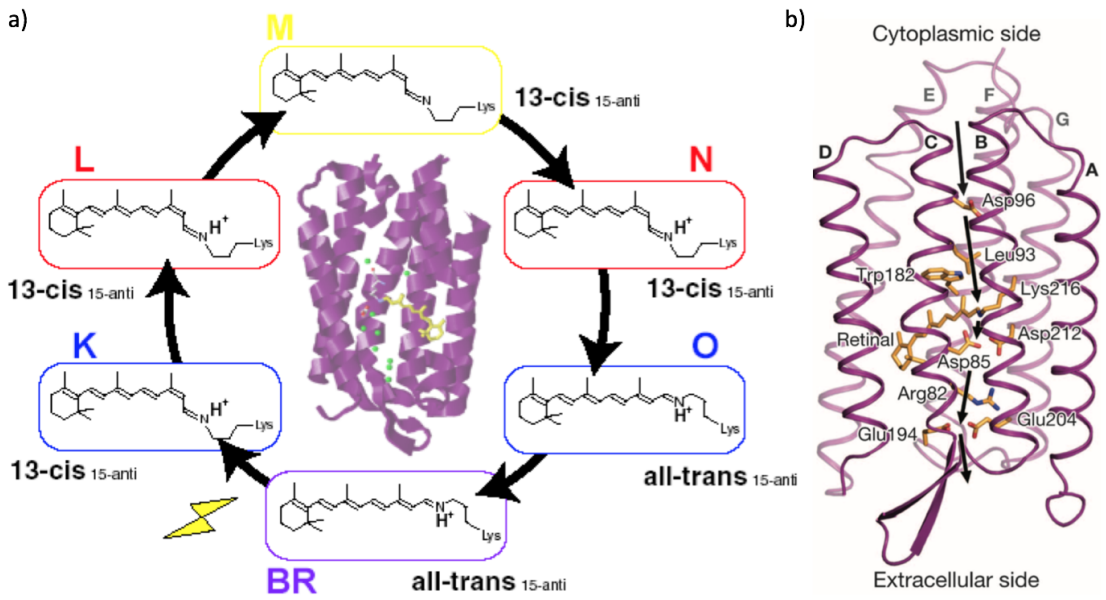

Figure 1.10: **Photocycle of bR.** a) photocycle of bacteriorhodopsin with all the different photo-intermediates b) Structural model of bacteriorhodopsin where different amino acids involved in the proton transfer are shown. Moreover, the direction of the proton transport is shown by an arrow on the left. Reproduced from [101, 104].

nearby residue D96 (N intermediate with an absorbance maximum of 560 nm, Figure 1.10) [107]. Continuing the photocycle, the retinal isomerizes back to an *all-trans* conformation (O state with an absorbance maxima of 640 nm) and the residue D85 is deprotonated by transferring a proton to the PRC concluding the photocycle and bringing the protein back to its initial ground state (Figure 1.10) [108]. Thanks to these extensive studies and chemical stability, microbial rhodopsins have found use in technical applications in bioelectronics or developing revolutionary techniques such as optogenetics [109, 110].

1.2.3.2 Bioelectronics

In the recent years, the technological advances in the field of electronics and silicon devices has taken a big leap forward, and its development has accelerated as the

size of these devices has decreased [109]. This miniaturisation has been one of the driving forces in the field so that these devices can be implemented and used in cell phones, cars or computers [109]. Unfortunately, Moore's Law predicts the doubling of transistors every year, but by the year 2030 silicon devices will have reached their miniaturisation limit [109, 111]. As an alternative, scientists are incorporating biology into electronics to surpass this problem and optimise electronic devices [109, 111]. Thanks to evolution, nature has developed molecules and 'machinery' at the nanoscale level which can be taken and used for our advantage [109]. Through a bottom-up approach and using synthetic biology, we can build nanostructures to solve our needs with a level of control not achieved before, through the design of molecules residue by residue, or atom by atom [109, 111].

bR has been extensively studied and used in bioelectronic applications. This protein is ideal due to its efficiency to harness solar energy while having a chemical and thermal stability capable of withstanding changes in pH, temperatures of 80 °C, or humid and dry conditions [109]. The applications where bR has been used ranged from biosensors and photovoltaic cells, to biomedicine and retinal implants, with patents filed using bR [112, 113, 114].

Our dependence as a society on computers has pushed for the application and integration of bacteriorhodopsin into the computing discipline [109]. This application takes advantage of the distinguishable photo-intermediates that appear on bR [115]. The idea is to have a medium of bacteriorhodopsin attached to a polymer base and play with the resting state of bR and the Q state of the photocycle, mimicking a binary code where the resting state is 0 and the Q state correspond to 1 (Figure

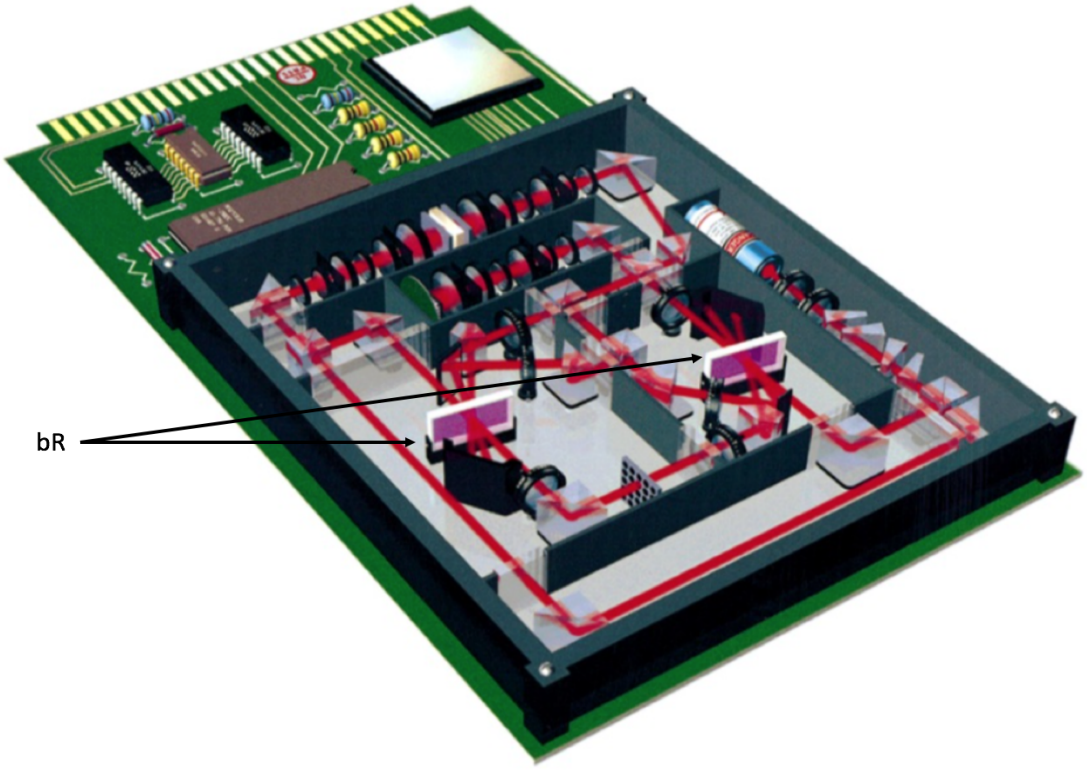

Figure 1.11: **Electronics and bR.** This is a representation of bR being used in electronics as a holographic memory using two different bR films. Reproduced from [115].

1.11) [115, 116, 117]. The protein therefore has a high storage ability in a very small volume, and allows for high-speed recordings based on the quick photochemistry of the protein [109, 115, 116, 117].

Another application of bR has been implemented into retinal implants for degenerative diseases [118]. This technology consists of implanting bR coupled to a biocompatible material to restore the proton gradient needed for the neural network [118, 119]. Retinal degenerative diseases are a very complicated condition to treat due to the individuality of each case, and the application of bR could facilitate in this endeavour [109, 118, 119].

1.2.3.3 Optogenetics

Around 14 years ago a paper was published in Nature in 2005 that revolutionised the field of neuroscience among the field of photoreceptors. In this article, Karl Deisseroth, Ed Boyden and Ernst Bamberg among others showed how we could activate neurons in a network through light with a photoreceptor called Channelrhodopsin-2 (ChR-2) [110]. Not only did the paper show this was possible, but did it in a non-toxic manner in mammalian cells, using light to trigger an action potential in neurons capable of stimulating the neuronal network (Figure 1.12) [110, 120]. Following this work, neuron silencing using light and chloride pumps was demonstrated in 2007 [121]. In 2010 this method, known as Optogenetics, was proclaimed by Nature and Science as the 'Method and Breakthrough of the decade' [122].

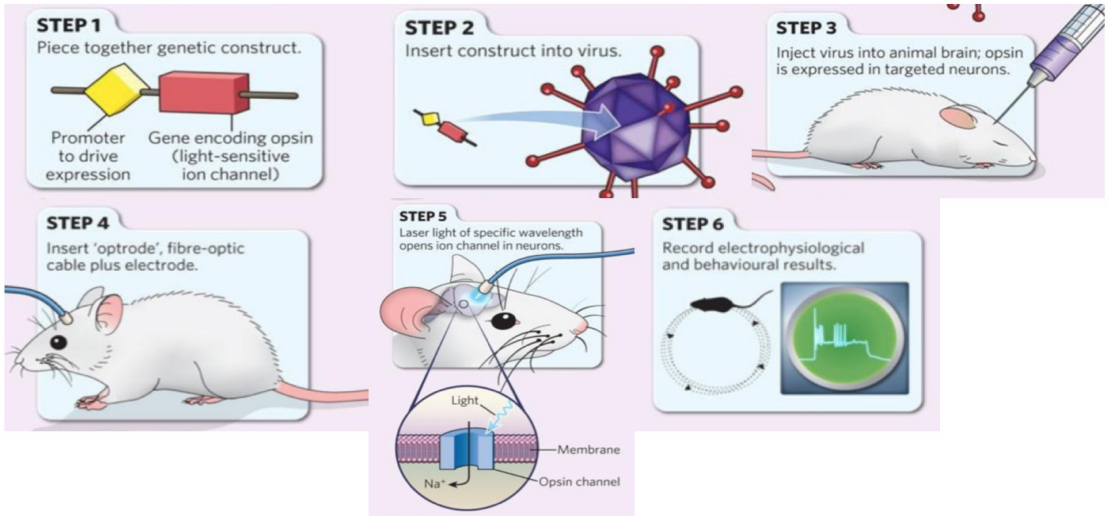

Figure 1.12: **How Optogenetics works.** This figure shows the typical steps involved into an optogenetics experiment. First the genetic construct is generated, then introduced into a virus which is used as a vector to get the genetic construct into an animal (in this case a mouse). Then an optrode is inserted into the animal and through light stimulate the opsins 'introduced' and record electrophysiological measurements. Reproduced from [122].

In recent years, the optogenetics field has expanded and developed in ways unimag-

inable. In optogenetics, light is used to cause alterations and molecular cascades in cells that can be recorded physiologically [123, 124]. A wide variety of microbial rhodopsins has been used as 'tools' to attain the goals of neuron activation and neuron silencing [121]. ChR-2 was the first to be used as a neuron excitatory tool, causing an action potential in neurons that can distort its membrane potential [121]. Additionally, other chloride pumps such as halorhodopsin or cruxhalorhodopsin have been employed for neural silencing as well as for control of the neuron electrical potential [125]. Lately, proteins taking an important role in this field are Archaerhodopsins, which are proton pumps capable of generating a high current output upon illumination, but are also capable of acting as a fluorescent voltage indicators to measure the membrane potential [126]. Moreover, Archaerhodopsins have a red-shifted absorption spectra (around 550 nm) compared to other proteins mentioned, such as chloride pumps that usually have an absorption around 400 nm - 500 nm (blue light) [125, 126, 127]. The development of Archaerhodopsins as tools in optogenetics has led to multicomplex imaging, where we can image and observe different cellular processes at the same time using two different wavelengths of light without the process of affecting each other (Figure 1.13) [123].

Although optogenetics is a young and fast developing field, its applications and advantages are many. Now using optogenetics, it is possible to transmit specific stimulus to observe specific reactions at a cellular level, by targeting specific cell types to try to address their function, or to target identification in drug discovery screenings for identification of drug targets for therapy [124, 129]. The field of Optogenetics, and its interplay with other technologies, has the potential to give an insight into

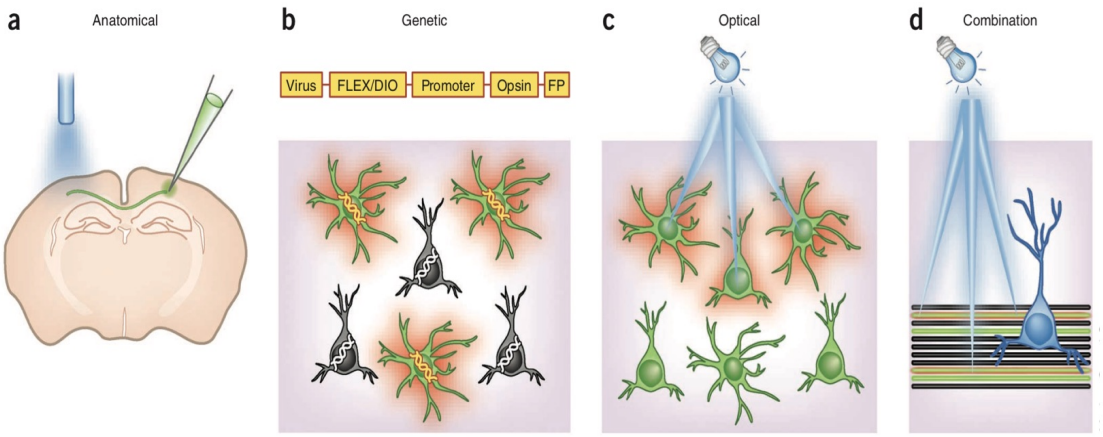

Figure 1.13: **Optogenetic targeting.** Representation of Optogenetics to target specific cell types. a) Insertion of the virus in a specific area of interest. b) Identification of the cell type desired to study can be identified with your opsin. c) Stimulation of the specific cells desired to study via a specific wavelength of light. d) Combine different opsins in different cell types to get a multicomplex imaging of two different species at the same time by using light at different wavelengths. Reproduced from [128].

understanding neuronal networks, and the role that specific neurons in neural network communications play [120].

1.3 Biophysical techniques

Studying proteins in biological membranes is very challenging; many models and systems have been developed over the years in order to study their functional characteristics. These systems often require the reconstitution of membrane proteins into environments that mimic membranes, such as liposomes, detergent micelles, or nanodiscs. These mimetics facilitate the use of biophysical techniques to study membrane proteins [2]. This section describes the biophysical techniques used to acquire data, namely droplet interface bilayers (DIB), atomic force microscopy (AFM) and membrane protein crystallisation. Additionally, we will introduce some membrane models,

such as planar lipid bilayers, used to reconstitute membrane proteins for study.

1.3.1 Droplet Interface Bilayers

1.3.1.1 Introduction

The diverse and complex interaction between all the molecules present in native membranes such as proteins, lipids and carbohydrates, provide significant challenges to generate suitable model systems, for structural and functional study [2, 1]. Liposomes are vesicles that are encircled by a bilayer made up of lipids [130]. Although versatile, and well-studied, liposomes do not readily allow control of both environments present, the one inside the vesicle and the one outside of the vesicle [131]. Furthermore, the orientation of reconstituted proteins within liposomes cannot be controlled. Studies of ion transporters and channels embedded within these systems still remain a challenge [131, 132]. In order to overcome these problems, a system known as planar lipid bilayers (PLB) was developed (Figure 1.14).

These systems require the formation of a lipid bilayer across a gap that connects two different aqueous sections, enabling control of both sides for electrophysiological studies [134]. It is important to remember that in cells, the membranes have a potential across them of -70mV, which drives the flow of ions from one side of the membrane to the other through channels and pores [135, 2]. Electrodes in both aqueous environments allow changes in current to be measured as charged molecules across the membrane [135]. Many improvements and developments have been made in PLB, with the most noteworthy being the one introduced by Mueller and Montal, in which a bilayer is formed by bringing two monolayers together [136]. This makes it easy to control for the composition of lipids making up each leaflet, allowing the

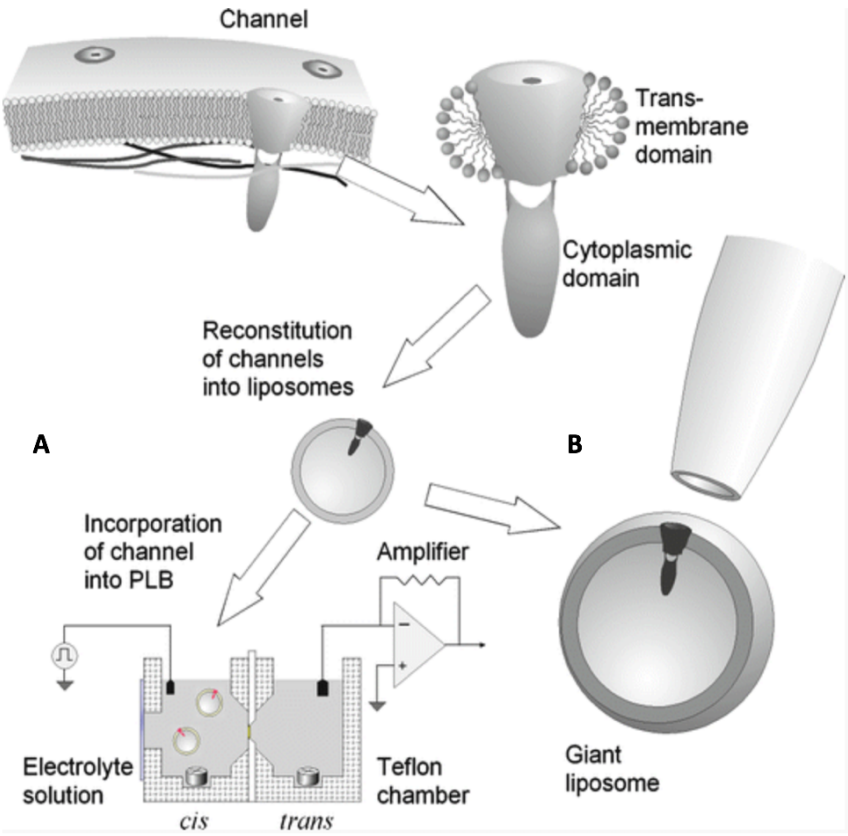

Figure 1.14: **Planar lipid bilayers.** Illustration of different models and systems to form planar lipid bilayers. Once proteins are purified, extracted from the cell membranes and reconstituted into liposomes, the proteins and liposomes are reconstituted into PLBs to measure current changes. Throughout the years many models of PLBs have been developed starting with: A) chamber method. B) tip-dip. Reproduced from [133].

formation of controlled asymmetric bilayers [136, 137].

Unfortunately, PLBs have a very short lifetime (seconds-minutes) due to their fragility restricting their use in microfluidic devices or in recording chambers [138]. They have the potential for incomplete bilayer formation, and the level of noise shown in experiments involving proteins with a small current flow, complicates reproducible data [139]. As a result, there is a need for a new system that would be easy to construct, more robust and with the facilities to have a control of both environments. A new system known as Droplet Interface Bilayer (DIB) has been developed in recent

years to tackle these needs [139, 140].

1.3.1.2 Principles

DIBs were developed by Prof. Hagan Bayley in Oxford and Prof. Takeuchi Soji in Tokyo, and they are based on the water-in-oil bilayer formation [139]. Figure 1.15 demonstrates how DIBs are formed with oil and aqueous phases [135]. A liposome is first formed in an aqueous environment, but its outer leaflet starts to peel off as it encounters the oil phase exposing the hydrophobic core of the inner leaflet. Through the progression of this event, the inner leaflet retains its encapsulated water molecules, forming a droplet surrounded by a monolayer [135, 140].

Taking advantage of this principle, DIBs were developed. The process consists in putting an aqueous droplet into an oil phase [141]. Usually this oil phase is a hydrocarbon such as hexadecane [139]. The droplet is attached to an electrode coated with agarose so that it does not come in contact with the oil. Once the droplets are in the oil, a monolayer of lipids is assembled around the aqueous phase. To form the DIBs, two droplets are brought into contact, and the oil that is in between them is excluded so that a bilayer can form at the interface. This is a very complicated and intricate process that can be done by hand or with micromanipulators [135, 139, 140, 141, 142, 143, 144]. Membrane proteins may be incorporated into the DIB when one of the original droplets placed in oil contains the membrane protein of interest (Figure 1.15) [144]. Once the interface is formed, and the electrodes are in place, an electrical potential, together with the capacity of measuring the change in current due to the presence of ion transporters, can be measured [135].

There are two configurations for DIBs. These are called the “lipid out” and the

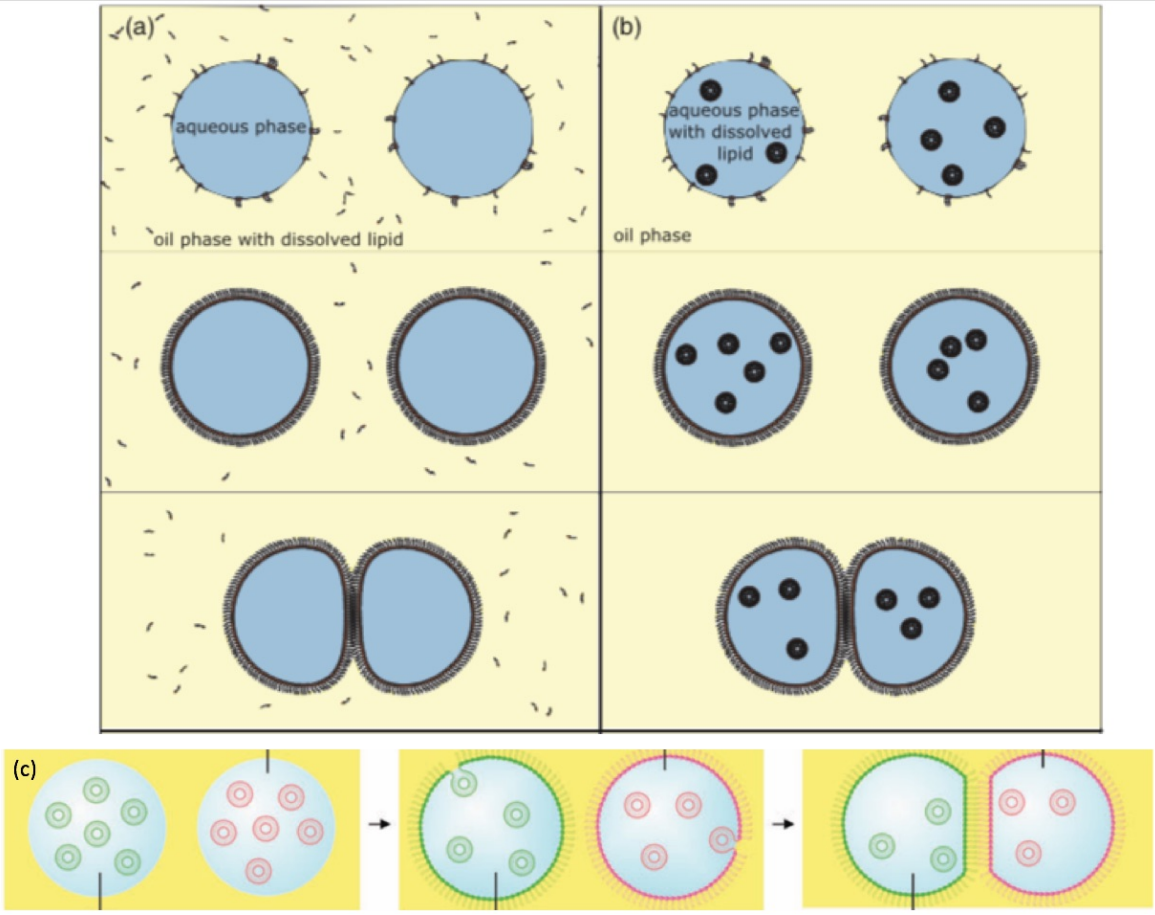

Figure 1.15: **Droplet interface bilayer.** Formation of Droplet Interface bilayers through the lipid-in and the lipid-out methods. a) lipid-out method to form a DIB in which the lipids are added onto the oil to form the droplet with the lipid of interest. b) lipid-in technique by which liposomes are used in order to form the droplets with the lipid of interest. c) formation of asymmetric DIB's by having two droplets with different lipids come into contact achieved using the lipid-in technique. Reproduced from [139, 145].

"lipid in" configuration (Figure 1.15) [142]. The "lipid" out" form introduces the lipids into the experiment by dissolving them in oil [144, 142, 146]. The "lipid in" uses liposomes as droplets to introduce the lipids into the system. The assembly of the monolayer has different time frames for each technique being around 5 minutes of incubation for the "lipid in" to 30 minutes of incubation for the "lipid out" technique [142, 147]. Both techniques have attributes. The "lipid out" technique is a fast and

easy way to form a large number of uniform droplets with the same lipid composition in their monolayers while in the oil phase [142]. On the other hand, the "lipid in" technique allows you to have in the same solution droplets with monolayers made up of different lipids, allowing you to create an asymmetric lipid interface bilayer, saving material and being more economical since you do not need to add the lipids in bulk to the oil phase [138, 144, 142, 146, 147, 145].

1.3.1.3 Incorporating membrane proteins into DIB

The method chosen to incorporate membrane proteins into droplets varies widely, depending on the nature of the protein and what kind of experiment is to be carried out [145]. In general, there are three different methods to incorporate proteins into DIBs: spontaneous incorporation from solution; incorporation from detergent micelles or liposomes reconstituted with the protein; and, directly from membrane fragments [145, 148, 149].

The first protein inserted into a droplet was the toxin $\propto$-hemolysin ($\propto$HL). This is a water-soluble channel forming protein that binds to the membrane, and the difficulties that a typical membrane protein spanning the membrane would pose are avoided. Inserting this protein into a DIB was straight forward, due to its characteristics, since its insertion into the membrane is spontaneous [145, 149]. $\propto$HL has become widely used in DIBs not only for its study, but also to permeate the membrane and alter the electrical conditions of the interface. As a protein, it has become a tool in different fields such as single molecule sensing and in the building of cellular systems [150, 151].

Secondly, the most common method of protein incorporation into DIBs is by using detergent micelles and liposomes. As mentioned earlier, most membrane proteins

such as transporters cannot be introduced into the DIB the same way as ∝HL since they are not water soluble. Additionally, when purifying these proteins, amphiphilic molecules such as detergents are required in order to extract, stabilise and purify the protein from cell membranes. Once in detergent, the protein can be reconstituted into DIBs [148]. An example of protein directly incorporated into DIBs from detergent is bacteriorhodopsin. Bacteriorhodopsin is solubilised in octyl glucoside (OG) and then spontaneously incorporates into the DIB [148, 143]. Other proteins are not as straightforward as bacteriorhodopsin, and require further steps where they are reconstituted into liposomes. The liposomes are then used directly as the source of lipids in the droplets, thus incorporating the protein into the droplets readily [145, 144]. Many proteins have been incorporated into DIBs using this approach (Table 1.1) [144].

Membrane proteins reconstituted into DIBs		
Protein	Type	Methods for incorporation into DIBs
∝HL	Pore forming barrel	Spontaneous incorporation
bR	Proton pump	Detergent incorporation
OmpG	Pore protein	Detergent incorporation
Kcv	Potassium channel	Spontaneous incorporation
KcsA	Potassium channel	Cell membrane incorporation
MmPiezo	Mechanosensitive cation transporter	Liposome incorporation
Nystatin	Pore forming protein	Liposome incorporation

Table 1.1: Reconstitution of different proteins into DIB's using different approaches and methods. The values and information were retrieved from [139, 145, 152].

Another method of incorporation of proteins into DIB is directly from membrane fragments, produced by lysing cells, isolating the membrane fragments and applying them onto an agarose layer (Figure 1.16) [139, 145, 152]. To this layer, a mix of the

lipid of interest and hydrocarbon is added as the 'oil phase' [145, 153]. A monolayer is formed, and then an aqueous environment is added to form a droplet that is at the interface with the agarose layer (Figure 1.16) [153]. This is a very promising technique for proteins that are difficult to purify and extract from cell membranes, but optimisation and obtaining the correct droplet size droplet for the protein of interest becomes technically difficult [145, 153].

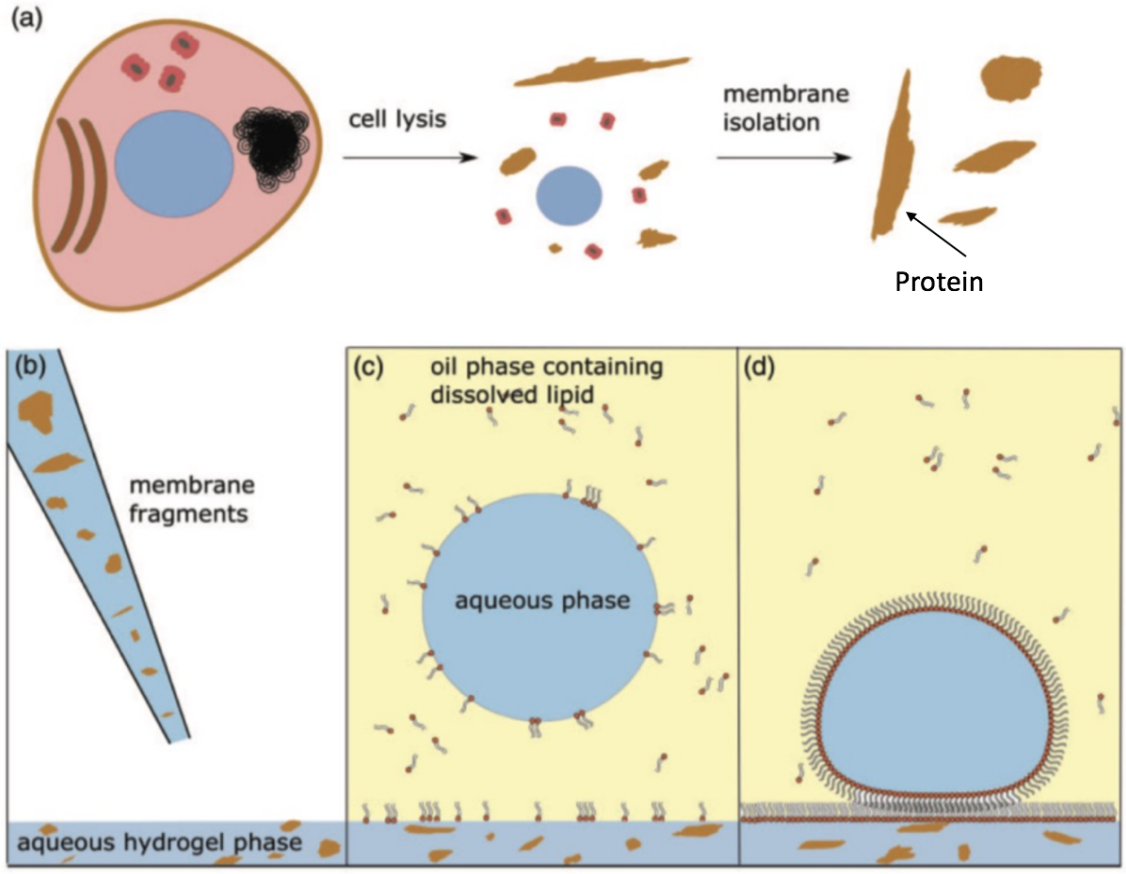

Figure 1.16: **Reconstitution of proteins into DIB from membranes.** Schematic of obtaining DIB's with protein directly from cell membranes. a) Cell lysis of the cells. b) Addition of membranes onto a hydrogel base. c) Addition of oil phase onto hydrogel with the lipid of interest for the droplets. d) Formation of DIB between water droplet and the hydrogel phase with the protein of interest. Reproduced from [145].

1.3.1.4 Properties of Droplet Interface Bilayers

DIBs are a good method for studying membrane proteins, but in addition they possess some unique properties that makes them very different from other systems such as PLBs or liposomes. One of the main advantages of DIBs is their stability. The lifespan of DIBs can be weeks, even under the application of electrical potential [154]. Taking advantage of this stability, functional systems can be created that otherwise would not be possible. Another feature of this system is the control over the interface area. By bringing the droplets together or pulling them apart, the area of the interface can be adjusted, to ensure the protein of interest is in the interface. Additionally, the surface area can be reduced to avoid additional incorporation of proteins, and thus permitting the study of single transporters [155, 139].

Although many studies have been carried out in PLBs or liposomes, these are very challenging when working with proteins that have low availability. To address this problem, the use of droplets requires a very small volume that ranges from microlitres down to nanolitres [145, 134]. This is not only an efficient use of material, saving on expensive products, but also of time and money since the amount of protein needed for insertion is very small compared to other systems. In addition, this characteristic permits the study of proteins synthesised in droplets in amounts high enough to conduct the experiments [156]. The small volumes provide an opportunity to do experiments that otherwise would not be possible for methods that require larger amounts of material. There is a limit to the size to which the nanodroplets can be reduced, and when trying to obtain droplets of femtolitres, it was found that the droplets were not stable and eventually collapsed [157, 158].

1.3.1.5 Electrophysiological applications

For a few years now, there has been a need to study co-occurring events at the optical and electrophysiological level. DIBs provide a platform with the potential to measure both at the same time and elucidate some interesting properties of transporters such as voltage-dependent gating [159, 139]. As shown earlier, many electrophysiological studies have been done in DIBs, but also single-molecule fluorescence studies have been developed in DIBs. These studies have been carried out in droplet hydrogel bilayers (DHB). DHBs are formed in the interface between an agarose layer and an aqueous compartment in the presence of an oil solution [160]. When the DHBs are in a solid support, total internal reflection fluorescence (TIRF) can be used to study proteins dynamics via change in fluorescence properties (Figure 1.17) [160, 161]. DIBs have the potential to couple both techniques, since they have been demonstrated individually, but they would be limited to DHBs for the moment [139].

1.3.1.6 Asymmetric DIBs

The formation *in vitro* of an asymmetric bilayer with a control of the lipid composition in each leaflet is very challenging, and DIBs provide a straightforward method to attain this goal, using the "lipid-in" [144, 142, 146, 147]. Furthermore, using fluorescent lipids, the transverse movement of lipids from one leaflet to the other has been studied, and it was observed that this movement takes hours or even days. Therefore, the asymmetry in the membrane is maintained whilst performing experiments [144, 145, 162].

Different studies have been performed in order to study the influence of membrane asymmetry on proteins. One study was centred around Piezo proteins that induce

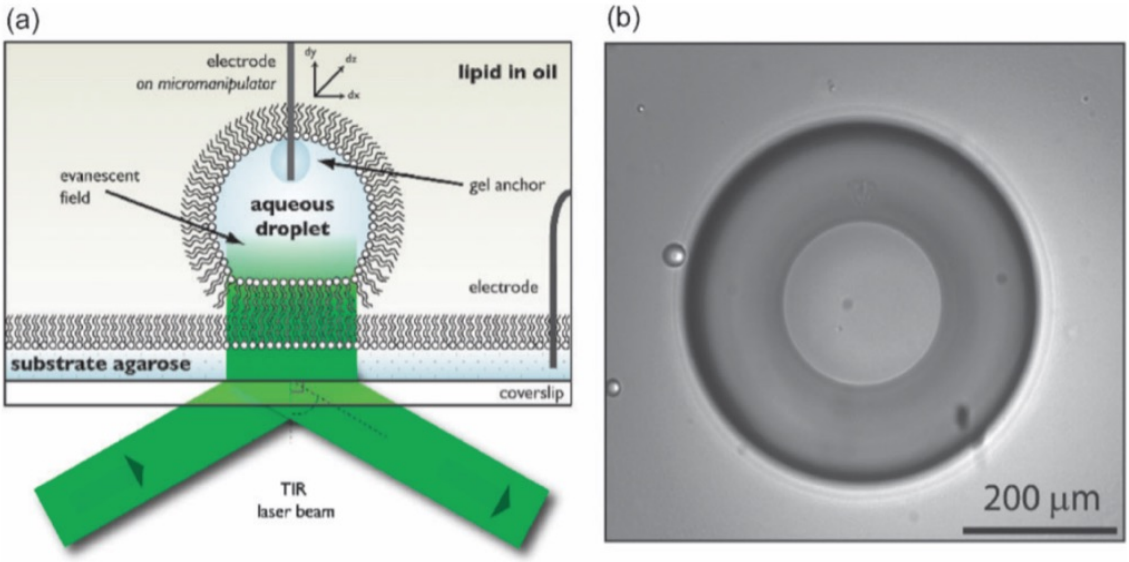

Figure 1.17: **Droplet hydrogel bilayer coupled with total internal reflection fluorescence.** Schematic of how we can couple electrophysiological and optical measurements. a) Illustration of the formation of a DHB droplet. The electrode placed in the hydrogel base is placed away from the hydrogel so that it does not make the optical recordings difficult. b) Optical image of a DHB's interface area. Adapted from [139].

cation transport in cells. The role of these proteins is not very well defined as to whether they regulate ion channels or are pore-forming ion channels in their own right. In this study, Piezo proteins were reconstituted into asymmetric DIBs as well as into lipid bilayers formed with asolectin lipids. The findings demonstrate the importance of asymmetry of DIBs for protein activity, and show that the protein is in fact an ion channel itself [152].

1.3.1.7 Multiple interface droplets

So far, we have focused on the idea of having a DIB formed from two droplets, however it is possible to form multiple interfaces in order to create a network of DIBs [143]. The idea behind this network would be to have an array of "protocells" connected to each other through the interfaces, whose internal aqueous environments are linked

via membrane proteins that they use to pass on information from one to another [143, 139]. A biomimetic sensor was constructed based on this idea, composed of five droplets in which one central droplet was connected individually to the other four. Three droplets had bR incorporated into their interface with the central droplet, meanwhile the other droplet had $\propto$HL incorporated into their interface (Figure 1.18).

Upon illumination with a green laser, a change of current was recorded, indicating that bR proteins in the interface where working and pumping protons from one side of the membrane to the other. This demonstrated that bR can be used as functional light-activated networks and has the potential to be used in a similar network where bR would constitute a pixel in an optical representation [143].

1.3.1.8 Summary of DIB

DIBs have significant applications and potential. Unlike other systems, they are very new and revolutionary technology, and the scope of its applications and potential is remarkable. They are a multifaceted system to study proteins *in vitro* and provide a platform for using these proteins in technological applications [139, 145, 150]. The further development of DIB is very important since it becoming important for the study of membranes and their components. Furthermore, the ability to perform optical and electrical measurements at the same time, offers the opportunity to resolve important mechanistic details of membrane proteins that might shed light and point the way towards a range of applications [139].

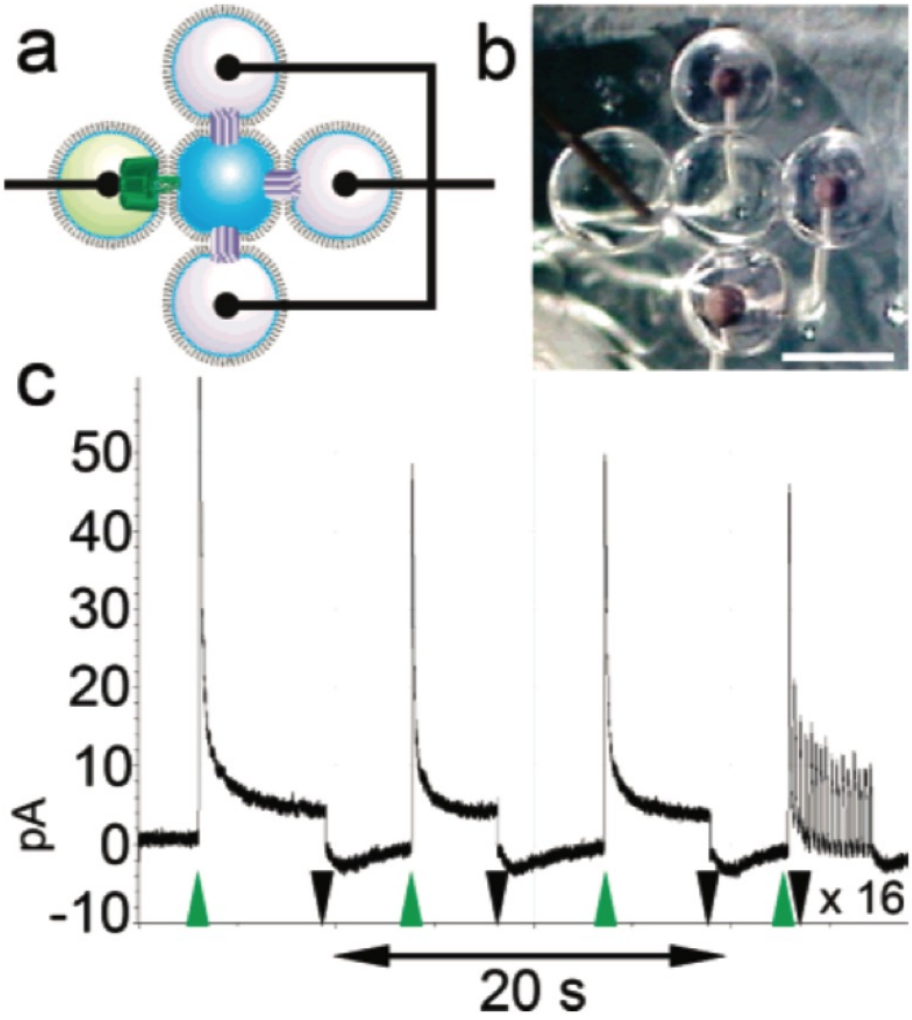

Figure 1.18: **Bacteriorhodopsin DIB network** a) Schematic of the DIB network in which five droplets form the network with three of them having bR, and one of them having αHL with a central one connecting all of them individually. b) Optical image of the network system. c) Electrical measurements of the changes in current when the system was illuminated. There were three cycles of 5 seconds illumination (green arrow) and 5 seconds without illumination (dark arrow) and final 15 short light pulses to show the rapid changes of the system. The traces show the changes in current up to 50 pA when the network is illuminated. Reproduced from [139]

1.3.2 Scanning Probe Microscopy

Scanning probe microscopy (SPM) is a technique used to obtain images of a sample surface at a nanoscale level. It was developed by G. Binning and W. Rohrer (awarded the Nobel Prize in 1986). From this development, many other techniques following

a similar principle have been produced, and now there is a wide array of tools that belong to the SPM family [163, 164]. SPM generates a topographical image that is produced by scanning a probe across the surface of the sample (Figure 1.19). This is a different approach to optical techniques, since the surface is not observed directly, but an image based on the scanning is generated [164, 165]. The advantage that SPM techniques provide is that they can measure the topography of the sample at the same time that other physical properties, such as conductivity, magnetic forces or interactions between molecules in the sample [165, 166].

SPM techniques have been increasingly important in chemistry, biology, physics and engineering over the years. The ability to measure the physical properties of samples in liquids as well as in dry films has expanded its application, specifically in biology, enabling studies concerned with protein interactions, imaging of membrane proteins embedded in lipid bilayers, electrical properties of ion transporters or protein folding and stability [168]. The invention of SPM lead to many other techniques being developed, such as atomic force microscopy (AFM) (see later), magnetic force microscopy (MFM) which uses a magnetic probe to measure the magnetic forces in a sample, or conductivity atomic force microscopy (C-AFM) [165, 166, 168, 169].

1.3.3 Atomic Force Microscopy

One of the most important techniques within the SPM family is atomic force microscopy (AFM). AFM was developed in 1986, and since then it has become increasingly important in the world of biology, biomedicine, engineering and nanotechnology for imaging [164]. The main scope of action for AFM is in the surface imaging of samples at the nanoscale level [170]. This fills a gap present in imaging and structural

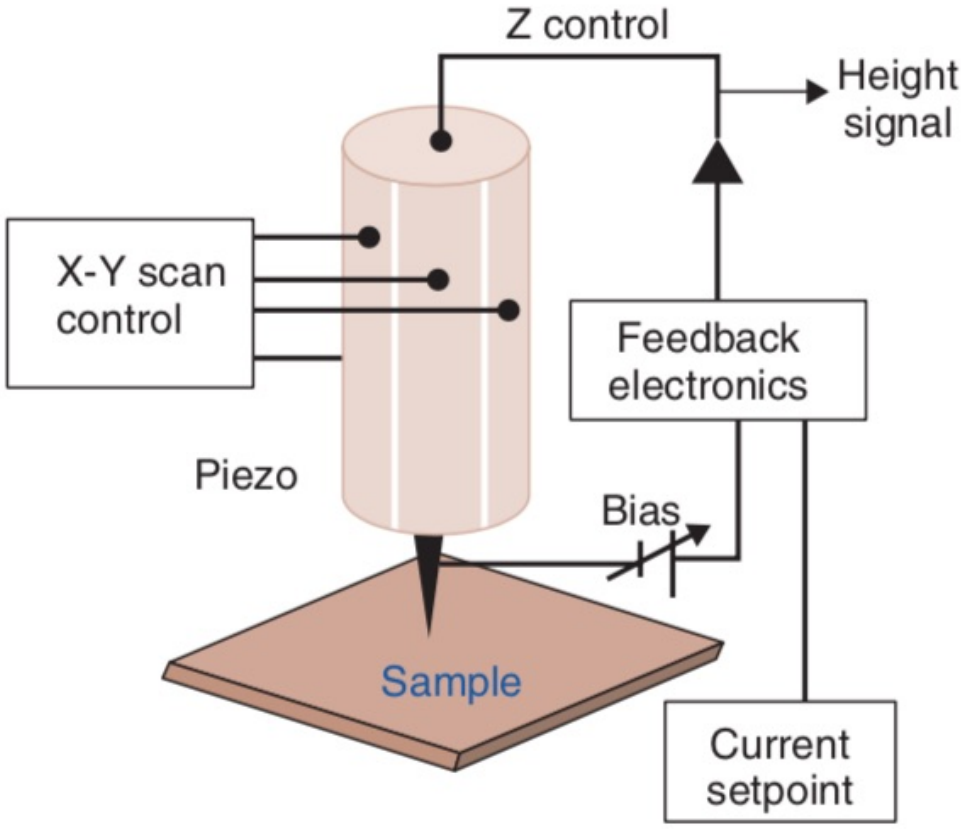

Figure 1.19: **Scanning probe microscopy.** Schematic of a simple scanning probe microscopy set-up, in this case the first designed; scanning tunnelling microscope (STM). The tip is brought close to the sample and scans the sample to give a topography overlook of the sample. In the STM case, the tip is not brought into contact, but gets its topography image based on the conductivity of the sample and tip. These changes are recorded through the feedback loop system which produce the image data in the computer. Adapted from [167].

techniques such as X-ray crystallography, NMR, EM, or light microscopy (Figure 1.20) [171]. AFM makes it possible to image molecules in their native conditions and without altering in any way the sample with any dyes or freezing and allows for time-resolved data in molecules (Table 1.2) [170, 171]. Its capacity to work in dry and liquid environments facilitates biological studies of molecules in buffers resembling their physiological conditions. Furthermore, it was a great development compared to

other SPM techniques such as for example STM due to its ability to image substrates regardless of their conductivity characteristics [164, 167]. AFM can not only provide a topographical picture of a sample, but also it can measure force and mechanical resistance [167, 172].

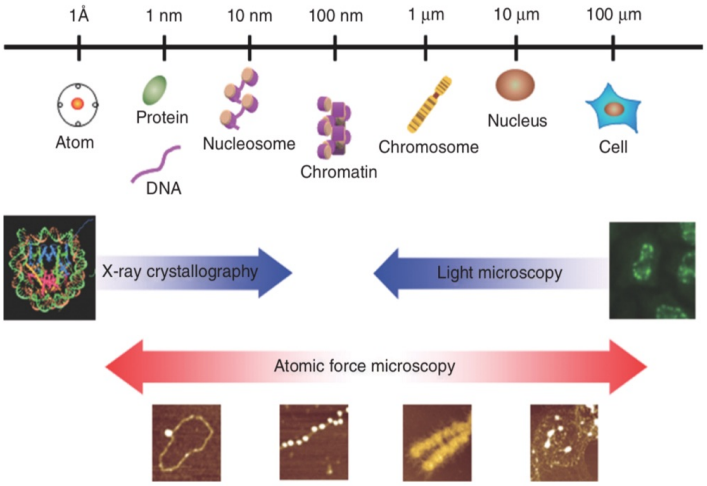

Figure 1.20: **Atomic force microscopy filling the gap** Illustration of how the AFM technique fits in the current biophysical techniques available. AFM bridges and fills the gap between static imaging such as X-ray crystallography that gives you a snapshot of proteins and molecules to optical microscopy where you get life images of bigger complexes such as cells and organisms. AFM works at the nanoscale level and provides information on the shape and topography of lipid bilayers and the proteins embedded in it. Reproduced from [171].

A typical AFM has four crucial components: a piezoelectric drive, a cantilever, a photodiode detector and a laser beam (Figure 1.21) [170]. A very sharp tip is mounted onto a cantilever that is in turn controlled by a piezoelectric drive that determines its movement in the plane [174]. In general, a laser beam is focused onto the cantilever, and as the cantilever scans the surface of the sample, any deflection of this will be measured by the photodiode, which will generate data as a topographical representation of the sample [170, 171, 167, 172, 174]. As seen, the different components have very different roles in the system.

High resolution techniques available			
Technique	Resolution	Advantages	Limitations
AFM	1-50 nm	Native condition and high SNR	Surface only
EM	0.2-10 nm	Protein complexes and structures of proteins	No life processes
Crystallography	1 Å	High resolution structures of molecules	No life processes and need 3D-crystals
NMR	1 Å	Protein dynamics and protein complexes structures	High protein amount and labelling of protein
Super resolution microscopy	20-50 nm	Life imaging of cells and cellular processes	Fluorescent tags or addition of dyes to cells

Table 1.2: Comparison of the advantages and limitations of the different techniques available in the field of biology to record cellular and molecular processes. The values were retrieved from [171, 173].

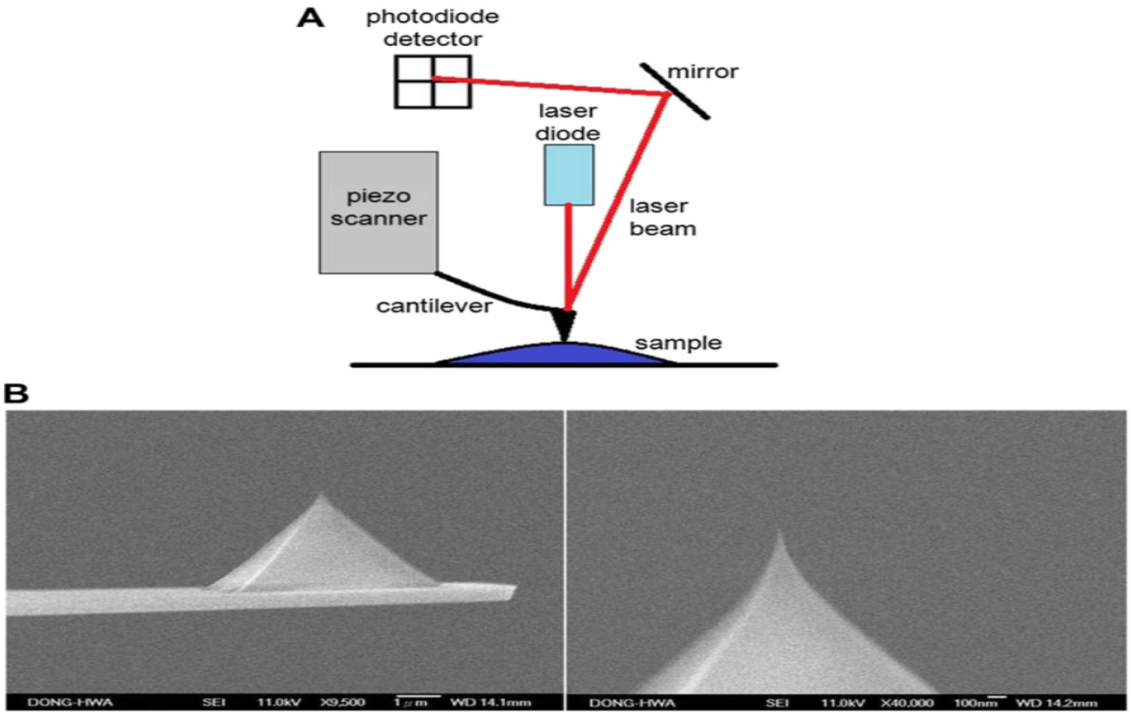

Figure 1.21: **AFM set-up.** A) Schematic representation of the AFM system with the necessary four sections: piezo scanner, photodiode, laser beam, and cantilever. B) Image of the AFM tip mounted onto the cantilever. Tips must be very sharp and have the right characteristics for the nature of the experiments, usually made of silicon. Reproduced from [164, 170].

First the cantilever has a crucial role in scanning the substrate. The cantilever has mounted onto it a very sharp tip, that can range in thickness from 1 nm to 100 nm which determines the maximum scanning resolution [173]. In general, these tips can be made of different materials, from gold to silicon, and can have a wide range of stiffness and spring constants from 10-20 Nm [164]. The tips and cantilevers are very sensitive, and any external vibrations could give false data. The smallest movement to even people talking in the room can affect the AFM experiment, therefore it is imperative to be mindful when conducting an AFM experiment.

The piezoelectric drive controls the cantilever and is responsible for the movement of the cantilever in the x-y plane as well as it is responsible of the z plane. The scanning range in the x-y plane can be varied, going from a few nanometres to micrometres but in general the scan does not exceed the 100 μm size [164, 175]. The piezoelectric is coupled with a feedback loop that controls the tip distances towards the sample, and maintains this distance also known as "set-point" constant [176]. As the tip scans the sample moving in the x-y plane the system measures the z movement of the tip. The measurement of this movement entails the work of the laser beam and the photodiode (Figure 1.21) [164, 170].

A laser beam is focused onto the cantilever (Figure 1.21), and it is very important that it is correctly aligned with the photodiode, which is made up of four different sections. The sections on top and sections on the bottom are compared to each other and give information on the z deflection of the cantilever when scanning the sample. Comparison of the sections of the left to the sections on the right gives information on the movement of the cantilever in the x-y plane. Thus, it is imperative that before

any measurement or experiment is conducted that the laser beam is correctly aligned with the photodiode in the centre of the sections or position '0' in order to get real and accurate data [177]. With all these components working together, we can obtain a topographical image of a sample in a similar way as a record player can play music from a vinyl disc [178].

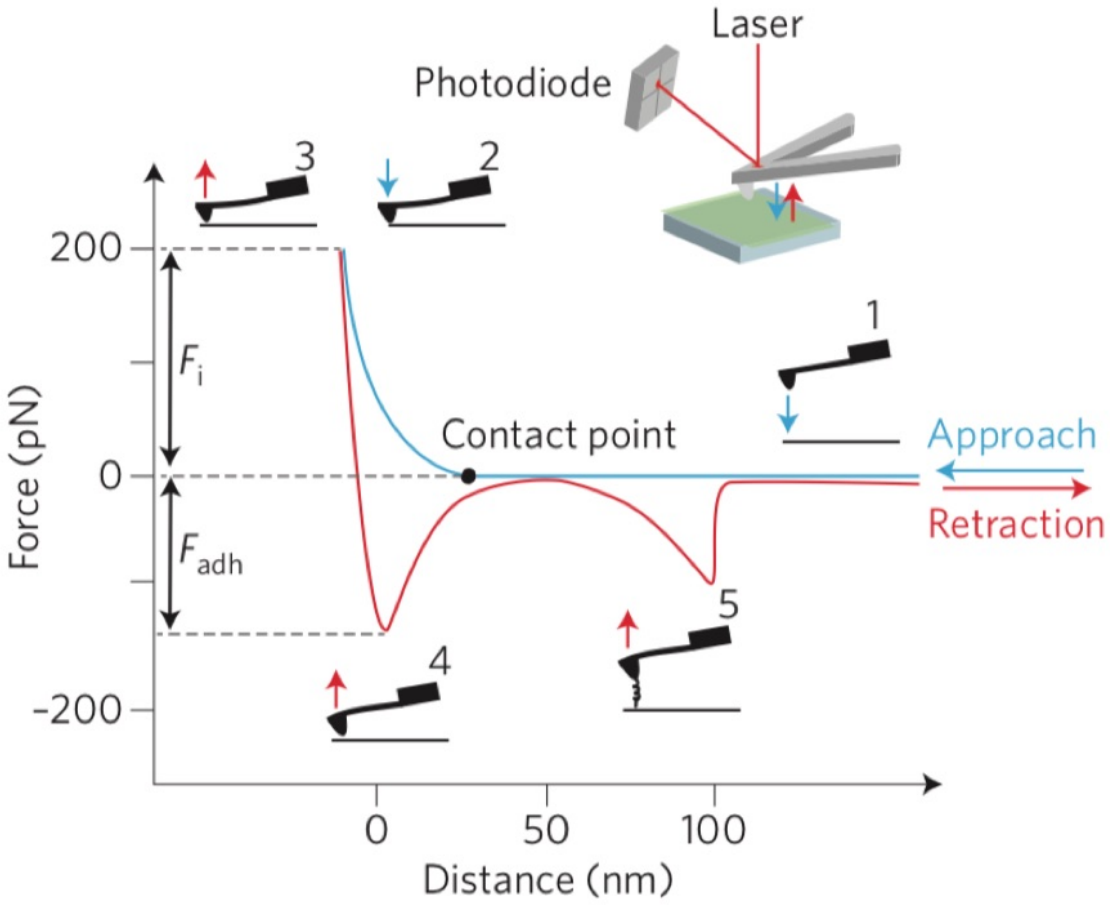

Figure 1.22: **Force-distance curve.** Schematic representation of the force-distance curve as the tip is approached onto the sample. (1-2) Approach of the tip to sample (3) Adhesive forces between the tip and the sample happen which can lead to (4-5) "snap" in and "snap out" events in the approach and retraction of the tip from the sample. Reproduced from [173].

Furthermore, the forces actuating in the system between the sample and the substrate can also be measured [179]. This data is usually presented as the force-distance

curve as illustrated in Figure 1.22 [179, 173]. First the tip is moved onto the sample and a deflection will happen upon interactive forces with the sample such as van der Waals [172]. At a determined point, these interactions take over and result in the tip bumping onto the surface of the sample [164]. This event is called 'snap in' and deflection is recorded until the 'set point' is established [164, 167]. Then experiments can proceed until retraction of the cantilever. 'Snap off' occurs when the interacting forces for the tip with the sample becomes smaller than the spring constant of the cantilever [164]. It is important to take these events into account when doing experiments, especially if they are concerned with high resolution, because the "snap in" during approach could destroy or affect the tip of the cantilever, and its quick and unexpected nature can avoid the observation of strong forces between the tip and the sample [164, 167]. Therefore, it is very important to use cantilevers with a fairly stiff spring constant, and be mindful of the different AFM modes that can be used to image [164, 180].

In order to obtain data for AFM, we can select different modes that best fit our experiments. These different modes take advantage of the forces between the tip and the sample to obtain data. Many different modes have been developed, but the most common ones used are contact mode and Tapping mode^{TM}.

1.3.3.1 Contact mode

In contact mode, the tip is in direct contact with the sample throughout the experiment [173]. As the tip scans the surface, the photodiode records deflections of the laser beam rendered by the contour found in the sample [164, 181]. Contact mode gives great resolution in liquid environments, but it is very important to be aware

of some problems that might be encountered [181, 182]. First, due to the constant touching of the tip with the sample it is possible that the tip might get contaminated by the adherence of substrate on it. Secondly, if excessive force is applied, the tip might break as well as the substrate might become damaged or deformed (Figure 1.23) [183].

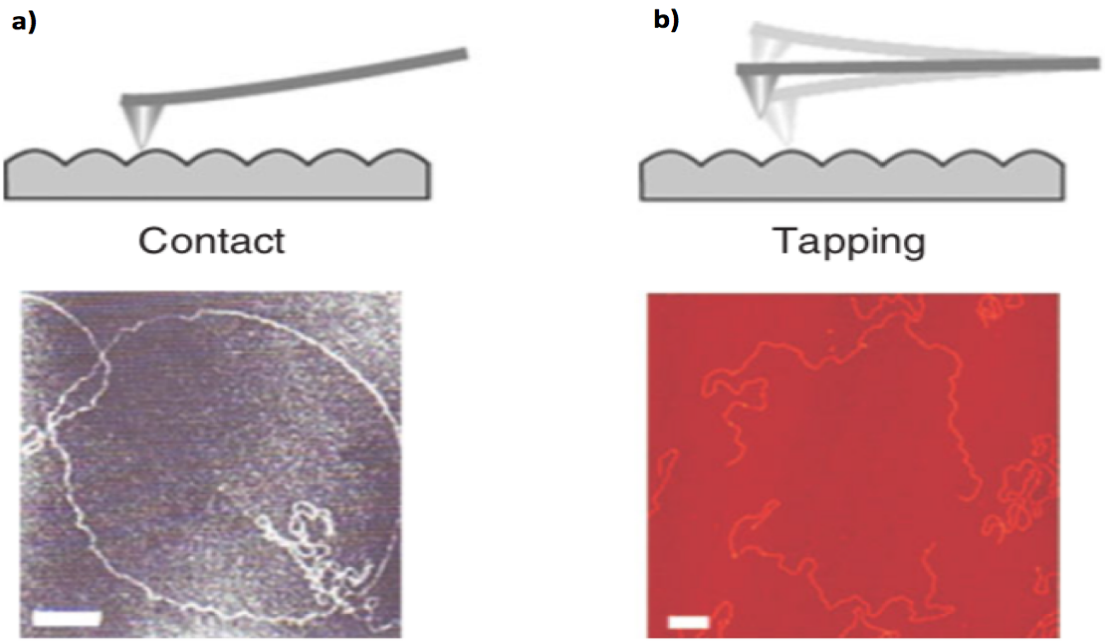

Figure 1.23: **AFM imaging modes.** Schematic representation of the AFM imaging modes. a) Contact mode AFM; the tip is in constant contact with the sample in order to obtain the data; a DNA image obtained by contact mode is shown. b) Tapping mode AFM; the tip is constantly oscillating at a set point over the sample in order to obtain the data; a DNA image obtained by tapping mode is shown. Scale bar: 200 nm. Reproduced from [171].

1.3.3.2 Tapping mode

Another common mode used in AFM is the intermittent-contact mode also known as "tapping mode". In tapping mode, the tip is constantly oscillating at a set frequency instead of being in direct contact with the sample [173]. The interactions of van der

Waals forces between the tip and the sample create a deflection which is measured based on the change of the oscillation [173, 164]. The advantage of tapping mode is its ability to generate phase imaging at the same time as topographical imaging [164, 173, 184, 185]. Phase imaging can be run in parallel with contact mode, and this can give information on the composition and friction of the sample, in many ways being able to show a clearer image [186, 164]. Additionally, tapping mode is widely used in High-speed AFM explained in detail later in this thesis. On the other hand, tapping mode does not provide such a high-quality resolution as contact mode might in liquid or air, and at some points the oscillation might cause deformation in the substrate if it is soft (Figure 1.23) [164, 170, 187].

1.3.3.3 Mica Substrate

Samples may be adsorbed onto a range of substrates from mica to gold, and they can be charged or neutral. In all the experiments performed in this thesis, the samples were absorbed onto mica. Mica is a very common substrate used in AFM due to its flat nature at the nanoscale level. On top of that, mica has a negative charge and interacts strongly with water, making it ideal for adsorption of biological samples. Mica discs and sheets are commercially available [188]. In order to use them, the general procedure consists of pasting the disc onto the AFM stage with glue (too much glue may enable the disc to move while imaging), and the mica is then cleared by pressing scotch tape onto it, to leave a freshly smooth mica surface. After incubation for 3-5 minutes to adsorb the sample, the mica is cleaned with the buffer, in order to remove any unbound molecules.

1.3.3.4 High-Speed AFM

Through many different techniques and methods, many structural details of biological molecules have been resolved through the use of X-ray crystallography, electron microscopy and many others. Although insightful and very promising, these different techniques provide images and structures of the protein that are static, meanwhile proteins and molecules are in a dynamic state, constantly changing internally or externally in response to different environments. The limitation of these techniques led to the development of other optical techniques such as fluorescence microscopy. This technique enables the optical observation of molecules in nature providing insights into the dynamics of molecules. On the other hand, this technique depends on the fluorescent tags and markers attached to different molecules that we want to observe, therefore affecting, to some degree, the action and dynamism of the molecules [189]. As a result, AFM was developed for this very specific reason, since it enables the observation of molecules in their native environment without altering the molecules. Although promising, AFM shows some limitations in this aspect because the timescale that imaging takes is in the minutes meanwhile the timescale for dynamics and movements of molecules take place in the milliseconds [188, 189]. Thus, High-Speed AFM (HS-AFM) was developed to enable the observation of dynamic movement of molecules obtaining 15 to 20 frames per second facilitating the observation and elucidation of different processes in the nanoscale range (Figure 1.24) [178, 189].

Many developments have been introduced in order to improve the timescale of AFM into HS-AFM. Some of the main developments were the improvement of the

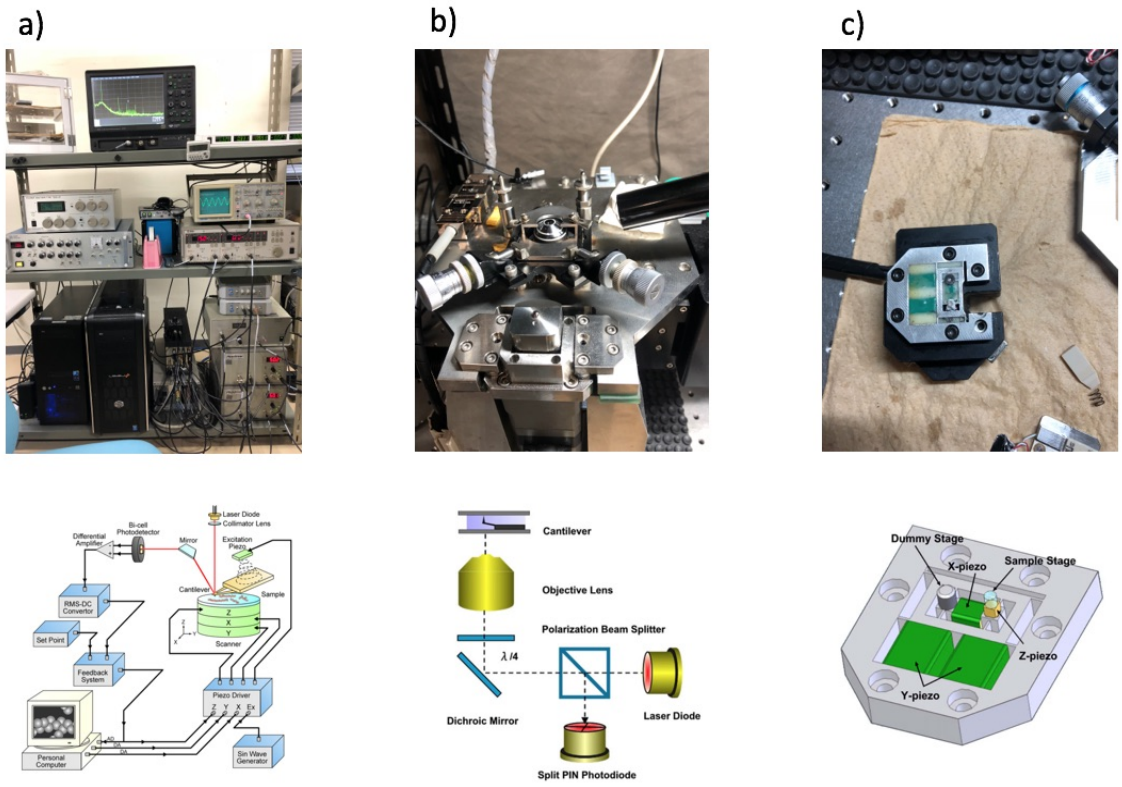

Figure 1.24: **HS-AFM instrumentation.** Actual pictures of the AFM instrument and a scheme of the different components of a HS-AFM instrument. a) Image of the different components making possible the readings connected to the computer such as the feedback loop, the sin wave detector, or the laser alignment b) Picture showing the position of the stage and the cantilever with a lens microscope that enables the alignment of the laser, or the approach and contact of the sample and the cantilever. c) HS-AFM scanner where the stage is mounted with the sample, and the piezo electric drive to move the tip across the system in the x-y-z plane. Adapted from [190].

scanner detector, or how the signal-to-noise ratio for the detection of amplitude in the oscillation was enhanced [191, 190]. Although HS-AFM would not be possible without these developments, the key improvement was the realisation of the cantilever role of the tip in spatial resolution [188, 189].

Due to the fast movement of molecules the cantilever needs to be sufficiently small to capture these movements and yet have a sufficiently soft spring constant to report the topography of the sample through oscillation [193]. To achieve this, a carbon tip is

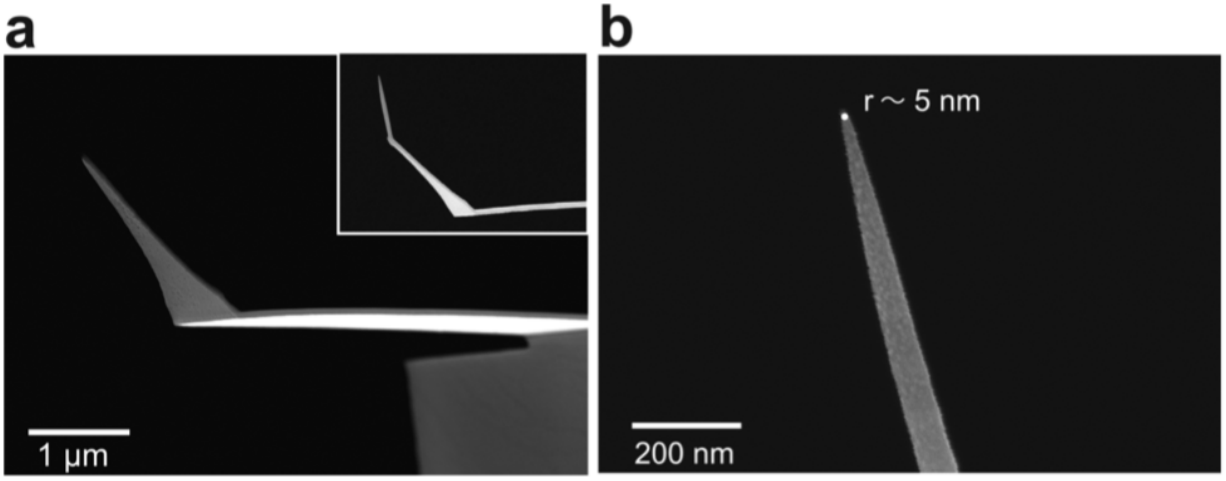

Figure 1.25: **HS-AFM tip.** Electron microscopy images of a HS-AFM. a) Image of the cantilever with the HS-AFM tip grown onto it. b) Reduction of the tip apex radius from 17 to 5 nm after etching with Argon gas of the tip. Adapted from [192]

grown in the original tip used for AFM using a Scanning electron microscopy chamber (SEM) and electron beam deposition (EBD). Once the new carbon tip has been created, the tip is further cleaned and sharpened through Argon etching reducing the tip radius greatly [189]. The tip improvement combined with all other improvements of the system lead to the development of HS-AFM, facilitating imaging of real-life dynamic processes in cells and molecules (Figure 1.25).

The development of HS-AFM has led to important discoveries never observed before. Thanks to its quick timeframe and imaging in physiological conditions, it was revealed or confirmed that there is an important movement of helical loops E-F in bR during its photocycle (bigger than expected from X-ray crystallography). This movement aids in proton translocation from one side of the membrane to the other by enabling amino acids to overcome the hydrophobic barrier and keep the translocation going (Figure 1.26) [194]. In addition, HS-AFM verified in real life the "walking" of Myosin-V and how it is powered by mechanical tension, unknown until then [195].

These are a few examples of the capacities and opportunities that HS-AFM provides to biological studies helping in the observation of dynamic movements of molecules, or even the diffusion of proteins in membranes in real life without altering the system, previously only studied through static techniques or using fluorescent tags [196].

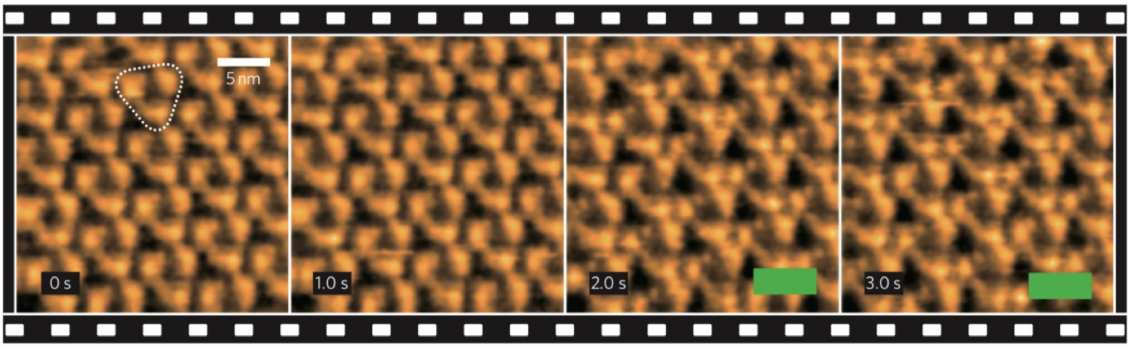

Figure 1.26: **Photoactivation of bR upon illumination.** Frames of a video capturing the conformational changes of the E-F helix upon illumination. In the first two frames bR is organised in trimers in purple patches in the dark. In the third and fourth frames bR undergoes conformational changes upon illumination (green bars) with a laser at 532 nm. Adapted from [194].

As discussed, HS-AFM is at the early stages with multiple applications. Efforts are being made to couple HS-AFM with Fluorescence Microscopy or Raman Spectroscopy, which would give insights and important information in molecular processes that remain unresolved so far. HS-AFM remains a technique that is not very widespread due to its difficulty to operate, its requirement of skill and knowledge to calibrate the system or align the laser to conduct the experiments. It is a very powerful tool for nanoscale imaging [196, 197]. Its improvement, development and flexibility to couple with other techniques makes it a very important technique for the future that could hold the key to elucidate different molecular processes as discussed above.

1.3.3.5 Limitations of AFM imaging

AFM has a wide scope of applications and advantages compared to other established techniques that makes it a great complement for any biological study. Nonetheless, when obtaining data using AFM or HS-AFM we have to be wary and vigilant of problems that might arise which could lead to false or altered data. The tip plays a crucial role in AFM, so we have to ensure that it is optimal for our experiments and that it is not damaged. If we are conducting an experiment and the tip has a radius larger than one of the molecules we would like to image, the image will render an altered representation of the molecule, since the object will appear larger than what it really is [198]. This phenomenon is known as "probe broadening" (Figure 1.27). Therefore, the smaller the tip, the better and more accurate images we would get. Furthermore, if we have to image holes or indentations in the sample with a bigger tip, we will not get a precise image since the tip would not be able to reach the bottom, and the image will appear smaller than what it is. Additionally, we have to be careful with the tip that it is not broken and at the correct angle. If the tip is broken it can give images with anomalous features. Moreover, the topographical image of the sample will greatly depend on the angle of the tip, so it is important to align it perpendicular to the substrate [199, 200].

Furthermore, the alignment of the laser is very important for accurate imaging. If the laser is not correctly aligned and calibrated in the x-y-z plane, then we will obtain distorted images [177]. For example, if not calibrated in the x-y plane imaging will represent samples on one side of the plane smaller and on the other side of the plane bigger even if they are the same size. On top of that, in AFM we have to be

Figure 1.27: **Peak broadening of AFM tips.** Schematic representation of how tip optimisation for experiments is crucial. If the tip is too big (10 nm) to image the sample (1 nm), the apparent feature of the sample imaged will seem bigger (10 nm) than the one it actually has (1 nm).

very careful with contamination in the sample as well as in the tip. If the tip gets contaminated, and for example, some of the substrate becomes bound to the tip, then we will observe the same pattern repeatedly all over the scan in which case needs the tip to be changed (Figure 1.28) [177, 198, 199, 200]. When preparing the sample, indentations might occur in the substrate, or contaminate it with fingerprints, which would lead to the imaging of artifacts [200].

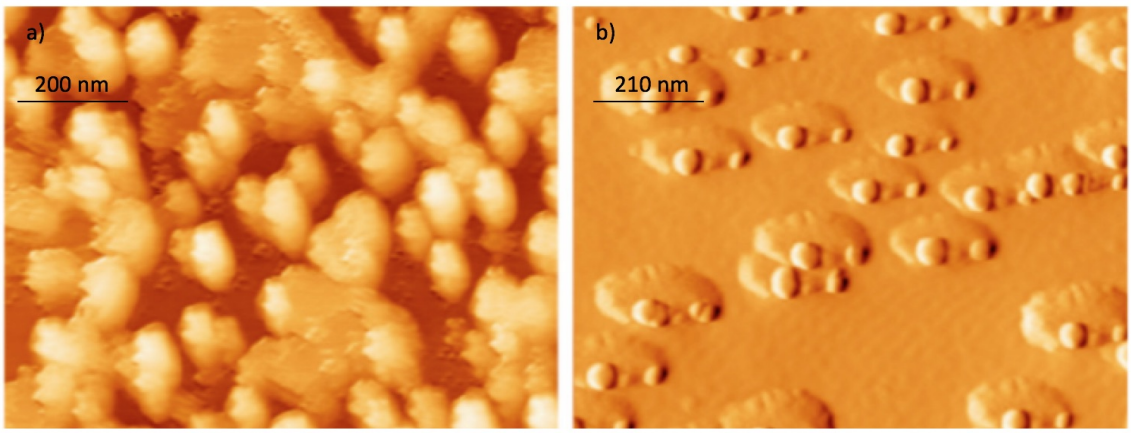

Figure 1.28: **Tip contamination or double tip in AFM.** These are actual images of what happens when the tip gets contaminated. Due to the interaction of the tip with the sample in some imaging modes, it is possible that the sample might attach to the tip, and the image rendered will be compromised. An easy way to identify this event is by noticing repetitive patterns in the image obtained. a) topography image of a sample with double tip repeatedly rendering the same pattern again in the sample. b) phase image of a sample with double tip creating the same pattern throughout the data. Reproduced from [198].

1.3.4 Membrane protein crystallisation

In the recent years a rise of protein structures being solved and deposited in the protein data bank (PDB) has taken place thanks to nonlamellar lipid phases [201]. Among these different techniques there is one technique known as lipidic cubic phase (LCP) that has emerged as a suitable technique for membrane protein crystallisation [202]. Different proteins have been crystallised succesfully using this technique from bR and heliorhodopsin (HeRs) [203, 204] to bigger complexes such as LHCII [205] achieving high resolutions of up to 1.3 $\mathring{A}$ [203]. Although a successful technique for crystal formation, its mechanism is still unclear (Figure 1.29) [205].

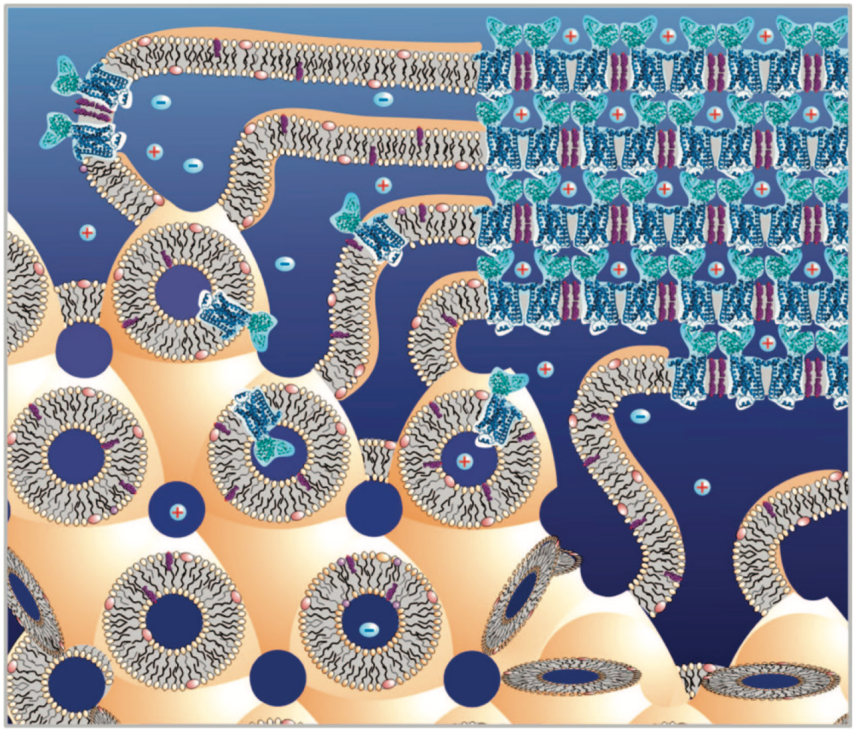

Figure 1.29: **LCP crystallisation.** This is a schematic of what the LCP crystallisation mechanism is believed to be. After treatment, the protein is incorporated into cubic phase bilayers. Next precipitants are added to achieve phase separation and isolate a lamellar phase with high concentrations of protein desired. The amount of protein coupled with other conditions enable the crystallisation process. Reproduced from [206].

It is believed that after treating the protein sample with detergent, and homogenising with monoacylglycerol, the protein is incorporated into the cubic phase bilayer [207]. In this environment, the protein can freely move and its native conformation and activity is conserved as evidenced by circular dichroism studies [208, 209, 210, 211] and fluorescence measurements [210, 211].

Precipitants are added to the mix in order to achieve phase separation [206]. In this phase separation a lamellar phase appears made up of stacked bilayers which contain high concentrations of the protein desired [207]. The amount of protein coupled with other conditions (bilayer structure, solution the sample is in...etc) help in the nucleation and crystallisation of the process (Figure 1.29) [207]. Protein crystallisation requires specific interactions to happen, and LCP supplies interactions with the hydrophobic region of the protein helping this process [212]. LCP has been proven to be a good technique to grow protein crystals for diffraction and use in X-ray crystallography [207].

1.4 Aims of the Thesis

In this thesis, microbial rhodopsin homolog of bacteriorhodopsin known as archaerhodopsin-3 (AR3) is studied extensively. AR3 have received a lot of attention lately due to its role in optogenetics as a fluorescence voltage indicator and as an optogenetic tool to stimulate neurons. Although of great importance and wide use, the structure of AR3 has not been resolved.

The aims of this thesis are:

Chapter 2:

- Crystallise the protein AR3 and gain structural information in the organisation of the protein at an atomistic level.
- Identify the differences between AR3 and bR that makes AR3 special and assess any differences between the dark-adapted and light-adapted states.
- Elucidate the oligomeric organisation of the protein in the native membrane.
- Use HS-AFM to directly visualise conformational changes happening in the photocycle upon illumination.

Chapter 3:

- Provide a functional method to reconstitute AR3 from its native environment in order to determine the key features of the protein involved in proton pumping.
- Using DIBs, study how illumination and lipid environment determine membrane potential and photocurrent.

- Investigate whether reproducible photoswitching of AR3 undergoing several illumination cycles or on constant illumination conditions is possible without a decrease in its activity.

- Study the functional roles of retinal and bacterioruberin separately and simultaneously in AR3.

- Investigate the role that bacterioruberin might have as a protective agent against photobleaching.

- Assess the photocurrent characteristics of AR3 once it has been bleached, to show the importance of retinal for protein function.

Chapter 4:

- Tune the spectral properties of AR3 to develop a mutant library with different spectral properties.

- Assess the proton pumping of the AR3 mutants in *E. coli* cell membranes.

- Assess the conductivity of the different AR3 mutants upon reconstitution into DIBs.

- Study how different mutations in the proton release complex affects the ion transport of the proteins using DIBs.

- Study the most red-shifted mutant obtained (D95T) and elucidate its proton pumping abilities.

Chapter 2

High-resolution structures of dark-adapted and light-adapted Archaerhodopsin-3

The work presented here focuses on the crystallisation of archaerhodopsin-3 (AR3) and the analysis of the high-resolution structures obtained in the light-adapted and dark-adapted states of AR3 with resolutions of 1.07 $\mathring{A}$ and 1.2 $\mathring{A}$, respectively. The high-resolution of these structures allows for the identification of key internal water molecules and hydrogen bonding networks crucial for the activity of AR3, giving insights into the mechanism of the proteins light adaptation. Furthermore, we use HS-AFM, time-resolved serial crystallography and X-ray free electron lasers to identify conformational changes that take place in the protein during the early stages (using XFEL) and the later stages (using HS-AFM) of the photocycle.

2.1 Introduction

2.1.1 Archaerhodopsin-3

The presence of proteins that establish an electrochemical gradient across the cell membrane is vital for all living organisms. Many of the proteins that can accomplish

this, either as channels or pumps, are light-activated [75, 213, 92, 110]. On the account of this feature, they have recently gained a lot of attention in the field of optogenetics, as versatile tools for hyperpolarising or depolarising membranes [214]. Among the wide variety of proteins used for these purposes, Archaerhodopsin-3 (AR3, or Arch3 in the optogenetics field) has become a particular focus of interest, as both a potent hyperpolarising tool and as a fluorescent voltage indicator [126, 123]. AR3 is naturally expressed in the archaea *Halorubrum sodomense* and is a homologue of bR and other archaerhodopsins, such as AR1, AR2, and AR4 [215]. It has 59% sequence identity with bR and up to 80% with the other archaerhodopsins just mentioned (Figure 2.1) [215, 103].

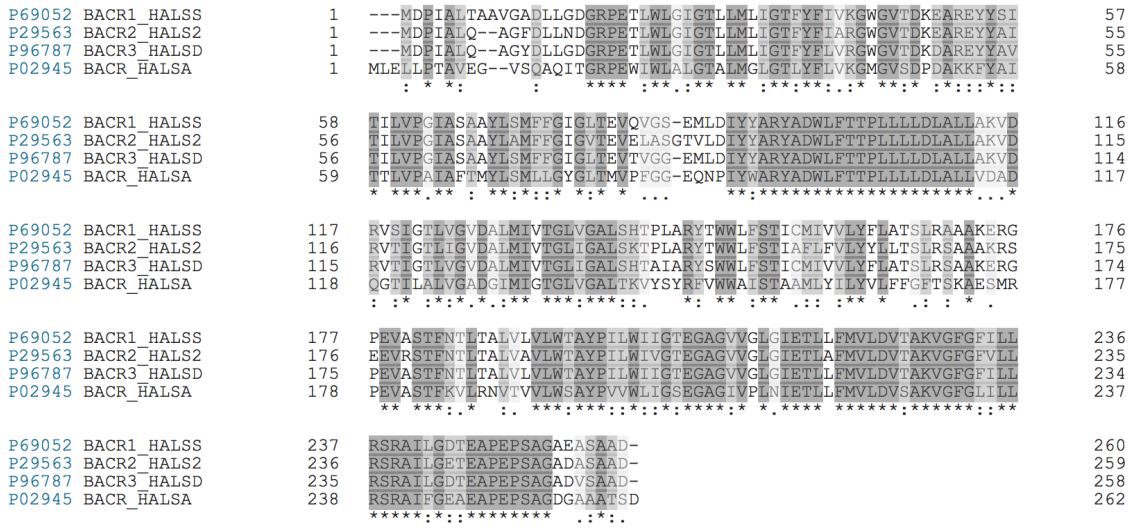

Figure 2.1: **Homology of archaerhodopsin and bR.** AR1 (P69052), AR2 (P29563), AR3 (P96787), and bR (P02945) sequences aligned. Similar amino acids properties are highlighted in grey.

Archaerhodopsins (ARs) are found in specialised regions of the membrane. These are known as patches of 'claret membrane', they present chromophores, which gives them their characteristic colour, the proteins themselves, and they have a high lipid-

protein ratio (typically 10:1) [216]. The difference in colour between the claret membrane and the purple membrane of bR is due to a carotenoid known as 'bacterioruberin' (Figure 2.2. a) [217].

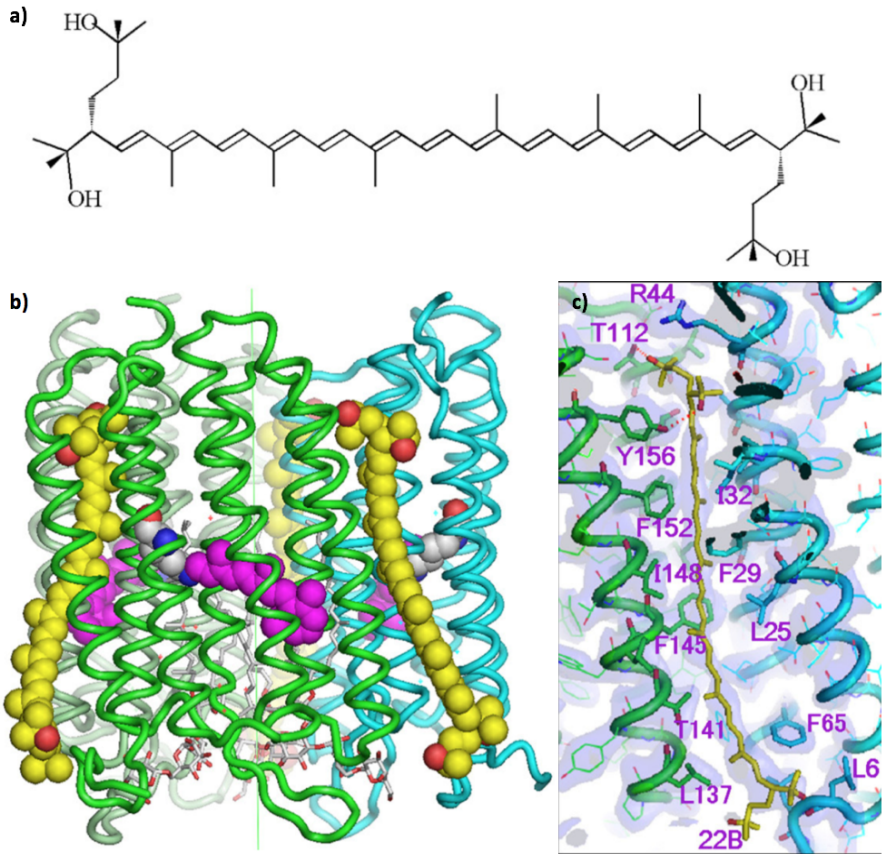

Figure 2.2: **Bacterioruberin role in AR2** a) Schematic representation of bacterioruberin structure. b) View of the AR2 trimer (represented in green and blue ribbon) on the side with bacterioruberin (represented in yellow balls and sticks) embedded within the trimer. c) Electron density map of the binding of bacterioruberin to AR2. Reproduced from [218].

Although bacterioruberin is present both in *H. salinarum* and *H. sodomense*, the purification of bR only yields the protein itself, whereas bacterioruberin is constantly co-purified with ARs [218, 219]. This suggests that there is a stronger association between bacterioruberin and the ARs proteins compared to bR (Figure 2.2. b-c) [218]. Additionally, spectroscopic studies have shown the particular interaction of ARs and

bacterioruberin which revealed the significance of bacterioruberin for these proteins [220, 221]. Thus, crystallography studies of AR2 showed how bacterioruberin binds between the protein crevices when forming trimers only observed in crystal structures when the trimeric organisation is present (Figure 2.2. b) [218].

Bacterioruberin is not the only key difference between AR3 and bR. Another one concerns their respective photocycles and the photocurrent change they produced [126]. As for their photocycles, the general opinion actually is that that of AR3 closely resembles bRs photocycle (Figure 2.3) [222], down to their photo-intermediates and ground states [222, 213]. Indeed, when AR3 is illuminated with green light (560nm), the retinal isomerizes from *all-trans* to *13-cis* (as in bacteriorhodopsin), and a sequence of conformational changes occurs (Figure 2.3), to transport protons from one side of the membrane to the other - just as what happens in bR [222, 213].

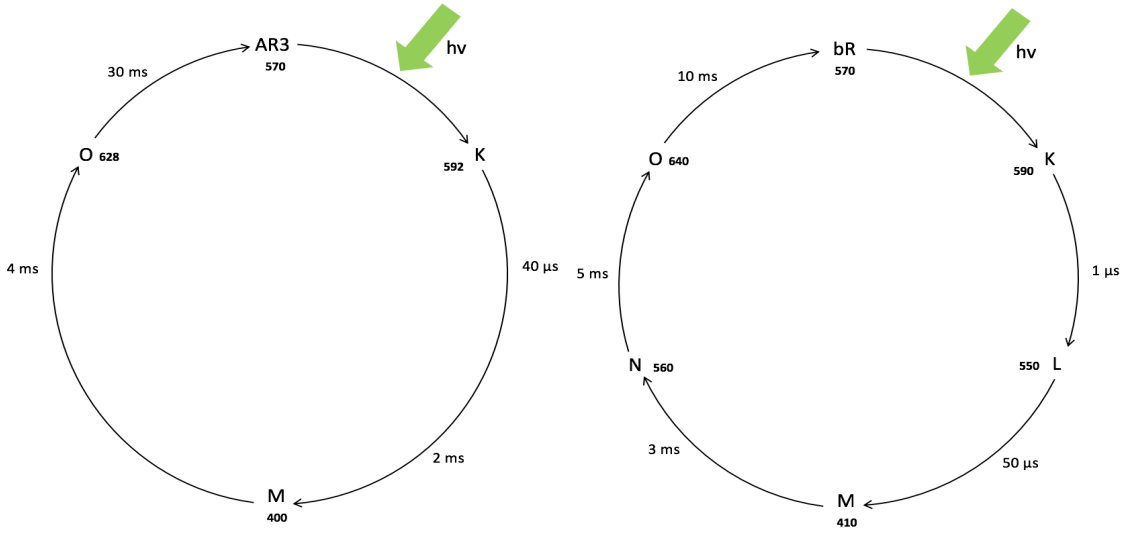

Figure 2.3: **Photocycle of AR3 and bR.** The proposed photocycle of AR3 is based on absorption, FTIR and fluorescence studies; the bR photocycle was determined using extensively studies using flash-photolysis, or time-resolved serial femtosecond crystallography. Adapted from [222, 89, 114].

Yet, despite this similarity in process, [222] and a sequence homology (Figure 2.1) that suggests a difference of only three amino acids in the proton channel, there is a significant discrepancy in the photocurrent between AR3 (300 pA) and bR (50 pA) produce [126, 223, 215]. Among the attempts to dispel our uncertainty over the actual difference between AR3 and bR photocycles, a Fourier-transform infrared (FTIR) spectroscopy study makes an intriguing point. It highlights how, while AR3 and bR both display similar structural changes, the main differences between them are concentrated around the water networks [224]. As an example, changes around the pentameric arrangement in AR3, conserved also in bR, were observed with a water molecule (Wat-401) which is in a different environment that results in a weaker hydrogen-bonding of the pentameric arrangement (Figure 2.4) [225]. The pentameric arrangement present in bR (Figure 2.4.a) is localised close to the Schiff base (SB) and is crucial for the deprotonation and protonation of D85 during the photocycle [225, 103]. This is also observed in AR2 (Figure 2.4.b), where the pentameric arrangement is also conserved, but it has been suggested that the different locations of the amino acids weaken the hydrogen bonding network (Figure 2.4) [226].

The small differences in water molecules and hydrogen bonding networks may have a significant impact on the photocurrent change of AR3 and bR (Figure 2.3) [225, 224]. The lack of a high-resolution structure for AR3 impedes the comparison between AR3, AR2 and bR, which would help in understanding the mechanism of AR3, and supply crucial information for protein engineering in this and other proteins, to alter their activity [225].

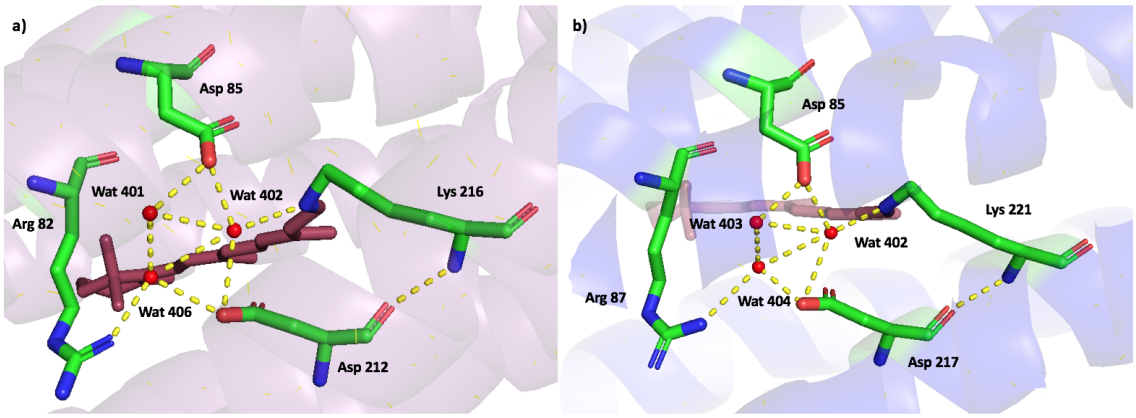

Figure 2.4: **Pentameric arrangement of bR and AR2** a) Pentameric arrangement of bR (PDB: 1C3W [103]) crucial in the proton translocation. b) Pentameric arrangement of AR2 (PDB: 3WQJ [74]) crucial in the proton translocation. The conservation of the pentameric arrangement in microbial rhodopsins is suggested to be key for proton translocation. Reproduced from [103, 74, 225].

2.1.2 Light- and Dark-adapted structure of bR.

Light is crucial for the functioning of microbial rhodopsins. In the absence of light many photoreceptors (including in bR) assume a desensitised or inactive form known as "dark-adapted state" [227, 228]. The differences between dark-adapted and light-adapted states are very subtle, since no large structural changes are observed between one form and the other. For this reason, a high-resolution X-ray structure of bR in both forms was needed [228]. Their comparison showed how the main difference between light- and dark-adapted forms in bR lies in the conformation of the retinal [229]. In the dark-adapted state, the retinal is found in a thermal equilibrium between the *all-trans* and the *13-cis* forms in a ratio of 1:2 (Figure 2.5) [230]. In the light-adapted state, retinal is in the *all-trans* form (Figure 2.5) [230]. Additionally, NMR studies suggest that there is a change in distance between the residue Trp86 and the retinal from 3.6 $\AA$ to 4.4 $\AA$, as well as between the residues Asp85 and Asp212 and the retinal (Figure 2.5) [228, 231, 232]. The changes between the two bR states are

very minor, and they are mainly localised to the side chain rotamer (Figure 2.5) [228].

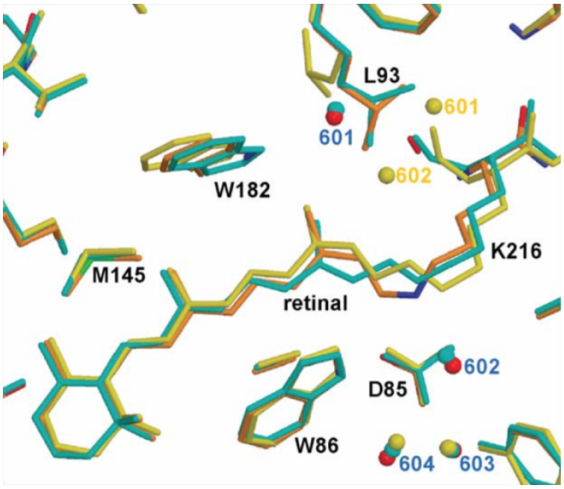

	bR_{trans}		bR_{cis}	
	X-ray	NMR	X-ray	NMR
Retinal-W86	3.6	3.8	4.4	4.6
Retinal-D85	5.8	>6	6.3	>6
Retinal-D212	4.6	4.4	4.9	>6

Figure 2.5: **Dark-adapted vs Light-adapted bR.** The different conformations of retinal in the dark-adapted (yellow and blue) and in light-adapted (orange) isomers and the surrounding residues and water molecules. The table presents the changes in the distances ($\AA$) between specific residues and the retinal in the bR_{trans} isomer and the bR_{cis} isomer. Reproduced and values retrieved from [228, 231, 232].

2.1.3 Photoisomerisation of bR.

The effect of light on bR has been also studied to asses the structural changes of the protein during the early photocycle stages, using X-ray free electron lasers (XFEL) and serial femtosecond crystallography (SFX) [233]. In 2016, Nango and colleagues were able to solve the structure of bR at various time points from 16ns to 250μs. The different changes in the residues they observed provided great insights into the proton translocation mechanism of bR (Figure 2.6) [233]. For example, the role of a water molecule becoming available between the SB and residue Thr89 creates a path

for proton movement to the residue Asp85. This explains the connection between the SB and Asp85 (Figure 2.6) [233].

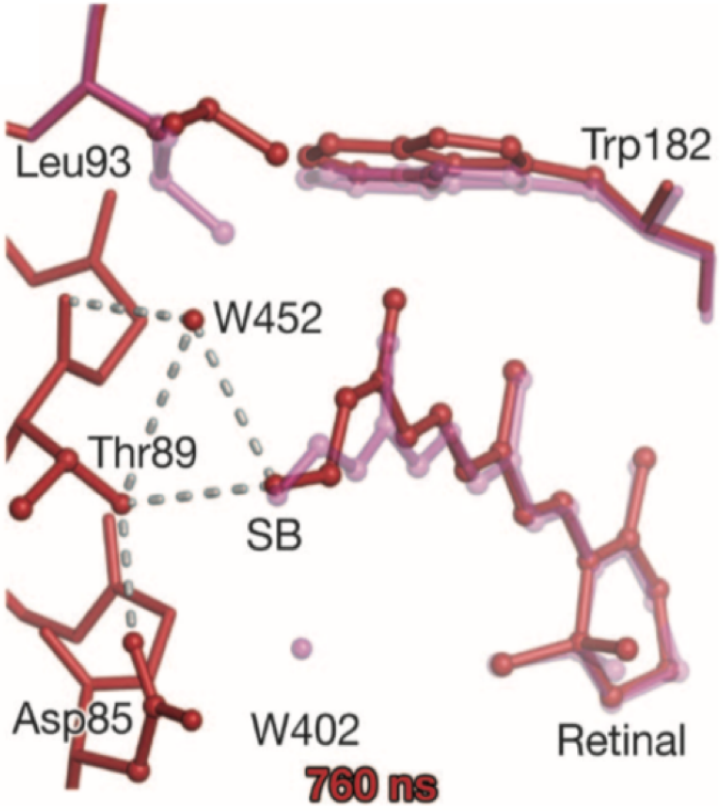

Figure 2.6: **Molecular changes in bR observed using XFEL.** Crystal structure of bR in the ground state (transparent purple) compared to the crystal structure obtained using XFEL at the 760 ns (red) time point. The changes in the positions of the residues and the water molecule movements during the photocycle to achieve proton translocation are resolved. Reproduced from [233].

On top of these insights into the early stages of the photocycle of bR, other studies have provided information on its later stages of the photocycle (Figure 2.3), which was unachievable using X-ray crystallography or other techniques, to show helical movements of the protein [194]. Shibata and colleagues in 2010 showed the helical movement that the E-F helices in bR were suspected to perform, using HS-AFM (Figure 1.26). This was the first study to visualise directly dynamic changes

of a photoreceptor upon illumination [194]. Moreover, this evidence could not be obtained through X-ray crystallography or the techniques of the previously mentioned structural activity [194].

The combination of all these studies have allowed us to understand better how bR functions [89]. This insightful information has been used to rationally design and then engineer bR variants to optimise its applications into biotechnology [109]. In stark contrast, the inner workings and functioning of AR3 are poorly understood [225]. The lack of an AR3 structure or of biophysical studies analysing the effects of light on it hamper the rational design and engineering of AR3 variants for optimised applications in optogenetics or biotechnology [225].

2.1.4 Aims

Here we aim to:

- Crystallise AR3 and gain structural information on the organisation of the protein at an atomistic level;
- Identify the differences between AR3 and bR which makes AR3 more efficient as a proton pump and assess any differences between AR3 dark-adapted and light-adapted states;
- Elucidate the oligomeric organisation of AR3 in the native membrane;
- Use HS-AFM to visualise directly any conformational changes occurring in the photocycle upon illumination.

2.2 Materials and Methods

2.2.1 Expression and purification of Archaerhodopsin-3

2.2.1.1 Culture of *Halorubrum sodomense* and isolation of Claret membrane

High salt concentrations of Na^+ and Mg^{2+} are necessary for the culture and expression of *Halorubrum sodomense* (strain RD-26). The cells were purchased from LGC Standards Ltd (Teddington, UK). Colonies of AR3 from stock were placed in 30 ml of culture media (composition in Appendix A.2) at 50°C shaking at 170 rpm for 10 days until the OD_{600} was 1. The cultures were inoculated in flasks with 500 ml of culture media and allowed to grow for an additional 20 days or until the OD_{600} reached 1.5. The cells were harvested through centrifugation (8,000 *g*, 20 min, 4°C). Once collected, the pellets were suspended in 4M NaCl with 5 mg of DNAse (Sigma), homogenised manually and dialysed overnight (5L; 0.1M NaCl). The membranes were collected by centrifugation (70,000 *g*, 60 min, 4°C), were resuspended into 10 ml of double-distilled water and placed in a sucrose gradient (w/v) made up of the layers: 30%, 35%, 40%, 45%, and 50% sucrose. The claret membrane was isolated by ultracentrifugation of the sucrose gradient (100,000 *g*, 17 hour, 15°C). The pink-coloured band between the layer 40% and 45% was collected and dialysed in 5L of double distilled water at 4°C overnight. The sample was further centrifuged (70,000 *g*, 60 min, 4°C) and the pellet with the claret membrane bearing AR3 was resuspended in double-distilled water (20 mg/ml) and then stored at 4°C.

2.2.1.2 Partial delipidation of Archaerhodopsin-3

The purified protein (AR3) was centrifuged (70,000 *g*, 60 min, 4°C) and resuspended in 6 ml of delipidation buffer (25 mM NaH_2PO_4, 2.5% w/v OG, pH 6.9). After a 1 min sonication at room temperature, the sample was incubated overnight at room temperature without any shaking. The pH was lowered to 5.5 and centrifuged (100,000 *g*, 60 min, 15°C). The supernatant was collected and placed onto a preparative gel column (Hi-Load 16/600, Superdex 200 pg) which had been equilibrated beforehand with delipidation buffer at pH 5.5. Coloured fractions were collected for measurements.

2.2.2 Characterisation of Archaerhodopsin-3

2.2.2.1 UV-Vis Spectroscopy

Absorption spectra were acquired with a Jasco V-630 instrument using a quartz cuvette (1cm).

2.2.2.2 Circular Dichroism

Following purification, the protein was centrifuged and resuspended in phosphate buffer (30 mM Na_2HPO_4, 20 mM NaH_2PO_4, pH 7.4) with no chloride to a concentration of 0.1 mg/ml. The measurements were performed in a Jasco J-815 Spectropolarimeter using a 1 mm cuvette. The spectra were analysed using CDSSTR [234] from the Dichroweb website [235].

2.2.2.3 High-Speed AFM imaging

AFM images were acquired by Javier Vinals in the tapping mode as described previously in the University of Kanazawa, in collaboration with Dr Mikihiro Shibata (1 month stay by invitation, Kanazawa Fellowship) [194]. The laser beam was focused

onto a small cantilever using a 50x objective lens. The cantilever (Olympus) had a spring constant of 0.1-0.2 Nm^{-1}. The resonant frequency and quality factor in aqueous solution were ∼1 and 2 MHz, respectively. In AFM imaging, the set point was 90% of the free amplitude (1 nm), and the estimated tapping force was less than 30 pN. A carbon tip was grown onto the original tip by electron beam deposition (EBD), and the tip apex was further sharpened to a 4 nm radius by plasma etching using argon gas. The measurements were performed in solution at room temperature, and for illumination of the sample a 532 nm laser was used. Images were imported and analysed with IGOR Pro [236].

2.2.2.4 Reconstitution of AR3 into nanodiscs

Dried lipid films were hydrated with 50 μL of HDFB (20 mM HEPES, 100 mM NaCl, pH 7.4) containing 4% DDM w/v. Samples were sonicated in order to prevent any aggregation, and 50 μL of solubilised AR3 (6mg/ml) and 50 μL of Membrane Scaffold Protein 1E3D1 (Sigma MSP1E3D1) at a concentration of 1mg/ml were added and allowed to incubate (1 hr, 4°C) in a rotating wheel. After one hour, Bio-beads (Bio-Rad, UK) were mixed with the sample in order to remove the detergent. The solution was allowed to mix (4°C, 12 hr). Samples were used within a week.

2.2.2.5 Dynamic Light Scattering

The size of the proteoliposomes were measured by DLS performed using a Malvern Zetasizer Nano S instrument (Malvern UK). The data was analysed using Malvern Zetasizer software. DLS measurements were independently repeated at least three times.

2.2.2.6 Electron Microscopy

Negative stain images of AR3 proteoliposomes were obtained at the following magnified sizes: 30000x, 49000x, 68000x, in collaboration with Juliette Devos in the Structural Biology Institute (IBS) of France (Grenoble, France). For proteoliposome size determination, the software used was ImageJ.

2.2.2.7 Crystallisation of AR3

Following purification, AR3 (20 mg/ml) was mixed with monoolein (Nu-Check) at a ratio of 40:60 respectively, using Hamilton syringes, and a syringe coupler in order to obtain the lipidic cubic phase (LCP). Many different conditions were screened, with the best condition giving crystals after 7 days, which was made up of 30% volume/volume polyethylene glycol 600 (PEG600, Fluka Analytical), 150 mM NaCl, 150 mM $CaCl_2$, 100 mM MES at pH 5.5. The measurements were performed at 100 K using liquid nitrogen at the I24 beamline at Diamond Light Source (DLS) in the UK. Diffraction patterns from a wide variety of crystals were combined via BLEND [237] and the AR3 phases were acquired using the AR1 structure (PDB: 1UAZ [226]) and molecular replacement in the Phaser software [238].

2.2.2.8 Serial femtosecond crystallography

The experiments were carried out in BL3 at SACLA in February 2019 following the protocol used previously by Nango and colleagues. The data collection and its processing was done using Cheetah [239] and CrystFEL [240], and as in Section 2.2.2.7, the AR3 phases were acquired using the AR1 structure (PDB: 1UAZ [226]) and molecular replacement in the Phaser software.

2.3 Results and Discussion

2.3.1 AR3 expression, detergent-free purification and characterisation

Archaerhodopsin-3 was expressed in its native organism *Halorubrum sodomense*. Its purification was performed similarly to bR, using sucrose gradient ultracentrifugation [241]. The sucrose gradient and the density of its different layers that makes it up had to be optimised in order to obtain pure protein (Figure 2.7.a), with a single band at 23 kDa, as observed in bR [241]. As for other archaerhodopsins, AR3 was co-purified with bacterioruberin, as evidenced by its absorbance spectra, where the characteristic three peaks of bacterioruberin are observed (Figure 2.7. b). To improve the resolution of the AR3 absorption peak, delipidation was performed using OG detergent.

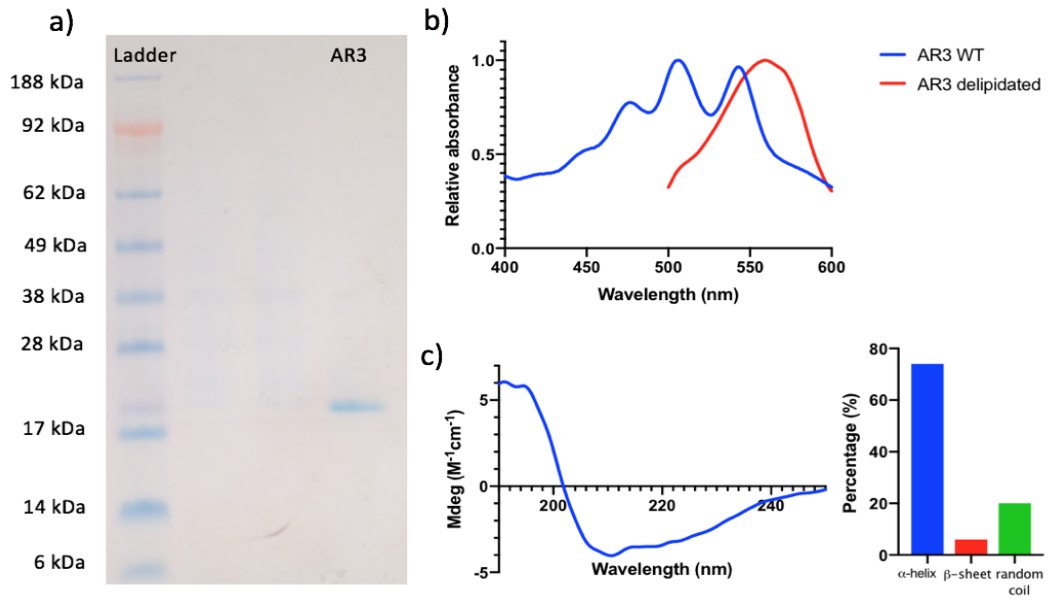

Figure 2.7: **Purification** a) SDS-PAGE of AR3 with a single band at 23 kDa. b) Absorbance spectrum of AR3 in claret membrane (blue) with three typical peaks characteristic of bacterioruberin, and the absorbance spectrum of AR3 delipidated (red). c) CD spectrum of AR3 and its secondary structure estimate using Dichroweb [235] with 74%helix, 6% sheet, 20% random.

The CD spectrum of the protein was measured and the predicted secondary structure content analysed (Figure 2.7.c). The values obtained for AR3 secondary structure (74% helix, 6% sheet and 20% random) are very similar to the ones obtained for bR (Figure 2.7.c) [242].

2.3.2 AR3 structure resolved by X-ray crystallography

Following the detergent-free purification of AR3 similar to bR [243], the protein was crystallised using monoolein to form the lipidic cubic phase (LCP) (Figure 2.8).

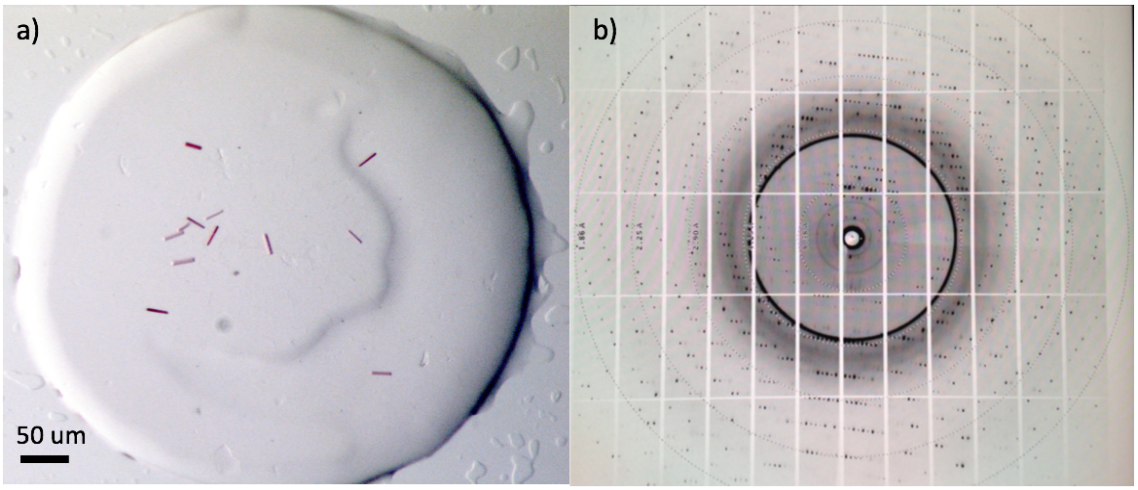

Figure 2.8: **AR3 crystals** a) Representative crystals of AR3 grown in lipidic cubic phase. b) Diffraction pattern of AR3 crystal. Bragg spots were observed up to 1.5 $\mathring{A}$ resolution.

Different structures were solved and deposited in the protein data bank (PDB) with the following PDB codes:

- PDB: 6GUX with a resolution of 1.3 Å
- PDB: 6GUY with a resolution of 2.2 Å
- PDB: 6GUZ with a resolution of 1.9 Å

- PDB: 6S6C with a resolution of 1.07 Å
- PDB: 6S63 with a resolution of 1.9 Å

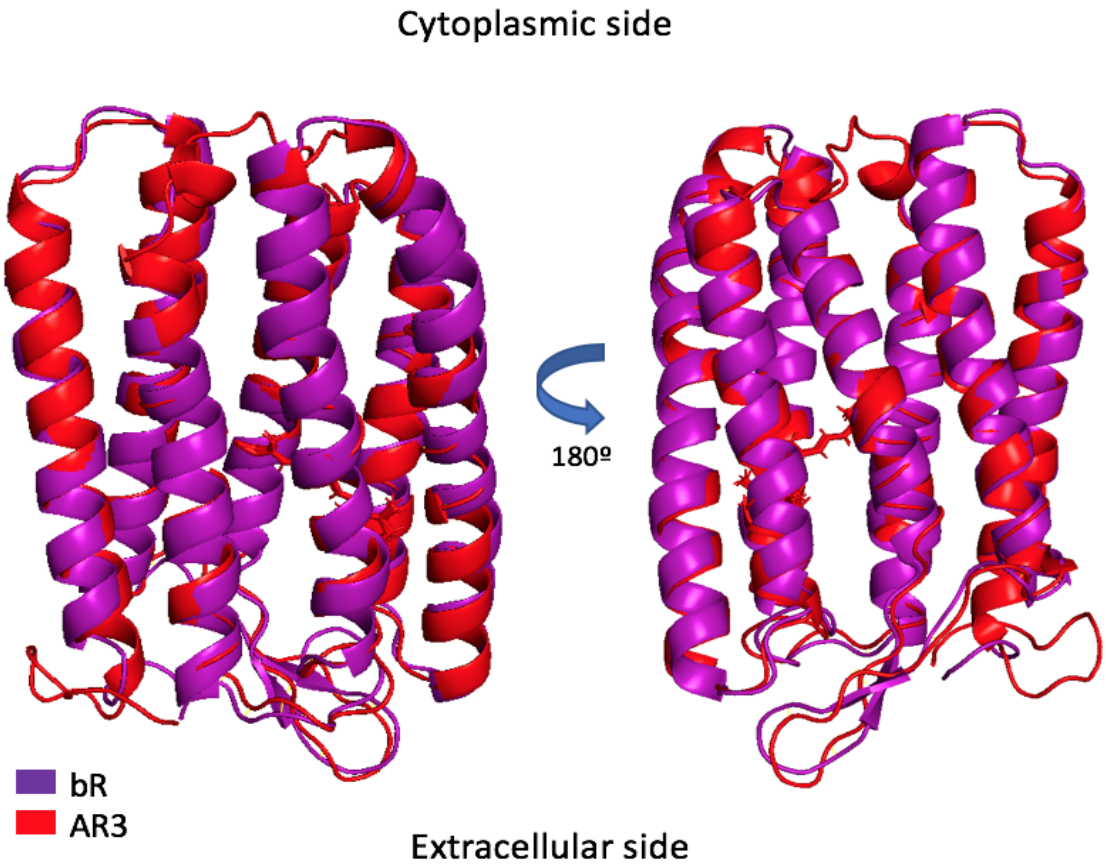

Figure 2.9: **AR3 vs bR** Crystal structures of AR3 coloured in red (PDB: 6S6C) and its homologue bR coloured in purple (PDB: 1C3W [103]) superimposed on each other with the orientation shown. A few differences can be observed in the loops (extramembrane part), but there is overall a high degree of similarity can be observed in the membrane spanning part (i.e. $\propto$-helix).

Here we focus on the light-adapted structure (6S6C) and on the dark-adapted structure (6GUX) of AR3, all obtained in collaboration with Dr Isabel Moraes from the National Physical Laboratory in the United Kingdom at the Diamond Light Source (DLS) Synchrotron, and Dr Juan Francisco Bada Juarez and Dr Peter Judge (Department of Biochemistry, University of Oxford). The data collection and refine-

ment statistics can be found in Appendix A.3, Table A.1. As shown in Figure 2.9, the secondary structure of AR3 is similar to bR [243], and is consistent with the CD spectrum in having significant α-helical content (Figure 2.7. c).

2.3.2.1 Dark-adapted vs Light-adapted AR3

As previously observed in bR and other archaerhodopsins, the retinal of AR3 is resolved in two different conformations (all-*trans* and 13-*cis*) in the dark-adapted state and only in one conformation (all-*trans*) in the light-adapted state (Figure 2.10) [228, 230]. Although resolved in both structures, the ratio of *cis* to *trans* retinal between the light-adapted (LA) structure and the dark-adapted (DA) structure is different. In the DA structure, there is a thermal equilibrium between the *cis* and *trans* isomers of the retinal present with a ratio of 70:30 respectively (Figure 2.10 a-b). The ratio here has been obtained after several rounds of refinement and are not derived from experimental data. Thereafter, the DA structure retinal ratio is of 67:33 *cis* to *trans* in bR, which is very similar to AR3 here, and suggests that we effectively have crystallised the DA state of the protein [230].

Conversely, in the LA structure, the retinal *all-trans* isomer is the only conformation resolved (Figure 2.10). This is consistent with the literature of bR and other archaerhodopsins, where the all-*trans* form is the most predominant form, up to 95% [230, 244]. Several factors can affect the retinal conformation such as pressure, temperature or pH and any of these conditions could have affected the isomer ratio, where one form may be favoured over the other [245, 246, 247].

Similarly to bR, no major changes are observed between the DA and the LA backbone of AR3 [228]. The only differences observed are localised to changes in distances

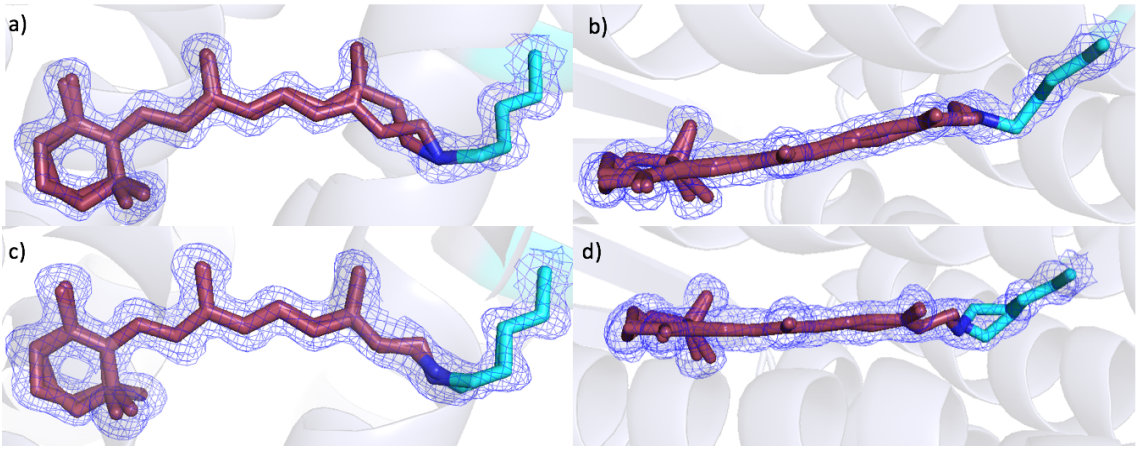

Figure 2.10: **Retinal Schiff base** Retinal Schiff base solved in a),b) DA (PDB: 6GUX) and c),d) LA (PDB: 6S6C) structure, showing the electron density of the retinal with the two conformations fitted. Electron density σ_{2Fo-Fc}=1.5. Retinal is coloured in dark red and SB lysine in sky blue

between residues (W96, D95, T99, D222) and the retinal, as observed previously in bR, suggesting that these residues are less rigid in the LA state (Figure 2.11) [228]. One change is localised to T99 (Figure 2.11), where the distance is shortened between the DA and LA, suggesting a stronger interaction which might indicate changes in the pentameric arrangement hydrogen bonding (Figure 2.12).

2.3.2.2 Hydrogen bonding networks in AR3

As in bR, AR3 presents a pentameric arrangement of hydrogen bonding. It is composed of six residues (D222, K226, D95, T99, R92 and Y185) and three different water molecules (Wat-401, Wat-402, Wat-406) (Figure 2.12) [248]. The distance of Thr99 is shortened relative to bR (Figure 2.11) [203, 228], while at the same time a partial breaking of the hydrogen bonding between Thr99 and D95 between the DA and LA is observed. On top of that, Wat-401 can be localised at two different points due to partial occupancies. This affects the hydrogen bond between Wat-406 and D95 (Figure 2.12). These events hint that the hydrogen network in the pentameric arrangement

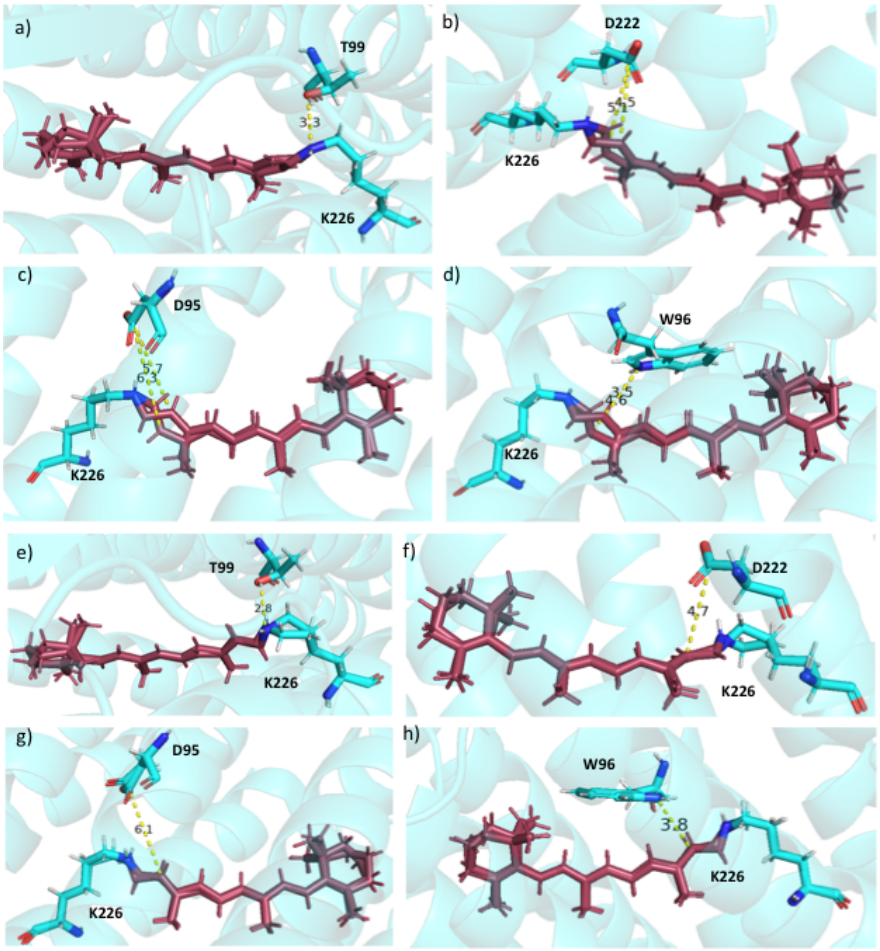

	Dark-adapted		Light-adapted
	$AR3_{trans}$	$AR3_{cis}$	$AR3_{trans}$
	X-ray	X-ray	X-ray
Ret C_{14}-W86-N^{ε}	3.5	4.6	3.8
Ret C_{14}-D85-C^{γ}	5.7	6.3	6.1
Ret C_{14}-D212-C^{γ}	4.5	5.1	4.7
Ret N-T89-O	3.3	3.3	2.8

Figure 2.11: **Changes in residue distances to the retinal chromophore in DA vs LA** a), b), c), and d) show the distances of the residues T99, D222, D95, and W96 to the retinal in the DA structure in the *13-cis* and *trans* conformation summarised in the Table. e), f), g), and h) show the distances of the residues T99, D222, D95, and W96 to the retinal molecules in the LA structure in and *all-trans* conformation summarised in the Table.

of AR3 is weaker than the one of bR, as suggested by FTIR measurements on AR3 [225].

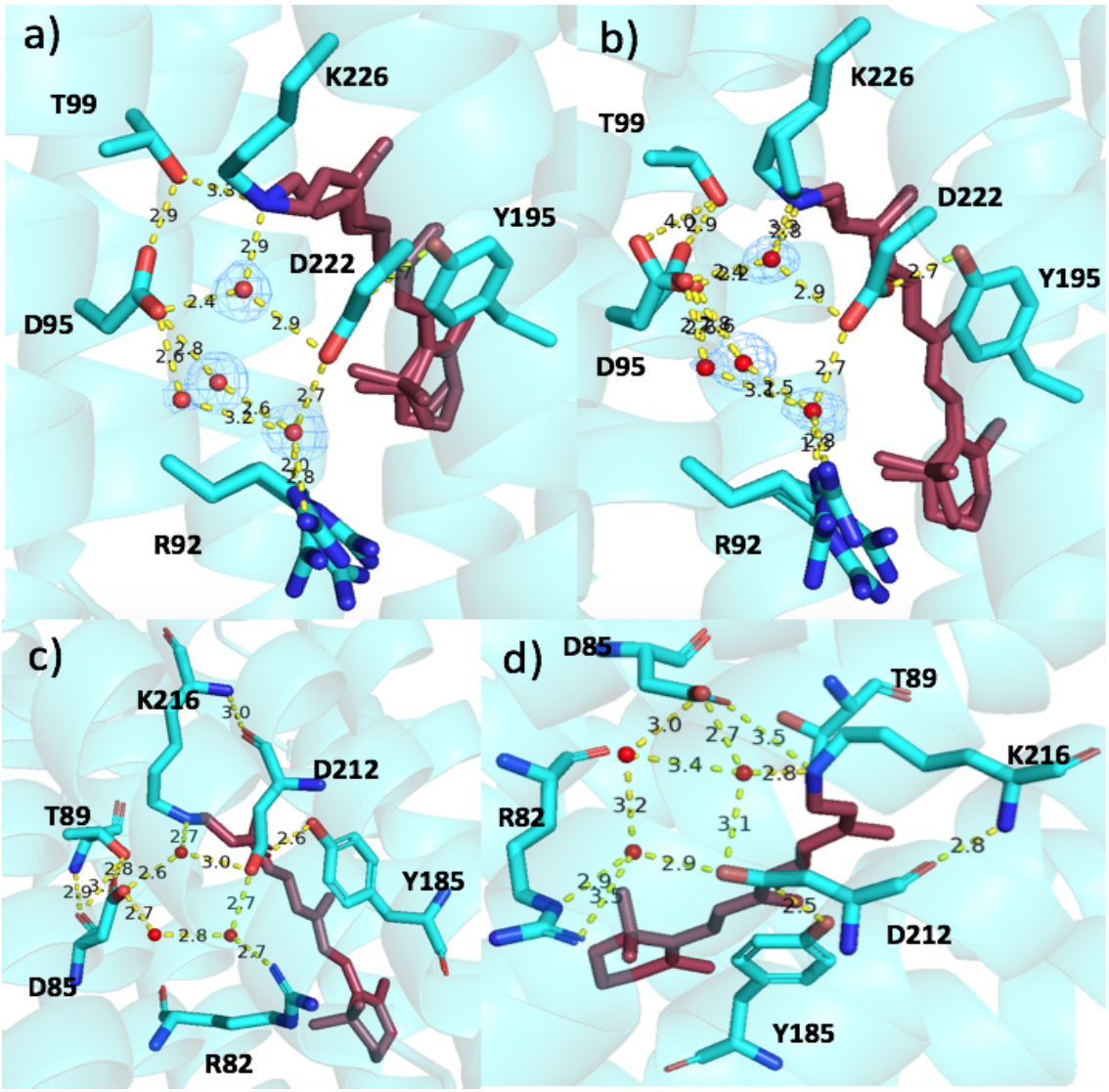

Figure 2.12: **Pentameric arrangement in AR3 and bR** a) and b) show the pentameric arrangement of AR3 in the DA (PDB: 6GUX) and LA (PDB: 6S6C) respectively. c) and d) show the pentameric arrangement of bR in the DA (c, PDB:5ZIM [203]) and LA (d, PDB: 1X0S [228]). The main distinction found between these are the partial occupancy where Wat-401 is found at in both AR3 structures compared to bR, and the different orientation R92 is found at compared to the orientation in bR structures. Electron density contoured at σ_{2Fo-Fc}=1.5. Distance unit is $\mathring{A}$.

Another residue indirectly participating in the pentameric arrangement of hydrogen bonding is R92 (Figure 2.12). FTIR has put forward that R92 has a weaker

interaction with Wat-406, and indeed in the latest high-resolution structure of bR (1.3 Å[203]) a change in the rotation of the residue towards the extracellular domain, and the proton release complex is observed [225, 203]. As in bR, the R92 residue in AR3 is resolved in very different orientations in both states with various water molecules surrounding it (Figure 2.13).

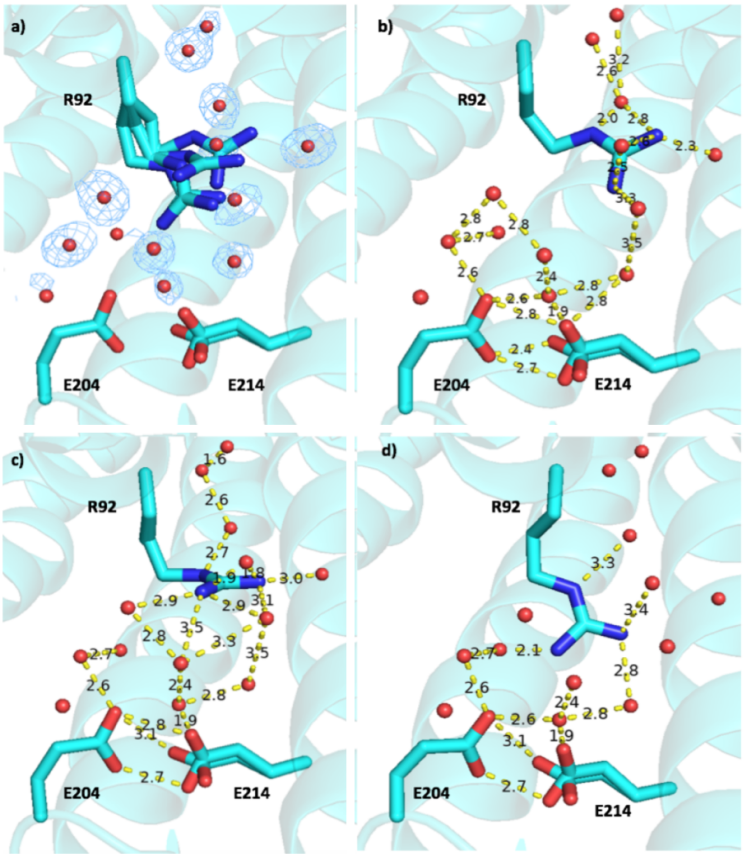

Figure 2.13: **R92 conformations and the hydrogen bonding network in the PRC for the AR3 DA structure.** a) shows the different conformations that R92 is found in the DA (PDB: 6GUX) structure and the water molecules around with the fitted electron density maps to the water molecules. b) hydrogen bonding between R92 and the glutamic pair E204/E194 corresponding to one of R92 conformations and hydrogen bonding pathways. c) hydrogen bonding between R92 and the glutamic pair E204/E194 corresponding to one of R92 conformations hydrogen bonding pathways. d) hydrogen bonding pathway of R92 and the glutamic pair E204/E194 corresponding to one of R92 conformations hydrogen bonding pathways. Electron density σ_{2Fo-Fc}=1.5.

These water molecules allow for an intricate hydrogen bonding network between

the R92 and the glutamic acid residues (E204, E214) forming the proton release complex (PRC) (Figure 2.13). In contrast with bR, the water molecules at partial occupancy coupled with R92 found in different conformations make for a higher complexity in this section of AR3 due to a larger cavity in this region compared to bR (Figure 2.13) [203]. The intricate hydrogen bonding network in this region and the number of water molecules (up to 9 in AR3), could explain the higher photocurrent and faster photocycle of AR3 (Figure 2.3) [222].

Despite the similarities between bR and AR3, AR3 presents a characteristic of all archaerhodopsins in AR3 which is absent in bR [218, 226]. As in AR2 and AR1, residues from Asp11 to Arg17 make up a structure known as an 'omega loop'. It has been proposed that this is a binding site for the chromophore bacterioruberin in AR2 (Figure 2.14) [226, 218].

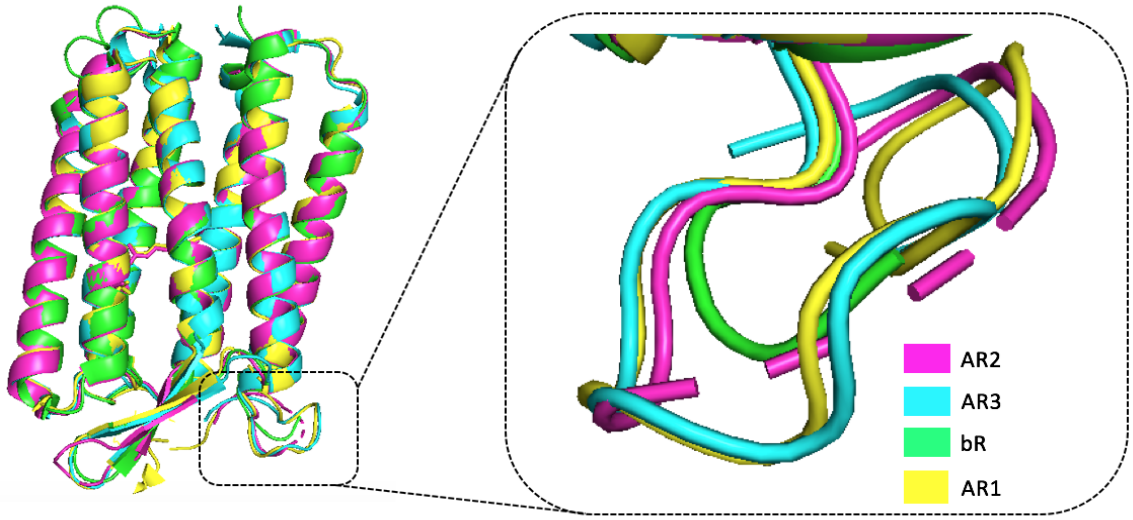

Figure 2.14: **Omega loop in archaerhodopsin** Overlay of the structures of AR1 (yellow, PDB: 1UAZ [226]), AR2 (pink, PDB: 3WQJ [74]), AR3 (cyan, PDB: 6GUX), and bR (green, PDB:5ZIM [203]). As observed, all the archaerhodopsins share this omega loop made up of the conserved residues (DLLGD) meanwhile in bR it is not present.

Unfortunately, the electron density could not allow for the fitting of bacterioruberin in this position in either structure. It has been suggested that bacterioruberin has an important role in the oligomerisation of archaerhodopsins and is resolved in the interface between monomers in the crystal structure of the AR2 trimer (Figure 2.2) [226, 218].

2.3.3 AR3 oligomerisation

As for bR and AR4, AR3 forms a trimeric lattice found in claret membrane patches (Figure 2.15) [249, 250]. The comparison of the area between the trimer of bR (15.24 $\pm$ 2.11^2) with that of AR3 (15.15 $\pm$ 1.10 nm^2) shows no difference in size between them (Figure 2.15) [194]. A similar trimeric packing is observed in AR4, and it is suggested that the key for the trimeric organisation are the residues L48, G113, and L117, conserved in archaerhodopsins as well as in bR [249]. Crystallographic data has suggested bacterioruberin is a key factor for inducing the trimeric organisation of AR2, by binding the crevices of the protein (Figure 2.2) [218].

To study the role of bacterioruberin in the oligomerisation of AR3, we expressed and purified AR3 from *E.coli* (AR3 EC), since bacterioruberin is not expressed in bacterial strains, therefore making the protein expressed without bacterioruberin. Once purified using detergent (DDM), we reconstituted the protein into lipid nanodiscs, similarly to how Shibata and colleagues proceeded with other microbial rhodopsins such as, halorhodopsin from *Natromonas pharaonis* (*Np*HR), rhodopsin from *Gloeobacter violaceus* (GR), and xenorhodopsin from *Parvularcula oceani* (PoXeR) [251]. In this study carried out, a wide screening of microbial rhodopsins reconstituted into Nanodiscs was performed to study their oligomerisation, demonstrating that micro-

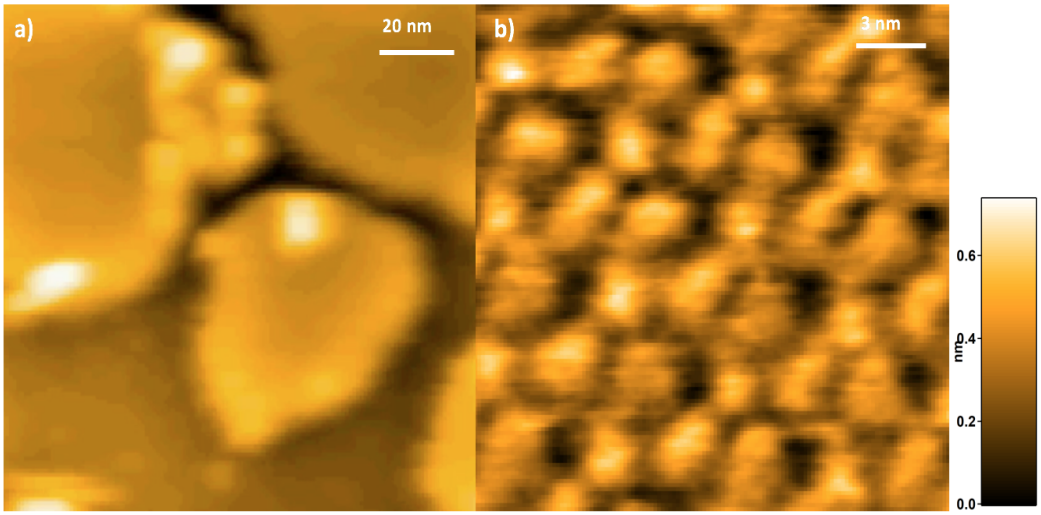

Figure 2.15: **Oligomerisation of AR3.** a) HS-AFM visualisation of claret membrane patches from Halorubrum sodomense. b) Oligomeric organisation of AR3 (area = 15.15 ± 1.10 nm^2, where N=5 trimers) in the claret membrane patches forming 2-D crystalline array where the protein is organised into trimers.

bial rhodopsins can oligomerise in Nanodiscs similarly as they do in native membranes [251]. In the current study, asolectin (a soybean extract) was chosen for reconstituting AR3 (Figure 2.16), since this has been already successfully used for Nanodisc reconstitution for HS-AFM [251]. Furthermore, we also reconstituted AR3 into DMPC nanodiscs, previously used to reconstitute bR into liposomes for EM experiments (Figure 2.16) [67].

Figure 2.16 depicts AR3 reconstituted into Nanodiscs with different lipid mixtures. In there, AR3 trimeric assembly can be observed in AR3 native proteoliposomes where bacterioruberin is present (Figure 2.15) but no array has been observed in non-native liposomes (Figure 2.16). No 2-D array formation or trimers were observed within the nanodiscs even though several experimental conditions were performed by changing lipids (DMPC and Asolectin), lipid-to-protein ratio (500:1, 200:1, 100:1) or pH reconstitution conditions (pH 5 to pH 10 studied). Additionally, we suggest that

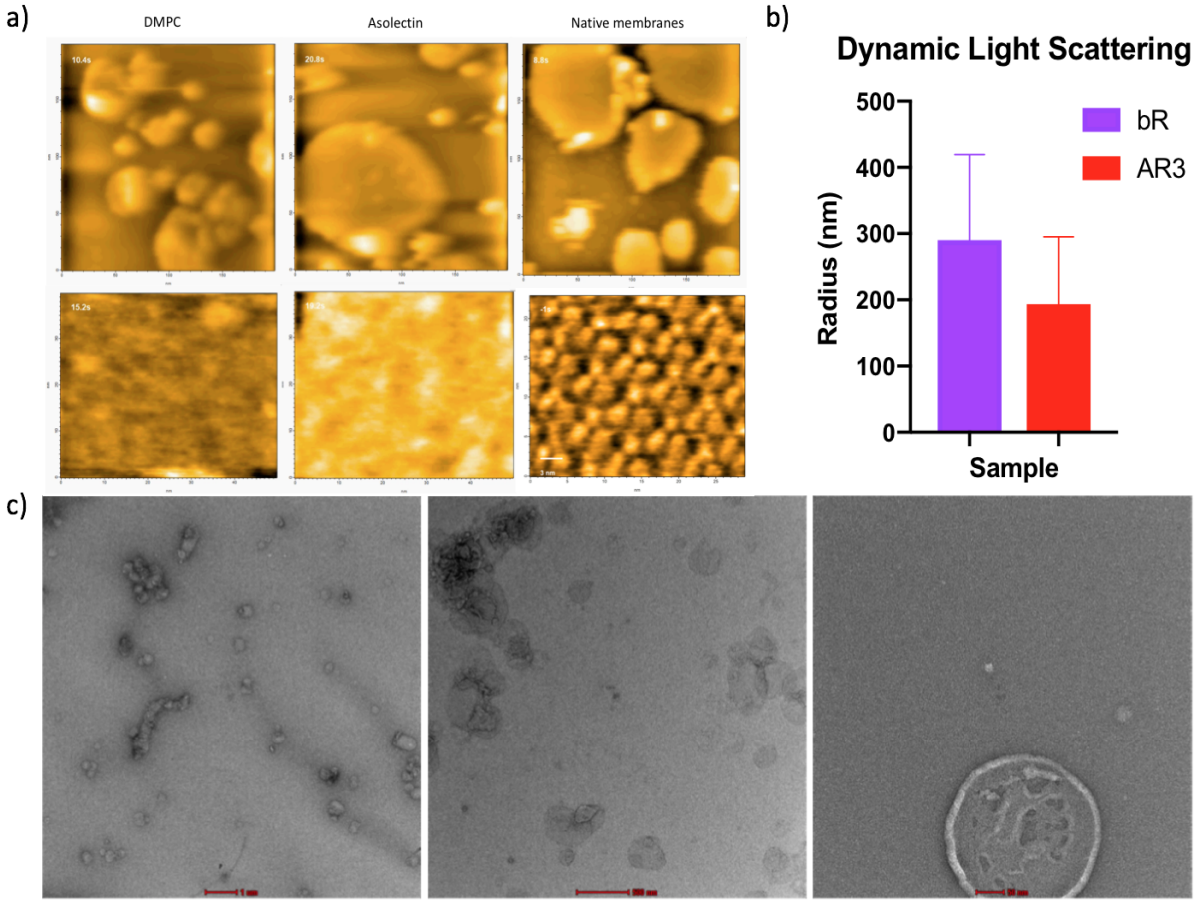

Figure 2.16: **Assessing the role of bacterioruberin.** a) HS-AFM imaging of AR3 purified from *E.coli* without bacterioruberin reconstituted in nanodiscs of DMPC and Asolectin compared to AR3 native proteoliposome from *H. sodomense*. Top figure: picture of patches formed by AR3 proteoliposomes and the DMPC and Asolectin nanodiscs, and underneath a close look at those patches to elucidate the oligomeric organisation of AR3. b) DLS measurements of the AR3 (193.7± 101.3 where N=3) proteoliposomes relative to bR (290± 129.3 nm, where N=3) to assess the curvature of the proteoliposomes. c) EM images of AR3 proteoliposomes at 1μm, 500nm and 50nm.

protein reconstitution in Nanodiscs is favouring the monomerisation of the protein (Figure 2.16).

These preliminary experiments on AR3 reconstituted into nanodiscs show that there is no trimer formation or creation of a 2-D crystalline array, as observed in the native membranes (Figure 2.15). Coupled with dynamic light scattering data (in

collaboration with Juan F. Bada Juarez, DPhil thesis) and the EM data collected which suggests that bacterioruberin might be important due to the small size of the native proteoliposomes observed when bacterioruberin is present (Figure 2.16). The particle size of AR3 proteoliposomes (193.7± 101.3 nm radius) compared to bR (290± 129.3 nm radius) have a difference of almost 100 nm in radius which may be due to a higher curvature in AR3 proteoliposomes compared to bR (Figure 2.16). Literature suggests that AR4 proteins expressed in cells without bacterioruberin have a larger particle size (similarly to bR), suggesting that bacterioruberin might be important for the tight packing, curvature and the protein-protein interactions enabling higher oligomeric state in AR3 proteoliposomes [252]. Moreover, this is accordance with crystallography experiments in AR2, where bacterioruberin is embedded in the crevices of the trimer which correlate with the fact that it can help structurally in the oligomeric organisation of the protein (Figure 2.2) [218]. Several additional experiments such as EM or HS-AFM experiments optimising lipid conditions or buffer salt concentrations as previously done in bR, would pave the way in helping to elucidate the role of bacterioruberin in AR3.

2.3.4 AR3 light dynamic changes

The conformational changes observed between AR3 and bR motivated the study of AR3 dynamic changes upon illumination, as shown for bR [233, 194]. To obtain information on how AR3 behaves in the early stages of illumination, we used x-ray free-electron lasers (XFEL) and time-resolved serial femtosecond crystallography (TR-SFX). For longer timescales (ms-s timescales) that entail large conformational movements we used high-speed atomic force microscopy (HS-AFM).

2.3.5 AR3 dynamic changes using XFEL

Synchrotron studies have been a powerful technique in biology and its development and their use has led to a leap forward in X-ray crystallographic studies [253]. Synchrotron studies have helped in the resolution of thousands of protein structures, including membrane proteins deposited in the PDB. In recent years, a new technique (X-ray free electron lasers, "XFELs") has been developed in order to study structural dynamics in proteins and, with time-resolved capability, [253], with a reduced radiation damage being reflected in the protein structure [254]. In XFELs, the X-ray source created from electrons travel through a linear path instead of the synchrotron circular one, generating a higher energy X-ray source passed through undulators [254]. The XFELs X-ray source generated increases the peak brilliance by 10^9 in comparison with Synchrotron X-rays [254, 255, 256, 257]. The peak brilliance is a measure of the number of photons that can be focused in a single point for a given period of time, allowing the data collection for each pulse (diffraction patterns) [255, 256, 257].

In this approach, a single crystal cannot be rotated several times as in synchrotrons, because the XFEL X-ray source destroys the crystal (Figure 2.17) [253]. However, simulations have demonstrated that such destruction has a delay, which can be used to obtain data collection and observe structural changes in the sample [258, 259]. This is known as "diffraction before destruction" and it is the foundation of the XFEL experiments [258, 259]. For this reason, the crystals needed for XFELs can be very small crystals, so that they can pass through the beam in succession in multiple orientations. This has lead towards the development of the technique known as "serial femtosecond crystallography" (SFX) (Figure 2.17) [253, 258, 259].

The advantage XFELs presents, in addition to the fast, dynamic changes observed in the protein, is the removal of radiation damage being recorded in the data that can occur in Synchrotrons [259].

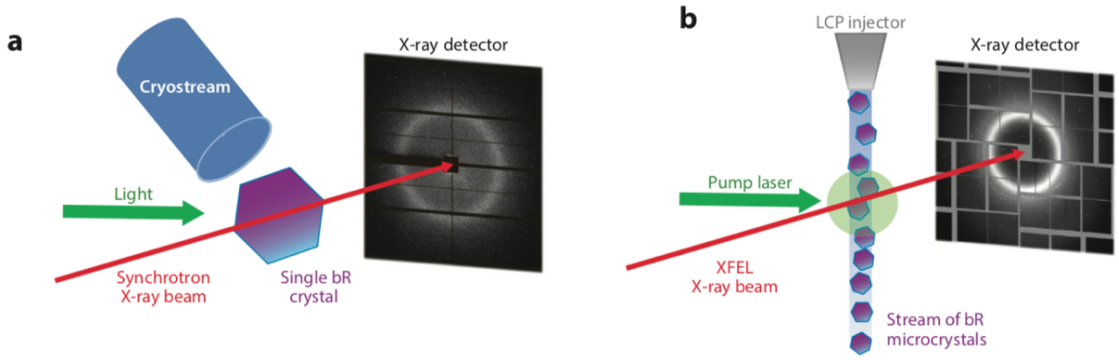

Figure 2.17: **Serial crystallography in XFEL** a) Schematic of Synchrotron data collection from a single crystal that is rotated several times under a cryostream. b) Schematic of XFEL data collection using SFX where a flow of crystals is exposed to the pump laser and X-ray source once for data collection. The time delay between the pump laser and the beam is controlled and can be used to study structural changes of the protein upon illumination. Reproduced from [253].

Therefore, the sum of all these developments has led to a new revolutionary technique that can be used to study ultrafast structural changes in light sensitive proteins upon illumination. XFEL and SFX have been used successfully to show conformational changes obtained for bR at different timescales; from ps to ms [233, 260]. Using a photo-irradiation set-up (Figure 2.18), the protein dynamics were studied at different time points that revealed important movements pertaining to water molecules and residues never observed before (Figure 2.6) [233, 260].

In the present work, XFEL was used here to resolve the crystal structure of AR3 at different time points of its photocycle to obtain dynamic conformational information about the early events in AR3 after illumination, using the same photo-irradiation set-up [233] (Figure 2.18.b,c). The crystallisation procedure was optimised so that

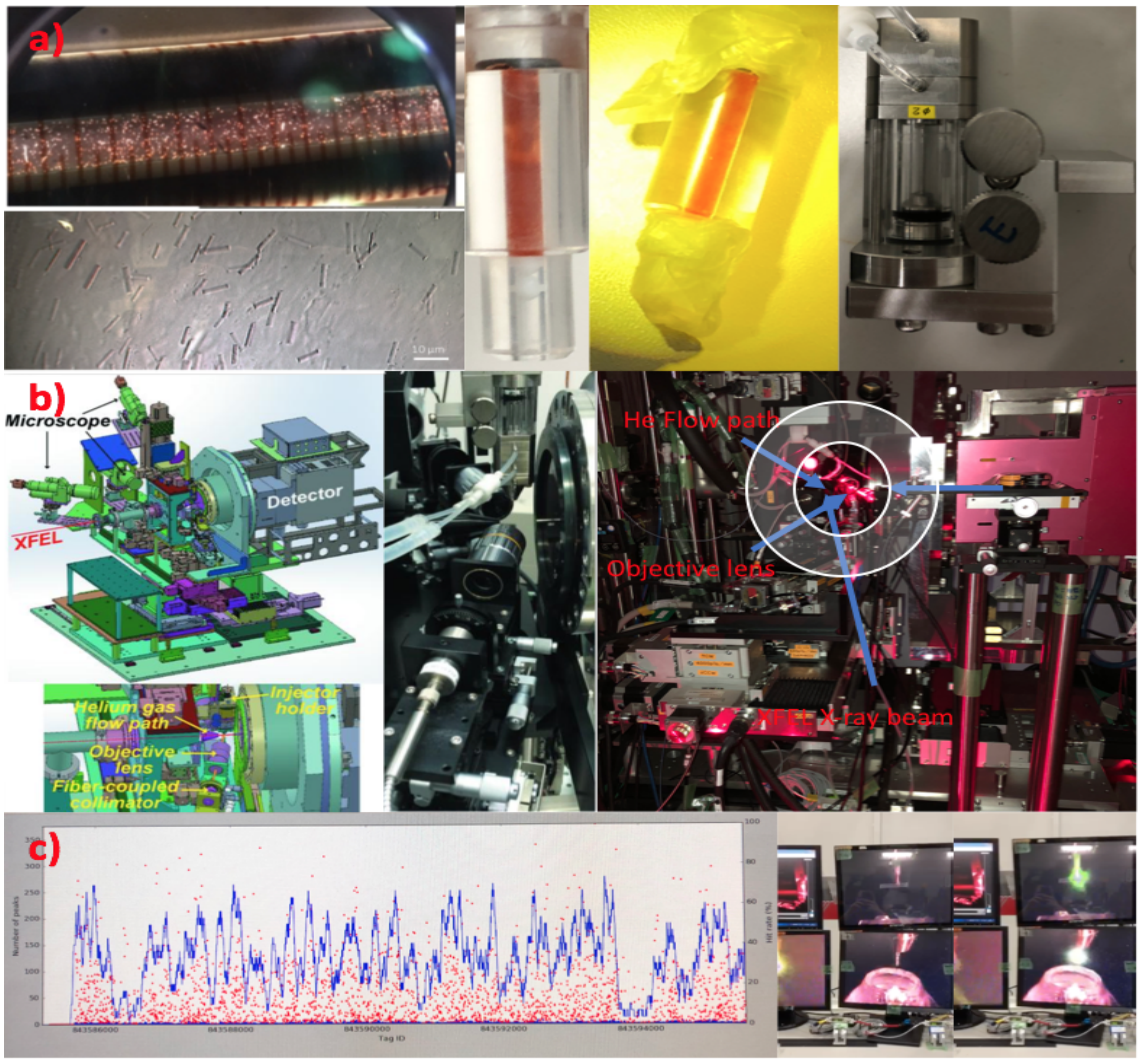

Figure 2.18: **XFEL set-up** a) Small crystals grown (left) in glass vial, the cartridge (middle) where protein crystals are deposited and the injectors (right) mounted with the cartridge. b) Scheme of the XFEL set-up showing the detector (left) and where the injector is deposited (middle, and highlighted by white circle in right panel) for the flow stream of crystals to pass through the X-ray beam (right). c) Left panel shows the hit rate (in blue protein crystals diffracted compared to total XFEL show) and red dots are the number of Bragg spots in every diffraction pattern recorded. Right panel shows the injector in a dark-room where the sample is flowing through the injector (top) and where the laser pump-probe is switch on (green dot below the injector). A sucking device is present to help the protein crystal to flow and collect LCP after being hit by the XFEL beam. Adapted from [261].

smaller crystals fit for XFEL experiments were available. The crystals were grown in glass vials (Figure 2.18.a), and were exposed to light (532 nm) similarly performed

for bR experiments to obtain the light-adapted state (Figure 2.18.a) as it was done in bR [233].

Different time points were studied through this experiment, namely; 16 ns, 40 ns, 110 ns, 290 ns, 760 ns, 2 μs, 5.25 μs, 13.8 μs, 36.2 μs, 95.2 μs, 250 μs, 657 μs, 1.2 ms, 1.725 ms.

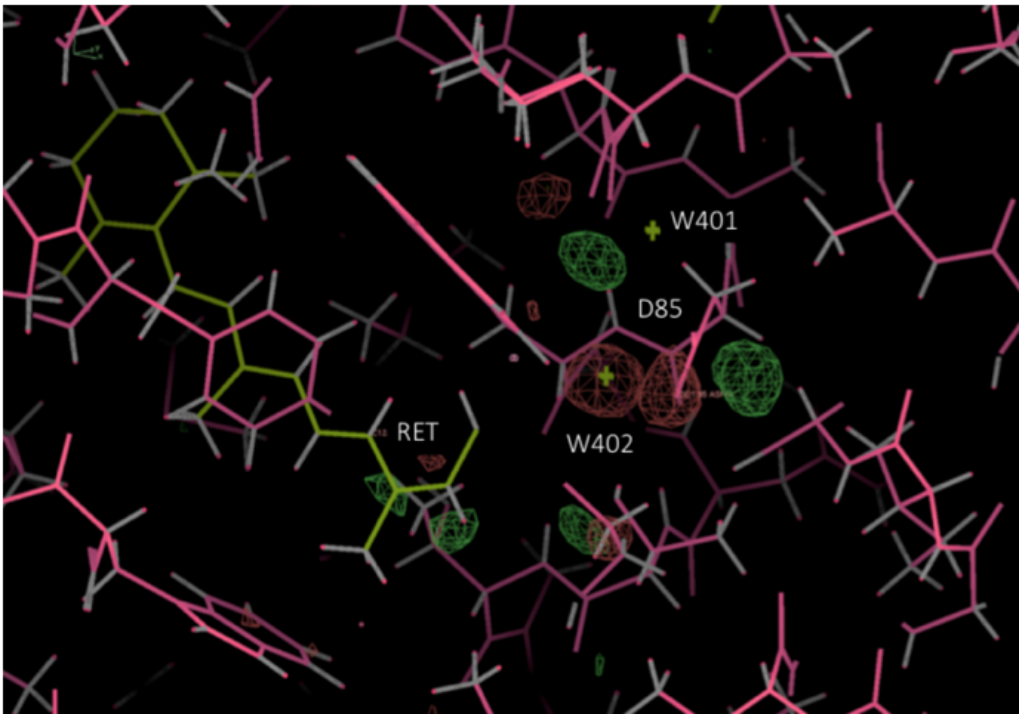

Figure 2.19: **5 μs time point.** 5 μs time point where Wat-402 is found at partial occupancy and D85 is orientated towards the retinal. The red colour represents the negative density and the green colour represents the positive density. Electron density σ_{2Fo-Fc}=1.5.

The data from the experiment is under refinement, thus no structures are available at present. Nevertheless, clearly the information collected will be very important for understanding the movements taking place during the AR3 photocycle, and could help in the understanding of the proton translocation mechanism. For example, such data collected at 5.25 μs provides information on AR3 structural changes since a water molecule (Wat-402) moves (low partial occupancy compared to ground state) and

a change in the orientation of D85 is observed (Figure 2.19) relative to the retinal similarly as in bR [253]. A comparison of these structures to bR would elucidate mechanistic differences between the proteins and help discern what small changes in the photocycle might lead to the large differences between these two protein in photocurrent production.

2.3.6 AR3 dynamic changes using HS-AFM

XFEL experiments allow for the observation of structural changes in the AR3 monomer at the nanosecond-to-microsecond timescale, but they do not provide information on the larger conformational changes of the trimer in the later photocycle intermediates (∼50ms) [233, 260]. Exploiting the rapid response of AR3 to light, HS-AFM can help address this aspect for AR3, and enable to directly visualise the conformational changes (Figure 2.20) that would complete the data obtained with XFEL.

For direct observation, the imaging of AR3 was performed in an alkaline pH (pH 10). It has been observed that an alkaline pH increases the M-state decay in comparison to pH 7. This facilitates the observation of any rapid changes in the molecule [194, 263]. Although no conformational changes were observed at pH 7, they were observed at pH 10. The trimer area of AR3 upon illumination was 19.26 ± 2.45 nm^2 while the area of the trimer under dark conditions was of 15.15 ± 1.1 nm^2 showing a displacement in the AR3 trimer (Figure 2.20). The change in size points towards the displacement of the E-F loop taking place during the M-state. Moreover, the surface map in Figure 2.20 illustrates how a monomer (symbolised by one single peak) in dark, (Figure 2.20. d top panel) is split into two minor protrusions upon illumination (Figure 2.20. d lower panel). The changes observed are believed to

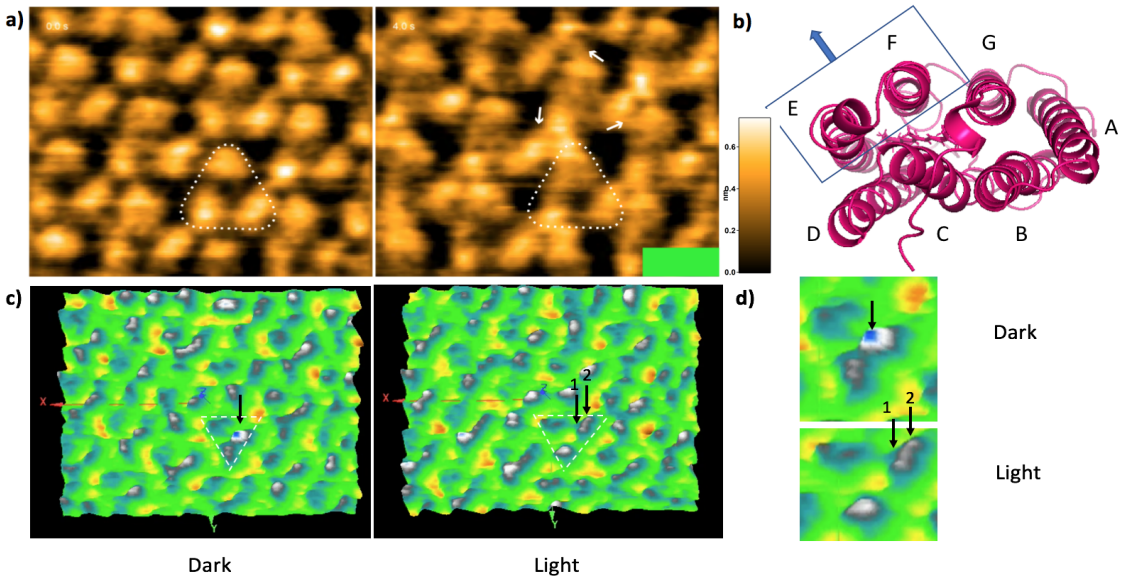

Figure 2.20: **HS-AFM images of AR3 under dark or illuminated conditions** a) AFM images of AR3 in dark (area = 15.15 ± 1.10 nm^2, where N=5) and illuminated (area = 19.26 ± 2.45 nm^2, where N=5) (green bar) condition with the trimer (dotted white line) and showing the movement of the protein (white arrows. b) AR3 structure highlighting the E-F loop displacement observed in AFM. c) 3D surface map of image in panel (a) with the trimer highlighted by a dotted line. A monomer under dark conditions (left arrow 1), and its conformational changes (right arrows 1 and 2) observed in AR3 upon illumination. d) Higher magnification of the protrusion that takes place in (c) Upon illumination of the trimer. A complete video of the movement of the protein can be found in the link in reference [262].

correspond to the E-F loop movements that take place in the M-state (Figure 2.20) [194]. Additionally, the movement is not restricted to one trimer, but is observed in surrounding trimers (Figure 2.20) consistent with the cooperative effect observed in bR [194].

The conformational changes observed point towards conformational changes in AR3 as reported for bR [194]. The E-F loop tilt had been observed in bR previously and is reported to lead to large conformational changes associated with the M and N photo-intermediates [264]. As in bR, such changes in AR3 (Figure 2.20) help with the opening of the proton channel towards the cytoplasmic surface in the M-state

[215, 89].

2.4 Conclusions

In this Chapter, we have described how AR3 has been crystallised and two high-resolution structures of AR3 have been obtained and modelled for the first time. We successfully obtained a light-adapted structure and a dark-adapted structure of AR3, and drew comparisons between these two structures, as well as between them and those in bR. We observed intricate hydrogen bonding networks around AR3 which are not present in bR. We also observed conformational changes localised to the orientation of some residues (such as R92 in the PRC) that might hint why the photocurrent of AR3 is higher than in bR.

Furthermore, we were able to determine the oligomeric organisation of AR3 in the native membrane not previously achieved in the literature. As seen, AR3 forms a crystalline 2-D array where it organizes itself into trimers. The presence of bacterioruberin and of an omega loop for its binding hints at the key role of this carotenoid in the oligomeric organisation of AR3. AFM results of AR3 in the absence of bacterioruberin, coupled with data in EM and DLS of the protein, support the role of bacterioruberin as a stabilizer of the trimeric structure of AR3.

Lastly, the conformational changes that the protein undergoes upon illumination were observed for the first time. Similarly to bR, there is an E-F loop displacement typically observed in the M-state as also happening in bR hinting at a similar sequence of proton uptake.

The data presented in this chapter provides for the first time crucial and new

information on the structure of AR3 at high-resolution. This allows us to understand the molecular basis of the protein, and it helps understand the proton translocation mechanism of the protein thanks to the AFM data obtained. These results provide the necessary knowledge for a better design of AR3 mutants to be used in different biotechnological applications.

Chapter 3

Biophysical characterisation of AR3 proton pumping, and photoconductivity

The work described here focuses on the biophysical characterisation of AR3 into droplet interface bilayer (DIB) for assessing the activity of the protein. We optimise the reconstitution of AR3 into DIB for the first time and assess its biophysical characteristics in this system. Furthermore, we investigate the role of some pigments present in the native environment, such as retinal and bacterioruberin.

3.1 Introduction

3.1.1 AR3 unique properties

As described in Chapter 2, the structure of AR3 and bR share a high degree of sequence identity in their structure (up to 59%, Figure 2.1)[215, 103] and they are believed to have similar photocycles (Figure 2.3) [222, 89, 114]. Still, the small changes observed between AR3 and bR result in a much enhanced photocurrent change (Figure 3.1). Other archaerhodopsins studied, such as AR2 and AR4, confirm how small changes in their structures and sequences, can affect their activity [215, 74]. For

example, in AR4 such changes mean that steps in the photocycle may be switched, and that the proton uptake is reversed, contrary to what happens in bR [215]. AR2 gives another example, where it was found that the transition from the K state to the L state was found to be slower in AR2 than in bR (Figure 2.3) [74]. Different explanations have been offered to explain this phenomenon. One of them is that the high photocurrent observed in AR3 (Figure 3.1) may be due to the fast photocycle of AR3 in comparison with bR (Figure 2.3) [215, 92]. Another suggestion is that these differences may be due to a difference in the pK_a of residues involved in the proton uptake pathway [126, 215, 223, 92].

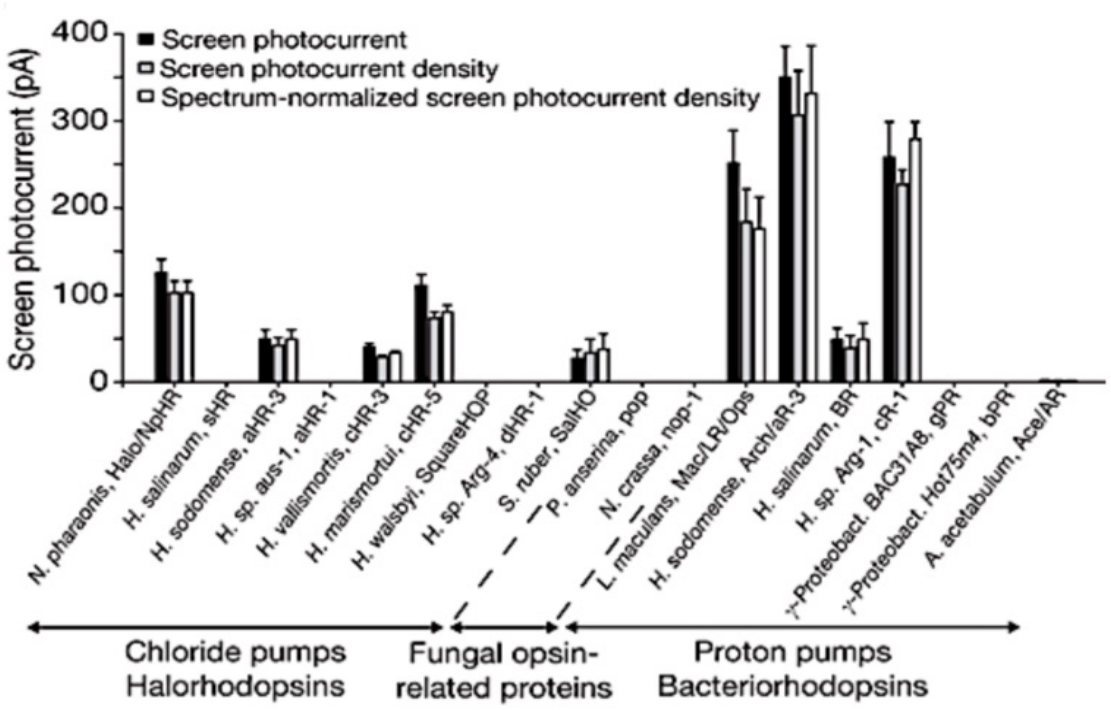

Figure 3.1: **Photocurrent screening of different rhodopsins from different organisms.** This screening was carried out in neurons by patch-clamp method, and shows the current output achieved by different proteins, with special emphasis in AR3 since it produces the largest photocurrent. Reproduced from [126].

Less is known about the structure and activity of AR3 (see Chapter 2), but the

change in current just mentioned has made AR3 an ideal optogenetic tool. In particular, AR3 has been used to induce neural silencing, thanks to its ability to transport protons, and to the higher level of photocurrent it can generate in comparison with other microbial rhodopsins (Figure 3.1) [126]. Upon illumination, protons start being transported from one side of the membrane to the other. This provokes hyperpolarisation of the membrane which in turn causes neural silencing [126]. Neural silencing enables the silencing of different neuronal populations by shining light onto the cells, thus giving the opportunity to clarify the role of neuronal populations in different pathologies both in *in vitro* as well as in *in vivo* models [126, 123, 222].

Moreover, AR3 has been used as a voltage indicator. One study by Cohen and colleagues identified a photo-intermediate, named Q state, in which AR3 fluoresces [265, 123, 222]. The intrinsic fluorescence of AR3 can be used to detect changes in the membrane potential of the cell, making AR3 a voltage indicator (Figure 3.2) [266]. Contrary to neural silencing, voltage indicators require that the protein does not pump protons, so that the membrane potential is not altered by illuminating the cells [265, 123, 222, 266].

In addition to its fluorescence properties and its ability to generate a higher photocurrent than bR (Figure 3.1), AR3 is significantly easier to express and mutate in various cell types including *Escherichia coli*, human embryonic kidney cells (HEK) and neuronal cells [126]. Conversely, many studies have documented the difficulty of expressing bR efficiently and of obtaining functional proteins in *E. coli* or HEK cells, mainly due to their non-natural archaeal lipid environment [267]. Another advantage over other proteins used in optogenetics such as ChR-2, is that AR3 has a

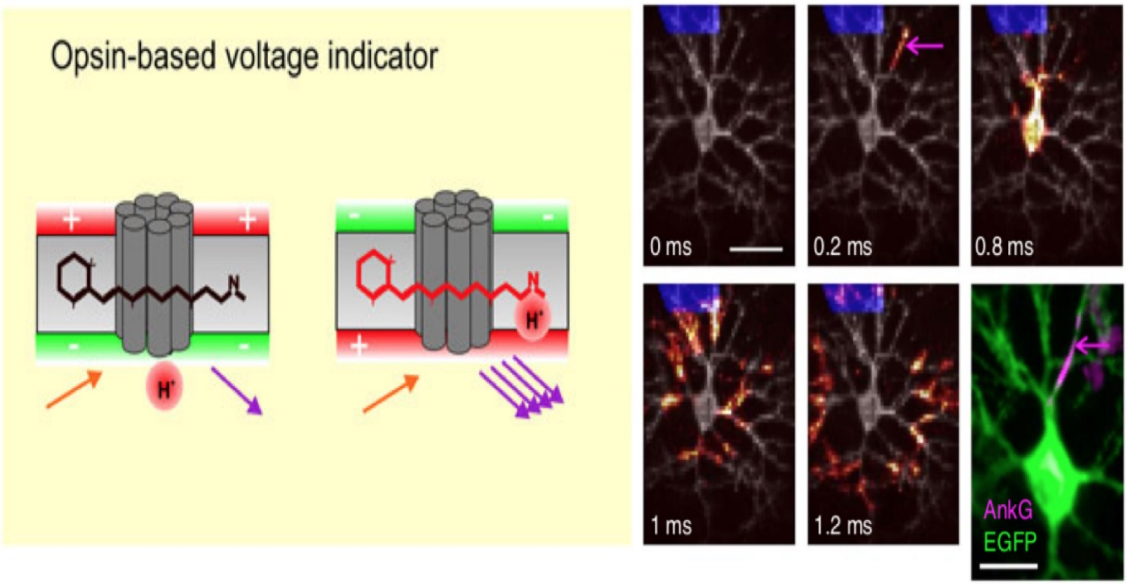

Figure 3.2: **Fluorescent voltage indicator.** Left: Schematic representation of how a fluorescent voltage indicator works, changing fluorescence as the membrane potential is altered. Right: Image of neurons expressing AR3. Upon illumination (blue square), AR3 acts as a fluorescent voltage indicator where the firing of neurons can be observed through fluorescence which changes as the membrane potential across the membrane changes Scale: 50 μm. Bottom right, immunostaining of cells with anti-GFP and anti-AnkyringG. Scale: 25 μm. Reproduced from [265, 123].

quick recovery period (μs) [268]. It has also been reported that, after illumination, the photocurrent of ChR-2 decreases or in some cases that ChR-2 becomes inactive ("desensitisation") over time (Figure 3.3) [268]. In contrast, AR3 recovers spontaneously (Figure 2.3) and very quickly (μs) after illumination, and therefore inducing depolarisation of neuronal cells more efficiently [126].

Bacterioruberin may contribute to protect the protein against bleaching and photobleaching [218, 249, 269]. Determining whether or not bacterioruberin plays a role in the protection against bleaching, would aid in understanding one of the main problems that occurs in optogenetics, that is, phototoxicity - the process by which proteins become inactive under constant illumination [123].

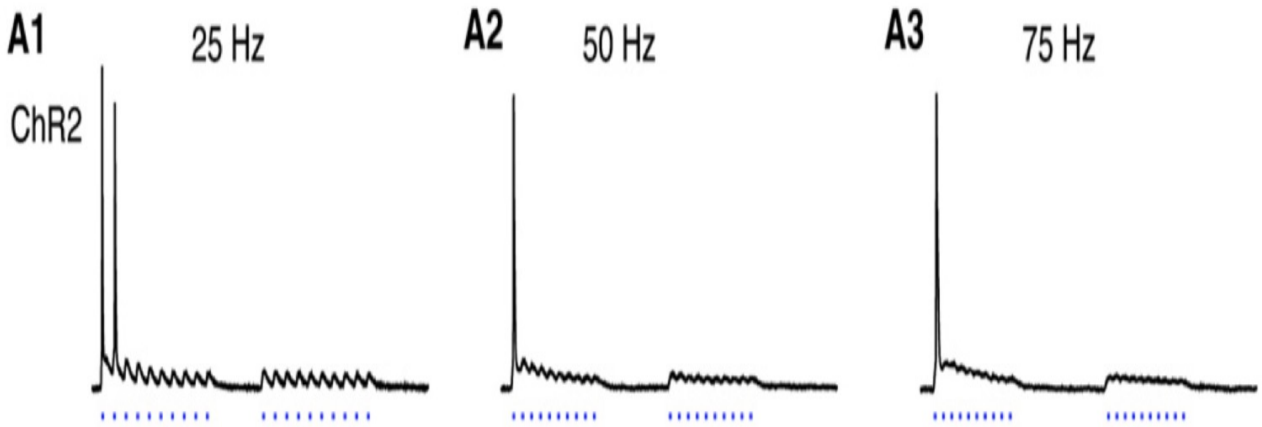

Figure 3.3: **ChR2 desensitisation.** Photocurrent measurements of ChR2 undergoing several illumination cycles (470nm, 4ms light pulse) at different stimulation frequencies (A1) 25Hz (A2) 50 Hz (A3) 75Hz) showing the decrease and inactivation of the protein's photocurrent. Blue dots represent light on; x-axis: time; y-axis: photocurrent generated. Reproduced from [268].

Analyses of the structure, properties, and mechanism of AR3 are still ongoing. These studies are crucial in serving the ultimate goal to develop better and more efficient voltage indicators or neural silencers, significant tools for optogenetics and other biotechnological applications. Moreover, thanks to its functional properties, and its productive expression in HEK cells or neurons, AR3 offers the opportunity to study different cell lines and, to assess the role that different cells may play in severe pathologies [126]. This in turn helps furthering our understanding of how neuronal circuits function and react to different stimuli [126]. Finally, the similarities between AR3 and bR, and in particular the enhanced photocurrent of AR3, makes AR3 the perfect candidate for bioelectronic applications, such as new biophotovoltaic cells or sensors.

3.1.2 Aims

Here, we aim to:

- Provide a method to reconstitute functional AR3 from its native environment in order to determine the key features involved in proton pumping;
- Study how illumination and lipid environment determine membrane potential and photocurrent, by using DIBs;
- Investigate whether it is possible to reproduce AR3 photoswitching during several illumination cycles or under constant illumination conditions without a decrease in its activity;
- Study the functional roles of retinal and bacterioruberin separately and simultaneously in AR3;
- Investigate the role that bacterioruberin might have as a protective agent against photobleaching; and,
- Assess the photocurrent characteristics of AR3 once it has been bleached, to highlight the importance of retinal for protein function;

3.2 Materials and Methods

3.2.1 Expression and Purification of AR3 in *H. sodomense*

AR3 was expressed and purified as described in Chapter 2. See "Materials and Methods" Section 2.2.1.1.

Once purified, AR3 was centrifuged (40,000 *g*, 30 mins, 4°C) and resuspended in Buffer Resuspension (Appendix 2). The sample was sonicated (30 minutes; water-bath at 20°C) to effect homogenisation for incorporation into DIBs, at a concentration of 0.3 mg/ml.

3.2.2 Reconstitution of AR3 into DIB

The reconstitution of AR3 in DIBs and subsequent measurements were carried out in collaboration with Charlotte Hoskin and Vanessa Restrepo-Schild from Professor Hagan Bayley's laboratory (University of Oxford, UK). For reconstitution of the protein, a protocol described previously was adapted [148]. The lipid used was 1,2-diphytanoyl-*sn*-glycero-phosphatidylcholine (DPhPC). The lipid was dissolved at a concentration of 10 mg/ml in pentane and then dried with nitrogen gas. The dried lipid film was resuspended at a 1:1 volume ratio of hexadecane and silicone oil (Sigma) to a final concentration of 10 mg/ml of DPhPC (lipid-in-oil bath). In the electrophysiological chamber, a 200 nL droplet containing AR3 was added onto each electrode submerged in a lipid-in-oil bath a "lipid-out" technique. Incubation (5 min) allowed the formation and attachment of the droplet onto the electrode, and using micromanipulators (Narishige, NMn-21) two droplets, one containing AR3 (*trans* droplet) and one without protein (*cis*), were brought into contact to form the droplet interface

bilayer (DIB) (Figure 3.4).

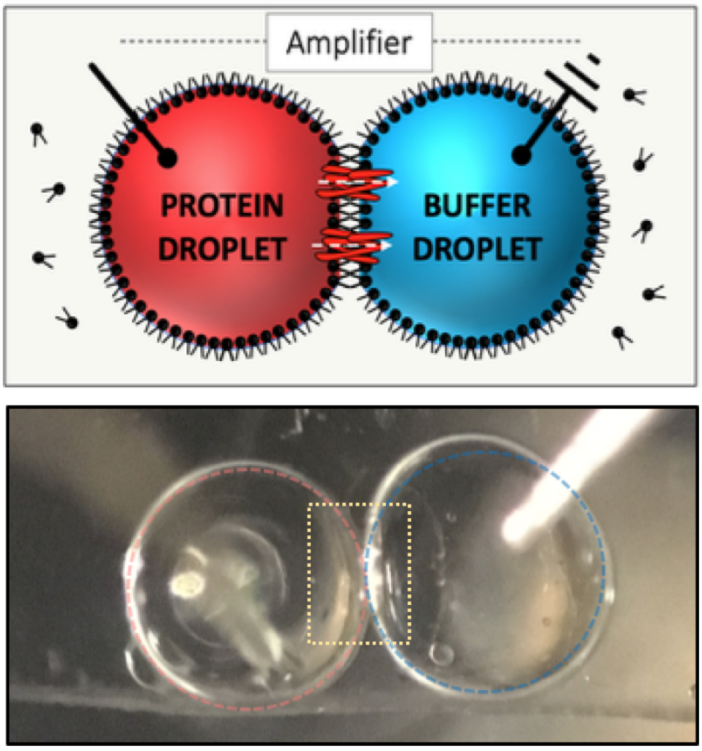

Figure 3.4: **AR3 reconstituted into DIB.** This figure shows a schematic representation of the reconstitution of AR3 into Droplet interface bilayers; Above: Schematic of how the system is set up with the droplet forming an interface with electrodes inserted into each one. The buffer droplet represents the *cis* droplet, and the protein droplet is the *trans* droplet. Below: an image of the two droplets forming an interface where the blue one is the *trans* droplet and the red one is the *cis* droplet. In collaboration with Charlotte Hoskin. Figure adapted from [270].

3.2.3 Electrical measurements

All measurements were done in a Faraday cage that had a patch-clamp amplifier (Axopatch 200B, Axon Instruments) and micromanipulators for the electrodes. On top of the Faraday cage, a fibre coupled LED (Mightex, WFC-H7-0560)is used for illumination. The wavelength of the LED available (390,430,490,530,560,590,630,660 nm) was selected accordingly to perform the experiment and monitor the current change according to a specific wavelength. The light was placed 4 cm above the

set-up, and the electrical signal were amplified and recorded by a digitizer (digidata 1440 A, Axon Instruments). All the measurements obtained were analysed using the software Clampfit provided by Axon Instruments. All electrical measurements were repeated independently at least three times.

3.2.4 Photocurrent changes

To obtain reproducible photocurrents, the experiments were repeated as in section 4.2.3 above, altering the time and illumination cycles for two different experiments. The light used for these experiments was a LED (38.4 mW, 560 + 590 nm). In a first experiment, the protein was illuminated (2 min) with ten illumination cycles (5 sec), followed by ten dark cycles where the light was turned off. Then in a second experiment, the protein was illuminated (5 min) at constant illumination cycle, followed by dark cycle (1 min) where the light was turned off followed by two short illumination cycles (5 sec) each with a dark cycle (5 sec) in between.

3.2.5 UV-Vis spectra

A Jasco V-630 instrument was used to obtain absorption spectra of samples in buffer at various wavelengths using a quartz cuvette (1cm).

3.2.6 Bleaching of AR3

Retinal was removed from AR3 and bR following the literature procedures for bR bleaching [40]. Bleaching was achieved by incubating the sample of bR or AR3 (0.2 mg/ml) in 0.2 M hydroxylamine (pH 7.2, Tris-HCl 20 mM) under continuous illumination with an LED lamp at 20 cm from the sample. The experiment was conducted at two temperatures, 4°C and 37°C, in order to assess how temperature

affects the photobleaching. To monitor the bleaching of the protein, absorbance measurements were taken to assess the decrease of the protein absorption λ_{max} at 560nm, and to observe the increase of the retinaloxime λ_{max} at 360 nm at the different timescales: 0, 30, 60, 120, 180 (minutes) and 12 hours later to achieve full bleaching of the protein. Once bleached, the sample was washed several times (up to 4x) by centrigutation (40,000 g; 30 mins; 4°C) with double distilled water to remove any remaining hydroxylamine or retinaloxime present.

For regeneration of the Schiff base after bleaching, the sample (0.2 mg/ml) was incubated (3 hours at room temperature) with an excess of all-*trans* retinal (dissolved in ethanol at a concentration of 5 mM). Several wash cycles in double-distilled water using centrifugation were performed in order to remove any free retinal.

3.3 Results and Discussion

3.3.1 Reconstitution of AR3 into DIB

Following AR3 purification from *H. sodomense* (as described in Chapter 3), the protein was reconstituted into DIBs in order to assess its biophysical properties. AR3 was incorporated into DIBs using detergent and sonication in order to avoid aggregation [148]. Figure 3.4 gives a schematic and image of the droplets with AR3 incorporated into the DIB. bR has been used to compare and contrast AR3 with bR. In this set-up illustrated, the *cis* droplet is the ground electrode and the *trans* droplet is the "working electrode" where AR3 is inserted [148, 271].

As expected, the incorporation of AR3 into the DIBs follows the same trend as bR [148, 271, 96]. The protein inserts mainly with its N-terminus orientated towards the *trans* droplet. The proton flow goes from one side of the droplet to the other in

the positive direction of current in the *cis* droplet. When the protein is in the *trans* droplet the flow of protons results in a negative current, as in bR [148, 96]. When the protein is added to both the *cis* and *trans* droplets nearly no current could be detected. This is consistent with a net symmetrical insertion. This suggests that the orientation and incorporation of the protein occurs equally in both directions.

3.3.2 Effect of detergents on proteins activity

A detergent screening for the optimised incorporation of AR3 into DIBs was performed. We focused on three widely used detergents such as n-Dodecyl-β-D-Maltoside (DDM), n-Octyl β-D-glucopyranoside (OG), and Triton X-100 [272].

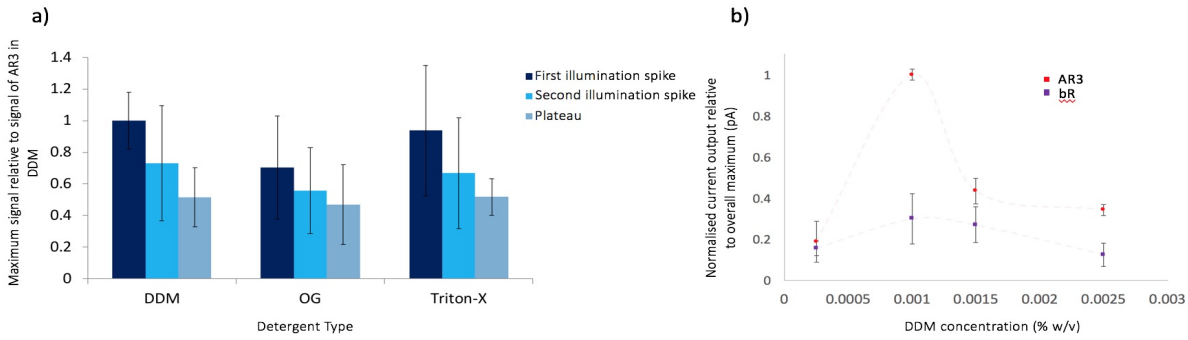

Figure 3.5: **Detergent screening for optimal reconstitution of AR3 into DIBs.** a) Screening of AR3 reconstituted into DIBs using OG, DDM, and Triton-X. The current outputs for the detergents at first, second, and stationary current of all three detergents are shown. b) Detergent concentration spectra of DDM to determine the optimal concentration of detergent to reconstitute AR3 into DIBs. A concentration of 0.001% renders the highest current signal when AR3 is reconstituted into DIBs, making it the optimal concentration for the experiment. In collaboration with Charlotte Hoskin.

As observed (Figure 3.5. a), AR3 proteins reconstituted into DIBs were observed to pump protons at first illumination spike, second illumination spike or plateau current in the presence of all detergents (Figure 3.5. a). This demonstrates the versatility and robustness of AR3. The optimal concentration of DDM (a detergent

widely used in microbial rhodopsins) for the reconstitution of AR3 into DIBs was evaluated. Figure 3.5. b) shows the different normalised current changes of the protein in relation to the maximum value obtained with different concentrations of DDM. As shown (Figure 3.5. b), the optimal concentration of detergent for incorporation into DIBs of AR3 is the same as for bR, with an optimal concentration below the critical micelle concentration (CMC) of DDM at 0.001% weight to volume ratio (w/v).

3.3.3 Photocurrent measurements

The current generated by reconstituted AR3 was measured [139, 140, 141, 142, 143, 144]. When the protein is illuminated with a green light (560 + 590 nm) a change in current is recorded (Figure 3.6. a). The same experiment was also performed for bR (Figure 3.6. a) and in the absence of protein, as control experiments (Figure 3.6. a). When no protein is present (Figure 3.6. b), no current generation is visible, even when the system is illuminated with different coloured lights. This indicates that no artefacts appear because of the photochemistry of the droplets itself or due to the droplet set-up (Figure 3.6. c). The amplitude of the current generated is up to two-fold larger in AR3 (10.65± 1.07 pA) in comparison to bR (5.56± 0.83 pA). The current generated by AR3 under illumination (Figure 3.6. b) achieve a large flow of ions from one droplet to the other and is in agreement with the literature reporting that AR3 current changes are as much as two to three-fold higher than bR changes in other systems (Figure 3.1) [126, 273, 274].

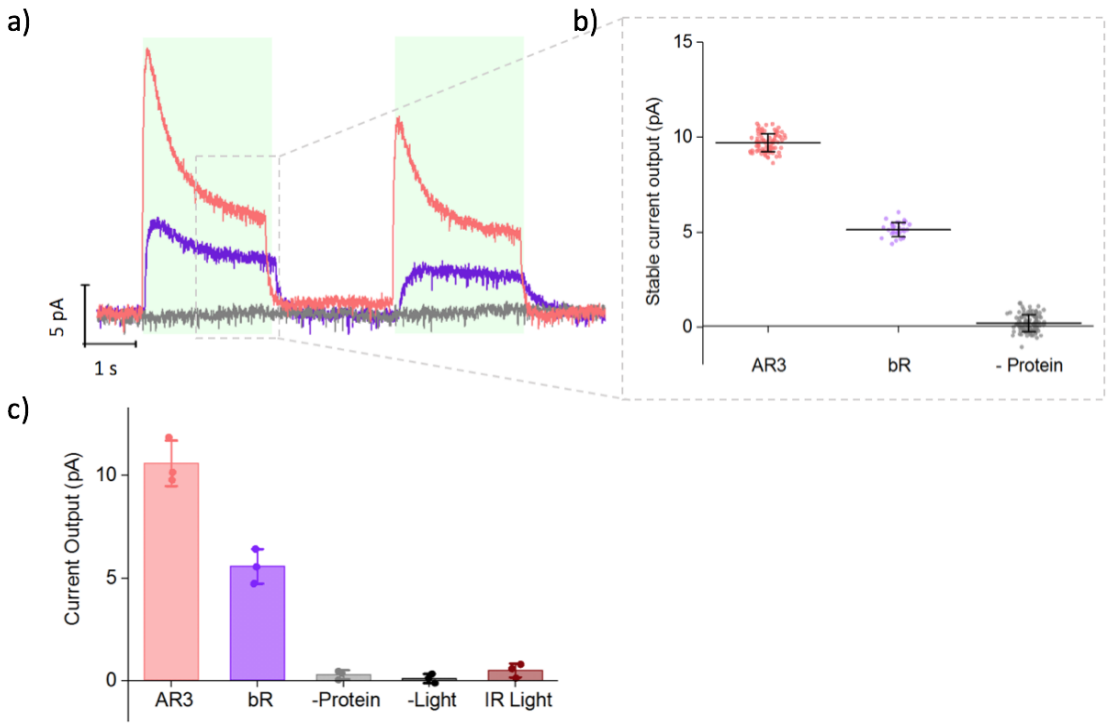

Figure 3.6: **Photocurrent traces of AR3 vs bR.** Current measurements produced by AR3 and bR upon illumination (560nm + 590nm, 5s light pulses) a) Current trace of AR3 (red), bR (purple), and no protein (grey) b) Stable current output achieved at stationary current by AR3, bR and no protein. c) Current output achieved by AR3 (red), bR (purple), no protein (grey), light at 560nm + 590nm, IR light at 740nm. In collaboration with Charlotte Hoskin.

3.3.4 AR3 proton pumping

The current generated by AR3 proton pumping were measured when a voltage was applied. Here we assessed the behaviour of AR3 from *H.sodomense* (pump or channel) once reconstituted in DIB. In the pump scenario, the proton transportation from one side of the membrane to the other would happen independently of the potential of the membrane. Conversely, in the case of the protein behaving as a channel, the transportation of protons would be regulated by the membrane potential [213, 275]. In the experiment, two different voltages were applied (+10 mV, and -10 mV) and compared to the system without any voltage (Figure 3.7).

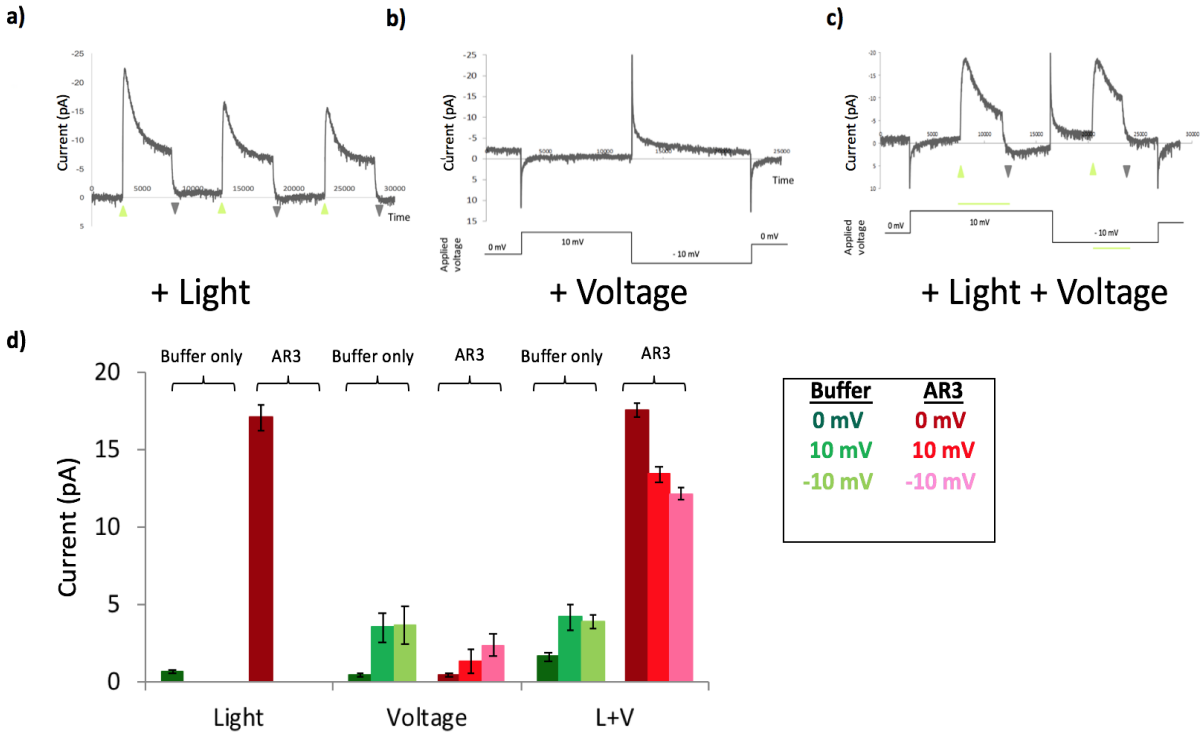

Figure 3.7: **AR3 as a proton pump.** Current traces of AR3 with the application of a voltage. a) shows the photocurrent trace upon illumination of AR3 when illuminated (green arrow). b) Shows the current trace of AR3 when a voltage is applied (First spike indicates the applied voltage (10mV) and the second spike indicates the applied voltage (-10mV)) without illumination. c) Shows the current traces when illumination and voltage are co-occurring. The current trace of AR3 displays a change of current upon illumination independently of voltage. d) Individual current values for each voltage applied in electrodes and AR3. Changes are observed upon illumination of AR3 (17.12± 1.72 pA) compared to electrodes alone, as well as it is observed when a voltage and illumination are applied. Upon voltage application, overall current values of AR3 (1.53± 0.85 pA) and electrodes (2.8± 1.4 pA) do not show much difference. AR3, upon illumination, shows a change in current compared to when illumination and voltage are applied together, as observed for 10 mV (13.51± 0.52 pA) and -10mV (12.32± 0.38 pA). In collaboration with Charlotte Hoskin.

Figure 3.7 shows the main differences between three scenarios; (a) where the sample is illuminated, (b) where a voltage is applied to the sample without illumination, or (c) both illumination and voltage are applied together (Figure 3.7). As the current traces in Figure 3.7 (a-c) show, the proton pumping of AR3 happens independently of the voltage applied. The change in current occurs upon illumination (Figure 3.7. a),

and there is no change in current in the absence of light even when voltage is applied (Figure 3.7. b). A proton channel would hold the voltage level, such as for example with αHL, but here such behaviour is not observed [275]. As seen (Figure 3.7. b,d), the voltage applied to the system does not play much of a role in the change of current, since there is no considerable change between the electrodes alone (2.8± 1.4 pA) or when AR3 is present (1.53± 0.83 pA, Figure 3.7. d). The current only increases when the sample is illuminated (Figure 3.7. a,d). Applying both illumination and voltage provokes the same current increase as illumination alone (Figure 3.7. c,d).

3.3.5 Action Spectra of AR3

It is important to determine both the wavelength and whether the activity of AR3 in DIBs acts like bR so that its photocurrent at a specific wavelength can be used similarly for biosensors and bioelectronics for a width narrower than 30 nm, compared to silicon-based biosensors that detect light over a broad 300 nm range from 400 nm to 700 nm [169, 276]. Hence, we proceeded to perform current measurements of AR3 when illuminated with different wavelengths in order to obtain the action spectra of AR3. Figure 3.8 presents the current traces of AR3 when illuminated at two different wavelengths, 560+590 nm (red trace) and at 740 nm (black trace).

As seen in Figure 3.8. a), upon illumination (green arrows), the 560+590 nm light induces a change in current when the sample is illuminated. However, when the sample is illuminated at 740 nm, no significant change in the current trace is observed. This demonstrates that the protein can only be activated at specific wavelengths. Figure 3.8. b) shows the normal distribution of current in the plateau phase, upon illumination with 560+590 nm where fluctuation in photocurrent upon illumination

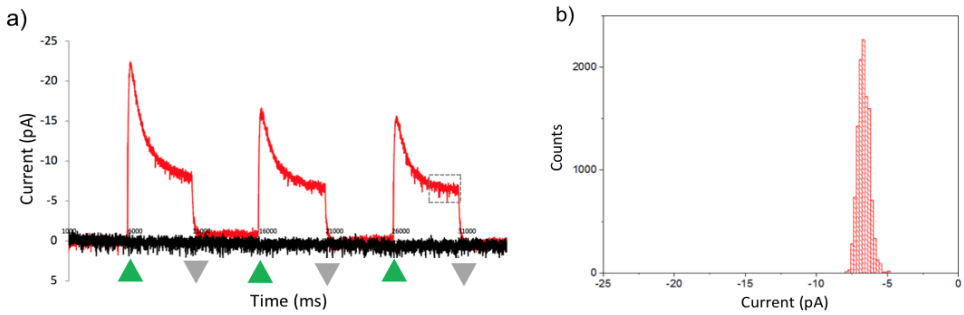

Figure 3.8: **AR3 wavelength-specific proton transport.** a) Photocurrent traces of AR3 respectively illuminated (green arrows). In red, the photocurrent of AR3 upon illumination with 560+590nm light. In black, the photocurrent of AR3 upon illumination with a 740nm light. The light illumination cycles of 5 seconds were applied. b) Normal distribution (counts vs current) at stationary current (wavelength 560+590 nm). In collaboration with Charlotte Hoskin.

is reproducible for AR3. When illuminated at various wavelengths an action spectra of AR3 was obtained when incorporated into DIBs as illustrated in Figure 3.9.

The current output values of AR3 and bR were normalised relatively to their maximum values, in order to easily compare both systems. As Figure 3.9 shows, the optimum light for AR3 to obtain a larger current change is ∼570 nm. On the other hand, the bR action spectrum has its maximum at 550 nm. The difference in action spectra between AR3 and bR is therefore around 20 nm. As indicated by the action spectra (Figure 3.9), it should be possible to develop AR3 mutants with an action spectrum closer to the near-infrared (NIR), a feat unachievable before with bR [14]. Due to the shift observed, this approach opens the way to produce several AR3 mutants that could be mutated to recreate a pallet of colours close to the infrared, which is less damaging to cells in optogenetics in comparison with blue light, thus facilitating the control of different behaviours in cells [126, 277].

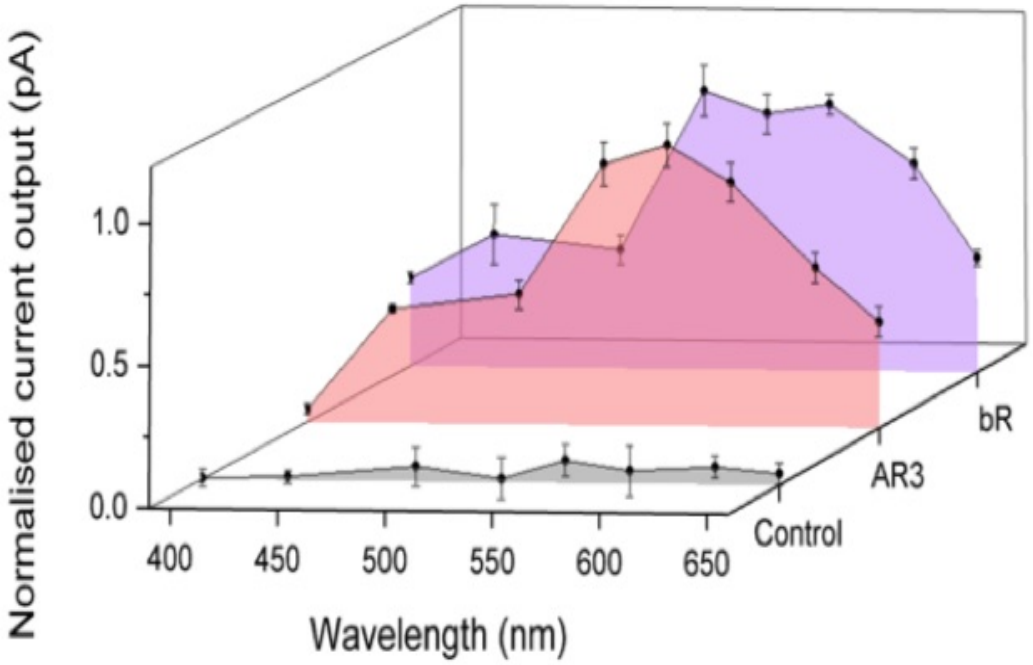

Figure 3.9: **Action spectra of AR3 and bR.** Action spectra of AR3 (red) and bR (purple) showing the photocurrent output generated at different wavelengths of light. The values of AR3 and bR were both normalised relative to their highest current output values to show the similarities between these two proteins. AR3 has a maximum current output at 570nm compared to bR with a maximum current output at 550nm. Control experiment is done (grey) with droplets without any protein reconstituted. In collaboration with Charlotte Hoskin.

3.3.6 Reproducible photocurrent changes

So far, we have demonstrated a difference in photocurrent changes between AR3 and bR (around two to three-fold), as well as showing that the activity of AR3 is wavelength-specific when reconstituted into DIBs. Yet we have to be mindful of the functions of the protein, and whether these changes in photocurrent can be repeatedly cycled, or whether the protein desensitizes as ChR-2 does after illumination cycles [278]. In order to properly address these issues, we performed several illumination cycles of the system. Figure 3.10. a) shows an experiment with 10 different

illumination cycles consisting 5 seconds with light, and 5 seconds without light. As the current trace shows (Figure 3.10. a), the change in current upon illumination is consistently observed and no desensitisation takes place, even during a long period of time (1 minute). Nevertheless, the change in current can be seen decreasing as time progresses. As the dot plot in Figure 3.10. c) shows, there is a change in intensity between the beginning (A; 6.62± 0.38 pA) and the end (B; 5.2± 0.3 pA) of the experiment. This could be due to the protein adapting to the light and achieving a plateau, or it could mean that the protein is progressively decreasing its activity. For bR, it has been demonstrated that the M-state of the photocycle might become longer after several illumination cycles, or that the protein itself starts to saturate [169, 222, 279, 280, 281]. In both cases, bR declines its activity [169, 222, 279, 280, 281].

In order to assess whether AR3 activity indeed declines over a period of time, we performed an additional experiment (Figure 3.10. b) with continuous illumination over 5 minutes, followed by 1 minute of dark, and then by two quick illumination cycles of 5 seconds each, as done in the previous experiment (Figure 3.10. a). As Figure 3.10. b) shows, the activity of AR3 throughout the 5-minute illumination cycle decreases until it reaches a plateau. However, after this point the photocurrent change remains constant and the proteins ability to generate photocurrent does not seem to diminish under constant illumination. Moreover, comparing the change in B (5.2± 0.3 pA in (Figure 3.10. c)) to D (5.5± 0.05 pA in (Figure 3.10. c)) from the two different illumination cycles, no difference between them can be detected. This implies that the photocurrent activity of the protein remains. Furthermore, the

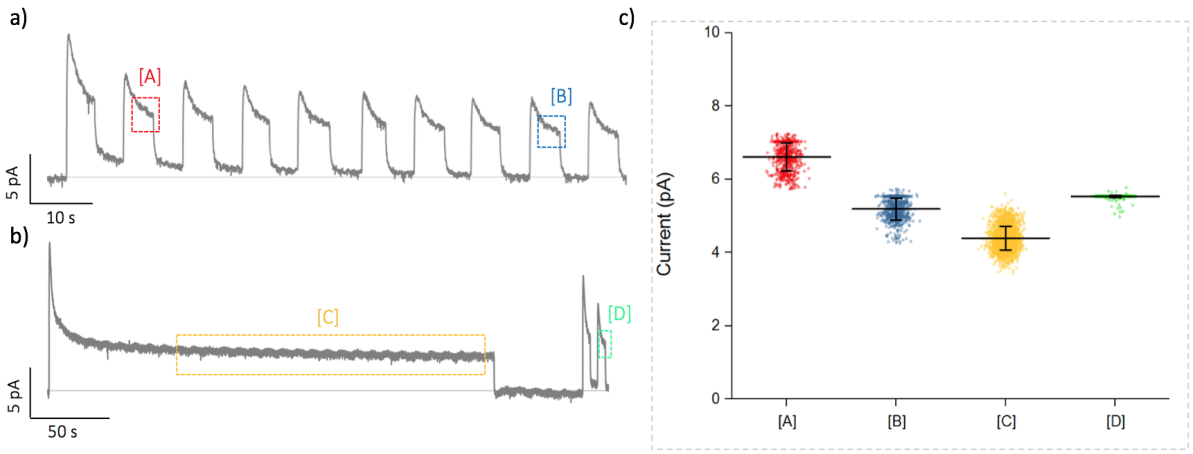

Figure 3.10: **Reproducible photoswitching.** a) Photocurrent trace of AR3 undergoing short light cycles of 5 seconds on, 5 seconds off for 1 minute, to observe the activity of the protein and its possible light desensitisation. Stationary current values show a small decrease in photocurrent from the second illumination cycle (A; 6.62± 0.38 pA) and the second to last illumination cycle (B; 5.2± 0.3 pA). b) Photocurrent change of AR3 under a long exposure to light (5 min), the light is switched off for 1 min and afterwards 2 short light pulses of 5 seconds each. c) Stationary current values for both experiments are: A; 6.62± 0.38 pA, B; 5.2± 0.3 pA, C; 4.39± 0.32 pA, D; 5.5± 0.05 pA. In collaboration with Charlotte Hoskin.

current increase is not only maintained during a long (5 min) exposure to light, but it also does not vanish or drop when illuminated again after a dark cycle (Figure 3.10. b,c). As the dot plot in Figure 3.10. c) shows, the change in photocurrent when the protein reaches its plateau is lower than the change during the first illumination or second illumination. Therefore, we suggest that if the cycles were longer, the change in current between the first and second illumination, when at plateau, would be the same.

3.3.7 Investigating the role of retinal

The role of retinal in microbial rhodopsins such as AR3 is crucial. Therefore, the bleaching process (removal of retinal molecules from the protein) is one of the main concerns for optogenetics and bioelectronics. In order to test the change in cur-

rent produced by the protein with and without retinal, we bleached the protein with hydroxylamine under continuous illumination (Figure 3.11). When performing this experiment, the main source of disturbance would be the presence of retinal oxime. Thus, in order to address this concern, we used absorbance spectrophotometry (Figure 3.11. a) to track the depletion of retinal from AR3. At different time points throughout the process, measurements were performed to assess how the typical λ_{max} of AR3 (570 nm) and bR (565 nm) decreased due to the Schiff base cleavage, and how the λ_{max} at 350 nm increases due to the formation of retinal oxime (Figure 3.11. a,b). Figure 3.11. a) shows how the retinal λ_{max} increases as the bleaching of AR3 proceeds, with measurements taken at the initial state, and then after 30, 60 120 and 180 minutes. The sample was left overnight to accomplish full bleaching of the protein.

Although the presence of bacterioruberin complicates the observation of bleaching in AR3, the cleavage of retinal following a similar process as what is observed for bR can be observed since the peak at 570 nm is decreasing (Figure 3.11. a-b). Although the kinetics of the bleaching reaction are faster at 37°C than at 4°C, both proteins behave similarly. Figure 3.12. a) shows the change in current in the bleached AR3 in comparison to that observed in the AR3 wildtype and in the reconstituted AR3 with retinal added after bleaching. As it can be observed (Figure 3.12. a), the photocurrent of the bleached protein compared to the non-bleached sample decreases from 1 to 0.20 pA (normalised values), possibly due to incomplete bleaching and a higher signal-to-noise ratio (SNR).

The current changes observed in bR and AR3 are very similar and follow a similar trend (Figure 3.12. b). Most importantly, the change in current when either protein

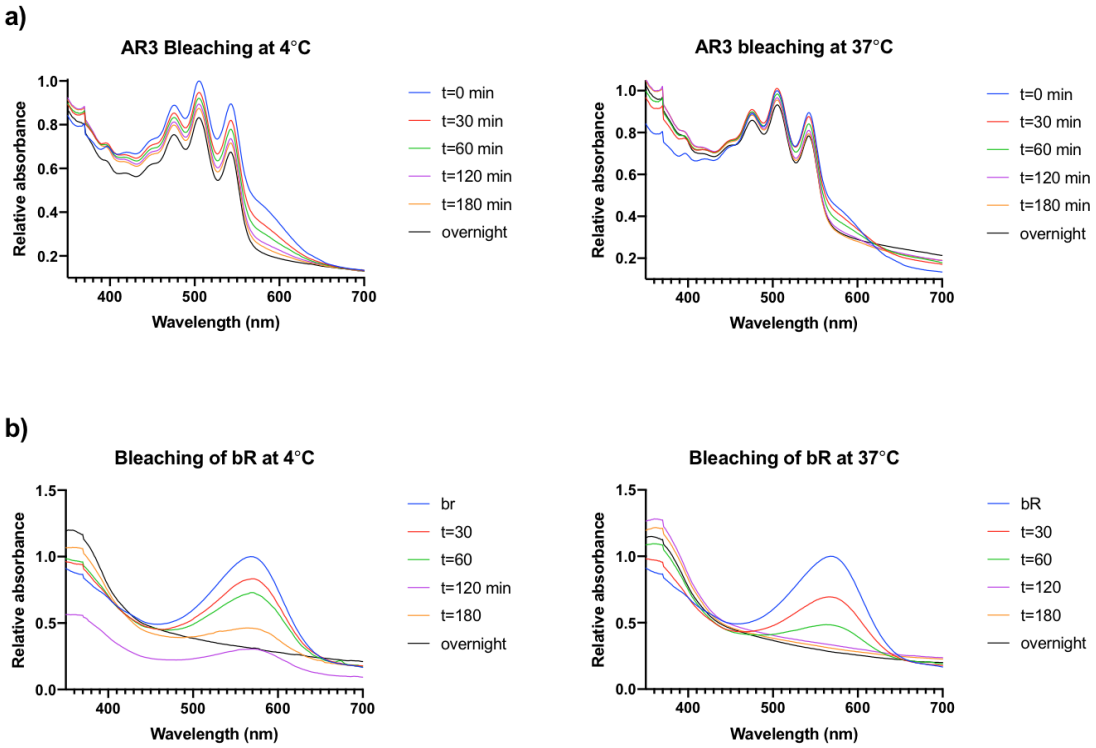

Figure 3.11: **AR3 vs bR bleaching.** Bleaching of AR3 and bR with 0.2M hydroxylamine under continuous illumination at 4°C and 37°C. a) AR3 bleaching at 4°C (left), and at 37°C (right). b) bR bleaching at 4°C (left), and at 37°C (right).

is bleached, is constant when illuminated with different lights ranging from 400nm to 700nm. In comparison, the current change in the AR3 or bR non-bleached is increased at optimum wavelength of light, such as 560 nm or 590nm (Figure 3.12. b). Furthermore, when the protein is reconstituted with retinal, not only there is a change in colour observed, as shown in Figure 3.12. c), but a change in the action spectra is also observed, where a change in current at optimum wavelengths of 530 nm was observed (Figure 3.12. a). This is significant because it shows that, like bR, AR3 can be reconstituted with retinal and still retain some of its native activity (Figure 3.12. b) [282]. This experiment demonstrates the importance of retinal in a protein such as AR3. Without retinal, no photocurrent can be produced.

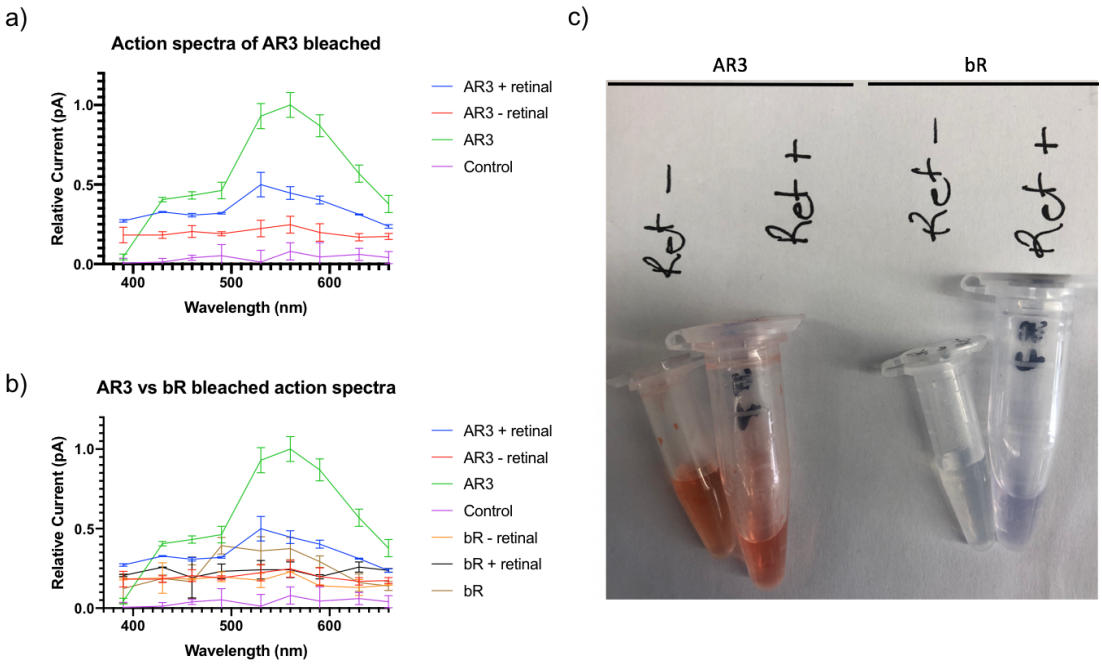

Figure 3.12: **Photocurrent and the importance of retinal.** a) Action spectra of AR3 non-bleached, AR3 bleached (AR3 - retinal) and AR3 reconstituted with retinal after bleaching (AR3 + retinal) with values normalised relative to the highest current value. b) Action spectra of AR3 and bR bleached and reconstituted with retinal with values normalised relative to the highest current value. c) Colour change of bR and AR3 upon bleaching and reconstitution with retinal. In collaboration with Charlotte Hoskin.

3.4 Conclusions

Any experiments performed before in AR3 have been done *in vivo* in different cellular environments, such as *Escherichia coli*, HEK cells or neurons. In this chapter, we have provided a novel method to incorporate AR3 in artificial membranes for its biophysical characterisation. AR3 photocurrent capabilities are maintained in artificial model membranes and have shown to be up to two times higher than bR (Figure 3.6), which up until now has been the model membrane protein for DIB.

The experiments in this chapter allow us to draw major conclusions and open up the path towards further applications of AR3. Its change in photocurrent is very

prominent upon illumination, and it is up to two-fold higher than bR. This feature, together with the chemical and thermal stability of the protein, and its ability to reproduce its photocurrent over longer periods of time (Figure 3.10.), makes AR3 an excellent candidate for bioelectronics and optogenetics [169]. Furthermore, the easiness of its incorporation into DIBs provides a new, innovative system to make functional bionetworks [148]. For example, AR3 could be used to develop a functional DIB network for image detection, as it was previously developed with bR (Figure 1.18) [148]. However, using AR3 would have significant advantages over the use of bR. The detection of light as a current trace would be easier to track, thanks to AR3 higher current generation and because of the difficulty in detecting photoswitching in bR due to its low signal [283]. Moreover, AR3 crucially offers a way to produce different coloured mutants in the NIR region [284]. As discussed, the expression and purification of AR3 in HEK cells, neurons, or even *Escherichia coli* is significantly easier than bR [267]. Exploiting our knowledge of the genetics of these organisms would enable us to use directed evolution or directed mutagenesis for engineering mutants with distinct absorbance range, to incorporate them as detectors in functional bionetworks or as silencers for neuronal populations [126, 143].

Chapter 4

Archaerhodopsin-3 spectral tuning and proton pumping

Previously, the high-resolution crystal structure of AR3, the electrical current AR3 generates upon illumination and its photoisomerisation, and the roles of the different chromophores embedded in the protein have been characterised. The work here focuses on altering the sensitivity of the protein to different wavelengths of light by site-directed mutagenesis. The abilities of the mutated proteins to pump ions across the DIBs were assessed. Hypsochromic (blue light shift) and bathochromic (red light shift) shifts were achieved.

4.1 Introduction

4.1.1 AR3 spectral properties and spectral tuning

Despite having similar structures and features, the spectral properties of microbial rhodopsins differ considerably [285], particularly in their absorption maxima, which span a range of 400 nm to 580 nm [286]. For example, just within proteorhodopsins (PRs) the range of absorption goes from green light to blue light, depending on the depth at which the organism expressing PRs is found in the ocean [287]. Given this

variety, directed evolution studies have been performed to tune the spectral properties of microbial rhodopsins such as bR, PRs and *Gloeobacter violaceus* (GR) [288].

One of the results of such studies has been the discovery of specific mutations which allow a colour change in Monterrey Bay PR [289]. Most of these mutations were localised around the retinal moiety (retinal pocket) of the protein, with a smaller amount distributed in other regions of the protein [289]. These finding have laid the ground for experiments in bR, where it has been shown that a change in the polarity of amino acids around the retinal could achieve a hypsochromic shift in the absorption spectrum [290]. Further support for this idea comes from studies on GR. There, changing the electrostatic environment of the β-ionone ring of the retinal, or increasing the hydrophobicity of the residues around the Schiff base (SB), yielded different protein absorption spectra (Figure 4.1) [288].

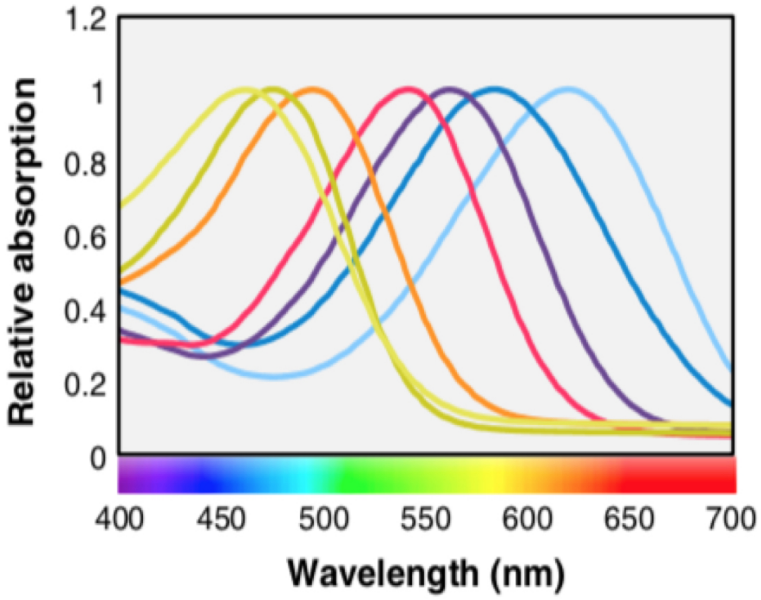

Figure 4.1: **Spectral tuning in GR.** Directed evolution study in GR where several variants of GR with different spectral properties were obtained. All the values are normalised relative to their highest absorption values. Reproduced from [288].

Another result of the many studies investigating the homology of different microbial rhodopsins was the development of proteins which not only had different spectral properties, but also altered functions [88, 287]. For example, bR was successfully converted from a proton pump into an inward chloride pump sensitive to green light (560 + 590 nm), and an inward proton pump in white light (400-700 nm) thanks to its homology to halorhodopsin (HR), by mutating an aspartate residue (D85) into a threonine (Figure 4.2) [88].

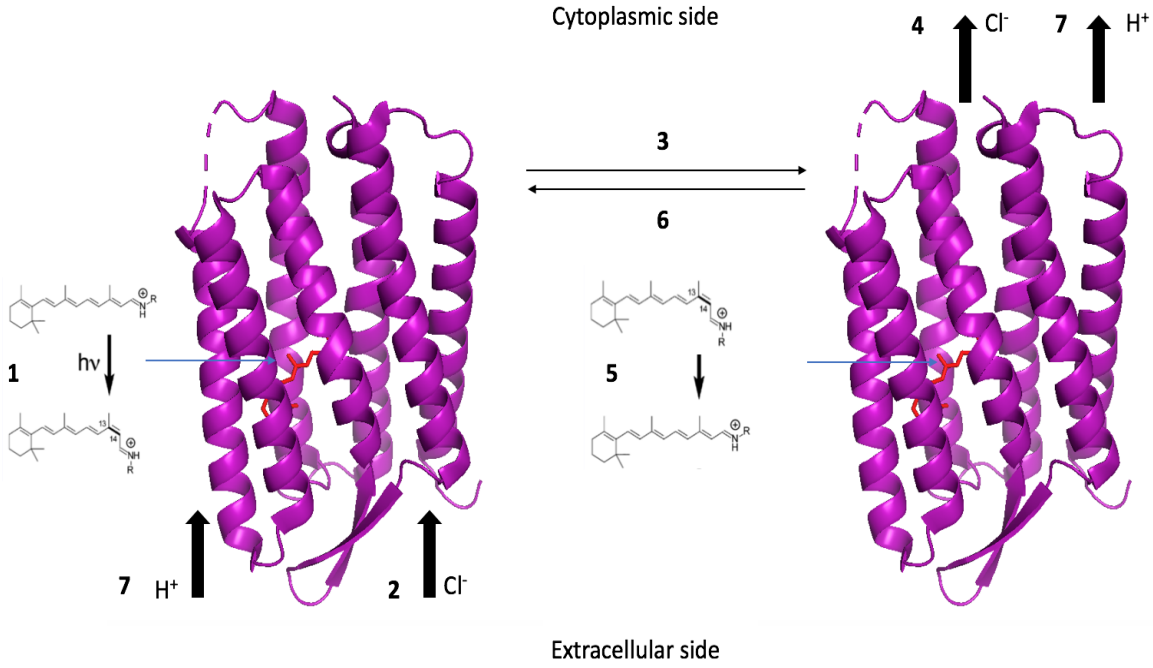

Figure 4.2: **bR (D85T) as a chloride pump.** Functional schematic of bR (D85T) as a chloride pump; 1) Photoisomerisation from *all-trans* to *13-cis* of the retinal. 2) Translocation of the chloride ion to the retinal moiety of the protein. 3) Rearrangement of bR in the M-state occurs. 4) Release of the chloride ion onto the cytoplasmic side. 5) Isomerisation from *13-cis* to *all-trans* of the retinal. 6) Reprotonation of residues involved in the photocycle. 7) Inward proton pumping of D85T in white light. Adapted from [88].

As for AR3 itself, different works on mutagenesis have attempted to achieve the

same results in terms of spectral property [288, 289, 290]. In 2014, a directed-evolution study focused on altering the fluorescent properties of AR3 managing to shift the emission maximum to the red end of the spectrum, a significant feature, because red light penetrates deeper than blue light into tissue and is a less damaging light to cells compared to blue light [291]. As discussed in Chapter 3, changes in the fluorescence spectra may be used to report changes in voltage, hence the need to develop mutants that can report changes in voltage at different wavelengths of light [284].

Mutating AR3 has also yielded meaningful results in terms of altered functions. In particular, a study focused on mutating three specific residues (A225T, G132V, M128A), managed to achieve the conversion of this protein into a channel pump, similarly to channelrhodopsins (Figure 4.3) [213].

Moreover, the AR3 variant thus produced (A225T, G132V, M128A) not only had the properties of a channel pump, but also showed a 90 nm blue shift [213]. Crucially, this was the first time that a proton pump was converted into a proton channel [213].

4.1.2 Study of AR3 proton pumping through mutagenesis

The abilities of microbial rhodopsins to transport ions have not only been exploited in optogenetics for silencing and exciting the neuronal network, but also for the development of photovoltaic cells and bioelectronical chips [169, 126]. By studying the sequence homology between these related proteins, specific residues can be identified and mutated in order to design more efficient proteins [169].

Site-directed mutagenesis studies have elucidated the role of key residues in the photocycle of bR and other microbial rhodopsins [215, 292], including those in the proton release complex (PRC) [293]. The outcome of these studies has highlighted

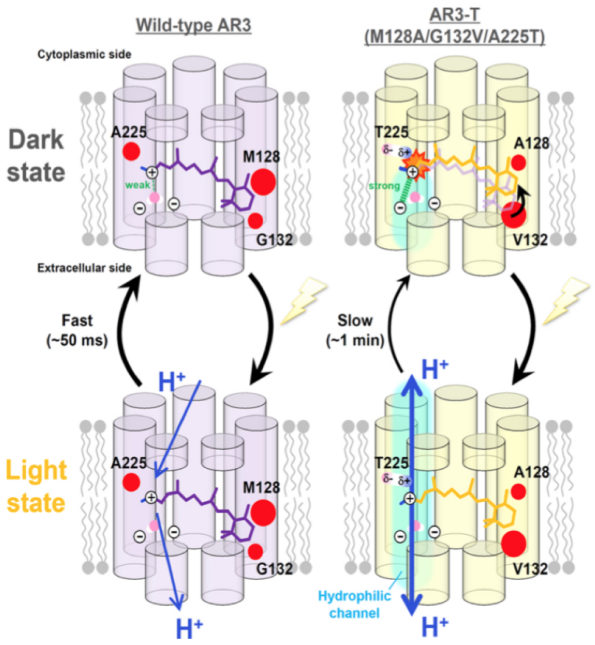

Figure 4.3: **From proton pump to proton channel.** Scheme of the proton pump mechanism in AR3 compared to its AR3-T variant (with three mutations: A225T/M128A/G132V) functioning as a proton channel. The mutations introduced in AR3-T modify the conformation of the retinal around the β-ionone ring, and the hydrophilicity of the residues involved in the pathway. The photocycle is slowed down to 1 min compared to AR3 WT ($\sim$ 50 ms). Reproduced from [213].

how in bR, mutations concerning the PRC such as R82Q, E194Q and E204Q, lengthen the photocycle by stabilizing the M-state [293, 294, 295]. The same mutations can also invert the steps of proton uptake and proton release [293, 294, 295]. Additionally, crystallographic studies have shown how the PRC changes across many microbial rhodopsins, for example in xanthorhodopsin (XR) in comparison to bR [296]. In the XR crystal structure (Figure 4.4, 1.9 Å, PDB code: 3DDL), the hydrogen water network is replaced by a hydrogen bonding network in between residues, and where only one glutamic acid is conserved [296]. All of these changes cause the restricted movement of Arg-93 in XR (Arg-82 homolog in bR) and to the inversion of the proton uptake and release in the photocycle in comparison with bR (Figure 4.4) [296].

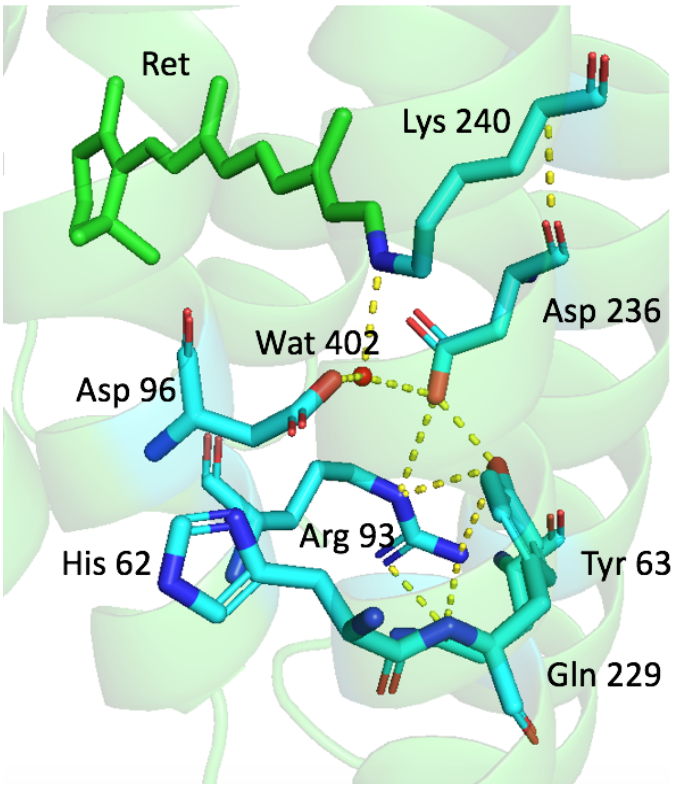

Figure 4.4: **Water molecules in XR.** Representation of the residues forming the pentameric arrangement that leads to the extracellular pathway in xanthorhodopsin (PDB code: 3DDL). Figure adapted from [296].

Site-directed mutagenesis in the PRC also helped to explain how the proton release and proton uptake mechanism in AR4 differ from bR [215]. Since AR4 and bR have a high level of sequence identity (59% [215, 103], Figure 2.1), similarities in their photocycles were expected. However, different mutations have demonstrated that the proton release and uptake in AR4 reversed compared to bR. This mechanism in AR4 enables the deprotonation of the residue D85 (bR numbering) in the O-state of the photocycle (Figure 2.3) [215, 103].

4.1.3 Aims

Here, we aim to:

- Tune the spectral properties of AR3 to develop a mutant library with bathochromic or hypsochromic spectral properties;
- Assess the proton pumping of the AR3 mutants in *E. coli* cell membranes;
- Assess the conductivity of the different AR3 mutants upon reconstitution into DIBs;
- Study how different mutations in the proton release complex affect the ion transport of the proteins using DIBs;
- Study the most red-shifted mutant obtained (D95T) and determine its proton pumping ability.

4.2 Materials and Methods

4.2.1 Plasmids and bacterial strains

Plasmid pET28b (Addgene ID: 58487) containing the AR3 gene, was obtained from Addgene. The plasmid possesses a kanamycin resistance gene to facilitate its growth, a T7 promoter, and an AR3 open reading frame (ORF) with a C-terminal histidine tag (His6). The plasmid map and AR3 gene can be found in Appendix B.1, Figure B.1 and Figure B.2. The plasmid was then transformed into the *E. coli* DH5$\propto$ cells which were used for all mutagenesis work. *E. coli* strain BL21 (DE3) was used for expression of mutants. The amino acids for site-directed mutagenesis were identified on the basis

of previous work with homologous proteins (bR, and GR), and the structure obtained in Chapter 2 (Figure 2.9).

4.2.2 Site-directed mutagenesis

The plasmid pET28b was used for all site-directed mutagenesis studies. The primers for mutant introduction (see Appendix B.1, Figure B.3) were designed using the plasmid map and the Thermo Fisher primer design tools [297]. Each 20-base primer was designed with a melting temperature (T_m) between 65-70°C. PCR was performed to introduce mutations using a QuickChange II Site-Directed Mutagenesis Kit (Agilent, USA). First the samples underwent one cycle of a full minute at 95°C, followed by a three-step cycles (30 sec 95°C; 1 min 55°C; 10 min 68°C) repeated 20 times overall. After this cycle, the sample was further incubated (68°C, 10 min) and then stored at 4°C.

Following PCR, the solution was incubated with DpnI (NewEngland Biolabs, USA) (1 hour, 37°C) to remove the template DNA. Next, newly formed DNA (5 μl) was used to transform BL21 (DE3) (Sigma, UK) cells through heat-shock. They were then plated on Luria Bertani (LB) agar, supplemented with kanamycin. Individual colonies were picked and extracted from the cells using a Qiagen QIAprep Spin Miniprep Kit (Qiagen, Netherlands). After extraction, the DNA was sent for sequencing to Source Bioscience to confirm the mutagenesis of the plasmid.

4.2.3 Expression and purification of AR3 in *E.coli* (AR3 EC)

Following mutagenesis, the AR3 variants were picked and incubated (50 ml LB, 100μg/ml kanamycin, 37°C, 170 rpm) shaking overnight. Then, the cultures were

transferred to 500ml of LB with 100μg/ml kanamycin and incubated (37°C, 170rpm) until an OD_{600}=0.6 was reached. Next, the cultures were induced with 0.5mM IPTG (Sigma, UK) and 5μM *all-trans* retinal (Sigma,UK) solubilised in ethanol. Cells were collected by centrifugation (8,000 g, 20 min, 4°C) and resuspended into sonication buffer (Appendix A.2). The samples were then sonicated 5 min, with repeated pulses of 10 seconds 'on' and 10 seconds 'off' with an amplitude of 50%. The lysate was then centrifuged (70,000 *g*, 60 min, 4°C) and the pellet was resuspended with solubilisation buffer (Appendix A.2) and finally incubated overnight for detergent solubilisation (DDM) at 4°C.

Once solubilisation was completed, the samples were centrifuged (70,000 *g*, 60 min, 4°C) and the supernatant was collected. Next, the supernatant was incubated with Ni/NTA beads (Thermo Fisher, UK) (1 hour, 4°C). The solution was then washed with Wash Buffer (Appendix A.2) three times by centrifugation (700 *g*, 3 min, 4°C) and placed onto filter columns. The protein was eluted using Elution Buffer (Appendix A.2). After elution, the samples were concentrated using a Vivaspin concentrator (Merck) with a 100,000 molecular weight cut-off (MWCO) up to 0.5 mL volume. The samples were applied onto a Superdex 200 10/300 GL column attached to an Akta Pure (GE Healthcare). The column was equilibrated with Equilibration Buffer (Appendix A.2, 3 column volumes (25 ml)) and the sample was introduced onto the column at a flow rate of 0.3 mL/min. Protein elution was followed using a UV-detector (280 nm) and the fractions were collected. Coloured fractions were pooled and further concentrated or kept at 4°C.

4.2.4 Spectral screening of mutant library

Absorption spectra of the purified AR3 mutants were measured with a Jasco V-630 using a quartz cuvette (1cm).

4.2.5 Proton pumping assay

The proton pumping capacity of AR3 and its variants was assessed using an adapted protocol from Frances H. Arnold et al [288]. The protein was expressed in *E.coli* for 2.5hr after addition of IPTG and *all-trans* retinal. The cell suspension was centrifuged (8,000 *g*, 5min, 4°C) and washed with phosphate buffer (1mMKH_2PO_4, 50 mM KCl pH 7.5). After wash, the cells were resuspended into 1 ml of phosphate buffer with 1μM of H33342 (2'-(4-ethoxyphenyl)-5-(4-methyl-1-piperazinyl)-2,5'-bi-1H-benz- imidazole). The cell cultures were further incubated in the dark (2.5 hr, 30°C, 180rpm) before fluorescence measurements were performed in the dark using a LS50B Luminescence Spectrometer (Perkin Elmer). The excitation wavelength used was 346 nm and the emission range was measured from 400 nm to 600 nm at 30°C. After measurements, visible light was applied for 25 minutes onto the sample using a 30-W LED flood light from Meridian Lighting at a 20 cm distance. Fluorescence spectra were recorded after illumination. As a positive control, *E.coli* cells were used without any AR3 protein expressed but with the addition of glucose (final concentration of 40 mM) in order to activate the proton pumping mechanism regardless of illumination. As the negative control, we used the *E.coli* cells without protein expression and no glucose added.

4.2.6 Electrophysiology in DIBs

Reconstitution of samples and electrical measurements were performed as in Chapter 3 after sample purification.

4.2.7 Circular Dichroism

Following the purification of sample, CD measurements were performed as in Chapter 2.

4.3 Results and Discussion

4.3.1 Approach to AR3 spectral tuning

The environment where the retinal chromophore is located in microbial rhodopsins, known as "retinal-binding pocket" (RBP), has been the target of many spectral tuning studies with the aim of developing a mutant library with different spectral properties [285, 288]. Directed evolution has enabled the identification of residues, close to the retinal, which can be mutated to produce a large spectral shift in the protein [298]. To identify the amino acids relevant to achieve this in AR3, this protein was expressed and purified from *Escherichia coli*, since the creation of a mutant library is difficult to obtain in *Halorubrum sodomense* [299]. *E.coli* was thus chosen for the comparative ease in producing a sufficient amount of functional protein, which can be expressed and purified in a matter of days instead of the several weeks in *H. sodomense*.

Following the expression of AR3 in *E. coli* (AR3 EC), different detergents were used for the solubilisation of AR3 EC from the membranes, such as OG and DDM. DDM was ultimately chosen since OG lengthened the lifetime of the M-state (Appendix B.3, Figure B.4), as reported previously in bR [300]. Once extracted, the

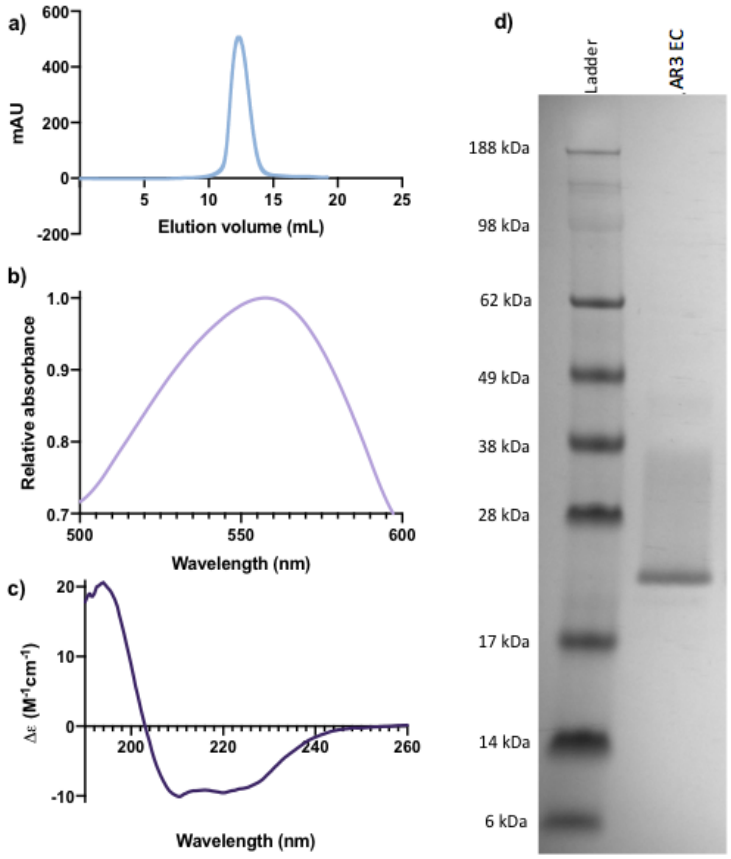

Figure 4.5: **Purification of AR3 in *E.coli* (AR3 EC).** a) Size-exclusion chromatogram of AR3 EC showing a single peak. b) UV-Vis absorbance spectra of AR3 EC. c) Circular dichroism trace of AR3 EC. d) SDS-PAGE of AR3 EC after SEC with a single band observed around ∼25kDa as expected.

protein sample was first purified using Ni-NTA resin, since the protein possess a His-Tag. SEC was used to ensure that the purification via the Ni-NTA column was successful and to remove possible contaminants (SEC, Figure 4.5.a). We used SDS-PAGE (Figure 4.5. d) to assess the purity of the protein sample with a single band around ∼25kDa as expected. Additionally, CD (Figure 4.5. c) was used to verify that the proteins folding was conserved after expression and purification in *E. coli* and its secondary structure content was assessed using Dichroweb [235] (∼65% helix, ∼7% sheet, and ∼18% random coil) with expected values as seen for bR (Appendix A.4,

Figure A.1), and AR3 from *Halorubrum sodomense* (Figure 2.7.). UV-Vis spectra were recorded to demonstrate that the retinal added during the growth is covalently bound to the Lys 226 (λ_{max} = 557 nm) (Figure 4.5. b).

4.3.2 Activity of wildtype AR3 expressed in *E. coli*

Once purified, the AR3 EC was reconstituted into DIBs in order to assess its ion conductivity characteristics. The insertion of AR3 EC into DIBs occurs in the opposite direction than the insertion of AR3 in *H. sodomense* (Figure 4.6. a-b), as observed previously in Chapter 3. In AR3 from *H. sodomense*, a positive current output instead of a negative current output is observed, and this might indicate that the protein inserts preferentially from the C-terminus into the droplet [148]. Additionally, the current change observed in AR3 EC is lower than the one obtained by AR3 from *H.sodomense* (Figure 4.6. c), but with similar values as those obtained for bR (Figure 4.6. c).

The difference could be due to various reasons, such as poor reconstitution of AR3 EC into DIBs from detergent in comparison with the reconstitution of AR3 from *H. sodomense*, or the efficient purification of AR3 from *H. sodomense* compared to the purification of AR3 EC, or a reduced net asymmetry of insertion. Alternatively, it could be due to the protein forming monomers instead of trimers (Figure 2.16), due to the absence of bacterioruberin or other lipids found in native membranes, which are crucial for optimal activity of AR3 as discussed in Chapter 2. Albeit with a lower current, similar action spectra are obtained (Figure 4.6. d, raw data to illustrate how the action spectra was obtained can be found in Appendix B.6 B.8) to the one observed for AR3 from *H. sodomense* (Figure 3.9), with a change in

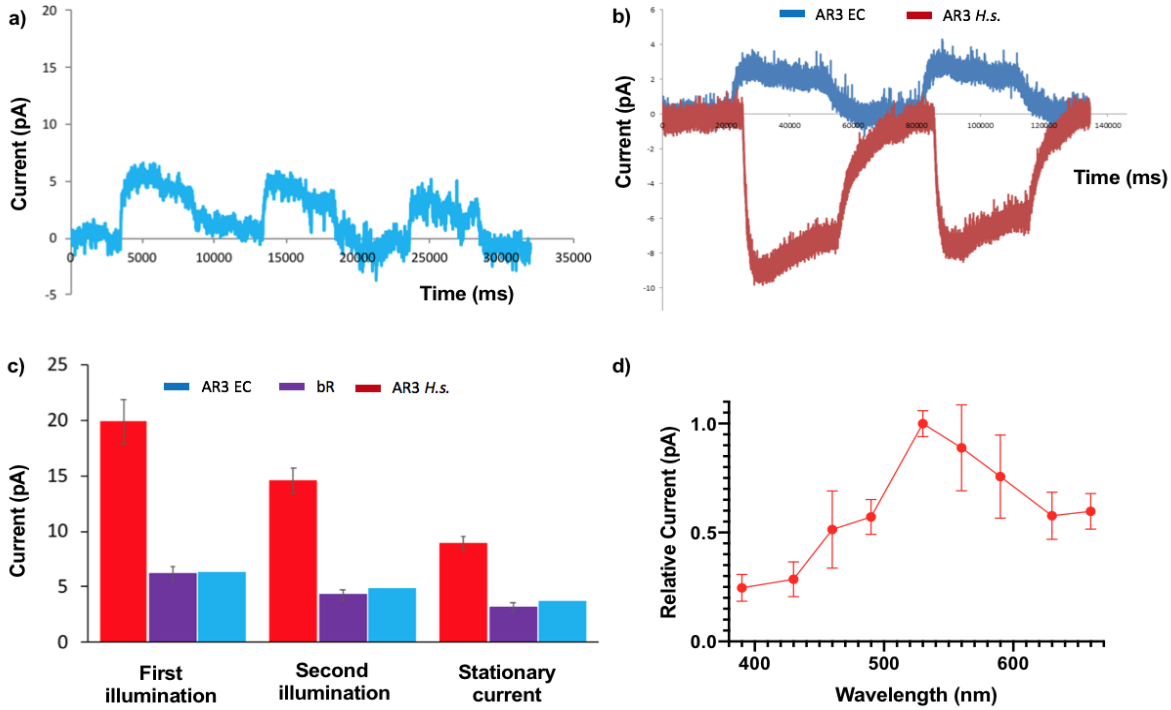

Figure 4.6: **Photocurrent of AR3 EC into DIB.** a) Current trace of AR3 EC showing the change in current of AR3 EC reconstituted in DIB upon illumination with a 560+590nm light. b) Difference of change in current of AR3 EC compared to AR3 from *Halorubrum sodomense* (AR3 H.s.) showing a different insertion into DIBs. c) Current output of AR3 from *H. sodomense* (red) compared to AR3 EC (blue) and bR (purple). The values of AR3 EC and bR are very similar compared to the values of AR3 from *H.sodomense*. d) Action spectra of AR3 EC in DIB with a specific wavelength of 530-560nm. 3 biological repeats were done independently. In collaboration with Charlotte Hoskin.

current specific to a wavelength of 530-560 nm (Figure 4.6. d). Therefore, despite the lower photocurrents obtained, this shows that the wavelength specificity has not been affected.

4.3.3 Site-directed mutagenesis of AR3

The retinal pocket of AR3 is very similar to the one in bR, except for four amino acids that differ (Figure 4.7). These changes correspond to the residues Val59, Tyr93, Ile132, and Phe218 in the pocket. Interestingly, these residues are more hydrophobic

than the ones found in bR [288]. If the average hydropathicity of the pocket is computed using the GRAVY [301] algorithm, the values obtained for AR3 (0.114) and for bR (-0.459) differ, meaning that AR3 presents a more hydrophobic environment (Figure 4.7). According to directed evolution studies and site-directed mutagenesis studies, an increased hydrophobicity around the retinal (as observed in many microbial rhodopsins) affects the spectral properties of the protein by shifting its absorbance towards the red [288, 302]. These findings could explain why the absorbance of AR3 is more red-shifted than bR (Figure 2.7), and why AR3 offers the opportunity of attaining larger red-shifted mutants compared to bR [288, 303].

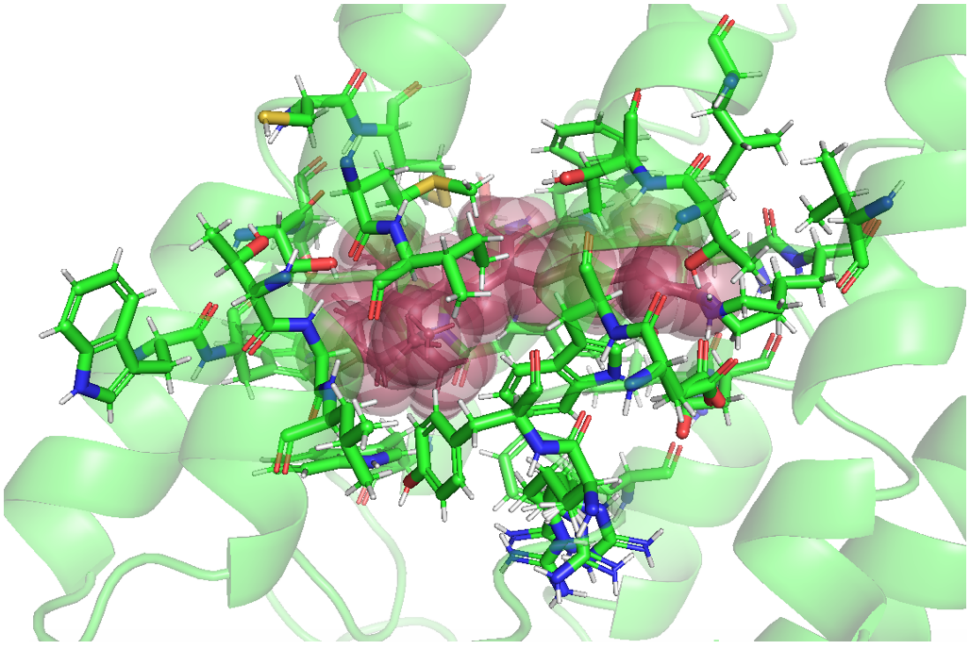

Protein	Aminoacids	GRAVY
Bacteriorhodopsin	WTTLM GWSTMWYPW DAK	-0.459
Archaerhodopsin-3	VYWTTLMIGWSTMWYPWFDAK	0.114

Figure 4.7: **Amino acids in the retinal pocket of AR3.** Above: Schematic representation of the residues in the retinal pocket of AR3 (PDB:6GUX) where retinal is represented in red and residues around in green sticks. Below: Values of the Grand average hydropathicity of the amino acids (GRAVY [301]) forming the retinal in bR and AR3.

Suitable mutation sites in AR3 were identified through homology modelling from other microbial rhodopsins such as GR and bR [288, 290]. These proteins, and AR3, possess 20 conserved residues in the RBP which are within 5 $\AA$ of the retinal. These residues studied in both GR and bR [288, 290] were also chosen here for changing the spectral properties of AR3 EC, to achieve hypsochromic and bathochromic shifted mutants compared to AR3 EC (Figure 4.8, SDS-PAGE of the different AR3 EC mutants purified in Appendix B.4, Figure 4.8).

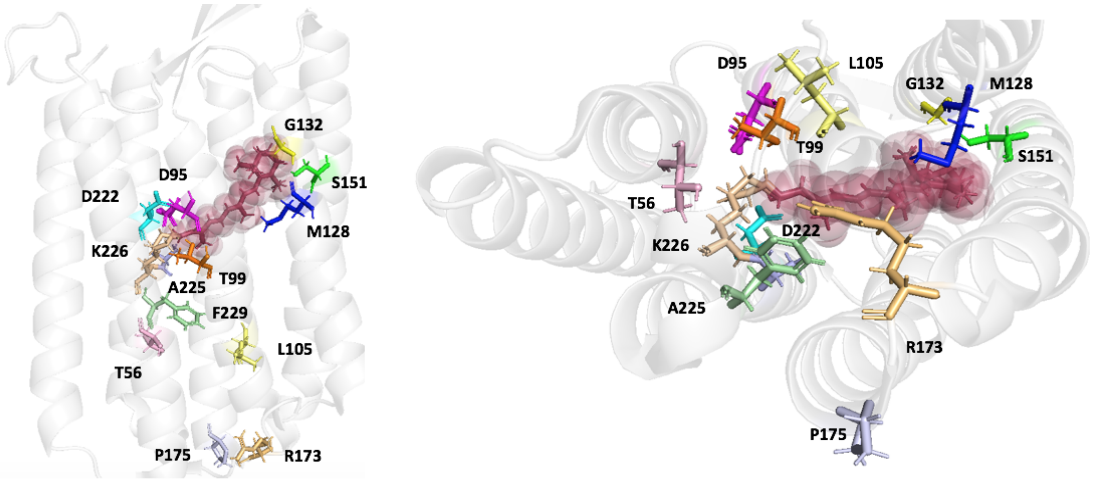

Figure 4.8: **Amino acids identified for spectral tuning.** Schematic representation of the different amino acids (coloured in the figure above, PDB: 6GUX) mutated in AR3 EC to obtain altered spectral properties.

Several combinations of these different mutations were performed and some of them issued further shifted mutants. Thus a diverse mutant library was developed, crucially with unique red-shifted and blue-shifted variants (Figure 4.9). As shown by Figure 4.9, most of the mutations performed yielded blue-shifted mutants. Mutant combinations rendered the highest shifts, such as the TSP variant (T99C/S151C/P175C), which exhibits a hypsochromic shift of 20 nm in comparison to AR3 EC (Figure 4.9). Other single mutants such as T99C, or S151C, yielded a hyp-

sochromic shift of 13 nm (Figure 4.9). There was a limit to the number of mutations it was possible to introduce, since they can destabilise the protein structure. The TAPS mutant (T99C/A225M/S151C/P175C), offers a telling example, since it does not produce any spectral shift, or even a visible colour (Appendix B.3, Figure B.4), meanwhile mutants such as TSP (T99C/S151C/P175C) or TAP (T99C/A225M/P175C) are able to provide a shift in absorption (Figure 4.9).

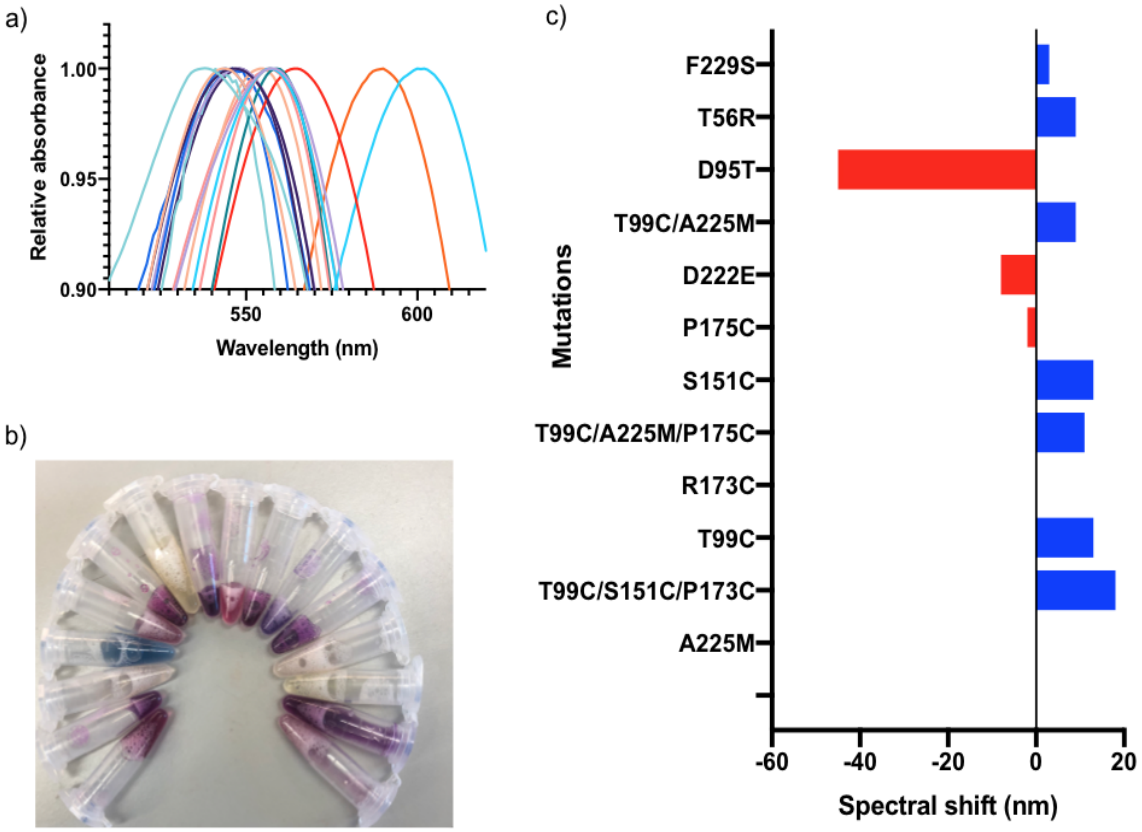

Figure 4.9: **Spectral tuning of AR3 EC.** a) UV-Vis absorption spectra of AR3 EC mutants bearing different spectral properties. b) Picture of the different colours of the purified protein obtained by mutations in AR3 EC. c) Histogram with the respective spectral shift for each AR3 EC mutant obtained.

Besides the hypsochromic variants, only three bathochromic mutants were produced and all of them were single mutants (Figure 4.9). These successful mutants

were D95T, P175C, and D222E (Figure 4.8). Both D95T and D222E are important residues in the photocycle (Figure 2.3), and they are relatively close to the SB [304]. Particularly, the residue D95 is one of the major players in the photocycle of AR3 (on the basis of homology to bR, Figure 2.1), since its protonation state enables the proton translocation across the protein [305]. It is possible that mutations in this specific amino acid site might change the kinetics of the photocycle, and affect the function of the protein as shown for bR (Figure 4.2) [305]. On the other hand, D222 is also an important residue, since it stabilizes the SB through hydrogen bonding to K226, since it contributes to the formation of an inner water network (pentameric arrangement, Figure 2.12). Such network is observed in many rhodopsins, and facilitates the proton translocation during the photocycle (Figure 2.3) [305]. It has been reported that some of these mutations of bR severely affect its original proton pumping, or effectively cancels it. This only highlights the need for a full biophysical characterisation of the AR3 EC variants [306].

4.3.4 Biophysical characterisation of AR3 EC variants

To determine the biophysical characteristics of the AR3 EC variants developed through mutagenesis, a comprehensive biophysical study of their properties was then carried out.

4.3.4.1 Proton pumping

The proton pumping capabilities of AR3 EC mutants were tested, as well as their photocurrent activity upon reconstitution into DIBs, for the study of their ion conductivity. A protocol developed by Arnold and colleagues, to determine the proton pump-

ing ability for photoreceptors expressed in *E.coli* membranes using a fluorophore, was followed (Figure 4.10) [288, 307]. The dye used was 2'-(4-ethoxyphenyl)-5-(4-methyl-1-piperazinyl)-2,5'-bi-1H-benz- imidazole (H33342), a DNA intercalating agent that has been widely used in fluorescent microscopy. When H33342 is located inside the cell, its fluorescence intensity is strong, and when exported outside of the cell, its fluorescence intensity is lower. In addition, *E.coli* cells possess multi-drug efflux proteins which take advantage of the proton gradient generated across the membrane to transport the fluorophore outside of the cell [288].

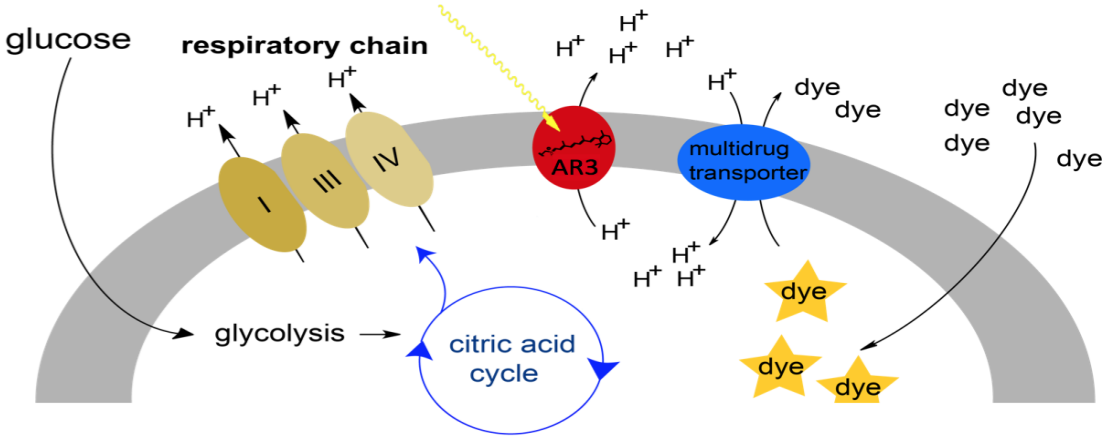

Figure 4.10: **Proton pumping assay.** When H33342 is inside the cell, it fluoresces strongly, and when exported outside of the cell the fluorescence decreases. On top of that, *E.coli* cells possess multi-drug efflux proteins which take advantage of the proton gradient generated across the membrane to transport the fluorophore outside of the cell. The proton pumping assay takes advantage of this multi-drug efflux created by the proton pumping of AR3. Thus, the fluorescence change of H33342 is used to assess the proton pumping efficiency of the different variants expressed in *E. coli*. Reproduced from [288].

The proton pumping assay takes advantage of these multi-drug efflux proteins and of the proton gradient created by an intercalated proton pump (Figure 4.10). The fluorescence of the dye changes due to its translocation from inside to outside the cells, and indirectly allows the assessment of the proton pumping of the AR3 EC mutants

(Figure 4.10). *E.coli* cells were grown in the absence of light for at least 2.5 hours, at which point the fluorescence is measured. Then, illumination is applied (400-700 nm LED light) to the sample for 25 minutes in order to trigger the proton pumping by AR3 EC. The proton pumping is consequently used by multi-drug efflux proteins to transport the dye to the outside of the cell (summarised Figure 4.10) [288, 307].

None of the AR3 EC mutants matched the proton pumping capacity in comparison to AR3 EC (Original data found in Appendix B.5, Figure B.6). Most mutants retained some proton pumping capabilities (Appendix B.5, Figure B.6, Figure 4.11), with A225M, T99C/A225M, T99C/A225M/P175C and T99C performing better-than-average proton pumping capacities by retaining more than 30% of the proton pumping capabilities of AR3 EC (Figure 4.11).

However, in the case of the S151C mutation, when it was present either as a single or a combined mutation caused proton pumping of the AR3 EC mutant to be severely decreased (Figure 4.11, Appendix B.5, Figure B.6). Now, contrary to bR, where no natural occurring cysteines are found in the amino acid sequence (Figure 2.1), AR3 does possess a cysteine (C154) (Figure 2.1), which forms a hydrogen bond with S151 residue (Appendix B.5, Figure B.7). By mutating S151 to a cysteine, the formation of a disulphide bond between these two residues is possible (Appendix B.5, Figure B.7). This might affect the overall structure and dynamics of the protein, thus severely hindering the photocycle (Figure 2.3). Furthermore, it has been suggested that residue S151 might have a role in the puckering of the β-ionone ring in AR3. Therefore, altering its distance from the retinal by 1 $\mathring{A}$ from one isomer to the other could potentially affect retinal isomerisation when this is changed to a cysteine (a

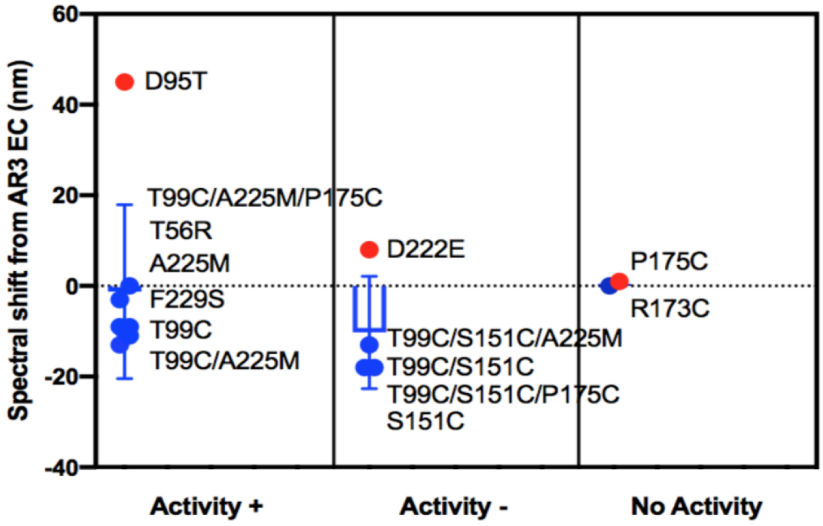

Figure 4.11: **Spectral shift and proton pumping of AR3 EC variants.** Box plot of the different AR3 EC mutants indicating their spectral shift and their proton pumping capabilities. The values are in a scale of no measurable activity (No activity), activity less than 30% of AR3 EC (Activity -), and activity higher than 30% of AR3 EC (Activity +). As observed, most mutants retain more than 30% of AR3 EC activity, with the bathochromic mutant D95T bearing the highest spectral shift while still functional. Three AR3 EC hypsochromic mutants showed a reduced activity compared to AR3 EC and other 4 mutants showed no activity at all. All these variants were a combination of mutations which in accumulation were detrimental for the protein e.g. the mutant TAPS (T99C/A225M/P175C/S151C).

bulkier side-chain than serine) [308, 309, 310].

Another example where the proton pumping ability of the cells have been reduced is the red-shifted mutants. They showed very attenuated proton pumping as expected from the literature (Figure 4.11) [306]. The red-shifted mutations were localised around the hydrogen bonding network (pentameric arrangement), and mutations in these residues, as well as their close proximity to the SB linkage, affected the proton pumping characteristics of the different variants.

In addition, a trend in the change of fluorescence in the proton pumping assay (Figure 4.12. b, Appendix B.5, Figure B.6) was observed for the red-shifted mutant D95T in AR3 EC, since the fluorescence of the dye increased compared to the AR3

EC (Figure 4.12. a-b).

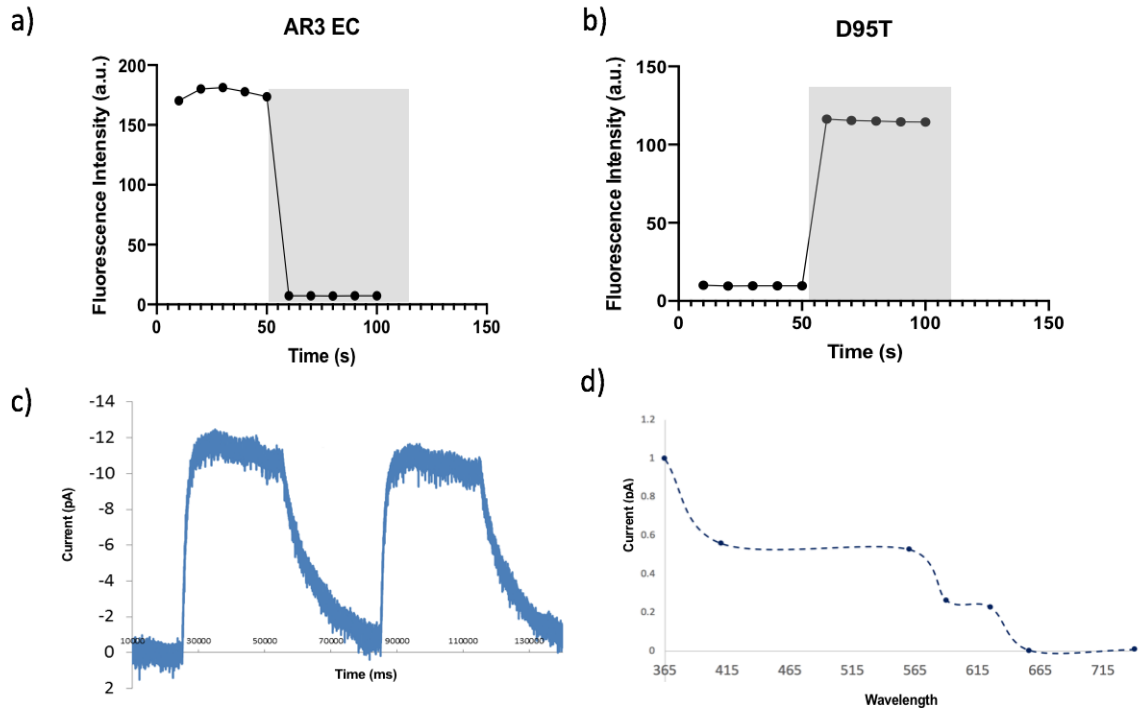

Figure 4.12: **Proton pumping in D95T.** a) Proton pumping assay in AR3 EC showing the decrease of fluorescence of the dye upon illumination (grey area). b) Proton pumping assay in D95T where the change of fluorescence of the dye shows an increase opposite to what is observed for AR3 EC upon illumination (grey area). c). Photocurrent trace of D95T with photocurrent values of -12 pA which are opposite values obtained for AR3 EC (positive generation of photocurrent), indicating a proton pumping occurring in the opposite direction to AR3 EC. d) Action spectra of D95T. In collaboration with Charlotte Hoskin.

These results indicate a different photocycle intermediate and proton pumping mechanism compared to AR3 EC, since it had been reported that this mutant might work as an inward proton pump in bR when illuminated with white light (400-700 nm) as well as an inward chloride pump when illuminated with green light (560+590 nm) [88, 311]. This observation for bR would explain the change in the polarity of the proton gradient compared to AR3 EC, where protons are being pumped inwardly. Furthermore, upon reconstitution of D95T into DIBs, a change in current opposite to

that observed in AR3 EC (Figure 4.6. a) was obtained (Figure 4.12. c). This means that the pumping of protons occurs in the opposite direction to what is observed in AR3 EC. The action spectra of D95T mutant (Figure 4.12. d) shows a constant change in current opposite to what is observed to AR3 EC, which suggests that the pumping capabilities of the mutant is not dependant on the wavelength of light as in bR [88, 311], but it acts as an inward proton pump across a wide range of light.

4.3.4.2 Reconstitution of AR3 EC mutants into DIBs

All mutants were reconstituted into DIBs to study their ion conductivity characteristics (Figure 4.13). The reconstitution of AR3 EC mutants into DIBs was challenging (Figure 4.6) in comparison to AR3 from *H.sodomense* (since this is spontaneous and straightforward due to the presence of the protein in proteoliposomes).

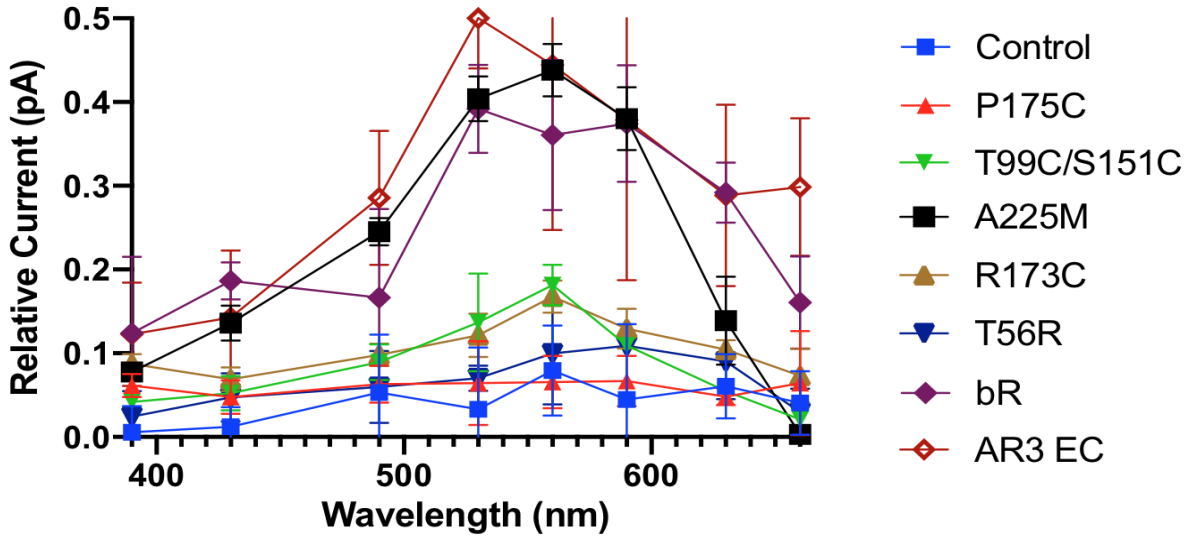

Figure 4.13: **Action spectra of AR3 EC variants.** Action spectra of AR3 EC variants that were able to be reconstituted into DIBs. The variants TS (T99C/S151C), A225M, and R173C show a detectable photocurrent. Mutants such as P175C, do not show any detectable photocurrent upon illumination. In collaboration with Charlotte Hoskin.

As seen in Figure 4.13, the mutant A225M generated a change in current similar to that of AR3 EC and with a similar action spectrum, with an optimum wavelength at 560 nm. Other mutations such as T99C/S151C, or R173C showed a photocurrent change specific to 560 nm, although the change observed was much reduced compared to AR3 EC (by 80% and 90% respectively) (Figure 4.13). Other mutants showed a photocurrent such as T56R specific to a wide range of wavelengths (Figure 4.13), from 490nm to 580 nm. As for the rest of the mutants reconstituted into DIBs, no photocurrent was measured as observed with mutant P175C (Figure 4.13), or the reconstitution into DIBs was not possible. Table 4.1 summarised the AR3 EC mutants developed in this spectral tuning study, and their biophysical characteristics studied.

AR3 EC mutants				
AR3 EC mutant	λ_{max}	Proton pumping in cells	Reconstitution in DIB	Photocurrent change specific to wavelength
AR3 EC	557 nm	Activity +	Succesful	Yes
T56R	548 nm	Activity +	Succesful	No
T99C/S151C	539 nm	Activity -	Succesful	Yes
T99C/S151C/A225M	400 nm	Activity -	Unsuccesful	NA
D222E	565 nm	Activity -	Unsuccesful	NA
A225M	557 nm	Activity +	Succesful	Yes
F229S	554 nm	Activity +	Unsuccesful	NA
P175C	558 nm	No Activity	Succesful	No
T99C	544 nm	Activity +	Unsuccesful	NA
T99C/A225M/P175C	546 nm	Activity +	Unsuccesful	NA
T99C/S151C/P175C	539 nm	Activity -	Unsuccesful	NA
T99C/A225M	548 nm	Activity +	Unsuccesful	NA
D95T	602 nm	Activity +	Succesful	Yes
R173C	557 nm	No Activity	Succesful	Yes
S151C	544 nm	Activity -	Unsuccesful	NA

Table 4.1: Summary table of all AR3 EC mutants developed and their biophysical characteristics. NA: not applicable.

4.3.5 Mutations affecting the proton release complex

Until now, the retinal pocket has been the main focus in tuning the spectral properties of AR3. Now, different mutations affecting the ion conductivity of AR3 are investigated by introducing specific mutations at residues R92 and E214, which are key players in the PRC of microbial rhodopsins (Figure 2.13) [293, 295]. Mutations on these residues in homologues, such as bR, affect the photocycle by delaying the M-state decay. In some cases, they trap the protein in the M-state, since the changes introduced in the PRC prevent the proton release [293, 295]. Specifically, the mutations introduced into the PRC were: R92S, R92T, E214Q, and E214T (Figure 4.14).

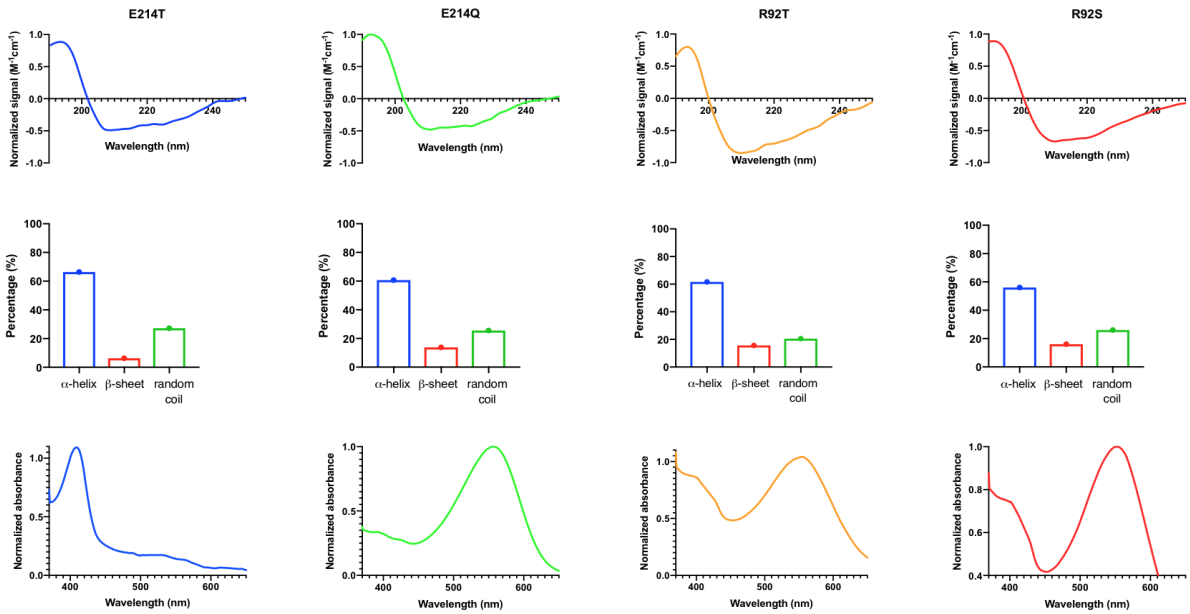

Figure 4.14: **CD and UV-Vis spectra AR3 EC PRC mutants.** Mutants after purification. According to the CD trace (top 4 spectra and the analyses underneath), the variants do not alter the folding of the protein (∼60% helix, ∼10% sheet, and ∼20% random coil). The UV-Vis (bottom 4 spectra) absorbance spectra, on the other hand, are strongly affected since the appearance of a new peak at around 400nm is observed. The mutant E214T shows a λ_{max} at 400nm, meanwhile the mutant R92S, and R92T show two absorbance signals at 400nm and 550nm. The mutant E214Q shows a single λ_{max} at 550nm.

No major structural changes were observed (Figure 4.14) for any of the mutants (R92S, R92T, E214Q, E214T), where the predicted secondary structure (∼60% helix, ∼10% sheet, and ∼20% random coil) corresponds to the ones seen for AR3 EC or bR (Appendix A.4, Figure A.1). On the other hand, the UV-Visible spectra of the mutants changes in comparison with AR3 EC (Figure 4.14). Indeed, only one mutation, E214Q, behaves as expected, displaying an unchanged absorbance spectrum with a single λ_{max} around 560 nm (Figure 4.14). Conversely, two other mutations, R92S and R92T, have their λ_{max} at around 560 nm, and also show an absorption signal at ∼410 nm (Figure 4.14). This suggests that the protein population is divided in two, with some proteins trapped in the M-state and some others in the 'ground state', as previously observed in bR [294].

To expand on what happened in bR, when the mutation R82Q (bR numbering) was introduced in bR, the proton release of the photocycle which corresponds to the M-state was delayed severely [294]. In addition, proton pumping appeared to happen only due to the PRC and not because of the half channels connecting the protein to the cytoplasm or extracellular environment [294]. These mutations (R92S, R92T) have a similar effect on AR3 EC, delaying the M-state as shown by the UV-Vis (Figure 4.14). This suggests that the PRC is essential to the correct functioning of the protein, and further shows how the PRC modulates the proton pumping of the protein.

The E214T mutant has a λ_{max} at 400nm (Figure 4.14), corresponding to the M-state (Figure 2.3) [222, 92, 89]. This suggests that the proton release in AR3 is blocked by the introduction of a threonine instead of glutamic acid. In bR, E194 and E204 (bR

numbering) stabilise a water network important for the activity of the photocycle, as in AR3 (Figure 2.13) [295, 296]. Introduction of a neutral residue, such as threonine, in this position in AR3 might affect not only the network, but also the events that happen in the second half of the photocycle (due to the change in pK_a), by blocking the protein in the M-state or making the process of protonation/deprotonation slower [293, 294, 295].

To determine the effect of these mutations (R92S, R92T, E214Q, E214T) on proton transport by AR3 EC, the mutants were successfully reconstituted into DIBs following the same protocol used for the spectral shifted mutants (Figure 4.15).

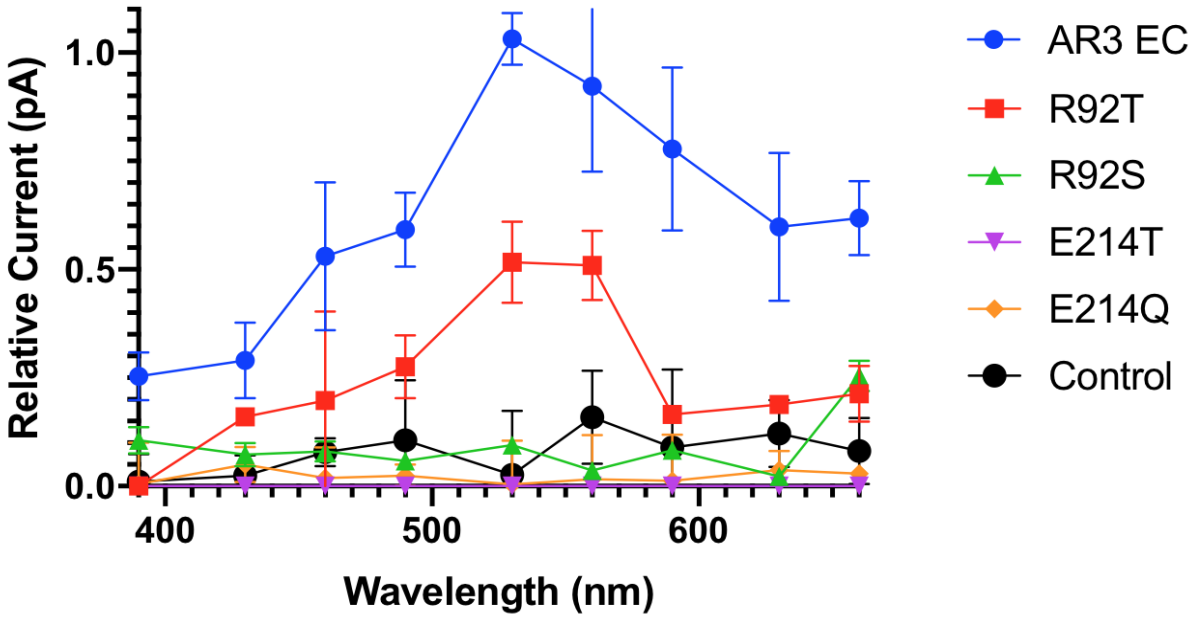

Figure 4.15: **Action spectra of mutants in the PRC.** Only R92T shows a detectable wavelength-specific photocurrent similar to AR3 EC. The other mutations E214Q, E214T, and R92S show no difference signal than the sample without protein. In collaboration with Charlotte Hoskin.

Only one mutant displayed a photocurrent change, R92T (Figure 4.15), whereas no photocurrent change was observed in R92S, nor in E214T, or E214Q (Figure 4.15).

In the case of the E214T residue, the effect of the mutation upon the aqueous network around the PRC (Figure 2.13) prevents it from transporting protons (Figure 4.15). Contrary to what has been observed in bR [293, 294, 295], where the introduction of a neutral residue at this position slows down the photocycle, in AR3 we observe that the photocycle is blocked at the M-state, as shown by E214T λ_{max} at 400 nm (Figure 4.14). For E214Q, we do observe a λ_{max} 560nm, similarly to the AR3 EC and yet no photocurrent change is observed. In bR it has been observed that the introduction of glutamine in this position delays the formation of O-state in the protein, delaying the N state decay by 10-fold [293]. The E214Q λ_{max} at 560nm in (Figure 4.14), where the N state absorbs, suggests that it is possible that this mutation blocks the formation of the O-state and thus prevents the proton uptake of the protein in AR3 as occurring for bR [293, 294, 295].

The mutations introduced in the PRC cancel the photocurrent generated by AR3 EC (Figure 4.6). Without photocurrent change, no hyperpolarisation of the membrane occur, and therefore these mutations (R92S, E241T, E214Q) are good candidates for fluorescent studies as voltage indicators for neuronal action potential mapping [284]. Furthermore, directed-evolution around these mutations could help in the design of AR3 mutants with enhanced fluorescence and no current change.

In addition to the non-photoswitching variants (R92S, E214T, E214Q), R92T exhibits a change in photocurrent (albeit attenuated) specific to 560 nm as AR3 EC (Figure 4.15). In this particular mutant, a neutral residue was introduced instead of a charged residue with a similar size. This consequently affected the photocurrent change by 50% lower in comparison to AR3 EC (Figure 4.15). It is possible that

this particular mutation might affect the usual proton release during the photocycle by destabilizing the inner water network around the AR3 cavity, as seen in bR, but without inhibiting the photocycle [294]. These findings suggest that R92 does not have a large influence on proton pumping as D95 or D106 [294], but nevertheless has an important role, since some mutations reduce (R92T) or cancel (R92S) the proton pumping ability (Figure 4.15).

4.4 Conclusions

A library of functional AR3 mutants with different spectral properties were expressed in *E.coli*. Mutants with different spectral properties that maintained the photocurrent as AR3 EC would be useful for:

- Optogenetics studies where we could silence different neuronal populations using different wavelengths of light
- Functional bionetworks or bio-electronical systems as biosensors for different wavelengths of light as done in bR, with a larger detectable photocurrent change.

Furthermore, mutants with different spectral properties that do not retain the photocurrent activity are also useful since they can be used as fluorescent voltage indicators. Their desired non-pumping properties makes them ideal for tracking the neuronal firing and action potential mapping without hyperpolarisation of the membrane [284]. Additionally, a new mutant was obtained (D95T) that changed the function of the protein from an outward proton pump to an inward proton pump (Figure 4.12), as in bR (Figure 4.2). This would be very useful in optogenetics

studies for controlling hyperpolarisation of neuronal membranes. The bathochromic spectral shift to 605 nm on the D95T mutant makes it ideal for optogenetics studies, where the red (or near infrared) light shift would be useful in animal studies, where deeper and less invasive treatments are required. Table 4.1 summarizes the AR3 EC mutants developed and their biophysical characteristics studied.

Finally, we demonstrated suitable targets to adapt the ion conductivity of AR3 to specific needs. By altering the inner pentameric hydrogen bonding network (Figure 2.12), and the mutagenesis in the proton release complex (Figure 2.13), we can modify the proton pumping to the extent of being depleted, or reduced as demonstrated (Figure 4.15). We believe that mutations around these residues could yield mutants with similar or larger photocurrents than AR3 EC.

An atomistic understanding of this protein is important for better rational design of variants as neural silencers or voltage indicators. The study here improves our knowledge of the spectral properties of the protein as well as furthering our knowledge of the photocycle, and the role of key functional residues in the protein. The identification of different AR3 variants and their comprehensive biophysical characterisation, as performed here, provides new candidates ready to be used in different biotechnological applications.

Chapter 5

Conclusions

The interplay between biology and technology is becoming more important nowadays, and the use of specific biomolecules to integrate into technology, bottom-up approach, is becoming a necessity. The miniaturisation of electronic devices coupled with the limiting size that silicon-based devices are approaching, find in biology a potential solution to develop detectors in the nanoscale range [109, 111]. In this thesis, we explore a microbial rhodopsin (AR3), capable of generating an electrochemical gradient in membranes [284]. Previous work in optogenetics exploited mutants of this protein to silence neuron impulses in response to light and to provide a fluorescent readout of membrane potential [126, 123]. Although AR3 has many applications, we know very little about this protein to date compared to other microbial rhodopsins since there is no crystal structure, no biophysical studies of the protein in artificial membranes, or mutagenesis studies of the photocycle as have been performed, as for bR [294, 203, 148]. Here we present, for the first time, a comprehensive study of AR3 that goes from resolving its structure in dark- and light-adapted state, its biophysical characteristics, and uses site-directed mutagenesis to tune its spectral properties as well as to identify important residues in ion transport.

Chapter 2 presents the first crystal structures of AR3 in the light- (LA) and dark-adapted state (DA). The high resolution obtained for both structures (LA resolved to 1.07 Å, and DA resolved to 1.2 Å) allows the observation of intricate hydrogen bonding networks. Additionally, the structures hint at the importance that water molecules play in these networks thus being crucial for ion transport. A comparison of LA and DA structures helps understanding the mechanism that AR3 undergoes from one conformation to the other when in presence or absence of light. AR3 hydrogen bonding network and water molecules presence specially around the residue R92 and residues E204, and E214 constituting the PRC supply the protein with more pathways for proton release that could explain why the kinetics of AR3 are faster or the photocurrent of the protein is larger compared to bR.

The presence of an omega loop as in archaerhodopsins [74] reveals a possible position where bacterioruberin, a chromophore co-purified with the protein, might bind to the protein and aid in the oligomerisation of AR3. As with bR, the oligomeric organisation of AR3 is a trimer and is found in claret membrane patches when bacterioruberin is present. When bacterioruberin is not present in AR3 nanodiscs of DMPC or Asolectin, no 2-D trimeric lattice array is observed. Thus, there is a hint that the possible role that bacterioruberin has in AR3 is in the oligomeric organisation, something that has been observed in AR2 [74]. Moreover, we take a look at the photo-intermediates of AR3 and the photo-induced conformational changes experienced by the protein upon illumination using XFEL and HS-AFM. The refinement of the structures at different time points in the photocycle is currently ongoing, but using HS-AFM we have been able to observe conformational changes belonging to the

E-F loop as in bR [194], indicating similar conformational change that takes place in the M-state in AR3.

Chapter 3 presents for the first time a biophysical study of AR3 from native membranes reconstituted into droplet interface bilayers. AR3 photocurrent capabilities are conserved in artificial bilayers as in membranes, and show a photocurrent change higher than bR (up to three-fold). AR3 is able to maintain its activity and photocurrent change over repeated illumination cycles or even constant illumination in contrast to ChR2 or bR, making it ideal for optogenetics and bioelectronics [169, 268]. Furthermore, we assess the role of retinal in the protein photocurrent as well as the role that bacterioruberin might have in the protection of the protein against bleaching.

In Chapter 4, we use the information gathered on the structure and biophysical properties of the protein to develop AR3 mutants suitable for bioelectronics as well as for optogenetics. Here we develop an AR3 mutant library with different spectral properties obtaining bathochromic and hypsochromic shifts pushing the absorbance of the protein as far as possible. The proton pumping capabilities of the protein are assessed, and mutants with different spectral properties which conserve proton pumping and photocurrent change are identified. Additionally, a mutagenesis study of specific residues important in the proteins photocycle is performed, where different mutants identified not only affect the spectral properties of the protein but also negate the photocurrent changes typically observed in AR3.

Mutation R92T does not abolish photocurrent capacity, however the absorbance spectrum of this mutant shows an absorbance peak at 400 nm and 560 nm, suggesting that the M-state dominates over the ground state. This properties make R92 a

suitable residue for directed evolution in studies looking to increase the photocurrent of AR3, as well as to attenuate the photocurrent generated. Additionally, E214 is a suitable residue for directed evolution studies to abolish proton pumping capacity of AR3. Flash photolysis would be an ideal technique to help better elucidate the role of residues where the delay or trapping of AR3 at specific photo-intermediates with distinguished absorbance spectra such as M-state or O-state take place. Furthermore, if coupled with X-ray crystallography, it would help to elucidate the movement and rearrangement of water molecules and adjacent residues, as shown for bR [294].

As discussed throughout the thesis, the photocurrent generated by AR3 is significantly higher than that of other microbial rhodopsins such as bR (three-fold higher). In addition, its capacity to remain active under continuous illumination or repeated illumination cycles makes it an ideal candidate for bioelectronics. The similarities between AR3 and bR suggest that the coupling of AR3 to a solid surface, for example via introduction of a cysteine as for bR [169], is possible, and its photoswitching capabilities could be exploited for biosensor applications. An enhanced change in photocurrent compared to bR would make it easier for the detector to measure and record the change in conductivity upon illumination, enabling the production of sensitive biosensors [169]. Moreover, the fact that AR3 activity is wavelength-specific, could help develop improved wavelength-specific biosensors, optical memory, or even cameras.

It has been proven that the reconstitution of AR3 in DIBs is possible and could help develop functional bionetworks that employ DIBs. Individual DIBs, each containing different AR3 mutants, could be coupled together as an array for use as a

camera as it has been done previously for bR [148] but with an improved conductivity easier to track and measure. Additionally, the AR3 mutants performed and developed in this thesis which possess proton pumping could be further used for neural silencing studies in optogenetics. Mutants that do not possess proton pumping capacities, but which still retain the spectral characteristics of AR3, could be further used in directed evolution studies for optimisation of fluorescent voltage indicators.

In this thesis we have presented an extensive biophysical study of the properties of AR3 from solving its structure in DA and LA state, to characterizing its photocurrent capabilities in a novel system of DIBs and developing a mutant library with different spectral properties. A myriad of experiments could be done using the information provided in this thesis for better protein engineering of AR3 mutants in optogenetics and bioelectronics, from the structural data to the mutant library.

Appendix A

A.1 SDS-PAGE

For SDS-PAGE the 4-12% Tris-Glycine gels NuPAGE (Invitrogen Novex) were used. The running buffer used was a 1x MES running buffer with a 180 V, 400 mA, for 40 minutes to run the gels in an X-cell Surelock minicell. The samples for the gel were prepared following with NuPAGE LDS sample buffer (6x). Using InstantBlue (Scientific Company, san Diego, USA) the gel was stained for 1 hour at room temperature and the protein bands were visualised and compared to protein markers (BioLabs, UK).

A.2 Buffers used in thesis

Resuspension buffer = 100 mM MES, 100 mM NaCl, 0.001% DDM, pH 7.

Sonication buffer = 150 mM NaH_2PO_4, 20 mM NaCl, 5 mM $MgCl_2$, pH 7.

Solubilisation buffer = 30 mM Na_2HPO_4, 20 mM NaH_2PO_4, 300 mM NaCl, 1% DDM, pH 7.

Wash buffer = 50 mM NaH_2PO_4, 100 mM NaCl, 30 mM Imidazole, 0.03% DDM, pH 7.

Elution buffer = 50 mM NaH_2PO_4, 100 mM NaCl, 300 mM Imidazole, 0.03%

DDM, pH 7.

Equilibration buffer = 50 mM NaH_2PO_4, 100 mM NaCl, 0.03% DDM, pH 7.

Culture media AR3 1L = 125 g NaCl, 160 g $MgCl_2$, 0.13 g $CaCl_2$, K_2SO_4, 1 g oxoid bacteriological peptone (LP72, Oxoid), 1 g Yeast extract, 2 g Soluble starch, pH 7.

Culture media bR 1L = 250 g NaCl, 10 g oxoid bacteriological peptone (LP72, Oxoid), 20 g $MgSO_4$, 3 g $Na_3C_6H_5O_7$, 2 g KCl, pH 7.

A.3 Data collection and statistics refinement

AR3 EC mutants		
	Dark-Adapted structure (PDB:6GUX)	Light-adapted structure (PDB:6S6C)
Data Collection		
Space group	$P2_12_12_1$	$P2_12_12_1$
Temperature	100 K	100 K
Number of crystals	2	17
Cell dimension		
a, b, c, (Å)	46.70, 47.52, 104.42	44.67, 47.36, 104.19
$\alpha, \beta, \gamma, (\mathring{A})$	90, 90, 90	90, 90, 90
$CC_{1/2}$	0.994 (0.057)	0.999 (0.179)
Mean I/$\sigma(I)$	7.0 (0.60)	9.2 (0.4)
Refinement		
Resolution range (Å)	43.29 - 1.30	52.10 - 1.07
Completeness (%)	94. 5 (68.8)	99.8 (94.8)
R_{work}/R_{free} (%)	0.14/0.17	0.15/0.17
Average B all atoms	17.44	17.97
R. m. s. deviations		
Bond lengths (Å)	0.006	0.004
Bond angles (°)	1.301	1.205
Ramachandran plot		
outliers (%)	0.0	0.0
allowed (%)	1.41	0.96
favoured (%)	98.59	99.04

Table A.1: **Data collection and statistics refinement of DA structure 6GUX and LA structure 6S6C.**

A.4 Purification of bacteriorhodopsin

Bacteriorhodopsin was purified following the protocol developed previously [241]. A colony of bR of was placed in 30 ml of culture media (composition in Appendix A.2) at 37°C shaking at 170 rpm for 7 days until the OD_{600} was 1. The cultures then were added onto a flasks with 500 ml of culture media and let grow for an additional 10 days until the OD_{600} reached 1.5. The cells were collected by centrifugation (8,000 *g*, 20 mind, 4°C). Once collected, the pellets were dissolved in 4M NaCl with 5 mg of DNAse (Sigma), homogenised manually and let dyalising onvernight in 5L of 0.1M NaCl. The membranes were collected by centrifugation (70,000 *g*, 60 min, 4°C) resuspended into 10 ml of double distilled water, and placed in a sucrose gradient made up of the layers: 60% sucrose, 40% sucrose, and 20% sucrose w/v. The claret membrane was isolated via ultracentrifugation of the sucrose gradient (100,000 *g*, 15 hour, 15°C). The purple-coloured band between the layer 40% and 20% was collected and further dialysed in 5L of double distilled water at 4°C overnight. The solution was further centrifuged (70,000 *g*, 60 min, 4°C)and the pellet containing the purple membrane with bR was resuspended in double distilled water (20 mg/ml) and stored at 4°C. The purification of bR was assessed through SDS-PAGE, UV-Vis and CD spectra (Figure A.1).

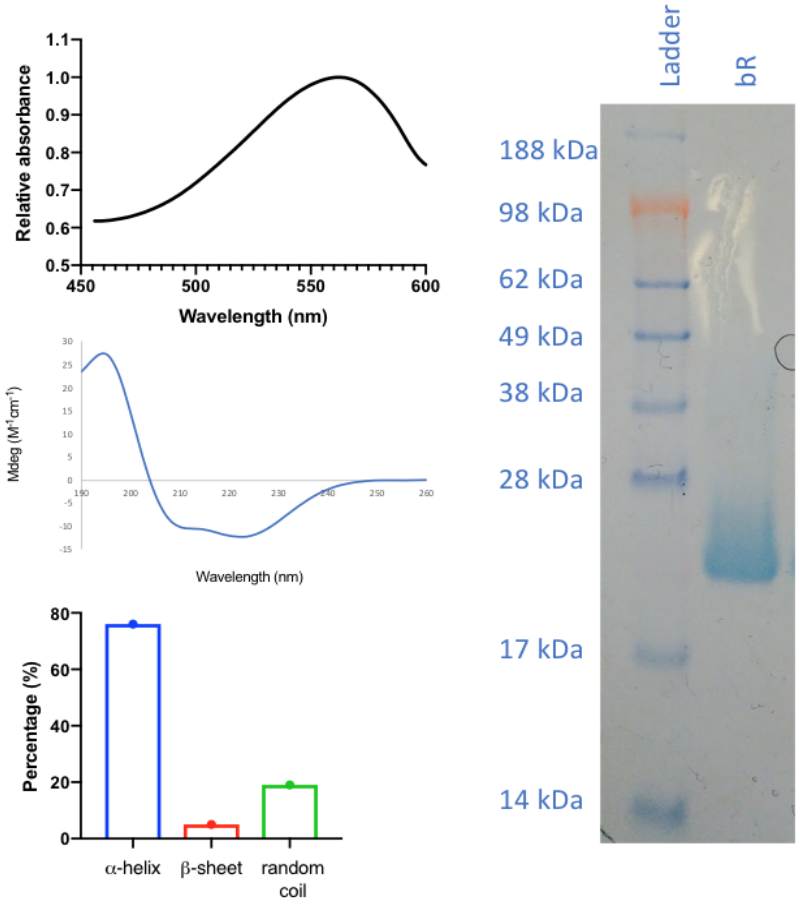

Figure A.1: **Purification of bR.** a) Absorbance spectra of bR in purple membrane (565 nm). b) CD spectra of bR and secondary structure estimate with (76% helix, 5% sheet, 19% random). c) SDS-PAGE of bR with a single band at 19 kDa.

Appendix B

B.1 Plasmid map of AR3 EC and its gene sequence

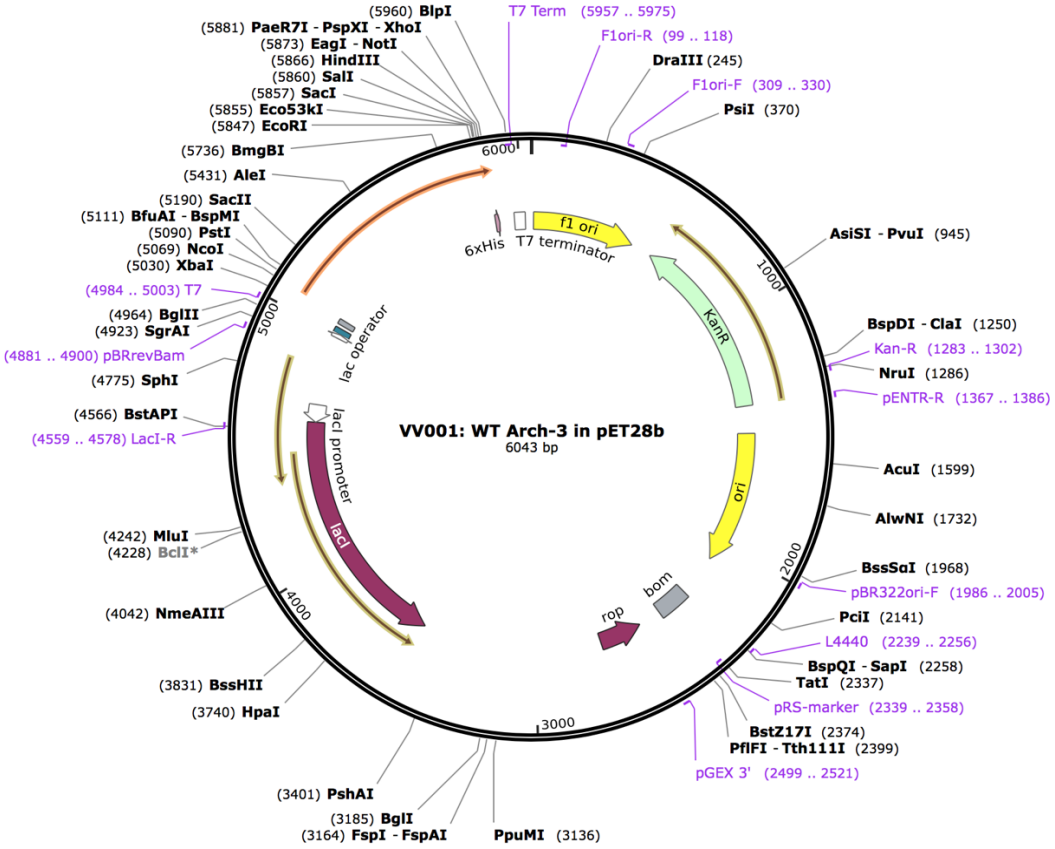

Figure B.1: **Plasmid map of AR3 EC.**

AR3-His_{6x}
5′ ➔ 3′

ATGGACCCCATCGCTCTGCAGGCTGGTTACGACCTGCTGGGTGACGGCAGA
CCTGAAACTCTGTGGCTGGGCATCGGCACTCTGCTGATGCTGATTGGAACCT
TCTACTTTCTGGTCCGCGGATGGGGAGTCACCGATAAGGATGCCCGGGAATA
TTACGCTGTGACTATCCTGGTGCCCGGAATCGCATCCGCCGCATATCTGTCTAT
GTTCTTTGGTATCGGGCTTACTGAGGTGACCGTCGGGGGCGAAATGTTGGA
TATCTATTATGCCAGGTACGCCGACTGGCTGTTTACCACCCCACTTCTGCTGCT
GGATCTGGCCCTTCTCGCTAAGGTGGATCGGGTGACCATCGGCACCCTGGTG
GGTGTGGACGCCCTGATGATCGTCACTGGCCTCATCGGAGCCTTGAGCCACA
CGGCCATAGCCAGATACAGTTGGTGGTTGTTCTCTACAATTTGCATGATAGTG
GTGCTCTATTTTCTGGCTACATCCCTGCGATCTGCTGCAAAGGAGCGGGGCC
CCGAGGTGGCATCTACCTTTAACACCCTGACAGCTCTGGTCTTGGTGCTGTG
GACCGCTTACCCTATCCTGTGGATCATAGGCACTGAGGGCGCTGGCGTGGTG
GGCCTGGGCATCGAAACTCTGCTGTTTATGGTGTTGGACGTGACTGCCAAG
GTCGGCTTTGGCTTTATCCTGTTGAGATCCCGGGCTATTCTGGGCGACACCG
AGGCACCAGAACCCAGTGCCGGTGCCGATGTCAGTGCCGCCGACGCGAATT
CGAGCTCCGTCGACAAGCTTGCGGCCGCACTCGAGCACCACCACCACCACC
ACTGA

Figure B.2: **Gene sequence of AR3 EC.** gene sequence of AR3 EC from 5' to 3' where in green is the sequence corresponding to the His-tag (His6).

B.2 AR3 mutants and the primers used

Mutant	Forward primer	Reverse primer
T99C	TGGCTGTTTTGCACCCCACTT	AAGTGGGGTGCAAAACAGCCA
S151C	CAGTTGGTGGTTGTTCTGTACAATTTGC	GCAAATTGTACAGAACAACCACCAACTG
D222E	ATGGTGTTGGAGGTGACTGCC	GGCAGTCACCTCCAACACCAT
A225M	GGACGTGACTATGAAGGTCGGCTTT	AAAGCCGACCTTCATAGTCACGTCC
R173C	CAAAGGAGTGCGGCCCCGA	CAAAGGAGTGCGGCCCCGA
P175C	CGGGGCTGCGAGGTGGCA	TGCCACCTCGCAGCCCCG
D95T	CCAGGTACGCCACCTGGCTGTTT	AAACAGCCAGGTGGCGTACCTGG
L105R	CTTCTGCTGAGGGATCTGGCC	GGCCAGATCCCTCAGCAGAAG
F229S	CCAAGGTCGGCTCTGGCTTTATC	GATAAAGCCAGAGCCGACCTTGG
T56R	TACGCTGTGAGAATCCTGGTGCC	GGCACCAGGATTCTCACAGCGTAATATC
D95N	CCAGGTACGCCAACTGGCTGTTT	AAACAGCCAGTTGGCGTACCTGG
A225T	GGACGTGACTACGAAGGTCGGCTTT	AAGCCGACCTTCGTAGTCACGTCC
R92T	TAT TAT GCC ACG TAC GCC GAC	GTC GGC GTA CGT GGC ATA ATA
R92S	TAT TAT GCC AGT TAC GCC GAC	GTC GGC GTA ACT GGC ATA ATA
E214Q	CTG GGC ATC CAA ACT CTG	CAG AGT TTG GAT GCC CAG
E214T	CTG GGC ATC ACA ACT CTG	CAG AGT TGT GAT GCC CAG

Figure B.3: **Mutants and their primers.** Mutations introduced into AR3 EC and their respective primers.

B.3 OG vs DDM for purification of AR3 mutants

Figure B.4: **Colour change after solubilisation with OG and DDM.** Colour change of mutant S151C after solubilisation overnight with DDM (right) and OG (left). The colour change can be appreciated when reconstituted with OG, giving a yellow colour typical of the M-state. In collaboration with Owen Crowther.

B.4 SDS-PAGE of AR3 mutants

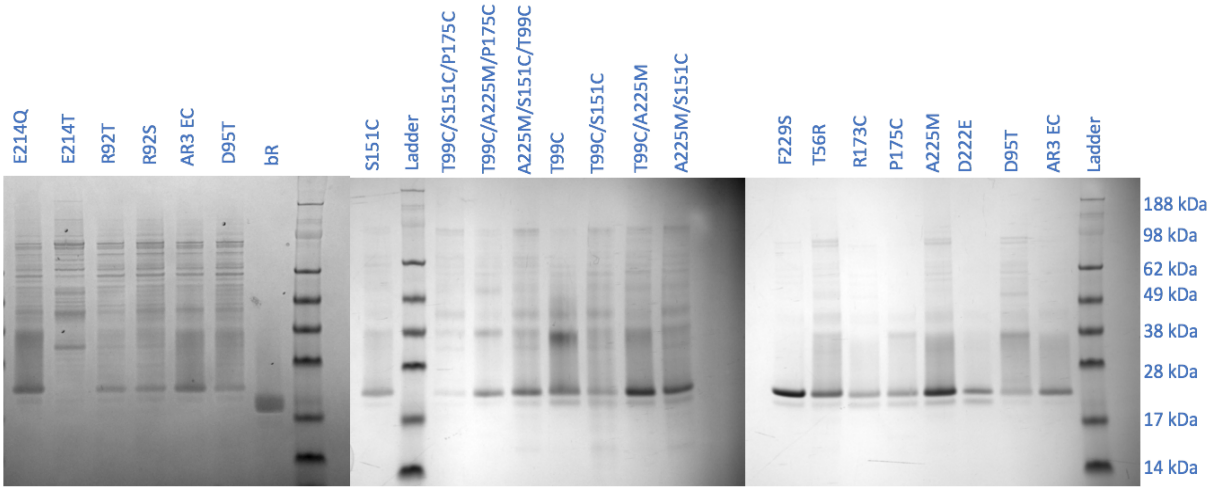

Figure B.5: **SDS-PAGE AR3 mutant.** SDS-PAGE of AR3 EC mutants.

B.5 Data for proton pumping assay of AR3 mutants

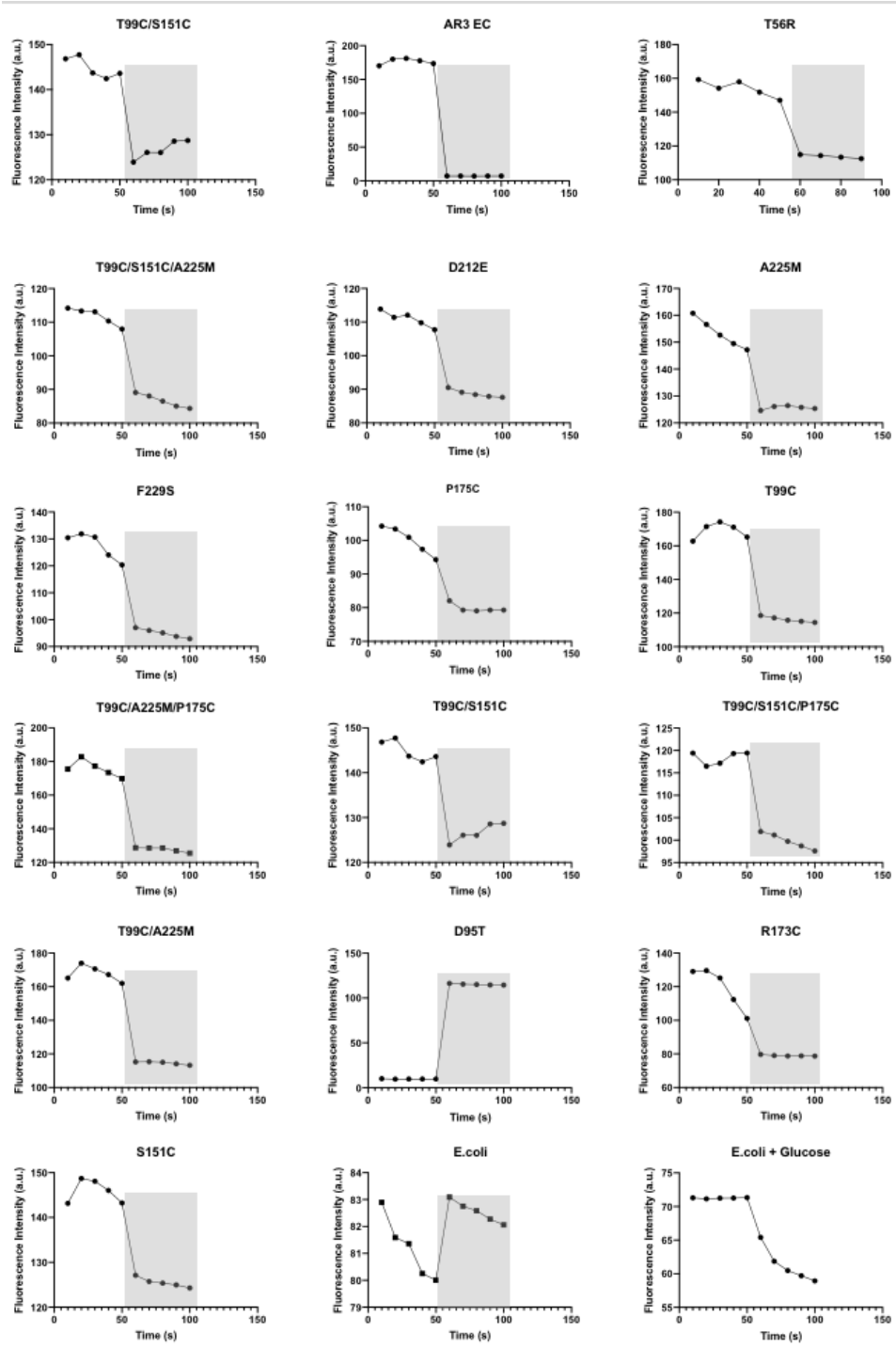

Figure B.6: **Proton pumping assay.** This figure illustrates the change in fluorescence upon illumination (grey area) of all mutants during the proton pumping assay.

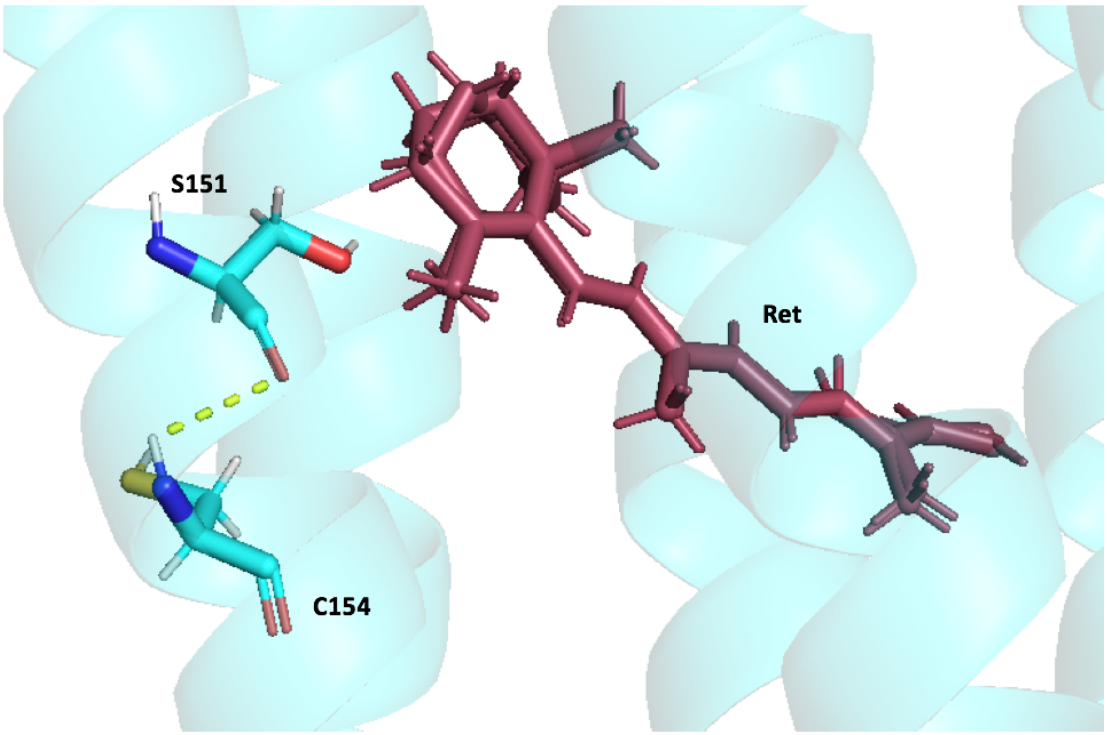

Figure B.7: **S151 hydrogen bonding to C154.** This figure illustrates the hydrogen bonding and close proximity between S151 and C154.

B.6 Action spectra traces of mutants in DIBs

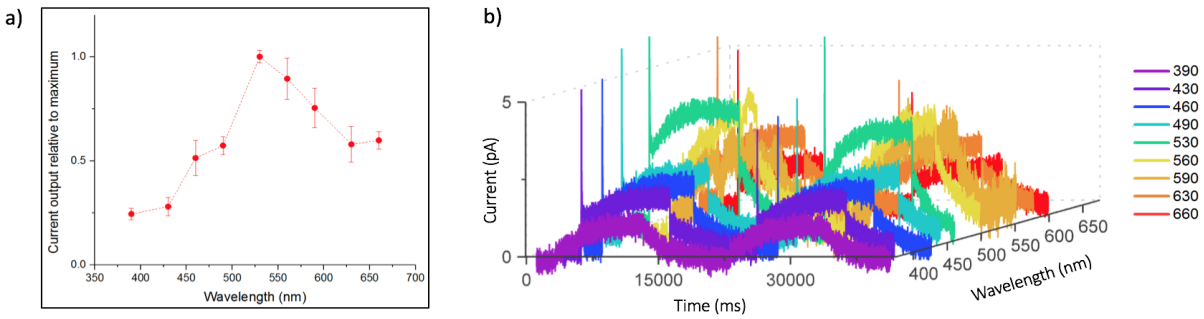

Figure B.8: **AR3 EC current traces at different wavelengths.** Current traces for AR3 EC at different wavelengths of light to show where the action spectra are obtained.

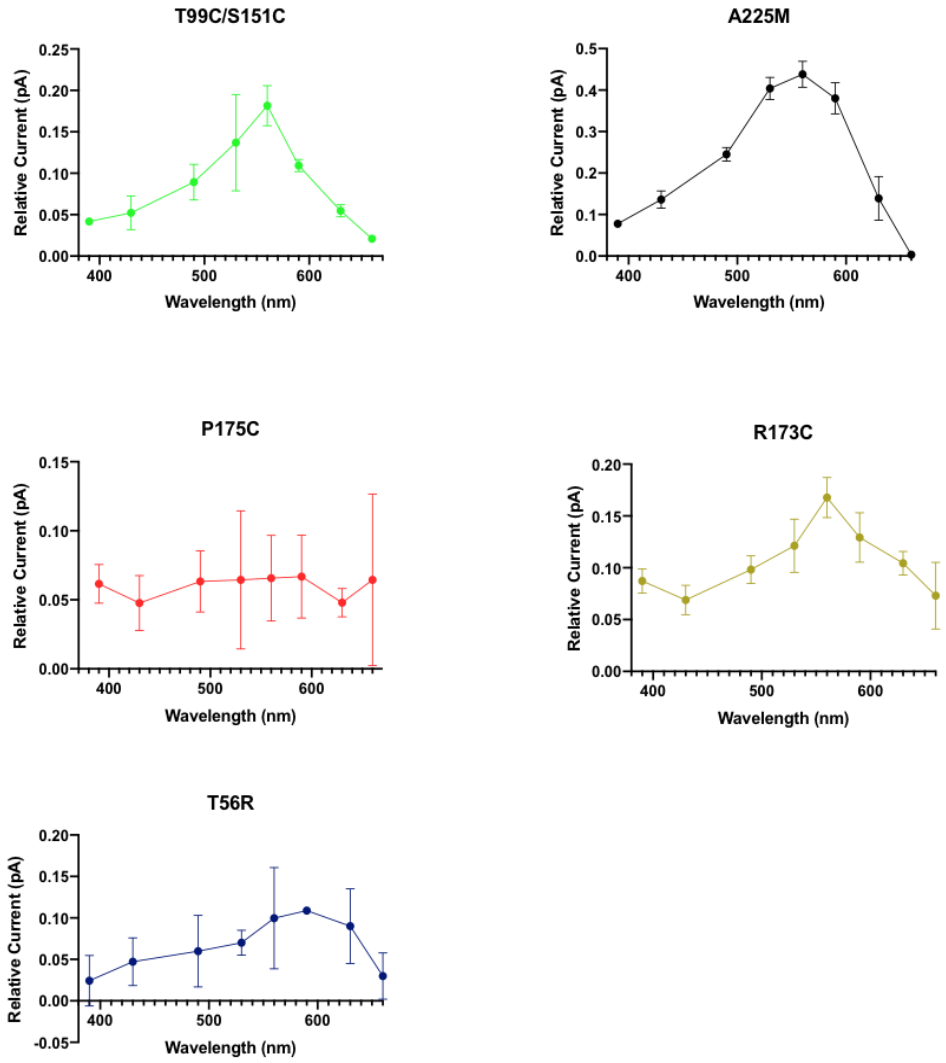

Figure B.9: **Action spectra of AR3 EC mutants.** Individual Action spectra traces for each AR3 EC mutant reconstituted into DIBs.

Bibliography

[1] Takeshi Harayama and Howard Riezman. Understanding the diversity of membrane lipid composition. *Nature Reviews Molecular Cell Biology*, 19(5):281, 2018.

[2] Mary Luckey. *Membrane structural biology: with biochemical and biophysical foundations*. Cambridge University Press, 2014.

[3] Gerrit Van Meer, Dennis R Voelker, and Gerald W Feigenson. Membrane lipids: where they are and how they behave. *Nature reviews Molecular cell biology*, 9(2):112, 2008.

[4] Bruno Antonny, Stefano Vanni, Hideo Shindou, and Thierry Ferreira. From zero to six double bonds: phospholipid unsaturation and organelle function. *Trends in cell biology*, 25(7):427–436, 2015.

[5] Takeshi Harayama, Miki Eto, Hideo Shindou, Yoshihiro Kita, Eiji Otsubo, Daisuke Hishikawa, Satoshi Ishii, Kenji Sakimura, Masayoshi Mishina, and Takao Shimizu. Lysophospholipid acyltransferases mediate phosphatidylcholine diversification to achieve the physical properties required in vivo. *Cell metabolism*, 20(2):295–305, 2014.

[6] David L Nelson, Albert L Lehninger, and Michael M Cox. *Lehninger principles of biochemistry*. Macmillan, 2008.

[7] S Jonathan Singer and Garth L Nicolson. The fluid mosaic model of the structure of cell membranes. *Science*, 175(4023):720–731, 1972.

[8] Philip L Yeagle. Lipid regulation of cell membrane structure and function. *The FASEB journal*, 3(7):1833–1842, 1989.

[9] Jonathan Lombard. Once upon a time the cell membranes: 175 years of cell boundary research. *Biology direct*, 9(1):32, 2014.

[10] Manish Sud, Eoin Fahy, Dawn Cotter, Alex Brown, Edward A Dennis, Christopher K Glass, Alfred H Merrill Jr, Robert C Murphy, Christian RH Raetz, David W Russell, et al. Lmsd: Lipid maps structure database. *Nucleic acids research*, 35(suppl_1):D527–D532, 2006.

[11] George Hedger and Mark SP Sansom. Lipid interaction sites on channels, transporters and receptors: recent insights from molecular dynamics simulations. *Biochimica et Biophysica Acta (BBA)-Biomembranes*, 1858(10):2390–2400, 2016.

[12] Manabu T Nakamura, Barbara E Yudell, and Juan J Loor. Regulation of energy metabolism by long-chain fatty acids. *Progress in lipid research*, 53:124–144, 2014.

[13] Takao Shimizu. Lipid mediators in health and disease: enzymes and receptors as therapeutic targets for the regulation of immunity and inflammation. *Annual review of pharmacology and toxicology*, 49:123–150, 2009.

[14] Bruno Antonny. Mechanisms of membrane curvature sensing. *Annual review of biochemistry*, 80:101–123, 2011.

[15] Robert Ernst, Christer S Ejsing, and Bruno Antonny. Homeoviscous adaptation and the regulation of membrane lipids. *Journal of molecular biology*, 428(24):4776–4791, 2016.

[16] Nermina Malanovic and Karl Lohner. Gram-positive bacterial cell envelopes: The impact on the activity of antimicrobial peptides. *Biochimica et Biophysica Acta (BBA)-Biomembranes*, 1858(5):936–946, 2016.

[17] Lukas Buehler. *Cell membranes*. Garland Science, 2015.

[18] Jenny Leopold, Yulia Popkova, Kathrin Engel, and Jürgen Schiller. Recent developments of useful maldi matrices for the mass spectrometric characterization of lipids. *Biomolecules*, 8(4):173, 2018.

[19] Joan M Boggs. Intermolecular hydrogen bonding between lipids: influence on organization and function of lipids in membranes. *Canadian journal of biochemistry*, 58(10):755–770, 1980.

[20] Bodil Ramstedt and J Peter Slotte. Sphingolipids and the formation of sterol-enriched ordered membrane domains. *Biochimica et Biophysica Acta (BBA)-Biomembranes*, 1758(12):1945–1956, 2006.

[21] Deborah A Brown and Erwin London. Structure and function of sphingolipid- and cholesterol-rich membrane rafts. *Journal of Biological Chemistry*, 275(23):17221–17224, 2000.

[22] J Thomas Hannich, Kyohei Umebayashi, and Howard Riezman. Distribution and functions of sterols and sphingolipids. *Cold Spring Harbor perspectives in biology*, 3(5):a004762, 2011.

[23] Todd PW McMullen, Ruthven NAH Lewis, and Ronald N McElhaney. Cholesterol–phospholipid interactions, the liquid-ordered phase and lipid rafts in model and biological membranes. *Current opinion in colloid & interface science*, 8(6):459–468, 2004.

[24] Derek Marsh. Lateral pressure profile, spontaneous curvature frustration, and the incorporation and conformation of proteins in membranes. *Biophysical journal*, 93(11):3884–3899, 2007.

[25] Harvey T McMahon and Jennifer L Gallop. Membrane curvature and mechanisms of dynamic cell membrane remodelling. *Nature*, 438(7068):590, 2005.

[26] Carl R Woese and George E Fox. Phylogenetic structure of the prokaryotic domain: the primary kingdoms. *Proceedings of the National Academy of Sciences*, 74(11):5088–5090, 1977.

[27] Thierry Benvegnu, Loïc Lemiègre, and Sandrine Cammas-Marion. Archaeal lipids: innovative materials for biotechnological applications. *European Journal of Organic Chemistry*, 2008(28):4725–4744, 2008.

[28] Edward F DeLong. Archaeal mysteries of the deep revealed. *Proceedings of the National Academy of Sciences*, 103(17):6417–6418, 2006.

[29] Samta Jain, Antonella Caforio, and Arnold JM Driessen. Biosynthesis of archaeal membrane ether lipids. *Frontiers in microbiology*, 5:641, 2014.

[30] Yosuke Koga and Hiroyuki Morii. Biosynthesis of ether-type polar lipids in archaea and evolutionary considerations. *Microbiol. Mol. Biol. Rev.*, 71(1):97–120, 2007.

[31] EL Chang. Unusual thermal stability of liposomes made from bipolar tetraether lipids. *Biochemical and biophysical research communications*, 202(2):673–679, 1994.

[32] Boris Tenchov, Erin M Vescio, G Dennis Sprott, Mark L Zeidel, and John C Mathai. Salt tolerance of archaeal extremely halophilic lipid membranes. *Journal of Biological Chemistry*, 281(15):10016–10023, 2006.

[33] KC Hsu, GW Rayfield, and R Needleman. Reversal of the surface charge asymmetry in purple membrane due to single amino acid substitutions. *Biophysical journal*, 70(5):2358–2365, 1996.

[34] Andrey A Gurtovenko and Ilpo Vattulainen. Lipid transmembrane asymmetry and intrinsic membrane potential: two sides of the same coin. *Journal of the American Chemical Society*, 129(17):5358–5359, 2007.

[35] Krishnakumar Balasubramanian and Alan J Schroit. Aminophospholipid asymmetry: a matter of life and death. *Annual review of physiology*, 65(1):701–734, 2003.

[36] Sumie Manno, Yuichi Takakuwa, and Narla Mohandas. Identification of a functional role for lipid asymmetry in biological membranes: Phosphatidylserine-skeletal protein interactions modulate membrane stability. *Proceedings of the National Academy of Sciences*, 99(4):1943–1948, 2002.

[37] A Imparato, Julian C Shillcock, and Reinhard Lipowsky. Lateral and transverse diffusion in two-component bilayer membranes. *The European Physical Journal E*, 11(1):21–28, 2003.

[38] Minoru Nakano, Masakazu Fukuda, Takayuki Kudo, Naoya Matsuzaki, Takuto Azuma, Kazuhisa Sekine, Hitoshi Endo, and Tetsurou Handa. Flip-flop of phospholipids in vesicles: kinetic analysis with time-resolved small-angle neutron scattering. *The Journal of Physical Chemistry B*, 113(19):6745–6748, 2009.

[39] David L Daleke. Phospholipid flippases. *Journal of biological chemistry*, 282(2):821–825, 2007.

[40] T Pomorski and AK Menon. Lipid flippases and their biological functions. *Cellular and Molecular Life Sciences CMLS*, 63(24):2908–2921, 2006.

[41] Mika Ikeda, Akio Kihara, and Yasuyuki Igarashi. Lipid asymmetry of the eukaryotic plasma membrane: functions and related enzymes. *Biological and Pharmaceutical Bulletin*, 29(8):1542–1546, 2006.

[42] Robert FA Zwaal and Alan J Schroit. Pathophysiologic implications of membrane phospholipid asymmetry in blood cells. *Blood*, 89(4):1121–1132, 1997.

[43] LA Woon, JW Holland, EPW Kable, and BD Roufogalis. Ca2+ sensitivity of phospholipid scrambling in human red cell ghosts. *Cell calcium*, 25(4):313–320, 1999.

[44] Patrick Williamson. Phospholipid scramblases. *Lipid insights*, 8:LPI–S31785, 2015.

[45] RFA Zwaal, P Comfurius, and EM Bevers. Surface exposure of phosphatidylserine in pathological cells. *Cellular and Molecular Life Sciences CMLS*, 62(9):971–988, 2005.

[46] Valeriya M Trusova, Galyna P Gorbenko, Julian G Molotkovsky, and Paavo KJ Kinnunen. Cytochrome c-lipid interactions: new insights from resonance energy transfer. *Biophysical journal*, 99(6):1754–1763, 2010.

[47] Linn Fagerberg, Kalle Jonasson, Gunnar von Heijne, Mathias Uhlén, and Lisa Berglund. Prediction of the human membrane proteome. *Proteomics*, 10(6):1141–1149, 2010.

[48] Oyvind Halskau, Arturo Muga, and Aurora Martínez. Linking new paradigms in protein chemistry to reversible membrane-protein interactions. *Current Protein and Peptide Science*, 10(4):339–359, 2009.

[49] Andreas Engel and Hermann E Gaub. Structure and mechanics of membrane proteins. *Annu. Rev. Biochem.*, 77:127–148, 2008.

[50] Andrei L Lomize, Irina D Pogozheva, Mikhail A Lomize, and Henry I Mosberg. The role of hydrophobic interactions in positioning of peripheral proteins in membranes. *BMC Structural Biology*, 7(1):44, 2007.

[51] Anna Mulgrew-Nesbitt, Karthikeyan Diraviyam, Jiyao Wang, Shaneen Singh, Paul Murray, Zhaohui Li, Laura Rogers, Nebojsa Mirkovic, and Diana Murray. The role of electrostatics in protein–membrane interactions. *Biochimica et Biophysica Acta (BBA)-Molecular and Cell Biology of Lipids*, 1761(8):812–826, 2006.

[52] Galyna P Gorbenko, Julian G Molotkovsky, and Paavo KJ Kinnunen. Cytochrome c interaction with cardiolipin/phosphatidylcholine model membranes: effect of cardiolipin protonation. *Biophysical journal*, 90(11):4093–4103, 2006.

[53] Hiroh Ikezawa. Glycosylphosphatidylinositol (gpi)-anchored proteins. *Biological and pharmaceutical bulletin*, 25(4):409–417, 2002.

[54] AG Tse, A Neil Barclay, Anthony Watts, and Alan F Williams. A glycophospholipid tail at the carboxyl terminus of the thy-1 glycoprotein of neurons and thymocytes. *Science*, 230(4729):1003–1008, 1985.

[55] Yusuke Maeda and Taroh Kinoshita. Structural remodeling, trafficking and functions of glycosylphosphatidylinositol-anchored proteins. *Progress in lipid research*, 50(4):411–424, 2011.

[56] Morihisa Fujita and Taroh Kinoshita. Gpi-anchor remodeling: potential functions of gpi-anchors in intracellular trafficking and membrane dynamics.

Biochimica et Biophysica Acta (BBA)-Molecular and Cell Biology of Lipids, 1821(8):1050–1058, 2012.

[57] Bruce Alberts, D Bray, Julian Lewis, Martin Raff, Keith Roberts, and JD Watson. Molecular biology of the cell garland. *New York*, pages 18–19, 1994.

[58] Marcella C Orwick, Peter J Judge, Jan Procek, Ljubica Lindholm, Andrea Graziadei, Andreas Engel, Gerhard Gröbner, and Anthony Watts. Detergent-free formation and physicochemical characterization of nanosized lipid–polymer complexes: Lipodisq. *Angewandte Chemie International Edition*, 51(19):4653–4657, 2012.

[59] Derek Marsh and László I Horváth. Structure, dynamics and composition of the lipid-protein interface. perspectives from spin-labelling. *Biochimica et Biophysica Acta (BBA)-Reviews on Biomembranes*, 1376(3):267–296, 1998.

[60] Anthony G Lee. How lipids and proteins interact in a membrane: a molecular approach. *Molecular BioSystems*, 1(3):203–212, 2005.

[61] Peter F Knowles, Anthony Watts, and Derek Marsh. Spin-label studies of lipid immobilization in dimyristoylphosphatidiylcholine-substituted cytochrome oxidase. *Biochemistry*, 18(21):4480–4487, 1979.

[62] Anthony Watts, Igor D Volotovski, and Derek Marsh. Rhodopsin-lipid associations in bovine rod outer segment membranes. identification of immobilized lipid by spin-labels. *Biochemistry*, 18(22):5006–5013, 1979.

[63] J Antoinette Killian and Thomas KM Nyholm. Peptides in lipid bilayers: the power of simple models. *Current opinion in structural biology*, 16(4):473–479, 2006.

[64] Joanne Oates, Belinda Faust, Helen Attrill, Peter Harding, Marcella Orwick, and Anthony Watts. The role of cholesterol on the activity and stability of neurotensin receptor 1. *Biochimica et Biophysica Acta (BBA)-Biomembranes*, 1818(9):2228–2233, 2012.

[65] Hui Zheng, Elizabeth A Pearsall, Dow P Hurst, Yuhan Zhang, Ji Chu, Yali Zhou, Patricia H Reggio, Horace H Loh, and Ping-Yee Law. Palmitoylation and membrane cholesterol stabilize μ-opioid receptor homodimerization and g protein coupling. *BMC cell biology*, 13(1):6, 2012.

[66] L-O Essen, R Siegert, Wolf D Lehmann, and Dieter Oesterhelt. Lipid patches in membrane protein oligomers: crystal structure of the bacteriorhodopsin-lipid complex. *Proceedings of the National Academy of Sciences*, 95(20):11673–11678, 1998.

[67] Brigitte Sternberg, Chantal L'Hostis, Clare A Whiteway, and Anthony Watts. The essential role of specific halobacterium halobium polar lipids in 2d-array formation of bacteriorhodopsin. *Biochimica et Biophysica Acta (BBA)-Biomembranes*, 1108(1):21–30, 1992.

[68] Michael Jawurek, Clemens Glaubitz, and Karin Hauser. Impact of the lipid environment on the protonation dynamics of bacteriorhodopsin studied with

time-resolved step-scan ftir spectroscopy. *Biomedical Spectroscopy and Imaging*, 5(2):167–174, 2016.

[69] Michael Jawurek, Jessica Dröden, Benedikt Peter, Clemens Glaubitz, and Karin Hauser. Lipid-induced dynamics of photoreceptors monitored by time-resolved step-scan ftir spectroscopy. *Chemical Physics*, 512:53–61, 2018.

[70] Derek Marsh. Energetics of hydrophobic matching in lipid-protein interactions. *Biophysical journal*, 94(10):3996–4013, 2008.

[71] Malin Svensson, Ann-Kristin Mossberg, Jenny Pettersson, Sara Linse, and Catharina Svanborg. Lipids as cofactors in protein folding: Stereo-specific lipid–protein interactions are required to form hamlet (h uman α-lactalbumin m ade le thal to t umor cells). *Protein Science*, 12(12):2805–2814, 2003.

[72] Eunyong Park and Tom A Rapoport. Mechanisms of sec61/secy-mediated protein translocation across membranes. *Annual review of biophysics*, 41:21–40, 2012.

[73] Derek Marsh and Tibor Páli. Orientation and conformation of lipids in crystals of transmembrane proteins. *European Biophysics Journal*, 42(2-3):119–146, 2013.

[74] Tsutomu Kouyama, Ryudo Fujii, Soun Kanada, Taichi Nakanishi, Siu Kit Chan, and Midori Murakami. Structure of archaerhodopsin-2 at 1.8 å resolution. *Acta Crystallographica Section D: Biological Crystallography*, 70(10):2692–2701, 2014.

[75] Elena G Govorunova, Oleg A Sineshchekov, Hai Li, and John L Spudich. Microbial rhodopsins: diversity, mechanisms, and optogenetic applications. *Annual review of biochemistry*, 86:845–872, 2017.

[76] John L Spudich, Chii-Shen Yang, Kwang-Hwan Jung, and Elena N Spudich. Retinylidene proteins: structures and functions from archaea to humans. *Annual review of cell and developmental biology*, 16(1):365–392, 2000.

[77] Oliver P Ernst, David T Lodowski, Marcus Elstner, Peter Hegemann, Leonid S Brown, and Hideki Kandori. Microbial and animal rhodopsins: structures, functions, and molecular mechanisms. *Chemical reviews*, 114(1):126–163, 2013.

[78] Mathias Grote, Martin Engelhard, and Peter Hegemann. Of ion pumps, sensors and channels—perspectives on microbial rhodopsins between science and history. *Biochimica et Biophysica Acta (BBA)-Bioenergetics*, 1837(5):533–545, 2014.

[79] Marie Kurihara and Yuki Sudo. Microbial rhodopsins: wide distribution, rich diversity and great potential. *Biophysics and physicobiology*, 12:121–129, 2015.

[80] Kenneth J Rothschild. Ftir difference spectroscopy of bacteriorhodopsin: toward a molecular model. *Journal of bioenergetics and biomembranes*, 24(2):147–167, 1992.

[81] Akio Maeda. Application of ftir spectroscopy to the structural study on the function of bacteriorhodopsin. *Israel journal of chemistry*, 35(3-4):387–400, 1995.

[82] Erin L Devine, Daniel D Oprian, and Douglas L Theobald. Relocating the active-site lysine in rhodopsin and implications for evolution of retinylidene proteins. *Proceedings of the National Academy of Sciences*, 110(33):13351–13355, 2013.

[83] Cecilia Wickstrand, Robert Dods, Antoine Royant, and Richard Neutze. Bacteriorhodopsin: Would the real structural intermediates please stand up? *Biochimica et Biophysica Acta (BBA)-General Subjects*, 1850(3):536–553, 2015.

[84] Paula J Booth. A successful change of circumstance: a transition state for membrane protein folding. *Current opinion in structural biology*, 22(4):469–475, 2012.

[85] Hartmut Luecke, Brigitte Schobert, Jean-Philippe Cartailler, Hans-Thomas Richter, Anja Rosengarth, Richard Needleman, and Janos K Lanyi. Coupling photoisomerization of retinal to directional transport in bacteriorhodopsin. *Journal of molecular biology*, 300(5):1237–1255, 2000.

[86] Thomas P Sakmar, Santosh T Menon, Ethan P Marin, and Elias S Awad. Rhodopsin: insights from recent structural studies. *Annual review of biophysics and biomolecular structure*, 31(1):443–484, 2002.

[87] Michael Hoffmann, Marius Wanko, Paul Strodel, Peter H König, Thomas Frauenheim, Klaus Schulten, Walter Thiel, Emad Tajkhorshid, and Marcus Elstner. Color tuning in rhodopsins: the mechanism for the spectral shift between bacteriorhodopsin and sensory rhodopsin ii. *Journal of the American Chemical Society*, 128(33):10808–10818, 2006.

[88] Jörg Tittor, Ulrich Haupts, Christina Haupts, Dieter Oesterhelt, Anja Becker, and Ernst Bamberg. Chloride and proton transport in bacteriorhodopsin mutant d85t: different modes of ion translocation in a retinal protein. *Journal of molecular biology*, 271(3):405–416, 1997.

[89] Janos K Lanyi and Hartmut Luecke. Bacteriorhodopsin. *Current opinion in structural biology*, 11(4):415–419, 2001.

[90] Hartmut Luecke. Atomic resolution structures of bacteriorhodopsin photocycle intermediates: the role of discrete water molecules in the function of this light-driven ion pump. *Biochimica et Biophysica Acta (BBA)-Bioenergetics*, 1460(1):133–156, 2000.

[91] Catie Leary. What makes salt lakes pinks. `https://www.mnn.com/earth-matters/wilderness-resources/blogs/why-are-salt-lakes-pink`, 2016.

[92] Janos K Lanyi. Proton transfers in the bacteriorhodopsin photocycle. *Biochimica et Biophysica Acta (BBA)-Bioenergetics*, 1757(8):1012–1018, 2006.

[93] H-J Freisleben, K Zwicker, P Jezek, G John, A Bettin-Bogutzki, K Ring, and T Nawroth. Reconstitution of bacteriorhodopsin and atp synthase from micrococcus luteus into liposomes of the purified main tetraether lipid from thermoplasma acidophilum: proton conductance and light-driven atp synthesis. *Chemistry and physics of lipids*, 78(2):137–147, 1995.

[94] Richard Henderson and P Nigel T Unwin. Three-dimensional model of purple membrane obtained by electron microscopy. *Nature*, 257(5521):28, 1975.

[95] Nikolaus Grigorieff, Thomas A Ceska, Kenneth H Downing, Joyce M Baldwin, and Richard Henderson. Electron-crystallographic refinement of the structure of bacteriorhodopsin. *Journal of molecular biology*, 259(3):393–421, 1996.

[96] Yoshiaki Kimura, Dmitry G Vassylyev, Atsuo Miyazawa, Akinori Kidera, Masaaki Matsushima, Kaoru Mitsuoka, Kazuyoshi Murata, Teruhisa Hirai, and Yoshinori Fujiyoshi. Surface of bacteriorhodopsin revealed by high-resolution electron crystallography. *Nature*, 389(6647):206, 1997.

[97] Hartmut Luecke, Hans-Thomas Richter, and Janos K Lanyi. Proton transfer pathways in bacteriorhodopsin at 2.3 angstrom resolution. *Science*, 280(5371):1934–1937, 1998.

[98] Paul Gale and Anthony Watts. Effect of bacteriorhodopsin on the orientation of the headgroup of 1, 2-dimyristoyl-sn-glycero-3-phosphocholine in bilayers: a 31p-and 2h-nmr study. *Biochimica et Biophysica Acta (BBA)-Biomembranes*, 1106(2):317–324, 1992.

[99] Hassan Belrhali, Peter Nollert, Antoine Royant, Christoph Menzel, Jurg P Rosenbusch, Ehud M Landau, and Eva Pebay-Peyroula. Protein, lipid and water organization in bacteriorhodopsin crystals: a molecular view of the purple membrane at 1.9 å resolution. *Structure*, 7(8):909–917, 1999.

[100] N Grigorieff, E Beckmann, and F Zemlin. Lipid location in deoxycholate-treated purple membrane at 2.6 å. *Journal of molecular biology*, 254(3):404–415, 1995.

[101] Eriko Nango, Antoine Royant, Minoru Kubo, Takanori Nakane, Cecilia Wickstrand, Tetsunari Kimura, Tomoyuki Tanaka, Kensuke Tono, Changyong Song,

Rie Tanaka, et al. A three-dimensional movie of structural changes in bacteriorhodopsin. *Science*, 354(6319):1552–1557, 2016.

[102] Gaoxiang Mei, Natalia Mamaeva, Srividya Ganapathy, Peng Wang, Willem J DeGrip, and Kenneth J Rothschild. Raman spectroscopy of a near infrared absorbing proteorhodopsin: Similarities to the bacteriorhodopsin o photointermediate. *PloS one*, 13(12):e0209506, 2018.

[103] Hartmut Luecke, Brigitte Schobert, Hans-Thomas Richter, Jean-Philippe Cartailler, and Janos K Lanyi. Structure of bacteriorhodopsin at 1.55 å resolution. *Journal of molecular biology*, 291(4):899–911, 1999.

[104] Akira Kawanabe and Hideki Kandori. Photoreactions and structural changes of anabaena sensory rhodopsin. *Sensors*, 9(12):9741–9804, 2009.

[105] Robin Rammelsberg, Gregor Huhn, Mathias Lübben, and Klaus Gerwert. Bacteriorhodopsin's intramolecular proton-release pathway consists of a hydrogen-bonded network. *Biochemistry*, 37(14):5001–5009, 1998.

[106] Velin Z Spassov, Hartmut Luecke, Klaus Gerwert, and Donald Bashford. pka calculations suggest storage of an excess proton in a hydrogen-bonded water network in bacteriorhodopsin. *Journal of molecular biology*, 312(1):203–219, 2001.

[107] Hironari Kamikubo, Toshihiko Oka, Yasushi Imamoto, Fumio Tokunaga, Janos K Lanyi, and Mikio Kataoka. The last phase of the reprotonation switch in bacteriorhodopsin: the transition between the m-type and the n-type protein conformation depends on hydration. *Biochemistry*, 36(40):12282–12287, 1997.

[108] Tobias Weinert, Petr Skopintsev, Daniel James, Florian Dworkowski, Ezequiel Panepucci, Demet Kekilli, Antonia Furrer, Steffen Brünle, Sandra Mous, Dmitry Ozerov, et al. Proton uptake mechanism in bacteriorhodopsin captured by serial synchrotron crystallography. *bioRxiv*, page 576629, 2019.

[109] Nicole L Wagner, Jordan A Greco, Matthew J Ranaghan, and Robert R Birge. Directed evolution of bacteriorhodopsin for applications in bioelectronics. *Journal of The Royal Society Interface*, 10(84):20130197, 2013.

[110] Edward S Boyden, Feng Zhang, Ernst Bamberg, Georg Nagel, and Karl Deisseroth. Millisecond-timescale, genetically targeted optical control of neural activity. *Nature neuroscience*, 8(9):1263, 2005.

[111] Michael Conrad and K-P Zauner. Conformation-based computing: a rational and a recipe. 2003.

[112] Jian Xu, P Bhattacharya, and G Varo. Monolithically integrated bacteriorhodopsin/semiconductor opto-electronic integrated circuit for a biophotoreceiver. *Biosensors and Bioelectronics*, 19(8):885–892, 2004.

[113] Qun Li, Jeffrey A Stuart, Robert R Birge, Jian Xu, Andrew Stickrath, and Pallab Bhattacharya. Photoelectric response of polarization sensitive bacteriorhodopsin films. *Biosensors and Bioelectronics*, 19(8):869–874, 2004.

[114] NA Hampp. Bacteriorhodopsin: mutating a biomaterial into an optoelectronic material. *Applied Microbiology and Biotechnology*, 53(6):633–639, 2000.

[115] Robert R Birge, Nathan B Gillespie, Enrique W Izaguirre, Anakarin Kusnetzow, Albert F Lawrence, Deepak Singh, Q Wang Song, Edward Schmidt, Jeffrey A Stuart, Sukeerthi Seetharaman, et al. Biomolecular electronics: protein-based associative processors and volumetric memories, 1999.

[116] Jeffrey A Stuart, Jack R Tallent, Eric HL Tan, and Robert R Birge. Protein-based volumetric memories. In *Proceedings of Nonvolatile Memory Technology Conference*, pages 45–51. IEEE, 1996.

[117] Jeffrey A Stuart, Duane L Marcy, Kevin J Wise, and Robert R Birge. Volumetric optical memory based on bacteriorhodopsin. *Synthetic metals*, 127(1-3):3–15, 2002.

[118] Nicole L Wagner, Jordan A Greco, and Robert R Birge. Visual restoration using microbial rhodopsins. *Bionanotechnology: Biological Self-Assembly and ts Applications*, pages 205–240, 2013.

[119] Zhongping Chen and Robert R Birge. Protein-based artificial retinas. *Trends in biotechnology*, 11(7):292–300, 1993.

[120] Edward S Boyden. Optogenetics and the future of neuroscience. *Nature neuroscience*, 18(9):1200, 2015.

[121] Feng Zhang, Li-Ping Wang, Martin Brauner, Jana F Liewald, Kenneth Kay, Natalie Watzke, Phillip G Wood, Ernst Bamberg, Georg Nagel, Alexander Gottschalk, et al. Multimodal fast optical interrogation of neural circuitry. *Nature*, 446(7136):633, 2007.

[122] Lizzie Buchen. Neuroscience: Illuminating the brain. *Nature News*, 465(7294):26–28, 2010.

[123] Daniel R Hochbaum, Yongxin Zhao, Samouil L Farhi, Nathan Klapoetke, Christopher A Werley, Vikrant Kapoor, Peng Zou, Joel M Kralj, Dougal Maclaurin, Niklas Smedemark-Margulies, et al. All-optical electrophysiology in mammalian neurons using engineered microbial rhodopsins. *Nature methods*, 11(8):825, 2014.

[124] Hongkang Zhang and Adam E Cohen. Optogenetic approaches to drug discovery in neuroscience and beyond. *Trends in biotechnology*, 35(7):625–639, 2017.

[125] Amy S Chuong, Mitra L Miri, Volker Busskamp, Gillian AC Matthews, Leah C Acker, Andreas T Sørensen, Andrew Young, Nathan C Klapoetke, Mike A Henninger, Suhasa B Kodandaramaiah, et al. Noninvasive optical inhibition with a red-shifted microbial rhodopsin. *Nature neuroscience*, 17(8):1123, 2014.

[126] Brian Y Chow, Xue Han, Allison S Dobry, Xiaofeng Qian, Amy S Chuong, Mingjie Li, Michael A Henninger, Gabriel M Belfort, Yingxi Lin, Patrick E Monahan, et al. High-performance genetically targetable optical neural silencing by light-driven proton pumps. *Nature*, 463(7277):98, 2010.

[127] Yongxian Xu, Peng Zou, and Adam E Cohen. Voltage imaging with genetically encoded indicators. *Current opinion in chemical biology*, 39:1–10, 2017.

[128] Adam M Packer, Botond Roska, and Michael Häusser. Targeting neurons and photons for optogenetics. *Nature neuroscience*, 16(7):805, 2013.

[129] Or A Shemesh, Dimitrii Tanese, Valeria Zampini, Changyang Linghu, Kiryl Piatkevich, Emiliano Ronzitti, Eirini Papagiakoumou, Edward S Boyden, and Valentina Emiliani. Temporally precise single-cell-resolution optogenetics. *Nature neuroscience*, 20(12):1796, 2017.

[130] Frances J Sharom and Paul DW Eckford. Reconstitution of membrane transporters. In *Membrane Transporters*, pages 129–153. Springer, 2003.

[131] Randy B Stockbridge and Ming-Feng Tsai. Lipid reconstitution and recording of recombinant ion channels. In *Methods in enzymology*, volume 556, pages 385–404. Elsevier, 2015.

[132] Hsin-Hui Shen, Trevor Lithgow, and Lisa Martin. Reconstitution of membrane proteins into model membranes: seeking better ways to retain protein activities. *International journal of molecular sciences*, 14(1):1589–1607, 2013.

[133] Shigetoshi Oiki. Planar lipid bilayer method for studying channel molecules. In *Patch Clamp Techniques*, pages 229–275. Springer, 2012.

[134] Michele Zagnoni. Miniaturised technologies for the development of artificial lipid bilayer systems. *Lab on a Chip*, 12(6):1026–1039, 2012.

[135] Shigetoshi Oiki and Masayuki Iwamoto. Lipid bilayers manipulated through monolayer technologies for studies of channel-membrane interplay. *Biological and Pharmaceutical Bulletin*, 41(3):303–311, 2018.

[136] M Montal and P Mueller. Formation of bimolecular membranes from lipid monolayers and a study of their electrical properties. *Proceedings of the National Academy of Sciences*, 69(12):3561–3566, 1972.

[137] Paul Mueller, Donald O Rudin, H Ti Tien, and William C Wescott. Methods for the formation of single bimolecular lipid membranes in aqueous solution. *The journal of physical chemistry*, 67(2):534–535, 1963.

[138] Li-Qun Gu and Ji Wook Shim. Single molecule sensing by nanopores and nanopore devices. *Analyst*, 135(3):441–451, 2010.

[139] Hagan Bayley, Brid Cronin, Andrew Heron, Matthew A Holden, William L Hwang, Ruhma Syeda, James Thompson, and Mark Wallace. Droplet interface bilayers. *Molecular BioSystems*, 4(12):1191–1208, 2008.

[140] Kei Funakoshi, Hiroaki Suzuki, and Shoji Takeuchi. Lipid bilayer formation by contacting monolayers in a microfluidic device for membrane protein analysis. *Analytical chemistry*, 78(24):8169–8174, 2006.

[141] William L Hwang, Matthew A Holden, Steven White, and Hagan Bayley. Electrical behavior of droplet interface bilayer networks: experimental analysis and modeling. *Journal of the American Chemical Society*, 129(38):11854–11864, 2007.

[142] Guru A Venkatesan, Joonho Lee, Amir Barati Farimani, Mohammad Heiranian, C Patrick Collier, Narayana R Aluru, and Stephen A Sarles. Adsorption kinetics dictate monolayer self-assembly for both lipid-in and lipid-out approaches to droplet interface bilayer formation. *Langmuir*, 31(47):12883–12893, 2015.

[143] Matthew A Holden, David Needham, and Hagan Bayley. Functional bionetworks from nanoliter water droplets. *Journal of the American Chemical Society*, 129(27):8650–8655, 2007.

[144] William L Hwang, Min Chen, Brid Cronin, Matthew A Holden, and Hagan Bayley. Asymmetric droplet interface bilayers. *Journal of the American Chemical Society*, 130(18):5878–5879, 2008.

[145] Maxwell Allen-Benton, Heather E Findlay, and Paula J Booth. Probing membrane protein properties using droplet interface bilayers. *Experimental Biology and Medicine*, 244(8):709–720, 2019.

[146] NE Barlow, E Smpokou, MS Friddin, R Macey, IR Gould, C Turnbull, AJ Flemming, NJ Brooks, O Ces, and LMC Barter. Engineering plant membranes using droplet interface bilayers. *Biomicrofluidics*, 11(2):024107, 2017.

[147] Nathan E Barlow, Halim Kusumaatmaja, Ali Salehi-Reyhani, Nick Brooks, Laura MC Barter, Anthony J Flemming, and Oscar Ces. Measuring bilayer surface energy and curvature in asymmetric droplet interface bilayers. *Journal of the Royal Society Interface*, 15(148):20180610, 2018.

[148] Vanessa Restrepo Schild, Michael J Booth, Stuart J Box, Sam N Olof, Kozhinjampara R Mahendran, and Hagan Bayley. Light-patterned current generation in a droplet bilayer array. *Scientific reports*, 7:46585, 2017.

[149] Giovanni Maglia, Andrew J Heron, William L Hwang, Matthew A Holden, Ellina Mikhailova, Qiuhong Li, Stephen Cheley, and Hagan Bayley. Droplet

networks with incorporated protein diodes show collective properties. *Nature nanotechnology*, 4(7):437, 2009.

[150] Stefan Howorka. Building membrane nanopores. *Nature nanotechnology*, 12(7):619, 2017.

[151] Fan Wu and Cheemeng Tan. The engineering of artificial cellular nanosystems using synthetic biology approaches. *Wiley Interdisciplinary Reviews: Nanomedicine and Nanobiotechnology*, 6(4):369–383, 2014.

[152] Bertrand Coste, Bailong Xiao, Jose S Santos, Ruhma Syeda, Jörg Grandl, Kathryn S Spencer, Sung Eun Kim, Manuela Schmidt, Jayanti Mathur, Adrienne E Dubin, et al. Piezo proteins are pore-forming subunits of mechanically activated channels. *Nature*, 483(7388):176, 2012.

[153] Sebastian Leptihn, James R Thompson, J Clive Ellory, Stephen J Tucker, and Mark I Wallace. In vitro reconstitution of eukaryotic ion channels using droplet interface bilayers. *Journal of the American Chemical Society*, 133(24):9370–9375, 2011.

[154] Benjamin Guiselin, Jack O Law, Buddhapriya Chakrabarti, and Halim Kusumaatmaja. Dynamic morphologies and stability of droplet interface bilayers. *Physical review letters*, 120(23):238001, 2018.

[155] Andrew J Heron, James R Thompson, Amy E Mason, and Mark I Wallace. Direct detection of membrane channels from gels using water-in-oil droplet bilayers. *Journal of the American Chemical Society*, 129(51):16042–16047, 2007.

[156] Heather E Findlay, Nicola J Harris, and Paula J Booth. In vitro synthesis of a major facilitator transporter for specific active transport across droplet interface bilayers. *Scientific reports*, 6:39349, 2016.

[157] Prachya Mruetusatorn, Jonathan B Boreyko, Guru A Venkatesan, Stephen A Sarles, Douglas G Hayes, and C Patrick Collier. Dynamic morphologies of microscale droplet interface bilayers. *Soft Matter*, 10(15):2530–2538, 2014.

[158] Jonathan B Boreyko, Prachya Mruetusatorn, Stephen A Sarles, Scott T Retterer, and C Patrick Collier. Evaporation-induced buckling and fission of microscale droplet interface bilayers. *Journal of the American Chemical Society*, 135(15):5545–5548, 2013.

[159] Vetal Borisenko, T Lougheed, J Hesse, E Füreder-Kitzmüller, N Fertig, JC Behrends, GA Woolley, and GJ Schütz. Simultaneous optical and electrical recording of single gramicidin channels. *Biophysical journal*, 84(1):612–622, 2003.

[160] Oskar B Jaggers, Pietro Ridone, Boris Martinac, and Matthew AB Baker. Fluorescence microscopy of piezo1 in droplet hydrogel bilayers. *Channels*, 13(1):102–109, 2019.

[161] James R Thompson, Andrew J Heron, Yusdi Santoso, and Mark I Wallace. Enhanced stability and fluidity in droplet on hydrogel bilayers for measuring membrane protein diffusion. *Nano letters*, 7(12):3875–3878, 2007.

[162] Graham Taylor, Mary-Anne Nguyen, Subhadeep Koner, Eric Freeman, C Patrick Collier, and Stephen A Sarles. Electrophysiological interrogation

of asymmetric droplet interface bilayers reveals surface-bound alamethicin induces lipid flip-flop. *Biochimica et Biophysica Acta (BBA)-Biomembranes*, 1861(1):335–343, 2019.

[163] Gerd Binnig, Heinrich Rohrer, Ch Gerber, and Edmund Weibel. Surface studies by scanning tunneling microscopy. *Physical review letters*, 49(1):57, 1982.

[164] H Fuchs, H Hölscher, and A Schirmeisen. Scanning probe microscopy. 2005.

[165] An NSF Nanoscale Science and Engineering Center. Protein based retinal implants. `https://teachers.stanford.edu/activities/SPMReference/SPMReference.pdf`.

[166] Bruker. Industry-leading surface and dimensional analysis tools. `https://www.bruker.com/products/surface-and-dimensional-analysis.html`.

[167] David P Allison, Ninell P Mortensen, Claretta J Sullivan, and Mitchel J Doktycz. Atomic force microscopy of biological samples. *Wiley Interdisciplinary Reviews: Nanomedicine and Nanobiotechnology*, 2(6):618–634, 2010.

[168] Shaoyang Liu and Yifen Wang. Application of afm in microbiology: a review. *Scanning*, 32(2):61–73, 2010.

[169] Olivia Berthoumieu, Amol V Patil, Wang Xi, Lubica Aslimovska, Jason J Davis, and Anthony Watts. Molecular scale conductance photoswitching in engineered bacteriorhodopsin. *Nano letters*, 12(2):899–903, 2012.

[170] Kai-Chih Chang, Yu-Wei Chiang, Chin-Hao Yang, and Je-Wen Liou. Atomic force microscopy in biology and biomedicine. *Tzu Chi Medical Journal*, 24(4):162–169, 2012.

[171] Yuki Suzuki, Yuko Yoshikawa, Shige H Yoshimura, Kenichi Yoshikawa, and Kunio Takeyasu. Unraveling dna dynamics using atomic force microscopy. *Wiley Interdisciplinary Reviews: Nanomedicine and Nanobiotechnology*, 3(6):574–588, 2011.

[172] Jacob N Israelachvili. *Intermolecular and surface forces*. Academic press, 2015.

[173] Yves F Dufrêne, Toshio Ando, Ricardo Garcia, David Alsteens, David Martinez-Martin, Andreas Engel, Christoph Gerber, and Daniel J Müller. Imaging modes of atomic force microscopy for application in molecular and cell biology. *Nature nanotechnology*, 12(4):295, 2017.

[174] Gerd Binnig, Calvin F Quate, and Ch Gerber. Atomic force microscope. *Physical review letters*, 56(9):930, 1986.

[175] Ozgur Sahin, Sergei Magonov, Chanmin Su, Calvin F Quate, and Olav Solgaard. An atomic force microscope tip designed to measure time-varying nanomechanical forces. *Nature nanotechnology*, 2(8):507, 2007.

[176] Justin Legleiter. The effect of drive frequency and set point amplitude on tapping forces in atomic force microscopy: simulation and experiment. *Nanotechnology*, 20(24):245703, 2009.

[177] Veeco Dimension. 3100 afm user manual. https://www.nist.gov/sites/default/files/documents/cnst/nanofab/Veeco_Dimension3100_AFM_USERMANUAL_v1.pdf.

[178] Frédéric Eghiaian, Felix Rico, Adai Colom, Ignacio Casuso, and Simon Scheuring. High-speed atomic force microscopy: Imaging and force spectroscopy. *FEBS letters*, 588(19):3631–3638, 2014.

[179] Hans-Jürgen Butt, Brunero Cappella, and Michael Kappl. Force measurements with the atomic force microscope: Technique, interpretation and applications. *Surface science reports*, 59(1-6):1–152, 2005.

[180] Ricardo Garcia and Elena T Herruzo. The emergence of multifrequency force microscopy. *Nature nanotechnology*, 7(4):217, 2012.

[181] Frank A Schabert, Christian Henn, and Andreas Engel. Native escherichia coli ompf porin surfaces probed by atomic force microscopy. *Science*, 268(5207):92–94, 1995.

[182] Daniel J Müller, Galen M Hand, Andreas Engel, and Gina E Sosinsky. Conformational changes in surface structures of isolated connexin 26 gap junctions. *The EMBO journal*, 21(14):3598–3607, 2002.

[183] Andreas Engel and Daniel J Müller. Observing single biomolecules at work with the atomic force microscope. *Nature Structural & Molecular Biology*, 7(9):715, 2000.

[184] Gajendra S Shekhawat and Vinayak P Dravid. Nanoscale imaging of buried structures via scanning near-field ultrasound holography. *Science*, 310(5745):89–92, 2005.

[185] Laurene Tetard, Ali Passian, Katherine T Venmar, Rachel M Lynch, Brynn H Voy, Gajendra Shekhawat, Vinayak P Dravid, and Thomas Thundat. Imaging nanoparticles in cells by nanomechanical holography. *Nature nanotechnology*, 3(8):501, 2008.

[186] Z Ye and X Zhao. Phase imaging atomic force microscopy in the characterization of biomaterials. *Journal of microscopy*, 238(1):27–35, 2010.

[187] Clemens Möller, Mike Allen, Virgil Elings, Andreas Engel, and Daniel J Müller. Tapping-mode atomic force microscopy produces faithful high-resolution images of protein surfaces. *Biophysical journal*, 77(2):1150–1158, 1999.

[188] Toshio Ando. High-speed atomic force microscopy and its future prospects. *Biophysical reviews*, 10(2):285–292, 2018.

[189] Daisuke Yamamoto, Takayuki Uchihashi, Noriyuki Kodera, Hayato Yamashita, Shingo Nishikori, Teru Ogura, Mikihiro Shibata, and Toshio Ando. High-speed atomic force microscopy techniques for observing dynamic biomolecular processes. In *Methods in enzymology*, volume 475, pages 541–564. Elsevier, 2010.

[190] Toshio Ando, Takayuki Uchihashi, and Takeshi Fukuma. High-speed atomic force microscopy for nano-visualization of dynamic biomolecular processes. *Progress in Surface Science*, 83(7-9):337–437, 2008.

[191] Noriyuki Kodera, Hayato Yamashita, and Toshio Ando. Active damping of the scanner for high-speed atomic force microscopy. *Review of scientific instruments*, 76(5):053708, 2005.

[192] Toshio Ando, Takayuki Uchihashi, and Simon Scheuring. Filming biomolecular processes by high-speed atomic force microscopy. *Chemical reviews*, 114(6):3120–3188, 2014.

[193] Toshio Ando, Noriyuki Kodera, Eisuke Takai, Daisuke Maruyama, Kiwamu Saito, and Akitoshi Toda. A high-speed atomic force microscope for studying biological macromolecules. *Proceedings of the National Academy of Sciences*, 98(22):12468–12472, 2001.

[194] Mikihiro Shibata, Hayato Yamashita, Takayuki Uchihashi, Hideki Kandori, and Toshio Ando. High-speed atomic force microscopy shows dynamic molecular processes in photoactivated bacteriorhodopsin. *Nature nanotechnology*, 5(3):208, 2010.

[195] Noriyuki Kodera, Daisuke Yamamoto, Ryoki Ishikawa, and Toshio Ando. Video imaging of walking myosin v by high-speed atomic force microscopy. *Nature*, 468(7320):72, 2010.

[196] Ignacio Casuso, Jonathan Khao, Mohamed Chami, Perrine Paul-Gilloteaux, Mohamed Husain, Jean-Pierre Duneau, Henning Stahlberg, James N Sturgis, and Simon Scheuring. Characterization of the motion of membrane proteins using high-speed atomic force microscopy. *Nature nanotechnology*, 7(8):525, 2012.

[197] George R Heath and Simon Scheuring. High-speed afm height spectroscopy reveals μs-dynamics of unlabeled biomolecules. *Nature communications*, 9(1):4983, 2018.

[198] F Gołek, P Mazur, Z Ryszka, and S Zuber. Afm image artifacts. *Applied Surface Science*, 304:11–19, 2014.

[199] FM Ohnesorge. Intricate stepline artifact can mimic true atomic resolution in atomic force microscopy. *Physical Review B*, 61(8):R5121, 2000.

[200] Natalia Starosina Paul West. A guide to afm image artifact. `https://www.physik.uni-wuerzburg.de/fileadmin/physik-fpraktikum/_imported/fileadmin/11999999/AFM/AFM_part3.pdf`.

[201] Niklaus Johner, Sayan Mondal, Giulia Morra, Martin Caffrey, Harel Weinstein, and George Khelashvili. Protein and lipid interactions driving molecular mechanisms of in meso crystallization. *Journal of the American Chemical Society*, 136(8):3271–3284, 2014.

[202] Vadim Cherezov, Hannan Fersi, and Martin Caffrey. Crystallization screens: compatibility with the lipidic cubic phase for in meso crystallization of membrane proteins. *Biophysical journal*, 81(1):225–242, 2001.

[203] Nagayuki Hasegawa, Hideyuki Jonotsuka, Kunio Miki, and Kazuki Takeda. X-ray structure analysis of bacteriorhodopsin at 1.3 å resolution. *Scientific reports*, 8(1):13123, 2018.

[204] W Shihoya, K Inoue, M Singh, M Konno, S Hososhima, K Yamashita, K Ikeda, A Higuchi, T Izume, S Okazaki, et al. Crystal structure of heliorhodopsin. *Nature*, 2019.

[205] Martin Caffrey. A comprehensive review of the lipid cubic phase or in meso method for crystallizing membrane and soluble proteins and complexes. *Acta Crystallographica Section F: Structural Biology Communications*, 71(1):3–18, 2015.

[206] Vadim Cherezov and Martin Caffrey. Membrane protein crystallization in lipidic mesophases. a mechanism study using x-ray microdiffraction. *Faraday discussions*, 136:195–212, 2007.

[207] Martin Caffrey. On the mechanism of membrane protein crystallization in lipidic mesophases. *Crystal Growth and Design*, 8(12):4244–4254, 2008.

[208] Vadim Cherezov and Martin Caffrey. Picolitre-scale crystallization of membrane proteins. *Journal of applied crystallography*, 39(4):604–606, 2006.

[209] Vadim Cherezov, Jeffrey Clogston, Miroslav Z Papiz, and Martin Caffrey. Room to move: crystallizing membrane proteins in swollen lipidic mesophases. *Journal of molecular biology*, 357(5):1605–1618, 2006.

[210] V Cherezov, E Yamashita, Wei Liu, M Zhalnina, WA Cramer, and M Caffrey. In meso structure of the cobalamin transporter, btub, at 1.95 å resolution. *Journal of molecular biology*, 364(4):716–734, 2006.

[211] Vadim Cherezov, Wei Liu, Jeremy P Derrick, Binquan Luan, Aleksei Aksimentiev, Vsevolod Katritch, and Martin Caffrey. In meso crystal structure and docking simulations suggest an alternative proteoglycan binding site in the opca outer membrane adhesin. *Proteins: Structure, Function, and Bioinformatics*, 71(1):24–34, 2008.

[212] Isabel Moraes, Gwyndaf Evans, Juan Sanchez-Weatherby, Simon Newstead, and Patrick D Shaw Stewart. Membrane protein structure determination—the next generation. *Biochimica et Biophysica Acta (BBA)-Biomembranes*, 1838(1):78–87, 2014.

[213] Keiichi Inoue, Takashi Tsukamoto, Kazumi Shimono, Yuto Suzuki, Seiji Miyauchi, Shigehiko Hayashi, Hideki Kandori, and Yuki Sudo. Converting a light-driven proton pump into a light-gated proton channel. *Journal of the American Chemical Society*, 137(9):3291–3299, 2015.

[214] Emily A Ferenczi, Johannes Vierock, Kyoko Atsuta-Tsunoda, Satoshi P Tsunoda, Charu Ramakrishnan, Christopher Gorini, Kimberly Thompson, Soo Yeun Lee, Andre Berndt, Chelsey Perry, et al. Optogenetic approaches addressing extracellular modulation of neural excitability. *Scientific reports*, 6:23947, 2016.

[215] Ming Ming, Miao Lu, Sergei P Balashov, Thomas G Ebrey, Qingguo Li, and Jiandong Ding. ph dependence of light-driven proton pumping by an archaerhodopsin from tibet: comparison with bacteriorhodopsin. *Biophysical journal*, 90(9):3322–3332, 2006.

[216] Antoinette M Dummer, Jessica C Bonsall, Jacob B Cihla, Stephanie M Lawry, Gabriela C Johnson, and Ronald F Peck. Bacterioopsin-mediated regulation of bacterioruberin biosynthesis in halobacterium salinarum. *Journal of bacteriology*, 193(20):5658–5667, 2011.

[217] Henry Van Den Bedem and James S Fraser. Integrative, dynamic structural biology at atomic resolution—it's about time. *Nature methods*, 12(4):307, 2015.

[218] Keiko Yoshimura and Tsutomu Kouyama. Structural role of bacterioruberin in the trimeric structure of archaerhodopsin-2. *Journal of molecular biology*, 375(5):1267–1281, 2008.

[219] SC Kushwaha, M Kates, and W Stoeckenius. Comparison of purple membrane from halobacterium cutirubrum and halobacterium halobium. *Biochimica et Biophysica Acta (BBA)-Biomembranes*, 426(4):703–710, 1976.

[220] Yasuo Mukohata, Kunio Ihara, Koichi Uegaki, Yukiya Mlyashita, and Yasuo Sugiyama. Australian halobacteria and their retinal-protein ion pumps. *Photochemistry and photobiology*, 54(6):1039–1045, 1991.

[221] Sergei P Balashov, Eleonora S Imasheva, and Janos K Lanyi. Induced chirality of the light-harvesting carotenoid salinixanthin and its interaction with the retinal of xanthorhodopsin. *Biochemistry*, 45(36):10998–11004, 2006.

[222] Dougal Maclaurin, Veena Venkatachalam, Hohjai Lee, and Adam E Cohen. Mechanism of voltage-sensitive fluorescence in a microbial rhodopsin. *Proceedings of the National Academy of Sciences*, 110(15):5939–5944, 2013.

[223] EP Lukashev, R Govindjee1, Masahiro Kono1, TG Ebrey†, 1, Yasuo Sugiyama2, and Yasuo Mukohata2. ph dependence of the absorption spectra and photochemical transformations of the archaerhodopsins. *Photochemistry and photobiology*, 60(1):69–75, 1994.

[224] Erica C Saint Clair, John I Ogren, Sergey Mamaev, Daniel Russano, Joel M Kralj, and Kenneth J Rothschild. Near-ir resonance raman spectroscopy of archaerhodopsin 3: effects of transmembrane potential. *The Journal of Physical Chemistry B*, 116(50):14592–14601, 2012.

[225] Erica C Saint Clair, John I Ogren, Sergey Mamaev, Joel M Kralj, and Kenneth J Rothschild. Conformational changes in the archaerhodopsin-3 proton pump: detection of conserved strongly hydrogen bonded water networks. *Journal of biological physics*, 38(1):153–168, 2012.

[226] Nobuo Enami, Keiko Yoshimura, Midori Murakami, Hideo Okumura, Kunio Ihara, and Tsutomu Kouyama. Crystal structures of archaerhodopsin-1 and-2: Common structural motif in archaeal light-driven proton pumps. *Journal of molecular biology*, 358(3):675–685, 2006.

[227] Steven O Smith, Huub JM De Groot, Ronald Gebhard, Jacques ML Courtin, Johan Lugtenburg, Judith Herzfeld, and Robert G Griffin. Structure and protein environment of the retinal chromophore in light-and dark-adapted bacteriorhodopsin studied by solid-state nmr. *Biochemistry*, 28(22):8897–8904, 1989.

[228] Taichi Nishikawa, Midori Murakami, and Tsutomu Kouyama. Crystal structure of the 13-cis isomer of bacteriorhodopsin in the dark-adapted state. *Journal of molecular biology*, 352(2):319–328, 2005.

[229] P Scherrer, MK Mathew, W Sperling, and Walther Stoeckenius. Retinal isomer ratio in dark-adapted purple membrane and bacteriorhodopsin monomers. *Biochemistry*, 28(2):829–834, 1989.

[230] Kunio Ihara, Tomohiro Amemiya, Yukiya Miyashita, and Yasuo Mukohata. Met-145 is a key residue in the dark adaptation of bacteriorhodopsin homologs. *Biophysical journal*, 67(3):1187–1191, 1994.

[231] Heiko Patzelt, Bernd Simon, Brigitte Kessler, Ronald Kühne, Peter Schmieder, Dieter Oesterhelt, Hartmut Oschkinat, et al. The structures of the active center in dark-adapted bacteriorhodopsin by solution-state nmr spectroscopy. *Proceedings of the National Academy of Sciences*, 99(15):9765–9770, 2002.

[232] JM Griffiths, AE Bennett, M Engelhard, F Siebert, J Raap, J Lugtenburg, J Herzfeld, and RG Griffin. Structural investigation of the active site in bacteriorhodopsin: geometric constraints on the roles of asp-85 and asp-212 in the proton-pumping mechanism from solid state nmr. *Biochemistry*, 39(2):362–371, 2000.

[233] Eriko Nango, Minoru Kubo, and So Iwata. A three-dimensional movie of structural changes in bacteriorhodopsin captured by x-ray free electron lasers. *Hoshako*, 30(5):218–227, 2017.

[234] W Curtis Johnson. Analyzing protein circular dichroism spectra for accurate secondary structures. *Proteins: Structure, Function, and Bioinformatics*, 35(3):307–312, 1999.

[235] Lee Whitmore and Bonnie A Wallace. Protein secondary structure analyses from circular dichroism spectroscopy: methods and reference databases. *Biopolymers: Original Research on Biomolecules*, 89(5):392–400, 2008.

[236] IGOR Pro website for HS-AFM analysis. High-speed afm analysis. `https://www.wavemetrics.com`, 2019.

[237] James Foadi, Pierre Aller, Yilmaz Alguel, Alex Cameron, Danny Axford, Robin L Owen, Wes Armour, David G Waterman, So Iwata, and Gwyndaf Evans. Clustering procedures for the optimal selection of data sets from multiple crystals in macromolecular crystallography. *Acta Crystallographica Section D: Biological Crystallography*, 69(8):1617–1632, 2013.

[238] Airlie J McCoy, Ralf W Grosse-Kunstleve, Paul D Adams, Martyn D Winn, Laurent C Storoni, and Randy J Read. Phaser crystallographic software. *Journal of applied crystallography*, 40(4):658–674, 2007.

[239] Anton Barty, Richard A Kirian, Filipe RNC Maia, Max Hantke, Chun Hong Yoon, Thomas A White, and Henry Chapman. Cheetah: software for high-throughput reduction and analysis of serial femtosecond x-ray diffraction data. *Journal of applied crystallography*, 47(3):1118–1131, 2014.

[240] Thomas A White, Richard A Kirian, Andrew V Martin, Andrew Aquila, Karol Nass, Anton Barty, and Henry N Chapman. Crystfel: a software suite for

snapshot serial crystallography. *Journal of applied crystallography*, 45(2):335–341, 2012.

[241] Dieter Oesterhelt and Walther Stoeckenius. Rhodopsin-like protein from the purple membrane of halobacterium halobium. *Nature new biology*, 233(39):149, 1971.

[242] E Karnaukhova, KL Schey, and RK Crouch. Circular dichroism and cross-linking studies of bacteriorhodopsin mutants. *Amino acids*, 30(1):17–23, 2006.

[243] Peter Nollert, Antoine Royant, Eva Pebay-Peyroula, and Ehud M Landau. Detergent-free membrane protein crystallization. *FEBS letters*, 457(2):205–208, 1999.

[244] Yongdong Jin, Noga Friedman, Mordechai Sheves, Tao He, and David Cahen. Bacteriorhodopsin (br) as an electronic conduction medium: Current transport through br-containing monolayers. *Proceedings of the National Academy of Sciences*, 103(23):8601–8606, 2006.

[245] Imre Kovács, G Ulrich Nienhaus, Robert Philipp, and Aihua Xie. Pressure effects on the dark-adaptation of bacteriorhodopsin. *Biophysical journal*, 64(4):1187–1193, 1993.

[246] T Kouyama, RA Bogomolni, and W Stoeckenius. Photoconversion from the light-adapted to the dark-adapted state of bacteriorhodopsin. *Biophysical journal*, 48(2):201–208, 1985.

[247] M Tsuda and TG Ebrey. Effect of high pressure on the absorption spectrum and isomeric composition of bacteriorhodopsin. *Biophysical journal*, 30(1):149–157, 1980.

[248] Marcel Baer, Gerald Mathias, I-Feng W Kuo, Douglas J Tobias, Christopher J Mundy, and Dominik Marx. Spectral signatures of the pentagonal water cluster in bacteriorhodopsin. *ChemPhysChem*, 9(18):2703–2707, 2008.

[249] Lin Tang, Qing'an Sun, Qingguo Li, Yibo Huang, Qingqing Wei, Yi Zhang, Jun Hu, Zhihong Zhang, Minqian Li, and Fujia Yang. Imaging bacteriorhodopsinlike molecules of claretmembranes from tibet halobacteria xz515 by atomic force microscope. *Chinese Science Bulletin*, 46(22):1897, 2001.

[250] Hayato Yamashita, Keiichi Inoue, Mikihiro Shibata, Takayuki Uchihashi, Jun Sasaki, Hideki Kandori, and Toshio Ando. Role of trimer–trimer interaction of bacteriorhodopsin studied by optical spectroscopy and high-speed atomic force microscopy. *Journal of structural biology*, 184(1):2–11, 2013.

[251] Mikihiro Shibata, Keiichi Inoue, Kento Ikeda, Masae Konno, Manish Singh, Chihiro Kataoka, Rei Abe-Yoshizumi, Hideki Kandori, and Takayuki Uchihashi. Oligomeric states of microbial rhodopsins determined by high-speed atomic force microscopy and circular dichroic spectroscopy. *Scientific reports*, 8(1):8262, 2018.

[252] Zhen Cao, Xiaoyan Ding, Bo Peng, Yingchun Zhao, Jiandong Ding, Anthony Watts, and Xin Zhao. Novel expression and characterization of a light driven

proton pump archaerhodopsin 4 in a halobacterium salinarum strain. *Biochimica et Biophysica Acta (BBA)-Bioenergetics*, 1847(4-5):390–398, 2015.

[253] Cecilia Wickstrand, Przemyslaw Nogly, Eriko Nango, So Iwata, Jörg Standfuss, and Richard Neutze. Bacteriorhodopsin: structural insights revealed using x-ray lasers and synchrotron radiation. *Annual review of biochemistry*, 88, 2019.

[254] Richard Neutze. Opportunities and challenges for time-resolved studies of protein structural dynamics at x-ray free-electron lasers. *Philosophical Transactions of the Royal Society B: Biological Sciences*, 369(1647):20130318, 2014.

[255] Anton Barty. Single molecule imaging using x-ray free electron lasers. *Current opinion in structural biology*, 40:186–194, 2016.

[256] A Aquila, A Barty, C Bostedt, S Boutet, G Carini, D DePonte, P Drell, S Doniach, KH Downing, T Earnest, et al. The linac coherent light source single particle imaging road map. *Structural Dynamics*, 2(4):041701, 2015.

[257] Michael J Bogan, W Henry Benner, Sébastien Boutet, Urs Rohner, Matthias Frank, Anton Barty, M Marvin Seibert, Filipe Maia, Stefano Marchesini, Saša Bajt, et al. Single particle x-ray diffractive imaging. *Nano letters*, 8(1):310–316, 2008.

[258] Janos Hajdu. Potential for biomolecular imaging with femtosecond x-ray pulses. In *International Conference on Ultrafast Phenomena*, page MC1. Optical Society of America, 2002.

[259] Linda C Johansson, Benjamin Stauch, Andrii Ishchenko, and Vadim Cherezov. A bright future for serial femtosecond crystallography with xfels. *Trends in biochemical sciences*, 42(9):749–762, 2017.

[260] Przemyslaw Nogly, Tobias Weinert, Daniel James, Sergio Carbajo, Dmitry Ozerov, Antonia Furrer, Dardan Gashi, Veniamin Borin, Petr Skopintsev, Kathrin Jaeger, et al. Retinal isomerization in bacteriorhodopsin captured by a femtosecond x-ray laser. *Science*, 361(6398):eaat0094, 2018.

[261] Minoru Kubo, Eriko Nango, Kensuke Tono, Tetsunari Kimura, Shigeki Owada, Changyong Song, Fumitaka Mafuné, Ken Miyajima, Yoshihiro Takeda, Jun-ya Kohno, et al. Nanosecond pump–probe device for time-resolved serial femtosecond crystallography developed at sacla. *Journal of synchrotron radiation*, 24(5):1086–1091, 2017.

[262] High speed atomic force microscopy video of ar3 trimer movement upon illumination. `https://drive.google.com/drive/my-drive`.

[263] Harald Otto, Thomas Marti, Martin Holz, Tatsushi Mogi, Manfred Lindau, H Gobind Khorana, and Maarten P Heyn. Aspartic acid-96 is the internal proton donor in the reprotonation of the schiff base of bacteriorhodopsin. *Proceedings of the National Academy of Sciences*, 86(23):9228–9232, 1989.

[264] Mikihiro Shibata and Hideki Kandori. Ftir studies of internal water molecules in the schiff base region of bacteriorhodopsin. *Biochemistry*, 44(20):7406–7413, 2005.

[265] Hiroki Mutoh and Thomas Knöpfel. Probing neuronal activities with genetically encoded optical indicators: from a historical to a forward-looking perspective. *Pflügers Archiv-European Journal of Physiology*, 465(3):361–371, 2013.

[266] Joel M Kralj, Adam D Douglass, Daniel R Hochbaum, Dougal Maclaurin, and Adam E Cohen. Optical recording of action potentials in mammalian neurons using a microbial rhodopsin. *Nature methods*, 9(1):90, 2012.

[267] Dmitry Bratanov, Taras Balandin, Ekaterina Round, Vitaly Shevchenko, Ivan Gushchin, Vitaly Polovinkin, Valentin Borshchevskiy, and Valentin Gordeliy. An approach to heterologous expression of membrane proteins. the case of bacteriorhodopsin. *PloS one*, 10(6):e0128390, 2015.

[268] John Y Lin, Michael Z Lin, Paul Steinbach, and Roger Y Tsien. Characterization of engineered channelrhodopsin variants with improved properties and kinetics. *Biophysical journal*, 96(5):1803–1814, 2009.

[269] Ian D Dundas and Helge Larsen. The physiological role of the carotenoid pigments of halobacterium salinarium. *Archiv für Mikrobiologie*, 44(3):233–239, 1962.

[270] Michael J Booth, Vanessa Restrepo Schild, Florence G Downs, and Hagan Bayley. Functional aqueous droplet networks. *Molecular BioSystems*, 13(9):1658–1691, 2017.

[271] Audrey Fischer, Matthew A Holden, Brad L Pentelute, and R John Collier. Ultrasensitive detection of protein translocated through toxin pores in

droplet-interface bilayers. *Proceedings of the National Academy of Sciences*, 108(40):16577–16581, 2011.

[272] Gilbert G Privé. Detergents for the stabilization and crystallization of membrane proteins. *Methods*, 41(4):388–397, 2007.

[273] Andrea Dolfi, Francesco Tadini-Buoninsegni, Maria Rosa Moncelli, and Rolando Guidelli. Photocurrents generated by bacteriorhodopsin adsorbed on thiol/lipid bilayers supported by mercury. *Langmuir*, 18(16):6345–6355, 2002.

[274] E Bamberg, H-J Apell, NA Dencher, W Sperling, H Stieve, and P Läuger. Photocurrents generated by bacteriorhodopsin on planar bilayer membranes. *Biophysics of structure and mechanism*, 5(4):277–292, 1979.

[275] Ruhma Syeda, Matthew A Holden, William L Hwang, and Hagan Bayley. Screening blockers against a potassium channel with a droplet interface bilayer array. *Journal of the American Chemical Society*, 130(46):15543–15548, 2008.

[276] P Saeedi, J Mohammadian Moosaabadi, S Sina Sebtahmadi, J Fallah Mehrabadi, M Behmanesh, and S Mekhilef. Potential applications of bacteriorhodopsin mutants. *Bioengineered*, 3(6):326–328, 2012.

[277] Angelo Homayoun All, Xiao Zeng, Daniel Boon Loong Teh, Zhigao Yi, Ankshita Prasad, Toru Ishizuka, Nitish Thakor, Yawo Hiromu, and Xiaogang Liu. Expanding the toolbox of upconversion nanoparticles for in vivo optogenetics and neuromodulation. *Advanced Materials*, page 1803474, 2019.

[278] John Y Lin. A user's guide to channelrhodopsin variants: features, limitations and future developments. *Experimental physiology*, 96(1):19–25, 2011.

[279] Sven Geibel, Thomas Friedrich, Pal Ormos, Phillip G Wood, Georg Nagel, and Ernst Bamberg. The voltage-dependent proton pumping in bacteriorhodopsin is characterized by optoelectric behavior. *Biophysical Journal*, 81(4):2059–2068, 2001.

[280] G Nagel, B Kelety, B Möckel, G Büldt, and E Bamberg. Voltage dependence of proton pumping by bacteriorhodopsin is regulated by the voltage-sensitive ratio of m1 to m2. *Biophysical journal*, 74(1):403–412, 1998.

[281] Ricardo CH del Rosario, Christoph Oppawsky, Jörg Tittor, and Dieter Oesterhelt. Modeling the membrane potential generation of bacteriorhodopsin. *Mathematical biosciences*, 225(1):68–80, 2010.

[282] Klára Magyari, Zoltán Bálint, Viorica Simon, and György Váró. The photochemical reaction cycle of retinal reconstituted bacteriorhodopsin. *Journal of Photochemistry and Photobiology B: Biology*, 85(2):140–144, 2006.

[283] YD Jin, Noga Friedman, Mordechai Sheves, and David Cahen. Bacteriorhodopsin-monolayer-based planar metal–insulator–metal junctions via biomimetic vesicle fusion: Preparation, characterization, and bio-optoelectronic characteristics. *Advanced Functional Materials*, 17(8):1417–1428, 2007.

[284] Daan Brinks, Yoav Adam, Simon Kheifets, and Adam E Cohen. Painting with rainbows: patterning light in space, time, and wavelength for multiphoton

optogenetic sensing and control. *Accounts of chemical research*, 49(11):2518–2526, 2016.

[285] CL Makino, TW Kraft, RA Mathies, J Lugtenburg, ME Miley, R Van der Steen, and DA Baylor. Effects of modified chromophores on the spectral sensitivity of salamander, squirrel and macaque cones. *The Journal of physiology*, 424(1):545–560, 1990.

[286] Nathan C Klapoetke, Yasunobu Murata, Sung Soo Kim, Stefan R Pulver, Amanda Birdsey-Benson, Yong Ku Cho, Tania K Morimoto, Amy S Chuong, Eric J Carpenter, Zhijian Tian, et al. Independent optical excitation of distinct neural populations. *Nature methods*, 11(3):338, 2014.

[287] Oded Béja, Elena N Spudich, John L Spudich, Marion Leclerc, and Edward F DeLong. Proteorhodopsin phototrophy in the ocean. *Nature*, 411(6839):786, 2001.

[288] Martin KM Engqvist, R Scott McIsaac, Peter Dollinger, Nicholas C Flytzanis, Michael Abrams, Stanford Schor, and Frances H Arnold. Directed evolution of gloeobacter violaceus rhodopsin spectral properties. *Journal of molecular biology*, 427(1):205–220, 2015.

[289] So Young Kim, Stephen A Waschuk, Leonid S Brown, and Kwang-Hwan Jung. Screening and characterization of proteorhodopsin color-tuning mutations in escherichia coli with endogenous retinal synthesis. *Biochimica et Biophysica Acta (BBA)-Bioenergetics*, 1777(6):504–513, 2008.

[290] Yuki Sudo, Ayako Okazaki, Hikaru Ono, Jin Yagasaki, Seiya Sugo, Motoshi Kamiya, Louisa Reissig, Keiichi Inoue, Kunio Ihara, Hideki Kandori, et al. A blue-shifted light-driven proton pump for neural silencing. *Journal of Biological Chemistry*, 288(28):20624–20632, 2013.

[291] R Scott McIsaac, Martin KM Engqvist, Timothy Wannier, Adam Z Rosenthal, Lukas Herwig, Nicholas C Flytzanis, Eleonora S Imasheva, Janos K Lanyi, Sergei P Balashov, Viviana Gradinaru, et al. Directed evolution of a far-red fluorescent rhodopsin. *Proceedings of the National Academy of Sciences*, 111(36):13034–13039, 2014.

[292] Jia Wu, Dewang Ma, Yazhuo Wang, Ming Ming, Sergei P Balashov, and Jiandong Ding. Efficient approach to determine the p k a of the proton release complex in the photocycle of retinal proteins. *The Journal of Physical Chemistry B*, 113(13):4482–4491, 2009.

[293] Saurav Misra, Rajni Govindjee, Thomas G Ebrey, N Chen, J-X Ma, and Rosalie K Crouch. Proton uptake and release are rate-limiting steps in the photocycle of the bacteriorhodopsin mutant e204q. *Biochemistry*, 36(16):4875–4883, 1997.

[294] Larry JW Miercke, Mary C Betlach, Alok K Mitra, Richard F Shand, Susan K Fong, and Robert M Stroud. Wild-type and mutant bacteriorhodopsins d85n, d96n, and r82q: purification to homogeneity, ph dependence of pumping and electron diffraction. *Biochemistry*, 30(12):3088–3098, 1991.

[295] Hazime Saitô, Satoru Yamaguchi, Keiji Ogawa, Satoru Tuzi, Mercedes Márquez, Carolina Sanz, and Esteve Padrós. Glutamic acid residues of bacteriorhodopsin at the extracellular surface as determinants for conformation and dynamics as revealed by site-directed solid-state 13c nmr. *Biophysical journal*, 86(3):1673–1681, 2004.

[296] Hartmut Luecke, Brigitte Schobert, Jason Stagno, Eleonora S Imasheva, Jennifer M Wang, Sergei P Balashov, and Janos K Lanyi. Crystallographic structure of xanthorhodopsin, the light-driven proton pump with a dual chromophore. *Proceedings of the National Academy of Sciences*, 105(43):16561–16565, 2008.

[297] Oligo design tools. `https://www.thermofisher.com/uk/en/home/life-science/oligonucleotides-primers-probes-genes/custom-dna-oligos/oligo-design-tools.html`.

[298] John Y Lin, Per Magne Knutsen, Arnaud Muller, David Kleinfeld, and Roger Y Tsien. Reachr: a red-shifted variant of channelrhodopsin enables deep transcranial optogenetic excitation. *Nature neuroscience*, 16(10):1499, 2013.

[299] John E Cronan. Escherichia coli as an experimental organism. *eLS*, 2001.

[300] Yuri Mukai, Naoki Kamo, and Shigeki Mitaku. Light-induced denaturation of bacteriorhodopsin solubilized by octyl-β-glucoside. *Protein engineering*, 12(9):755–759, 1999.

[301] Jack Kyte and Russell F Doolittle. A simple method for displaying the hydropathic character of a protein. *Journal of molecular biology*, 157(1):105–132, 1982.

[302] Federico Melaccio, Nicolas Ferré, and Massimo Olivucci. Quantum chemical modeling of rhodopsin mutants displaying switchable colors. *Physical Chemistry Chemical Physics*, 14(36):12485–12495, 2012.

[303] Srividya Ganapathy, Svenja Kratz, Que Chen, Klaas J Hellingwerf, Huub JM de Groot, Kenneth J Rothschild, and Willem J de Grip. Redshifted and near-infrared active analog pigments based upon archaerhodopsin-3. *Photochemistry and photobiology*, 2019.

[304] H Gobind Khorana. Two light-transducing membrane proteins: bacteriorhodopsin and the mammalian rhodopsin. *Proceedings of the National Academy of Sciences of the United States of America*, 90(4):1166, 1993.

[305] Janos K Lanyi. Proton translocation mechanism and energetics in the light-driven pump bacteriorhodopsin. *Biochimica et Biophysica Acta (BBA)-Bioenergetics*, 1183(2):241–261, 1993.

[306] Leonid S Brown and Kwang-Hwan Jung. Bacteriorhodopsin-like proteins of eubacteria and fungi: the extent of conservation of the haloarchaeal proton-pumping mechanism. *Photochemical & Photobiological Sciences*, 5(6):538–546, 2006.

[307] Naoki Kamo, Tsuyoshi Hashiba, Takashi Kikukawa, Tsunehisa Araiso, Kunio Ihara, and Toshifumi Nara. A light-driven proton pump from haloterrigena

turkmenica: functional expression in escherichia coli membrane and coupling with a h+ co-transporter. *Biochemical and biophysical research communications*, 341(2):285–290, 2006.

[308] Alain FL Creemers, Suzanne Kiihne, Petra HM Bovee-Geurts, Willem J DeGrip, Johan Lugtenburg, and Huub JM de Groot. 1h and 13c mas nmr evidence for pronounced ligand–protein interactions involving the ionone ring of the retinylidene chromophore in rhodopsin. *Proceedings of the National Academy of Sciences*, 99(14):9101–9106, 2002.

[309] Alain FL Creemers and Johan Lugtenburg. The preparation of all-trans uniformly 13c-labeled retinal via a modular total organic synthetic strategy. emerging central contribution of organic synthesis toward the structure and function study with atomic resolution in protein research. *Journal of the American Chemical Society*, 124(22):6324–6334, 2002.

[310] Jonathan C Lansing, Morten Hohwy, Christopher P Jaroniec, AFL Creemers, Johan Lugtenburg, Judith Herzfeld, and Robert G Griffin. Chromophore distortions in the bacteriorhodopsin photocycle: Evolution of the h- c14- c15- h dihedral angle measured by solid-state nmr. *Biochemistry*, 41(2):431–438, 2002.

[311] Inna V Kalaidzidis and Andrey D Kaulen. Cl–dependent photovoltage responses of bacteriorhodopsin: comparison of the d85t and d85s mutants and wild-type acid purple form. *FEBS letters*, 418(3):239–242, 1997.